

Sheffield Hallam University

Organo-iron compounds on clays and pillared clays.

HAMER, Julian C. E.

Available from the Sheffield Hallam University Research Archive (SHURA) at:

<http://shura.shu.ac.uk/19748/>

A Sheffield Hallam University thesis

This thesis is protected by copyright which belongs to the author.

The content must not be changed in any way or sold commercially in any format or medium without the formal permission of the author.

When referring to this work, full bibliographic details including the author, title, awarding institution and date of the thesis must be given.

Please visit <http://shura.shu.ac.uk/19748/> and <http://shura.shu.ac.uk/information.html> for further details about copyright and re-use permissions.

CITY CAMPUS POND STREET
GASTFIELD ST WID

101 585 580 6



BRN 386702

REFERENCE

ProQuest Number: 10697050

All rights reserved

INFORMATION TO ALL USERS

The quality of this reproduction is dependent upon the quality of the copy submitted.

In the unlikely event that the author did not send a complete manuscript and there are missing pages, these will be noted. Also, if material had to be removed, a note will indicate the deletion.



ProQuest 10697050

Published by ProQuest LLC (2017). Copyright of the Dissertation is held by the Author.

All rights reserved.

This work is protected against unauthorized copying under Title 17, United States Code
Microform Edition © ProQuest LLC.

ProQuest LLC.
789 East Eisenhower Parkway
P.O. Box 1346
Ann Arbor, MI 48106 – 1346

Organo-iron compounds on clays and pillared clays.

Julian C. E. Hamer

**A thesis submitted in partial fulfilment of the
requirements of Sheffield Hallam University
for the degree of Doctor of Philosophy.**

March 1998.

Sponsored by Sheffield Hallam University.



Organo-iron compounds on clays and pillared clays.

Julian C. E. Hamer.

A thesis submitted in partial fulfilment of the requirements of Sheffield Hallam University for the degree of Doctor of Philosophy.

(Ferrocenylmethyl)dimethylammonium chloride has been synthesised and the cation intercalated into the montmorillonite Westone-L. Variable temperature Mössbauer spectroscopy indicated that the molecule had a similar Debye temperature in each environment (144 ± 5 K and 140 ± 5 K respectively). The intercalated Mössbauer spectra revealed a Karayagin effect above 80 K. The cation occupies 80 % of the total exchange capacity of the clay, most likely orientated with the cyclopentadienyl rings perpendicular to the silicate layers. Thermal decomposition of the intercalate involved the volatilisation of iron containing fragments below 350°C. Variable-temperature XRD showed the intercalated sample had a d_{001} -spacing of 1.55 nm at room temperature, which decreased at 200°C to give a d_{001} -spacing of 1.3 nm. An iron oxide probably remains within the interlayer after the inserted molecule has decomposed.

2, 2''-bis[(dimethylamino)methyl]biferrocene has been synthesised and intercalated into acid exchanged Westone-L. Variable temperature Mössbauer spectroscopy revealed a Debye temperature of 172 ± 5 K which dropped to 150 ± 5 K on intercalation. The molecule was shown to occupy 75 % of the total CEC of the clay and most likely resides with the cyclopentadienyl rings perpendicular to the silicate sheet. Thermal decomposition of the biferrocene intercalate indicated the loss of iron containing fragments below 430°C. Variable-temperature XRD indicated a d_{001} -spacing of 1.65 nm at room temperature which collapsed to 1.41 nm at 250°C, after which it slowly decreased to 1.29 nm at 400°C. An iron oxide was probably left within the interlayer after the intercalated molecule had decomposed.

Contact of the biferrocene with the acid Westone-L for 3 and 48 hours resulted in 2 and 11 % oxidation to biferrocenium respectively. Contact of iodine with a suspension of the intercalated biferrocene resulted in *ca.* 16 % oxidation to biferrocene. The biferrocenium intercalate exhibited "domain" type valence electron de-trapping above 200 K until by 250 K only a single charge averaged doublet was observed.

The molecule N, N-dimethylaminomethylferrocene was successfully intercalated into aluminium pillared Westone-L, occupying 30 % of the total CEC of the original clay. The inserted molecule was found to have a Debye temperature of 113 ± 5 K as determined by variable temperature Mössbauer spectroscopy. Decomposition of the inserted molecule involved the loss of iron containing fragments below 350°C.

When heated in air the inserted molecule gave rise to high spin iron(III) in a distorted octahedral environment. Heating the sample in nitrogen and hydrogen resulted in a species characteristic of high spin octahedrally co-ordinated iron(II). At the higher temperatures, the sample heated in hydrogen exhibited a further high spin octahedrally co-ordinated iron(II) species, with a less symmetric co-ordination sphere than the first.

Dedication.

This work is dedicated to the memory of Mark Wilde B. Sc. (Hons.) Chem.
who died, tragically, in September 1997.

If I were to have a wish, it is that the “Almighty Apple” might grant you in
death what was denied you in life.

Acknowledgements.

I wish to thank the following people for their contributions, whether intellectual, emotional or material, in the production of this work.

Firstly those in the front line, my supervisors. To Chris Breen for believing, John (without an 'e') Brooks for disbelieving, and Sue Forder for pretending to believe. I think we covered almost all eventualities between us.

Next I'd like to thank my colleagues, notably Dr. Simon Scullion for providing gossip, Dr. Ruth Watson for providing papers and Dr. John Davidson for demonstrating that I could be a lot worse off.

That done I also wish to thank the following technicians: Charlie, of the headless chicken football squad, for his perseverance with the Mössbauer laboratory - even if he did end up hiding when the laboratory door opened. Thanks also to the lovely Lynn in inorganic for always being ready to drop everything in order to help.

Thanks also should be given to the "Gym Rats", Pete Hanley, Rajiv Rajan, Mo Hegaig, Levi Ferguson, Morris Berhane and Russell Limbert to name but a few, who were always there to take my mind away from what it should have been doing. Never mind, we lifted a lot of weight, played a lot of football, and visited a lot of bars - what more can you ask?

Mention should also be made of the late Mark Wilde. Mark was always quick to pull me up short when I lagged, encourage me when needed, and finally intoxicate and drag me round the clubs in a variety of locations around the U.K. when it was required. I only regret that I didn't say thank-you earlier.

Lastly I'd like to thank my family and especially one Olga Zaragoza-Gray. These took the full force of my outbursts without a comment, before kindly offering a cup of tea and a word of encouragement. (This usually occurred after a certain Dr. Breen kindly informed that my latest offering was well written, interesting, accurate and probably correct, but that in general a standard thesis shouldn't fit on the back of a post-card).

A late but vital addition to my list of thanks, goes to Norman Wight who lent me his printer (and indeed a spare refill cartridge) at the height of the printing crisis. Quite literally, this work would not be here without you, thank-you.

Contents.

1. INTRODUCTION.....	5
1.1 COMPOSITE MATERIALS.....	5
1.1.1 SOLUBLE HOSTS.....	6
1.1.1.1 Inclusion Compounds.....	6
1.1.2 INSOLUBLE HOSTS.....	9
1.1.2.1 3-Dimensional Structures.....	9
1.1.2.1.1 Zeolites.....	9
1.1.2.1.2 Aluminium Phosphates.....	11
1.1.2.2 Characterisation.....	12
1.1.2.3 2-Dimensional (Layered) Compounds.....	13
1.1.2.3.1 Non-Swelling hosts.....	14
1.1.2.3.2 Swelling hosts.....	16
1.2 CLAY.....	19
1.2.1 BACKGROUND.....	19
1.2.2 MONTMORILLONITE.....	20
1.2.3 BRØNSTED AND LEWIS ACIDITY.....	22
1.2.4 INSERTING MOLECULES INTO THE CLAY INTERLAYER.....	23
1.2.5 PILLARED CLAYS.....	25
1.2.6 PROPERTIES AND USES.....	26
1.3 CATALYSTS.....	29
1.3.1 HETEROGENEOUS IRON CATALYSTS.....	29
1.3.2 NECESSARY REQUIREMENTS.....	30
1.3.3 SYNTHESIS OF IRON IMPREGNATED MATERIALS.....	32
1.4 BIFERROCENE AND BIFERROCENIUM.....	34
1.4.1 BACKGROUND.....	34
1.4.2 PROPERTIES.....	35
1.4.3 VALENCE ELECTRON DE-TRAPPING PHENOMENA.....	37
1.5 MÖSSBAUER SPECTROSCOPY.....	41
1.5.1 INTRODUCTION.....	41
1.5.2 THEORY.....	42
1.5.2.1 Line-width and Resolution.....	47
1.5.2.2 Recoil Free Fraction.....	48
1.5.2.3 Resonant Absorption Cross Section and Re-absorption.....	53
1.5.3 EXPERIMENTAL.....	57
1.5.3.1 Source choice.....	57
1.5.3.2 Sample Preparation.....	60
1.5.3.3 Equipment.....	62
1.5.3.3.1 Transducers.....	62
1.5.3.3.2 Counters.....	63
1.5.3.3.3 Cryogenics.....	65
1.5.3.4 Acquiring a Spectrum.....	71
1.5.3.4.1 Isomer Shift.....	74
1.5.3.4.2 Quadrupole Splitting.....	78
1.5.3.4.3 Hyperfine Splitting.....	82
1.5.3.4.4 Calibration of the Spectrum.....	84
1.5.3.5 Data analysis.....	85

1.5.3.5.1 The Lorentzian Line.....	85
1.5.3.5.2 The Fitting of Complex Spectra.....	86
1.5.3.5.3 The Analysis of Variable Temperature Data; LNAT and ISODS.	89
1.5.3.6 Information available from experiment.....	92
1.5.3.6.1 Oxidation state.....	92
1.5.3.6.2 Local environment.....	93
1.5.3.6.3 More Complicated Spectra.....	95
1.6 OTHER TECHNIQUES.....	96
1.6.1 ULTRA-VIOLET SPECTROMETRY (U.V.).....	96
1.6.2 C, H, N ANALYSIS.....	96
1.6.3 X-RAY FLUORESCENCE SPECTROMETRY (XRF).....	96
1.6.4 VARIABLE TEMPERATURE INFRA-RED SPECTROSCOPY (VT-IR).....	97
1.6.5 THERMOGRAVIMETRIC ANALYSIS.....	98
1.6.6 THERMAL DESORPTION MASS SPECTROSCOPY (TD-MS).....	98
1.6.7 VARIABLE TEMPERATURE X-RAY DIFFRACTION (VT-XRD).....	99
1.7 THE PROJECT.....	100
1.7.1 N, N - DIMETHYLAMINOMETHYLFERROCENE ON CLAY.....	100
1.7.2 BIFERROCENE/BIFERROCENIUM ON CLAY.....	101
1.7.3 SYNTHESIS AND HEAT TREATMENTS OF A-APWL.....	102
1.7.4 GLOSSARY OF TERMS.....	103
<u>2. N, N-DIMETHYLAMINOMETHYLFERROCENE ON WESTONE-L.....</u>	<u>104</u>
2.1 EXPERIMENTAL METHODS.....	104
2.1.1 MATERIALS.....	104
2.1.2 PREPARATION.....	104
2.1.2.1 Sodium Exchanged Westone-L.....	104
2.1.2.2 Acid Exchanged Westone-L.....	105
2.1.2.3 (ferrocenylmethyl)dimethylammonium chloride.....	105
2.1.3 EXCHANGE PROCEDURES.....	105
2.1.3.1 The intercalation of (ferrocenylmethyl)dimethylammonium into Westone-L.....	105
2.1.3.2 Intercalation of N,N-Dimethylaminomethylferrocene into Na-WL.....	106
2.1.4 ADSORPTION ISOTHERMS.....	107
2.2 RESULTS AND DISCUSSION.....	108
2.2.1 ADSORPTION ISOTHERMS.....	108
2.2.2 X-RAY FLUORESCENCE.....	110
2.2.3 INFRA-RED SPECTROSCOPY.....	112
2.2.4 THERMOGRAVIMETRIC ANALYSIS.....	113
2.2.5 THERMAL DESORPTION MASS SPECTROSCOPY.....	115
2.2.6 VARIABLE TEMPERATURE X-RAY DIFFRACTION.....	118
2.2.7 VARIABLE TEMPERATURE MÖSSBAUER SPECTROSCOPY.....	123
2.3 CONCLUSIONS.....	135
2.4 FUTURE WORK.....	136
<u>3. BIFERROCENE / BIFERROCENIUM ON CLAY.....</u>	<u>138</u>
3.1 EXPERIMENTAL.....	139
3.1.1 MATERIALS.....	139
3.1.2 COMPOUND PREPARATION.....	139
3.1.2.1 2,2'' - and 2,5'' - bis[(dimethylamino)methyl]biferrocene.....	139
3.1.2.2 [2,2'' - bis[(dimethylammonium)methyl]biferrocene] Westone-L.....	140

3.1.2.3 [2,2'' - bis[(dimethylammonium)methyl]biferrocenium]-HWL	141
3.2 RESULTS AND DISCUSSION.....	142
3.2.1 INFRA-RED SPECTROSCOPY	142
3.2.2 THERMOGRAVIMETRIC ANALYSIS.	142
3.2.3 THERMAL DESORPTION MASS SPECTROSCOPY.	144
3.2.4 VARIABLE TEMPERATURE X-RAY DIFFRACTION.	147
3.2.5 VARIABLE TEMPERATURE MÖSSBAUER SPECTROSCOPY.	151
3.2.5.1 2,2''-bis[(dimethylammonium)methyl]biferrocene.....	151
3.2.5.2 Mössbauer spectra of AA-HWL, AA-HWL(48) and AA ⁺ -HWL	153
3.3 CONCLUSIONS.	168
3.4 FUTURE WORK.....	170

4. THE SYNTHESIS AND HEAT TREATMENTS OF A-APWL.....172

4.1 EXPERIMENTAL.	173
4.1.1 MATERIALS.....	173
4.1.2 SAMPLE PREPARATION.	173
4.1.2.1 Sodium Exchanged Westone-L.	173
4.1.2.2 Pillaring of Westone-L.	174
4.1.2.3 Insertion of N,N-Dimethylaminomethylferrocene into APWL.....	174
4.1.2.4 Heat Treatment of A-APWL in Air.....	175
4.1.2.5 Heat Treatment of A-APWL in Nitrogen.	175
4.1.2.6 Heat Treatment of A-APWL in Hydrogen.....	176
4.1.2.7 Heat treatment of Na-WL and APWL.....	176
4.2 RESULTS AND DISCUSSION.....	177
4.2.1 XRF AND CHN ANALYSIS.	177
4.2.2 INFRA-RED SPECTROSCOPY.	177
4.2.3 THERMOGRAVIMETRIC ANALYSIS.	178
4.2.4 THERMAL DESORPTION MASS SPECTROSCOPY.	180
4.2.5 X-RAY DIFFRACTION.	182
4.2.6 MÖSSBAUER SPECTROSCOPY.....	183
4.2.6.1 APWL	183
4.2.6.2 A-APWL	187
4.2.6.3 Fitting of Mössbauer spectra for heated samples.	192
4.2.6.3.1 Sample Heat Treated in Air	193
4.2.6.3.2 Sample heat treated in nitrogen.....	198
4.2.6.3.3 Samples Heat Treated in Hydrogen.....	201
4.3 CONCLUSIONS.	206
4.4 FUTURE WORK.....	208

5. CONCLUSIONS.210

6. TABLE OF EQUATIONS.215

7. TABLE OF FIGURES.217

8. INDEX OF TABLES.....219

9. REFERENCES.....220

10. POSTGRADUATE STUDY.....226

10.1 COURSES AND CONFERENCES.226

10.2 PUBLICATIONS.227

1. Introduction.

1.1 Composite Materials.

Composite materials are the result of incorporating a “guest” species into a “host” lattice. The resulting materials often show different physical properties to either of the precursors. Such properties include changes, either enhancing or diminishing by many orders magnitude, the electrical resistivity^{1,2}, the super-conducting temperature^{3,4,5}, the specific heat and related properties of the solid⁶, the optical^{7,8,9} and magnetic^{10,11} properties, and even the structural properties of the system^{12,13,14}.

Although exchange of cations within clays (see section 1.2) and zeolites (see section 1.1.2.1.1) has been known for some time¹⁵, it was not until the early sixties when

¹ F. Kanamaru, M. Shimada, M. Koizumi, and T. Takada, *J. Solid State Chem.*, **1973**, 7, 1.

² S. Kikkawa, F. Kanamaru, and M. Koizumi, *Bull. Chem. Soc. Jpn.*, **1979**, 52, 963.

³ S. M. Whittingham, *Prog. Solid State Chem.*, **1978**, 12, 41.

⁴ R. Schollhorn, A. Lerf, F. Sernetz, *Z. Naturforsch.*, **1974**, 29B, 810.

⁵ *Mater. Res. Bull.*, **1974**, 9, 1597.

⁶ S. F. Meyer, R. E. Howard, G. R. Stewart, J. U. Acrivos, T. H. Geballe, *J. Chem. Phys.*, **1975**, 62, 441.

⁷ S. A. Solin, *Physica B+C*, **1980**, 99, 443.

⁸ R. J. Nemanich, S. A. Solin, and D. Guérard, *Phys. Rev. B*, **1977**, 16, 2965.

⁹ C. Underhill, S. Y. Leung, G. Dresselhaus, and M. S. Dresselhaus, *Solid State Commun.*, **1979**, 29, 769.

¹⁰ T. R. Halbert, D. C. Johnston, L. E. McCandlish, A. H. Thompson, J. C. Scanlon, and J. A. Dumesic, *Physica B+C*, **1980**, 99, 128.

¹¹ M. Eibschutz and F. DiSalvo, *Phys. Rev. Lett.*, **1976**, 36, 104.

¹² R. R. Chianelli, J. C. Scanlon, M. S. Whittingham, and F. R. Gamble, *Inorg. Chem.*, **1975**, 14, 1691.

¹³ R. R. Gamble, J. H. Osiecki, and F. J. DiSalvo, *J. Chem. Phys.*, **1971**, 55, 3525.

¹⁴ G. A. Wieggers, *Physica B+C*, **1971**, 99, 151.

¹⁵ R. L. Grim, “*Clay Mineralogy*”, **1953**, McGraw and Hill, London, UK.

Hagenmuller *et al.*^{16,17} demonstrated the ability of lamellar oxide halides of transition metals $M^{III}OX$ ($X = Cl, Br$) to undergo intercalation, that interest in composite materials began to really take-off. In an effort to give an idea of how composite materials are formed, we are going to divide them into two groups. In the first instance we will consider those materials formed using a soluble host, and later on we will consider insoluble hosts. (As this work is concerned with ferrocene type molecules, most of the following will be centred around composite materials containing a metallocene).

1.1.1 Soluble Hosts.

1.1.1.1 Inclusion Compounds.

Inclusion compounds are formed by crystallisation from a solution containing both the host and guest species. Common hosts include such structures as urea, thiourea and cyclodextrins. Lately the unusual and somewhat exotic, Buckminster fullerene or C_{60} molecule, has not only been used as a host¹⁸, but also as a guest within a γ -cyclodextrin¹⁹. Thiourea and urea have similar structures formed of hexagonal channels with trigonal symmetry, stacking in a spiral arrangement. Urea has a smaller channel diameter able to encapsulate small linear and branched hydrocarbon chains²⁰, while thiourea can

¹⁶ P. Hagenmuller, J. Rouxel, J. David, A. Colin, and B. Le Neindre, *Z. Anorg. Allg. Chem.*, **1963**, *323*, 1-12.

¹⁷ P. Hagenmuller, J. Portier, B. Barbe, and P. Bouclier, *Id.*, **1967**, *355*, 209.

¹⁸ J. Reichenbach, F. Rachdi, I. Lukyanchuk, M. Ribet, G. Zimmer, and M. Mehring, *J. Chem. Phys.*, **1994**, *101(6)*, 4585-4592.

¹⁹ K. Kanazawa, H. Nakanishi, Y. Ishizuka, T. Nakamura, and M. Marsumoto, *Fullerene Science and Technology*, **1994**, *2(2)*, 189-194.

²⁰ W. Schlenk, *Justus Liebigs Ann. Chem.*, **1949**, *565*, 204.

accommodate larger bulky molecules such as cyclic hydrocarbons²¹. The first metallocene inclusion was a clathrate formed of ferrocene and thiourea by Clement *et al*²² in 1974. As far as the author is aware, this is the first composite material to contain a metallocene. Cyclodextrins are naturally occurring macrocyclic glucose polymers containing a minimum of six D(+)-gluco-pyranose units, attached by α -(1,4) linkages. These usually stack-up side by side to give a channel type structure. Interestingly, it is only recently (1984), that a metallocene has been incorporated within a cyclodextrin²³.

One of the main obstacles in characterising a composite material is in trying to verify that the guest moiety is actually contained within the host, and not merely a physical mixture or chemisorbed to the surface. Techniques such as infra-red and ultra-violet/visible spectroscopy can be used to establish an interaction between the host and guest, but are not often conclusive. In the case of most inclusion compounds, the use of single crystal x-ray diffraction is critical to unambiguous assignment of the structure.

In some cases even this does not give the whole story. Guest dynamics and electron transfer can lead to complicated and misleading spectra. For instance, the ferrocene-thiourea clathrate was originally synthesised in 1974²². A Mössbauer study by Gibb²⁴ in 1976 indicated that the ferrocene molecules were orientated either parallel or perpendicular to the channels (but not tilted) in approximately a 50:50 ratio, possibly alternating between the two. In addition, between 141 and 153 K all the ferrocenes perpendicular to the channels began to reorient rapidly about the channel axis (A further

²¹ W. Schlenk, *Justus Liebigs Ann. Chem.*, **1951**, 573, 142.

²² R. Clement, R. Claude, C. Mazieres, *J. Chem. Soc., Chem. Commun.*, **1974**, 654-655.

²³ A. Harada and S. Takahashi, *J. Chem. Soc., Chem. Commun.*, **1984**, 645.

Mössbauer study refined the phase change temperature to 160 K²⁵). By 200 K transformation between the perpendicular and parallel orientations occurs, so that by 295 K almost all the ferrocene molecules are averaged on the Mössbauer time-scale ($\leq 10^7$ s⁻¹). In 1978 this was confirmed using single crystal x-ray diffraction²⁶. In 1980, a study using ¹H nuclear magnetic resonance (NMR) showed a proton second moment below 140 K consistent with a reorientation process about the C₅ axis of the ferrocene molecules. This decreased steadily until 200 K, where it decreased only marginally, until by 295 K it had reached a value consistent with an isotropic distribution of ferrocene. This is broadly consistent with the phase changes at 160 and 200 K observed in the Mössbauer experiment²⁷. In 1986 a further study using cross polarisation ¹³C NMR, confirmed that there were at least two reorientation processes in effect²⁸. The first involved the onset of rotation about the C₅ axis of the ferrocene at 160 K, and the second process involved a switching between the parallel and perpendicular arrangement in the channels over the temperature range 125-294 K. In 1991 yet another study was published. In this, ²H NMR was used to show that the ferrocenes did indeed reorientate about the C₅ axis at 160 K, and more specifically that the molecule switched between three orientations perpendicular to the channels²⁹. In addition it appeared that interchange between the perpendicular and parallel orientations also began at this temperature, and that by 220K, the reorientation was too fast to observe by ²H NMR.

²⁴ T. C. Gibb, *J. Phys. C: Solid State Phys.*, **1976**, *9*, 2627-2642.

²⁵ M. D. Lowery, R. J. Wittebort, M. Sorai, and D. N. Hendrickson, *J. Am. Chem. Soc.*, **1990**, *112*, 4214-4225.

²⁶ E. Hough and D. G. Nicholson, *J. Chem. Soc., Dalton. Trans.*, **1978**, 15-18.

²⁷ R. Clément, M. Gourdjji and L. Guibé, *Chem. Phys. Letters*, **1980**, *72*, 466.

²⁸ T. Nalai, T. Terao, F. Imashiro and A. Saika, *Chem. Phys. Letters*, **1986**, *132*, 554-557.

²⁹ S. J. Heyes, N. J. Clayden, and C. M. Dobson, *J. Phys. Chem.*, **1991**, *95*, 1547-1554.

The preceding 17 year saga demonstrates that guest species dynamics can be a complicated field, requiring many techniques to obtain a full picture of the composite material produced.

1.1.2 Insoluble Hosts.

1.1.2.1 3-Dimensional Structures.

Channel structures are porous networks similar to a bath sponge. Common examples include zeolites and aluminium phosphates. Insertion of the guest is normally achieved by one of two methods. The first involves contacting the dehydrated host with a solution of the guest, while the second involves contacting the dehydrated host with a liquid or gaseous guest.

1.1.2.1.1 Zeolites.

Zeolite chemistry is a large field, so here follows a brief overview for those unfamiliar with the basic features of these materials. Zeolites are 3-dimensional porous networks of AlO_4 and SiO_4 tetrahedra, linked by the sharing of oxygen atoms. The general composition can be written as $[(\text{M}^{n+})_{x/n}(\text{AlO}_2)_x(\text{SiO}_2)_{1-x}]$; where M^{n+} is a charge compensating cation, and x can assume values between 0 and 0.5. They are widespread naturally, although chemical synthesis has been possible since the early 1940's³⁰.

³⁰ R. M. Barrer, "*Hydrothermal Chemistry of Zeolites*", 1972, Academic Press, New York, USA.

Substitution of the Al and Si ions is common, leaving the framework with a net negative charge which is counterbalanced by the aforementioned cations. Under favourable conditions it is possible to exchange these cations. The zeolites occur in numerous structures, some of which are constituted of channels (mordenite, zeolite-L, mazzite), and others which are comprised of cage-like voids called super-cages (faujasite).

Many different types of molecules have been inserted into zeolites since the 1960's, although the earliest metallocene insertion did not occur until 1986³¹. It was found that the uptake of ferrocene by the zeolite Na-Y (zeolite Y is a faujasite type zeolite), was prevented by water molecules blocking the entrance to the super-cages. However, after extensive dehydration of the zeolite followed by contact of a pentane solution of ferrocene, 90% of the ferrocene was absorbed within 3 minutes³². An attempt to insert ferrocene into the acid zeolite H₄₈Na₈Y resulted in the exclusive incorporation of ferrocenium ions³². It was discovered that this was concurrent with the loss of α -cage hydroxyl groups. As these groups are homogeneously distributed throughout the zeolite lattice, this is a good indication that the ferrocenium molecules are evenly distributed throughout, and more importantly within, the zeolite crystals. This was confirmed by using isotopically H/D labelled zeolites. The results showed an α -cage Brønsted acid site-specific electron transfer, a redox-induced H atom/lattice OH radical production of H₂O, and concurrent production of ferrocenium, with three co-ordinate Al and Si framework radical centres³². Thermal treatment of the resulting material led to a zeolite

³¹ G. A. Ozin and J. P. Godber, "In Intrazeolite Organometallics: Spectroscopic Probes of Internal versus External Confinement of Metal Guests. *Excited States and Reactive Intermediates: Photochemistry, Photophysics and Electrochemistry*", 1986, ACS Symposium Series 307, American Chemical Society, Washington DC, USA.

³² G. A. Ozin, J. Godber, *J. Phys. Chem.*, 1989, 93, 878.

anchored half-sandwich complex³³. These studies illustrate that metallocenes are well suited for anchoring organoiron fragments to specific binding sites in molecular sieve supports, by establishing a stable bond to the ring-shaped oxygen co-ordination sites in the cage system. This is a very valuable property in the synthesis of heterogeneous catalysts (see section 1.3).

1.1.2.1.2 Aluminium Phosphates.

Aluminium phosphates (AlPO_4) are channel structures formed from alternating AlO_4 and PO_4 tetrahedra. The framework is electrically neutral, without ion-exchange properties or strong acid sites. The two main structural isotopes are the orthorhombic AlPO_{4-8} and the smaller hexagonal AlPO_{4-5} ³⁴, although a larger channel version designated VPI-5³⁵ is also widespread. The VPI-5 structures converts to AlPO_{4-8} at temperatures greater than 60°C ³⁶.

To date various metallocenes have been incorporated in aluminium phosphates, the first being ferrocene in 1991³⁷.

³³ A. Borvornwattanont, K. Moller, T. Bein, *J. Phys. Chem.*, **1989**, *93*, 4562.

³⁴ S. T. Wilson, B. M. Lok, C. A. Messina, T. R. Cannan, and E. M. Flanigen, *J. Am. Chem. Soc.*, **1982**, *104*, 1146.

³⁵ M. E. Davis, C. Saldarriaga, C. Montes, J. Garces, and C. Crowder, *Nature(London)*, **1988**, 698.

³⁶ E. T. C. Vogt and J. W. Richardson, *J. Solid State Chem.*, **1990**, *87*, 469.

³⁷ T. Lindblad and B. Rebenstorf, *J. Chem. Soc. Faraday Trans.*, **1991**, *87(15)*, 2473-2478.

1.1.2.2 Characterisation.

Characterisation of these 3-dimensional networks is extremely difficult. Single crystal x-ray diffraction is not possible due to the inability to grow a single crystal. Powder diffraction techniques are limited in use as the dimensions of the host do not usually change on insertion, and the inserted molecule may be very dilute or arranged with little or no long range order. In order to confirm that the guest has successfully inserted, other techniques have to be utilised. These include: (i) size exclusion involving both host and guest variations³⁸; (ii) size/shape-discerning chemical/catalytic reactions³⁹; (iii) size dependant poisoning reactions⁴⁰; (iv) mid-IR vibrational symmetry/frequency perturbations of the guest molecule⁴¹; (v) perturbations of the far IR cation translatory modes by the guest⁴²; (vi) electron paramagnetic resonance⁴³ (EPR) and NMR⁴⁴ relaxation effects; (vii) surface and bulk sensitive spectroscopy probes (e.g. x-ray photoelectron spectroscopy⁴⁵ (XPS), tunnelling emission microscopy⁴⁶ (TEM) and XRD⁴⁷); (viii) in the case of zeolites, spatially resolved intra-zeolite redox titrations involving Brønsted acid sites (see section 1.1.2.1.1, page 10). In the quest for an

³⁸ G. A. Ozin, D. M. Haddleton, and C. J. Gil, *J. Phys. Chem.*, **1989**, *93*, 6710.

³⁹ T. Huang and . Schwartz, *J. Am. Chem. Soc.*, **1982**, *104*, 5244.

⁴⁰ N. Herron, G. D. Stucky, and C. A. Tolman, *Inorg. Chim. Acta.*, **1985**, *100*, 135.

⁴¹ T. Bein, S. J. McLain, D. R. Corbin, R. D. Farlee, K. Moller, G. D. Stucky, G. Woolery, and D. Sayers, *J. Am. Chem. Soc.*, **1988**, *110*, 1801.

⁴² G. A. Ozin and J. P. Godber, "In Intrazeolite Organometallics: Spectroscopic Probes of Internal versus External Confinement of Metal Guests. *Excited States and Reactive Intermediates: Photochemistry, Photophysics and Electrochemistry*", **1986**, ACS Symposium Series 307, American Chemical Society, Washington DC, USA.

⁴³ M. Koichi, S. Imamura, and J. H. Lunsford, *Inorg. Chem.*, **1984**, *23*, 3510.

⁴⁴ E. H. Yonemoto, Y. I. Kim, R. H. Schmehl, J. O. Wallin, B. A. Shoulders, B. R. Richardson, J. F. Haw, and T. E. Mallouk, *J. Am. Chem. Soc.*, **1994**, *116*(23), 10557-10563.

⁴⁵ Y. S. Yong and R. F. Howe, *J. Chem. Soc., Faraday Trans.*, **1986**, *82*, 2887.

⁴⁶ G. Meyer, D. Wohrle, M. Mohl, and G. Schultz-Ekloff, *Zeolites*, **1984**, *4*, 30.

⁴⁷ W. V. Cruz, P. C. W. Leung, and K. Seff, *J. Am. Chem. Soc.*, **1978**, *100*, 6997.

unambiguous characterisation of the structure, a combination of two or more of the techniques listed above are used. For instance, in the case of the ferrocene- $\text{AlPO}_4\text{-5}$ and ferrocene- $\text{AlPO}_4\text{-8}$ complexes, a combination of extended x-ray absorption fine structure (EXAFS) analysis and Mössbauer Spectroscopy was used to characterise the materials^{48,49}. This revealed that the ferrocene resided within the channel, and that apart from the $\text{AlPO}_4\text{-5}$ at temperatures below 20 K, the ferrocene exhibited a dynamically averaged spectrum⁴⁹. Calcination of the complexes indicated that the ferrocene had decomposed within the channel (none was sublimed), and that the iron had not formed clusters, but had been co-ordinated within one of the six-membered oxygen rings surrounding the channel⁴⁸.

1.1.2.3 2-Dimensional (Layered) Compounds.

2-dimensional compounds generally consist of strong covalently bonded layers in the *ab* plane, which then stack up with weak Van der Waals or Coulombic interactions in the *c* direction. The best known examples of layered structures are probably graphite and clay (see section 1.2). In 1975 the first metallocene intercalation into a layered structure was reported by Dines⁵⁰, since when this area of research has grown into a field in its own right^{51,52}. Layered compounds fall into two main categories, non-swelling and swelling hosts.

⁴⁸ A. Lund, D. G. Nicholson, G. Lambie, and B. Beagley, *J. Mater. Chem.*, **1994**, *4*(11), 1723-1730.

⁴⁹ A. Lund, D. G. Nicholson, R. V. Parish, and J. P. Wright, *Acta Chemica Scandinavica*, **1994**, *48*, 738-741.

⁵⁰ M. B. Dines, *Science*, **1975**, *188*, 1210.

⁵¹ R. P. Clement, W. B. Davies, K. A. Ford, M. L. H. Green, and A. J. Jacobson, *Inorg. Chem.*, **1978**, *17*, 2754.

1.1.2.3.1 Non-Swelling hosts.

Non-swelling hosts have a constant distance separating the layers. They do not normally have molecules (such as water) present in the interlayer, and so are impervious to atmospheric conditions. In addition they are unlikely to separate when placed in solution. As an example of a non-swelling host, let us consider graphite.

To date a number of atomic and molecular species have been inserted into graphite, from alkali metals⁵³ to transition metal halides⁵⁴. The author has found no reports concerning the intercalation of metallocenes. Intercalation into graphite normally involves the use of high temperatures and reduced pressure, which is normally accompanied by some sort of redox process. These conditions are not conducive to the innocuous insertion of metallocenes. It is likely that any attempt to insert a metallocene by this route would result in the decomposition of the metallocene, or in serious disruption of the graphite lattice.

Non-swelling lattices have provided many novel materials. For instance, there are examples of semi-conducting layered structures resulting from the introduction of metals into a layered hosts such as LiTiS_2 ⁵⁵. The layered structure FePS_3 is a semiconductor. However, intercalation with tetraethylammonium, followed by reaction with $(\text{TTF})_3(\text{BF}_4)_2$ affords $\text{Fe}_{(1-x)}\text{PS}_3(\text{TTF})_2$, ($x \approx 0.18$, TTF = tetrathiafulvalene), which is

⁵² J. Rouxel, "Layered Materials and Intercalates", 1980, pp 3-11, North Holland, Amsterdam, Netherlands.

⁵³ L. E. Campbell, G. L. Montet, and G. J. Perlow, *Phys. Rev. B*, 1977, B15, 3318.

⁵⁴ N. Saito, T. Tominaga, M. Takeda, Y. Ohe, F. Ambe, and H. Sano, *Nippon Arsatapu Kaigi Hobunshu*, 1967, 231.

metallic in character⁵⁶. In effect, by introducing an organic molecule into a semi-conducting material, a metal-like material is produced. In addition Gamble *et al.*⁵⁷ have intercalated organic amides into tantalum/niobium dichalogenides to give a two dimensional superconductor.

O'Hare⁵⁸ and co-workers have intercalated cobaltocene into tin dichalogenides ($\text{SnS}_x\text{Se}_{(1-x)}$), and by a combination of neutron diffraction and deuterium NMR showed that the inserted cobaltocene molecules line up with their principal (C_5) axis parallel to the layers. They went on to show that the conductivity of the intercalated material varied, from metallic in character, where there was a high sulphur and low selenium ratio, through semi-conducting, to super-conducting materials where the sulphur ratio was low and the selenium ratio high.

The most cogent information on the characterisation of these intercalated compounds comes from x-ray diffraction. When a molecule is inserted within the layers, an increase in the interlayer spacing is observed on the XRD trace. This increase is directly related to the size of the inserted molecule. Therefore, if the inserted molecule is not spherical/cubic, then the orientation of the molecule in the interlayer can be deduced. In addition, if the molecule is distributed homogeneously throughout the solid, then only the one spacing will be observed. If the molecule is present only in certain domains, then a peak will be observed for both the inserted and non-inserted regions. Coupled with the

⁵⁵ P. C. Klipstein and R. H. Friend, *J. Phys. Chem.*, **1984**, *17*, 2713-2721.

⁵⁶ L. Lomas, P. Lacroix, J. P. Audière, and R. Clément, *J. Mater. Chem.*, **1991**, *1(3)*, 475-476.

⁵⁷ F. R. Gamble, F. J. DiSalvo, R. A. Klemm, and T. H. Gaballe, *Science*, **1970**, 568-575.

⁵⁸ D. O'Hare, *Chem. Soc. Rev.*, **1992**, 121-126.

techniques utilised in the characterisation of zeolitic type hosts (see section 1.1.2.2), this makes the explicit assignment of structures considerably less obscure.

1.1.2.3.2 Swelling hosts.

Swelling hosts have a variable interlayer distance. Often they have molecules (such as water) present in the interlayer, and so the interlayer gap can vary with different atmospheric conditions or solvents. Generally, intercalation involves the contact of the dried host with a solution of the guest.

The sheer volume of literature on intercalation compounds with swelling hosts is staggering. As an example, Rodríguez-Castellón *et al.* have intercalated pyridine type compounds into tin hydrogenphosphate hydrate⁵⁹. Successful intercalation into the tin hydrogenphosphate hydrate, was found to depend on the basicity of the nitrogen. Hence, weak bases such as bipyridines were not intercalated, whereas stronger bases, such as pyridines were intercalated. Interestingly, only 20% exchange was achieved with pyridine itself. It was suggested that the pyridine was binding to the strong Brønsted acid sites within the structure, thus preventing further access to the weaker Lewis acid sites.

Other work has focused upon the intercalation of organometallic molecules, notably metallocenes. Reports by Palvadeau *et al.*⁶⁰, show that inclusion of ferrocene into FeOCl,

⁵⁹ E. Rodríguez-Castellón, A. Rodríguez-García, and S. Bruque, *Inorg. Chem.*, **1985**, *24*(8), 1187-1190.

⁶⁰ P. Palvadeau, L. Coïc, J. Rouxel, F. Mènil, and L. Fournès, *Mat. Res. Bull.*, **1981**, *16*, 1055-1065.

leads to partial oxidation of the ferrocene, which then exhibits an electron delocalised structure above 245 K.

Ferrocene, together with the associated alkyl derivatives, have also been inserted into vanadylphosphates⁶¹. This is basically a redox process. The ferrocene is oxidised and the vanadium reduced. This reaction provides the driving force for the intercalation. It was found that progressively extending the alkyl chain resulted in less intercalation. This was possibly due to the increasing bulkiness of the side chain approaching some steric limit. Investigations of the intercalation and subsequent oxidation of ferrocenylalkylammonium cations into vanadylphosphates, indicated that the orientation and amount of oxidation of the inserted molecule, was related to a) the length of the alkyl chain, and b) the interaction between the ammonium group and the vanadium centre⁶².

O'Hare *et al.*⁶³ have also studied the intercalation of aminoferrocenes into layered hosts. Using a variety of techniques, it was demonstrated that when 2-aminoethylferrocene was intercalated into MoO₃, the inserted molecules formed a bilayer, with the C₅ axis of the rings perpendicular to the layers. However, when inserted into Zr(HPO₄)₂, the 2-aminoethylferrocene formed a bilayer with the C₅ axis of the rings parallel to the layers.

Lately there have been reports of the intercalation of biferrocene molecules into VOPO₄ and V₂O₅⁶⁴. The intercalation of VOPO₄ with a biferrocene containing a methylene

⁶¹ G. Matsubayashi, S. Ohta, and S. Okanu, *Inorg. Chim. Acta*, **1991**, *184*, 47-52.

⁶² S. Okanu and G. Matsubayashi, *J. Chem. Soc., Dalton Trans.*, **1992**, 2441-2445.

⁶³ S. J. Mason, L. M. Bull, C. P. Grey, S. J. Heyes, and D. O'Hare, *J. Mater. Chem.*, **1992**, *2(11)*, 1189-1194.

⁶⁴ S. Okuno and G-E. Matsubayashi, *Chemistry Letters*, **1993**, 799-802.

bridge resulted in one of the ferrocene centres being oxidised to give biferrocenium. However, when a biferrocene containing an ethylene bridge was intercalated, both the ferrocene centres were oxidised. Both the molecules were thought to lie with their long axis parallel to the host lattice sheet. The ethylene bridged complex however, was just long enough for the second ferrocene centre to interact with next nearest vanadium centre, enabling the second oxidation to occur. In the V_2O_5 the vanadium centres are closer together and both the methylene and ethylene bridged complexes are fully oxidised upon intercalation.

It is obvious from these findings, that there is a subtle interplay between host and guest which defines the orientation of the included molecule, and also the final properties of the material.

Once again the principal technique in the characterisation of swelling hosts is x-ray diffraction. As with the swelling hosts this can provide information as to whether and to what extent the molecule has inserted, and also how it is orientated. However, there is a limiting factor with swelling lattices. It has been noted by various people, that the increase in interlayer distance is not commensurate with the dimensions of the inserted molecule^{65,66}. Typically there is a 0.1-0.2 nm deficit between the observed and predicted values. In the case of molecules which are close to spherical/cubic in shape, this prevents definitive conclusions concerning the orientation of the inserted molecule.

⁶⁵ J. W. Johnson, *J. Chem. Soc. Chem. Commun.*, **1980**, 263.

⁶⁶ P. Aldebert and V. Paul-Boncour, *Mater. Res. Bull.*, **1983**, *18*, 1263.

1.2 Clay

1.2.1 Background

Clays are layered aluminosilicate materials, a little like a 2-dimensional zeolite but without the channels. Phyllosilicates, as they are sometimes known, are essentially made up of layers formed by the condensation of sheets of linked $\text{Si}(\text{O},\text{OH})_4$ tetrahedra with those of linked $\text{M}_{2-3}(\text{OH})_6$ octahedra, where M is either a divalent or trivalent cation. Condensation in a 1:1 ratio gives rise to the two-sheet or dimorphic minerals of general formula $\text{M}_{2-3}\text{Si}_2\text{O}_5(\text{OH})_4$, of which kaolinite is the best known example. Condensation in a 2:1 ratio gives rise to the three sheet or trimorphic clays of general formula $\text{M}_{2-3}\text{Si}_4\text{O}_{10}(\text{OH})_2$, of which mica is probably the best known. Four-sheet or tetramorphic minerals also exist, in which the trimorphic units alternate with $\text{M}(\text{OH})_{2-3}$ sheets of octahedrally co-ordinated M^{2+} or M^{3+} ions. An example of this sort of structure would be chlorite. These layers stack up like a pile of paper, although a more realistic analogy would be to throw the pile of paper in the air, and then look at the resulting disordered arrangement on the floor.

The Si^{4+} and / or $\text{M}^{2+/3+}$ in the layers can be replaced by cations of similar size, but a different, usually lower, valency. This is known as isomorphous substitution or replacement. As a result of isomorphous substitution, the layers in many phyllosilicates are negatively charged. This is usually overcome by the sorption of cations into the interlayer spaces, and very occasionally by internal substitution. Under favourable conditions these interlayer cations can be exchanged. The amount as well as the site of the isomorphous replacement influences the surface and colloidal properties of the clay

(e.g. swelling in water), since they dictate the surface density of charge and the cation-silicate layer interaction. The charge per unit formula, (x), thus becomes an important parameter and can be used to classify phyllosilicates (as recommended by the Nomenclature Committee of the Clay Minerals Society⁶⁷). The resident interlayer cations play an important role in determining the interlayer spacing. A high, densely charged cation will pull the layers closer together, while a large highly hydrated cation will push the layers apart.

1.2.2 Montmorillonite

In our work, we used the Texas montmorillonite Westone-L. Montmorillonite is a dioctahedral smectite, a subgroup of the 2:1 type minerals. The basic structure was first given by Hofmann, Endell, and Wilm⁶⁸, although further modifications by Marshall⁶⁹, Maegdefrau and Hofmann⁷⁰, and Hendricks⁷¹ were later incorporated to give the structure generally accepted today⁷². The structure is based on that of pyrophyllite, composed of a sheet of edge sharing alumina octahedra, sandwiched between two sheets of corner sharing silica tetrahedra. The silica tetrahedra all point inwards towards the alumina octahedra. The octahedral aluminium is frequently replaced by such ions as Mg^{2+} and $Fe^{2+/3+}$, and somewhat less frequently the tetrahedral silicon is replaced by Al^{3+} . Although a little internal compensation may occur, the final result is a layer that carries a

⁶⁷ P. G. Nahin, *Clays Clay Minerals*, 1963, 10, 257-271.

⁶⁸ U. Hofmann, K. Endell, and D. Wilm, *Z. Krist.*, 1933, 86, 340-348.

⁶⁹ C. E. Marshall, *Z. Krist.*, 1935, 91, 433-449.

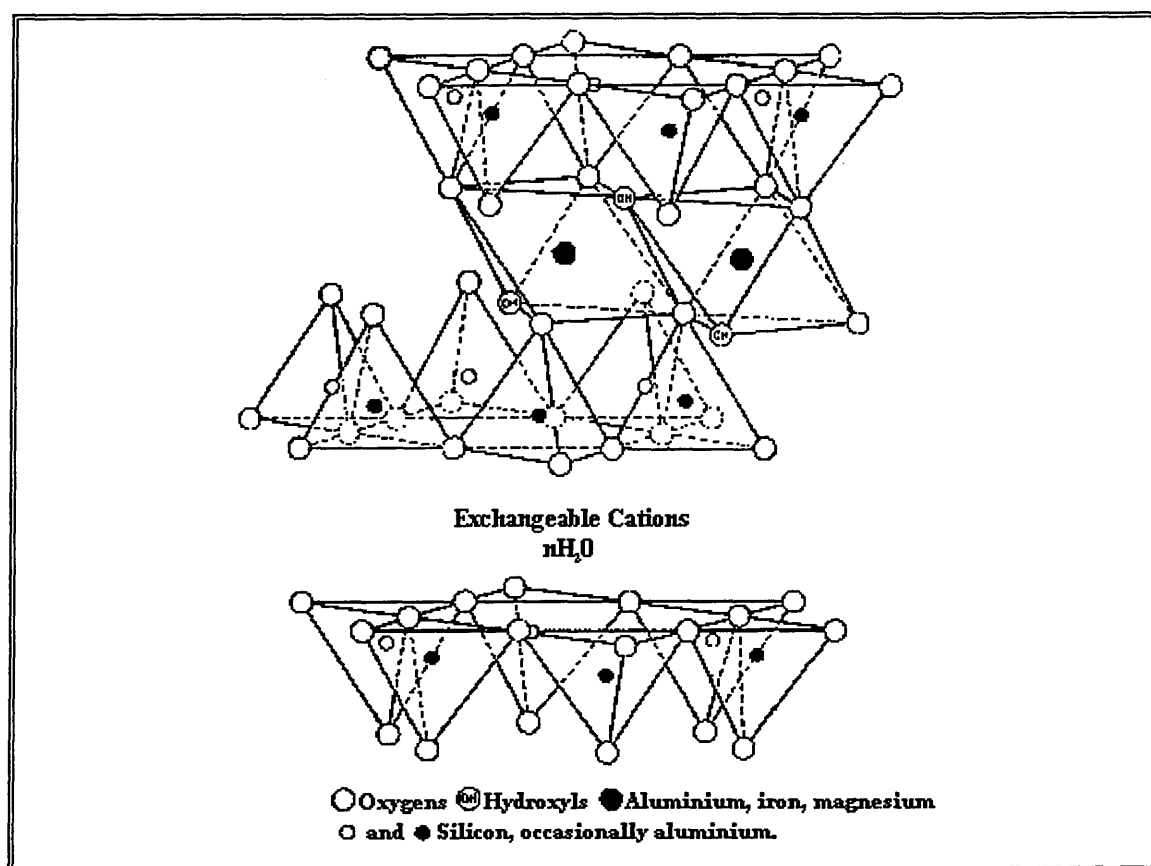
⁷⁰ E. Maegdefrau and U. Hofmann, *Z. Krist.*, 1937, 98, 299-323.

⁷¹ S. B. Hendricks, *J. Geol.*, 1942, 50, 276-290.

⁷² J. W. Jordan, *Clays Clay Minerals*, 1963, 10, 299-308.

permanent net negative charge. This is counterbalanced by the sorption of exchangeable cations, a fraction (20%) of which are associated with external crystal surfaces, although the majority (80%) are situated between the randomly superposed layers within the crystal⁷⁰ (see Figure 1.1)¹⁵.

Figure 1.1 The structure of montmorillonite.



Water is readily absorbed into this interlayer space, where it appears to enter as an integral number of layers of molecules^{15,73,74}. As each successive layer of water is absorbed, the interlayer spacing will increase. This is known as the swelling of the clay.

The d(001) spacing in Na⁺ exchanged montmorillonite varies from 0.95 nm when totally

⁷³ R. W. Mooney, A. G. Keenan and L. A. Wood, *J. Am. Chem. Soc.*, **1952**, *74*, 1367-1374.

⁷⁴ K. Norrish, *Disc. Faraday. Soc.*, **1954**, *18*, 120-134.

dehydrated, to 1.9 nm when hydrated⁷⁵. If montmorillonite exchanged with a small monovalent cation such as Na⁺ is placed in a dilute (<0.03 M) salt solution, extensive interlayer expansion is possible, and under optimum conditions the layers can dissociate completely. It has been pointed out by Walker *et al.*⁷⁶ that there are in fact two main types of interlayer water. The first type (I) constitutes the inner (primary) hydration shell around the exchangeable cation. The second type (II), forms the outer co-ordination sphere of the cation; being indirectly linked to the cation and being more mobile, this water is more labile than that of the type I. It is obvious that the size and charge (and consequently the polarising power) of the exchangeable cation is responsible for both the adsorption and character of the interlayer water⁷⁷.

1.2.3 Brønsted and Lewis Acidity.

Clays contain both Brønsted and Lewis acid sites. The Brønsted acid activity in montmorillonite is derived from two sources. The first is from structural hydroxyl groups in the clay layer. This is most likely located at the Al(VI)-O-Mg linkage, where Al(VI) is the octahedrally co-ordinated aluminium, and magnesium has substituted another aluminium in the octahedral layer. The second is from the dissociation of water molecules in the interlayer, caused by polarisation by the exchangeable cations⁷⁸. This proton-donating ability is also dependant on the hydration of the clay and the interlayer

⁷⁵ B. K. G. Theng, "*The Chemistry of Clay-Organic Reactions*", 1974, p10, Adam Hilger, London, UK.

⁷⁶ G. F. Walker, "*The X-Ray Identification and Crystal Structures of Clay Minerals.*", 1961, p297-324, Mineral Soc., London, UK.

⁷⁷ R. A. Leonard, *Soil Sci. Soc. Am. Proc.*, 1970, 34, 339-343.

⁷⁸ B. K. G. Theng, "*The Chemistry of Clay-Organic Reactions*", 1974, p261, Adam Hilger, London, UK.

charge⁷⁹. In the case of high humidity, the polarisation effect of the cation is dissipated among a large number of water molecules, and the *pK* approaches that of the exchangeable ion in aqueous solution. As the water content of the system decreases, the polarising forces act on the few residual water molecules causing an increase in their dissociation, and hence, their proton donating properties (*i.e.* The interlayer shows more Brønsted acidity).

Lewis acidity arises from exposed octahedrally co-ordinated aluminium ions at the crystal edges⁸⁰, and also ferric (or other isomorphous) ions within layers^{81,82,83,84}. Because of the nature of these sites, it is difficult to assign a precise value to the Brønsted or Lewis acidity of the clay.

1.2.4 Inserting Molecules into the Clay Interlayer.

As has been mentioned in the previous section (1.2.2), under favourable conditions it is possible to exchange the cations present in the interlayer. It is also possible to absorb molecules without displacing these cations. All types of materials have been inserted into clays, from inorganic ions, through organometallic compounds to organic molecules. The method of insertion is essentially the same for all. The material to be inserted is placed in solution with the clay, separated, washed and dried.

⁷⁹ M. M. Mortland and K. V. Raman, *Clays Clay Minerals*, **1968**, *16*, 393-398.

⁸⁰ D. H. Solomon, B. C. Loft, and J. D. Swift, *Clays Clay Minerals*, **1968**, *7*, 399-408.

⁸¹ H. Weil-Malherbe and J. Weis, *J. Chem. Soc.*, **1948**, 2164-2169.

⁸² S. B. Hendricks and L. T. Alexander, *J. Am. Chem. Soc. Argron.*, **1940**, *32*, 455-458.

⁸³ J. B. Page, *Soil Sci.*, **1941**, *51*, 133-140.

The key phrase in the preceding paragraph is “under favourable conditions”. Just what these conditions are is a complex and sometimes unpredictable science. If the clay contains small highly charged cations, the layers are unlikely to separate when placed in suspension. In addition, polar molecules are unlikely to compete effectively with water molecules for ligand positions or sites around this sort of cation⁸⁵. For this reason, the exchange is usually carried out in water, or as polar a solvent as possible, so as to ensure the clay platelets have the greatest possible chance to separate. Furthermore, the clay is normally exchanged with a large diffuse cation such as Na⁺ which can be easily displaced. In addition, if the insertion reaction is not to be carried out in water, then the clay is dried prior to use.

For example, Traynor *et al.*⁸⁶ intercalated iron, copper, and ruthenium trisbipyridyl complexes into a sodium exchanged hectorite using a fourfold excess of the complex salts. They found that prior to washing excess salt could be intersalated within the clay interlayer, although this salt was lost upon washing. This suggests that the M(bipy)₃²⁺ ions are very effective at shielding the anions from the charge of the silicate layer. The molecules lined up with their pseudo threefold axis perpendicular to the silicate sheet. The complexes were found to be unusually resistant to oxidation, although whether this was due to a modification of their redox potentials or the reaction was simply kinetically slow was unclear.

⁸⁴ J. M. Bloch, J. Charbonelle, and F. Kayser, *C. R. Acad. Sci. (Paris)*, **1953**, 237, 57-59.

⁸⁵ V. C. Farmer, and M. M. Mortland, *J. Chem. Soc.*, **1966**, 344-351.

⁸⁶ M. F. Traynor, M. M. Mortland, and T. J. Pinnavaia, *Clays and Clay Minerals*, **1978**, 26(5), 318-326.

1.2.5 Pillared Clays.

Considerable effort has been directed towards permanently propping the layers apart, in order to leave a permanently porous network. This can be done by the insertion of large organometallic molecules, or more frequently, by the formation of metal oxide pillars.

The latter method of pillaring of the clay involves the exchange of the small inorganic cations by large oxyhydroxy cations, which upon insertion form pillars in the interlayer, permanently holding the layers apart and leading to a three dimensional structure similar to a zeolite. This was first achieved by Brindley and Sempels⁸⁷ in the late nineteen-seventies. However, whereas a zeolite has a set cavity size, almost any cavity size is conceivable with clays, by careful manipulation of the pillaring conditions. In addition the pillared clays exhibit a higher thermal stability. These pillared clays, apart from their potential as molecular sieves, may then have other molecules inserted in them, leading to a new range of materials. For instance, the insertion of organoiron compounds, followed by calcination could lead to finely dispersed catalytic iron nodules in a matrix which exhibits shape selectivity⁸⁸.

The insertion of organometallic molecules as pillars opens up a whole new field. For instance, complex metal catalysts such as $\text{RhH}(\text{CO})_x(\text{PPh}_3)_2$ ($x = 1,2$), have been immobilised by intercalation into clays such as montmorillonite⁵⁷. The introduction of large organometallic molecules can impart high interlayer areas and large pore volumes. For instance, the intercalation of N-methyl-(3-triphenylstannyl)pyridinium into

⁸⁷ G. W. Brindley and R. E. Sempels, *Clay Miner.*, 1977, 12, 107.

montmorillonite⁸⁹ gives an interlayer spacing of 1.9 nm, with only 40% of the exchange sites occupied. By careful manipulation of the tin oxidation state, and further exchange with catalytically active molecules, it may be possible to engineer a heterogeneous catalyst with size/shape/stereo-chemical selectivity⁹⁰.

1.2.6 Properties and Uses.

Clays have many uses. One of the earliest recorded use of clay, the Fulling process, can be traced back to biblical times. In this, an aqueous slurry of crude clay is used to remove the grease from raw wool. Since then, it has been used in diverse situations, from the decolourising of edible oils⁹¹ to the clarifying of alcoholic beverages⁹². Modern uses of clays are even more diverse, from house bricks and catalysts⁹³, to paper⁹⁴ and toothpaste.

The potential of pillared clays to act as catalysts has enjoyed a remarkable amount of interest since their inception⁹⁵. To date they have been used for various reactions, from catalytic cracking^{96,97} and alkylation⁹⁸, to alcohol dehydration^{99,100} and the reduction of nitrogen oxides¹⁰¹.

⁸⁸ G. Ozin and C. Gil, *Chem. Rev.*, **1989**, *89*, 1749-1764.

⁸⁹ K. C. Molloy, C. Breen, and K. Quill, *Applied Organometallic Chemistry*, **1987**, *1*, 21-27.

⁹⁰ E. Kikuchi, T. Matsuda, H. Fujiki, and Y. Morita, *Appl. Catal.*, **1984**, *11*, 331.

⁹¹ R. E. Grim, *Applied Clay Mineralogy*, **1962**, McGraw-Hill, New York, USA.

⁹² M. K. H. Siddiqui, *Bleaching Earths*, **1968**, Pergamon Press, Oxford, UK.

⁹³ J. P. Chen, M. C. Hausladen, and R. T. Yang, *Journal of Catalysis*, **1995**, *151*, 135-146.

⁹⁴ B. K. Green, *Pressure-sensitive record material*, **1950**, *US. Pat.*, 2,505,470.

⁹⁵ F. Figueras, *Catal. Rev. Sci. Eng.*, **1988**, *30*, 457.

⁹⁶ J. Stert and J.-E. Otterstedt, *Appl. Catal.*, **1988**, *38*, 131.

⁹⁷ D. Tichit, F. Fajula, F. Figueras, B. Doucourant, G. Mascherpa, C. Gueguen, and J. Bousquet, *Clays Clay Miner.*, **1988**, *36*, 369.

The use of clays as catalysts touches on the edge of this work. Although the use of clays as catalysts is a diverse field in itself, most of the reactions make use of either the Lewis or Brønsted acidity of the clay. In order to demonstrate this, let us consider two types of reaction; polymerisation, and transformation and decomposition.

Polymerisation reactions are of great industrial importance. For instance, using acid washed montmorillonite it is possible to obtain polystyrene in substantial yields¹⁰². The mechanism is thought to involve the octahedrally co-ordinated aluminium at the crystal edges. These Lewis acid sites can receive an electron from an absorbed styrene monomer to produce a radical cation, which then reacts further to produce a dimer¹⁰³. In this case the clay is acting as an initiator. This sort of behaviour has also been utilised in the polymerisation of olefins¹⁰⁴, dienes¹⁰⁵ and 4-vinylpyridine¹⁰⁶. This Lewis acidity can also inhibit polymerisation however. Methyl methacrylate normally polymerises by free radical initiation, the reactive species being formed by heating. Addition of montmorillonite inhibits this reaction. This is due to the reactive intermediate being absorbed at the mineral edge and losing an electron to form an unreactive cation. In addition to mineral edge reactions, reactions within the interlayer have also been reported. For example, certain hydroxymethacrylate monomers form interlayer complexes with

⁹⁸ J.-R. Butruille and T. J. Pinnavaia, *Catalysis Today*, 1992, 14, 141-154.

⁹⁹ R. Burch and C. I. Warburton, *J. Catal.*, 1986, 97, 511.

¹⁰⁰ M. L. Occelli, R. A. Innes, F. S. S. Hwu, and J. W. Hightower, *Appl. Catal.*, 1985, 14, 69.

¹⁰¹ J. P. Chen, M. C. Hausladen, and R. T. Yang, *J. of Catal.*, 1995, 151, 135-146.

¹⁰² J. A. Bittles, A. K. Chaudhuri, and S. W. Benson, *J. Polymer Sci.*, 1964, A2, 1221-1231.

¹⁰³ D. H. Solomon and M. J. Rosser, *J. Appl. Polymer Sci.*, 1965, 9, 1261-1271.

¹⁰⁴ H. Z. Friedlander, *J. Polymer Sci.*, 1964, C4, 1291-1301.

¹⁰⁵ H. Z. Friedlander and C. R. Frink, *Polymer Letters*, 1964, 2, 475-479.

¹⁰⁶ H. Z. Friedlander, *Am. Chem. Soc. Polymer Reprints*, 1963, 4, 300-306.

montmorillonite¹⁰⁷. These compounds spontaneously polymerise if the montmorillonite contains a transition metal ion, usually iron, in its lower valency state in the silicate layer. In the case of hydroxyethylmethacrylate, an electron is accepted from the clay to form a radical anion. Abstraction of a proton from any handy water molecule gives rise to a free radical which then propagates from between the layers outwards.

The ability of clays to activate transformation and decomposition reactions has long been recognised¹⁰⁸. Probably the best known example is the cracking of petroleum¹⁰⁹. In the presence of an acid clay, a hydride ion can be abstracted to form a carbonium ion. This can then undergo various rearrangements and reactions, such as β -splitting, methyl group shift, hydride ion abstraction and hydrogen shift. This is known as catalytic cracking. There is a second type of cracking known as thermal cracking. In this, a hydrogen atom is lost giving rise to a hydrocarbon radical. This can then crack or undergo radical isomerisation, which involves rearrangement to form a more stable cation. Cracking occurs at the C-C bond in the β -position to the carbon lacking a hydrogen atom, forming a primary radical and an α -olefin¹¹⁰. It is probable that in clays both types of cracking, catalytic and thermal, are in operation at the same time.

¹⁰⁷ D. H. Solomon and B. C. Loft, *Appl. Polymer Sci.*, **1968**, *12*, 1253-1262.

¹⁰⁸ G. Broughton, *J. Phys. Chem.*, **1940**, *44*, 180-184.

¹⁰⁹ E. Eisma and J. W. Jurg, "*Organic Geochemistry*", **1969**, p676-698, Springer Verlag, Berlin, Deutschland.

¹¹⁰ R. C. Hansford, *Advanced Catalysis*, **1952**, *4*, 1-29.

1.3 Catalysts

Even the most minimal literature search is likely to encounter some reference to catalysis (See section 1.2.6). The vast majority of chemical products rely at some point on a catalyst, whether to reduce operating temperatures (and cost) or to favour a particular product. Not surprisingly, the amount of literature available is enormous, and even a most basic overview would overwhelm the scope of this work. Consequently this summary concentrates on one particular group of catalysts, heterogeneous, and one particular element, iron.

1.3.1 Heterogeneous Iron Catalysts.

There has been a considerable amount of work lately, in trying to disperse catalysts on a solid support. This has several advantages. Firstly, the ease of separation of the reactants, products and catalyst over homogenous systems, where often the catalyst is abandoned after use^{111, 112}. Secondly, the possibility of using a wider range of solvents since the catalyst's solubility is no longer an issue^{113, 114}. Finally, the ability to work at elevated temperatures should overcome any diffusional impediments, and promote reactions with high activation energies^{115, 88}.

¹¹¹ B. V. Romanovski, "Proc. 5th Int. Symp. on Relations between Homog. Heterog. Catal.", 1986, p343, VNU Science press.

¹¹² R. Parton, D. De Vos, and P. A. Jacobs, "Zeolite Microporous Solids: Synthesis, Structure and Reactivity", 1992, p552, Kluwer Academic Publishers.

¹¹³ B. V. Romanovski, *Acta Phys. Chem.*, 1985, 31, 215.

¹¹⁴ D. R. C. Huybrechts, R. F. Parton, and P. A. Jacobs, *Stud. Surf. Sci. Catal.*, 1991, 60, 225.

¹¹⁵ R. F. Parton, D. R. C. Huybrechts, Ph. Buskens, and P. A. Jacobs, *Stud. Surf. Sci. Catal.*, 1991, 65, 47-54.

Iron is very commonly used in catalysts. It is relatively cheap, widely available, and also extremely versatile. Iron catalysts come in many different forms. Metallic iron is the catalyst used in the ammonia and Fischer-Tropsch synthesis¹¹⁶. In other instances it is combined with other metals such as palladium¹¹⁷. Iron oxide is used in the high temperature carbon monoxide shift conversion, the hydrogenation of ethylbenzene to styrene, and the removal of hydrogen sulfide from reducing gas mixtures¹¹⁶. Other iron oxides such as FeAsO₄ are used in reactions such as the dehydration to olefins¹¹⁸.

1.3.2 Necessary Requirements

In order to produce a likely heterogeneous catalyst, a number of factors need to be considered. The first is the oxidation state of the iron. The Fischer-Tropsch and ammonia synthesis require metallic (Fe⁰), and will not proceed if the catalyst is oxidised. However, in the carbon monoxide shift conversion, and the removal of hydrogen sulfide from reducing gas mixtures, the presence of metallic iron causes unwanted side-reactions. Therefore, not only should the iron be in the correct oxidation state, but also reasonably resistant to a change in oxidation state¹¹⁹.

The second factor to consider is the presence of water within the host¹²⁰. The reaction for the removal of hydrogen sulfide requires water to be present in order to prevent

¹¹⁶ J. W. Geus, *Applied Catalysis*, **1986**, *25*, 313-333.

¹¹⁷ R. L. Garten, *Mössbauer Effect Methodology*, **1976**, *10*, 69.

¹¹⁸ B. C. Gates, J. R. Katzer and G. C. A. Schuit, "*Chemistry of Catalytic Processes*", **1979**, McGraw and Hill, London, UK.

¹¹⁹ A. J. H. M. Kock and J. W. Geus, *Progr. Surface Sci.*, **1985**, *20*, 165.

¹²⁰ R. Dutartre, P. Bussiere, J. A. Dalmon, and G. A. Martin, *J. Catal.*, **1979**, *59*, 382.

poisoning of the catalyst. However, periodically the catalyst has to be heated to over 250°C in order to remove sulphur deposits¹²¹. The ability to readily re-hydrate is therefore necessary. In the carbon monoxide conversion and Fischer-Tropsch synthesis, the presence of water is not desired. Any water present in these reactions reduces activity, either by blocking active sites in the former case, or by oxidising the iron surface in the latter.

The third factor to consider is reaction of the iron species with the support¹²². In the removal of hydrogen sulfide, interaction with the support can prevent reduction to metallic iron, which is desirable. In the carbon monoxide conversion, the prevention of formation of metallic iron is again desirable. However, an intermediate state, FeO, is sometimes stabilised¹²³. This is not as active as the preferred oxide Fe₃O₄, and so interaction with the support in this case is not so beneficial. In the Fischer-Tropsch synthesis, interaction with the support can prevent the reduction to metallic iron, and thus the production of the active catalyst.

The fourth factor to consider is the pore volume. This has several consequences. Firstly the required reactant molecules must be able to enter the host (undesired molecules should preferably be excluded). Secondly, the product molecules must be free to exit the host. Thirdly, structures with small pores will tend to absorb and retain more water. This is advantageous in reactions such as the removal of hydrogen sulfide. Structures with

¹²¹ A. Kool and F. Riesenfeld, "*Gas Purification*", 1979, 381, Gulf Publishing Company Book Division, Houston, USA.

¹²² H. M. Fortuin, A. J. H. M. Kock, and J. W. Geus, *J. Catal.*, 1985, 96, 261.

¹²³ A. J. van Dillen, J. W. Geus, and K. P. de Jong, "*Transport in Non-Stoichiometric Compounds*", 1982, 467, Elsevier Science Publishing Co., Amsterdam, Netherlands.

large pores will allow water to escape easily. This is important in reactions such as the carbon monoxide shift¹²⁴ and Fischer-Tropsch synthesis.

The final factor to consider is the iron particle size. Large particles have been shown to have a shape bounded almost exclusively by (110) surfaces, whereas small particles contain a number of crystallographic planes. The (110) surface is the only surface where complete removal of oxygen occurs. The removal of oxygen from the other planes, notably the (100), does not occur measurably¹²⁵. Any oxygen present will prevent hydrogen or nitrogen adsorption, and thus large particles are preferred in the ammonia synthesis. In addition, it has been shown that water is more firmly held by small particles. This favours reactions such as the removal of hydrogen sulfide.

1.3.3 Synthesis of Iron Impregnated Materials

Pertinent to us is the use of zeolites and related compounds as a solid support for small particles of iron¹²⁶. There are four main methods of synthesising such materials. The first involves incorporating the iron at the same time as the synthesis of the support. This is done in zeolites by using the iron cation as a template for the zeolite super-cage¹²⁷, and in pillared clays the iron becomes part of the pillar propping the layers apart¹²⁸. However, this method can leave the iron in dense clusters or inaccessible to reactants. The second

¹²⁴ H. Bohlbro, "An Investigation on the Kinetics of the Conversion of Carbon Monoxide by Water Vapour over Iron Oxide Based Catalysts", 1966, Gjellerup, Copenhagen, Denmark.

¹²⁵ T. J. Vink, O. L. J. Gijzeman, and J. W. Geus, *Surface Sci.*, **1985**, *150*, 14.

¹²⁶ J. Galuszka, T. Sano, and J. A. Sawicki, *Journal of Catalysis*, **1992**, *136*, 96-109.

¹²⁷ A. Hagen, F. Roessner, I. Weingart, and B. Spliethoff, *Zeolites*, **1995**, *15*, 270-275.

¹²⁸ F. J. Berry, K. K. Rao and G. Oats, *Hyperfine Interactions*, **1994**, *83*, 343-345.

method involves cationic exchange into the host. In clays and zeolites, cations within the host can be readily exchanged with cations in solution (See sections 1.2 and 1.1.2.1.1). Exchange with iron cations can thus give rise to an iron impregnated solid¹²⁹. Again however, the number of iron cations per super-cage is difficult to control, and isolated clumps of iron atoms are possible. The third method involves the adsorption of a neutral gaseous iron complex into the (usually dried) solid host. The resulting material is then heated until the iron complex decomposes leaving the iron behind. This has been attempted very successfully with iron carbonyl compounds^{130, 131}. The final route is a variation of the second method. In this, large organo-metallic molecules are exchanged in solution, and then decomposed by heating in the host matrix. Again, much success has been attained in this field, such as the introduction of ferrocene into the zeolite Na-Y³³.

¹²⁹ K. Lázár, I. Manninger, and B. M. Choudary, *Hyperfine Interactions*, **1991**, *69*, 747-750.

¹³⁰ D. Ballivet-Tkatchenko, G. Coudurier, and H. Mozzanegg, *Stud. Surf. Sci. Catal.*, **1980**, *5*, 309.

¹³¹ D. Ballivet-Tkatchenko and I. Tkatchenko, *J. Mol. Catal.*, **1981**, *13*, 1.

1.4 Biferrocene and Biferrocenium

1.4.1 Background

The background to biferrocene synthesis starts with the discovery of the cyclopentadienyl anion by Thiele¹³² in 1900. Half a century later in 1951, a remarkably stable complex incorporating an iron atom sandwiched between two cyclopentadienyl rings, ferrocene, was reported by Kealy and Pauson¹³³. The earliest recorded biferrocene was, surprisingly perhaps, biferrocene itself. In a communication to the editor of *Chemistry and Industry* in 1959, Goldberg and Mayo described how they had isolated an orange crystalline material from the reaction of a mixture of mono- and di-lithioferrocene with tri-*n*-hexylbromosilane, which they called “diferrocene”¹³⁴. Since then, biferrocene, as it has become known, and its substituted derivatives, have been synthesised by a number of different methods. Previous routes have included the use of silylferrocene¹³⁵, diferrocenylmercury¹³⁶, ferrocenylboronic acid; coupling reactions of haloferrocenes using copper (Ullman¹³⁷), halogens¹³⁸, and even polyhalogenated alkanes¹³⁸, but all are restricted by the many different isomers and oligomers formed, and consequently low yields. One of the more successful reactions was the synthesis of

¹³² J. Thiele, *Ber. Dtsch. Chem. Ges.*, **1900**, *33*, 660.

¹³³ M. Rosenblum, “*Chemistry of the Iron Group Metallocene*”, **1965**, Wiley, New York, New York, USA.

¹³⁴ S. I. Goldberg and D. W. Mayo, *Chemistry and Industry*, **1959**, 671.

¹³⁵ M. Rausch, M. Vogel, and H. Rosenberg, *J. Organic Chem.*, **1957**, *22*, 900-908.

¹³⁶ M. D. Rausch, *Inorganic Chemistry*, **1962**, *1(2)*, 414-417.

¹³⁷ M. D. Rausch, *J. Organic Chem.*, **1961**, *20*, 1802-1805.

¹³⁸ R. F. Kovar, M. D. Rausch, and H. Rosenberg, *Organometallic Chemical Synthesis*, **1970**, *1*, 173-181.

bis[(dimethylamino)methyl]biferrocene by Rockett *et al.*¹³⁹ from dimethylaminoferrocene. Using butyl-lithium to remove a proton, and the amine functionality on the ferrocene ring to stabilise the intermediate complex, the addition of cobalt(II)chloride affords a mix of unreacted ferrocene, with the 2, 2''- and 2, 5''- bis[(dimethylamino)methyl]biferrocene in 85% yield overall. This high yield is especially necessary herein, since large amounts are required for successful intercalation into the clay.

1.4.2 Properties.

Biferrocenes are not particularly interesting molecules in themselves, but partial oxidation to biferrocenium compounds opens a whole new vista. Biferrocenium compounds have one Fe(II) and one Fe(III) centre which have the potential to transfer an electron between themselves via the cyclopentadienyl rings. This electron transfer is similar to that found in many biological processes, such as electron transport trains^{140,141,142}. However, in the biological processes many of the rates are considerably slower than they should be. The precise factors influencing the rate of this electron transfer are still poorly understood. It has been suggested that motion of one or more amino acid moieties at a rate of 10^2 - 10^4 s⁻¹ in a region near to the heme in cytochrome-*c* modulates the rate of electron transfer into or out of the redox site of this important respiratory electron transport protein¹⁴³. By studying simpler systems like biferrocenium,

¹³⁹ D. J. Booth, G. Marr, and B. W. Rockett, *J. Organometallic Chemistry*, **1973**, 227-230.

¹⁴⁰ R. A. Marcus and N. Sutin, *Biochim. Biophys. Acta*, **1985**, 811, 265.

¹⁴¹ D. DeVault, "*Quantum Mechanical Tunnelling in Biological Systems*", 1984, 2nd Edition, Cambridge University Press, Cambridge, UK.

¹⁴² R. D. Cannon, "*Electron Transfer Reactions*", Butterworths, 1980, Boston, MA, USA.

¹⁴³ G. Williams, G. R. Moore, and R. J. P. Williams, *Comments Inorg. Chem.*, **1985**, 4, 55-98.

it is possible to determine which factors influence the electron transfer rate, and help to unravel the complexity found in nature.

On a more academic front, the discussion into whether slow reorganisation of the immediate solvent structure affects the rate of outer sphere electron transfer between transition metal complexes in solution is ongoing¹⁴⁴. One of the problems in studying solution chemistry is the uncertainty involved in the precise arrangement and structure of the molecules during the experiment. By studying biferrocenium compounds which are solids, this uncertainty is removed, as the crystal structure can be determined by such techniques as X-ray diffraction.

In a slightly different vein, a large third order non-linear optical response has been measured for similar compounds such as 1, 4-bis(ferrocenyl)butadiyne¹⁴⁵. This leads to the possibility that some biferrocenium compounds may behave in a similar manner.

Following on the back of this work is the possibility that if the factors influencing the electron transport process are known, then a compound could be designed that showed novel electronic properties, e.g. super-conductivity.

¹⁴⁴ J. Jortner and M. Bixton, *J. Chem. Phys.*, **1988**, *88*, 167-170.

¹⁴⁵ J. W. Perry, A. E. Stiegman, S. R. Marder, and D. R. Coulter, *Organic Materials for Non-linear Optics*, **1988**, *69*, 189.

1.4.3 Valence Electron De-trapping Phenomena.

The transfer of an electron between atoms in a molecule above a certain temperature is known as valence electron de-trapping (VEDT). The factors determining the rate of electron transfer in biferrocenium compounds have been studied extensively by a few select groups since about 1967^{146,147,148}, but most notably by Hendrickson *et al.*¹⁴⁹. By a careful choice of substituent on the biferrocene ring, and systematically changing the anion and solvate molecules in the crystal, Hendrickson *et al.* discovered that the temperature of the onset of VEDT was extremely sensitive to the immediate environment around the biferrocenium cation. For instance, while studying the cation 1',1''-dibenzylbiferrocenium triiodide, Hendrickson *et al.* noted that upon changing the anion from PF₆⁻ to SbF₆⁻ to I₃⁻, the cation de-trapped at 170 K, 220 K and 270 K, respectively¹⁵⁰. Even more interesting perhaps, was what was observed in a later study of the 1',1''-dibenzylbiferrocenium triiodide compound¹⁴⁹. Hendrickson *et al.* discovered that the compound was composed of two distinct crystal structures, one formed of needle-like crystals and the other of plate-like crystals. The plate-like crystals were valence trapped on the Mössbauer time scale. The needle-like crystals on the other hand showed signs of de-trapping above 25 K, until by 150 K the sample had completely de-trapped. However, grinding of the needle-like crystals produced a resonance characteristic of a valence trapped species, which persisted even up to and above 300 K. This was ascribed to the

¹⁴⁶ M. B. Robin and P. Day, *Adv. Inorg. Chem. Radiochem*, **1967**, *10*, 247.

¹⁴⁷ G. C. Allen and N. S. Hush, *Prog. Inorg. Chem.*, **1967**, *8*, 357.

¹⁴⁸ N. S. Hush, *Prog. Inorg. Chem.*, **1967**, *8*, 391.

¹⁴⁹ R. J. Webb, T.-Y. Dong, G. C. Pierpont, S. R. Boone, R. K. Chadha, and D. N. Hendrickson, *J. Am. Chem. Soc.*, **1991**, *113*, 4806-4812.

¹⁵⁰ R. J. Webb, S. J. Geib, D. L. Staley, A. L. Rheingold, and D. N. Hendrickson, *J. Am. Chem. Soc.*, **1990**, *112*, 5031-5042.

formation of defects in the crystal. Defects in the crystal will lead to a more asymmetric environment around the cation, which in turn leads to a more asymmetric ground state potential. This means that more energy is required to overcome the potential gap to enable electron transfer, leaving a valence trapped species to higher temperatures.

It should be noted that three separate examples of de-trapping have been observed in biferrocenium salts.

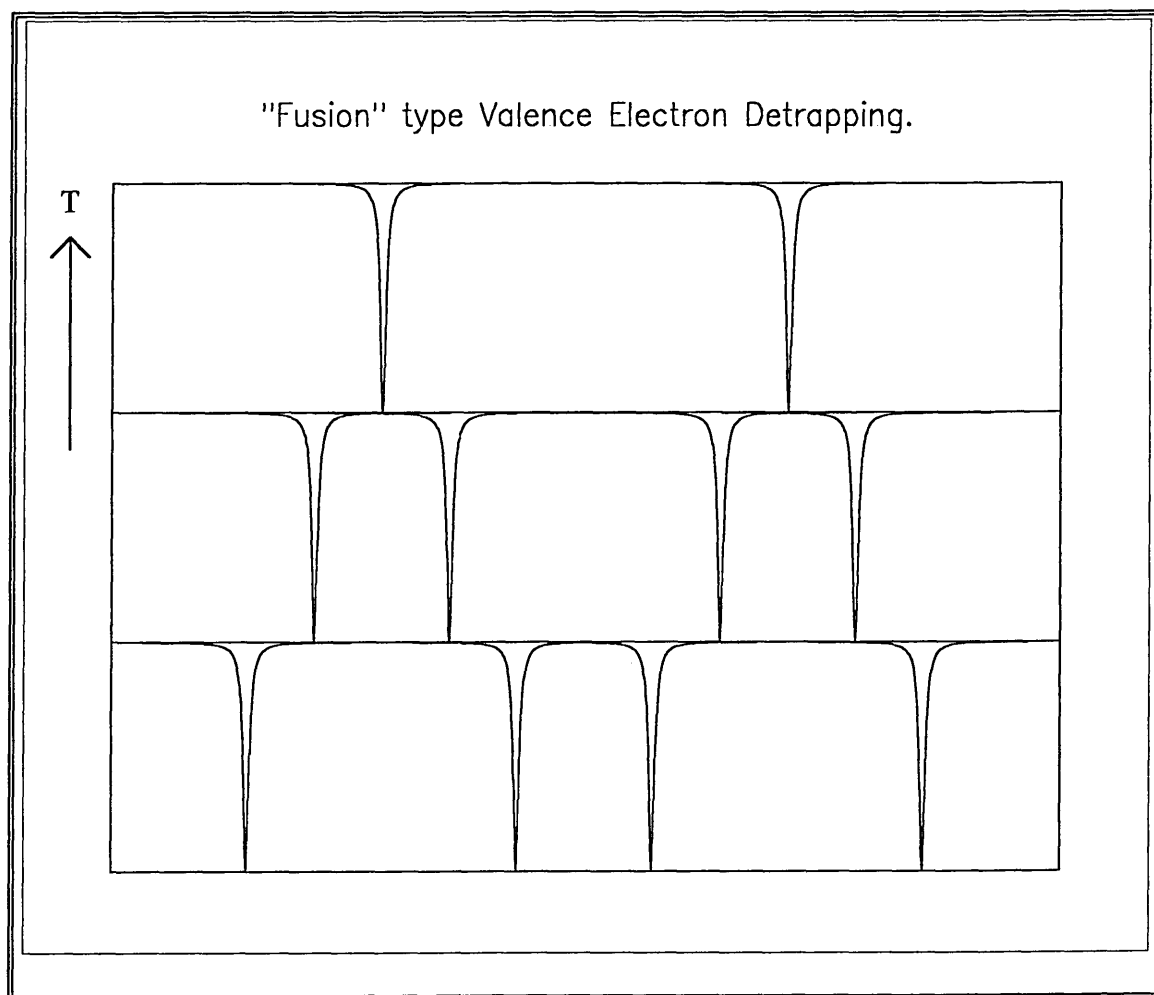
The first is really more a case of de-trapped than de-trapping. Dibromo-biferrocenium triiodide is de-trapped on the Mössbauer time-scale even down to 4K¹⁵¹. In this case the cation is in an extremely symmetric environment, and so only a very small amount of energy is required to allow an electron to transfer between the two atoms. As the temperature was raised this transfer rate occurred faster and faster. By 4K the rate was so fast that only a single valence averaged doublet was seen. Note however that no line broadening was evident in the spectra. This indicates that the cause of the increased electron transfer was not internal to the molecule (*i.e.* the activation barrier to transfer one electron), but the result of some external process.

In the case of the PF₆⁻ and SbF₆⁻ salts of 1',1''-dibenzylbiferrocenium, the resonances due to the iron(II) and iron(III) species moved together with increasing temperature, until a single resonance was observed¹⁵⁰. Again, at no point was any line broadening evident. This type of de-trapping is sometimes called “fusion” type de-trapping. In this case, it was proposed that the anion changed from being static to dynamic in the

¹⁵¹ T.-Y. Dong, D. N. Hendrickson, C. G. Pierpont, and M. F. Moore, *J. Am. Chem. Soc.*, **1986**, *108*, 963-971.

temperature region where valence electron de-trapping became evident. This led to a more symmetric environment around the cation, leading to a more symmetric ground state potential, allowing electrons to tunnel between the states. As the temperature was raised, this transfer became faster, until only the one resonance characteristic of iron(2.5) was seen.

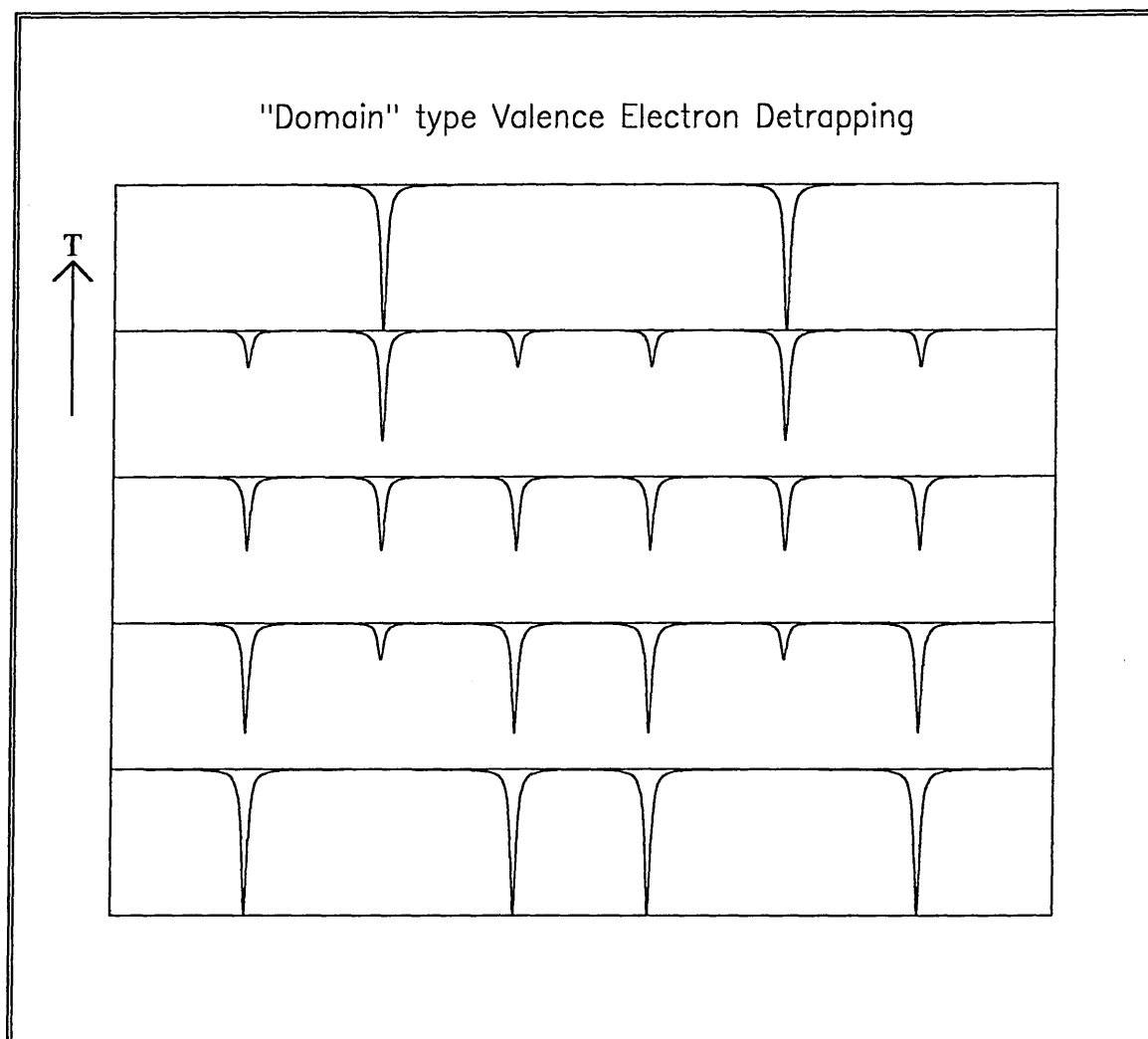
Figure 1.2 Diagram showing VEDT type II.



In the case of 1,1'-dibenzylbiferrocenium triiodide a third type of de-trapping was observed¹⁵⁰. In this example, both the iron(II) and iron(III) resonances were visible, but a third average doublet with parameters consistent with an iron(2.5) species, grows at the expense of the two former doublets with increasing temperature. This they claimed was due to defects within the crystal. The domains far from the defect would be quite symmetric and so de-trap early. The closer to the defect, the more asymmetric the

environment around the cation, and so more energy was required for the transfer of an electron. Therefore as the temperature was raised, the domains away from the defect would de-trap first, followed gradually by those closer to the defects until the whole solid had de-trapped. Interestingly, this behaviour was observed by Hendrickson *et al.* when studying the diethylbiferrocenium - SWY-1 montmorillonite clay composite¹⁵².

Figure 1.3 Diagram showing de-trapping type III.



¹⁵² U. Sinha, M. D. Lowery, W. W. Ley, H. G. Drickamer, and D. N. Hendrickson, *J. Am. Chem. Soc.*, **1988**, *110*, 2471-2477.

1.5 Mössbauer Spectroscopy

1.5.1 Introduction.

Ever since Victorian times, people have used radiation to probe the nature of matter. One of the first was a German chemist called Robert Bunsen who tried to identify the elements by their individual emission spectra.

In 1900 a physicist called Max Planck came up with the idea that radiation, like matter, was composed of discrete packets, which he called “quanta”.

In 1907 Einstein wrote that a solid can be thought of as a large number of independent linear harmonic oscillators, each vibrating at a frequency ω_E . This view was somewhat simplistic, but a useful model to explain the specific heat of solids.

In 1912, Debye proposed another model for solids, based on a continuum of oscillator frequencies ranging from 0 up to a maximum ω_D . This was again somewhat simplistic, but can be used cautiously.

In 1913 another physicist Neils Bohr, using Planck’s idea, proposed a model for the hydrogen atom, where the electrons were only allowed a fixed set of allowed orbits, based on their energy. Although later shown to be strictly incorrect, he was on the right track.

In 1924 De Broglie proposed the theory of wave-particle duality. This idea was further expanded in 1927 by Schrödinger. Schrödinger proposed that electrons could be described by considering the electron as a wave function, where the square of the wave function represents the probability of finding the electron at that point. A working model for the atom was now in place, which could be used as a fundamental base for the theory of spectroscopy.

In 1939, Lamb set out his theory for the absorption of neutrons based on zero-phonon events¹⁵³. This is particularly pertinent to the discussion in this section, as it shares the same basic theory as the Mössbauer effect.

The principle of modern spectroscopy is surprisingly simple. A sample is excited using radiation. The sample absorbs the radiation, and then re-emits it in all directions. The emitted radiation enters a detector, and any difference between the initial and final radiation is measured. Considering the theory was in place by 1927, it is perhaps surprising that the phenomenon of resonant absorption followed by recoil free emission by nuclei, was in fact not discovered until 1957¹⁵⁴.

1.5.2 Theory.

When an atom emits radiation it experiences recoil, in accordance with the principle of the conservation of momentum. With most spectroscopic techniques the recoil is too

¹⁵³ W. E. Lamb, Jr, *Phys. Rev.*, **1939**, *55*, 190.

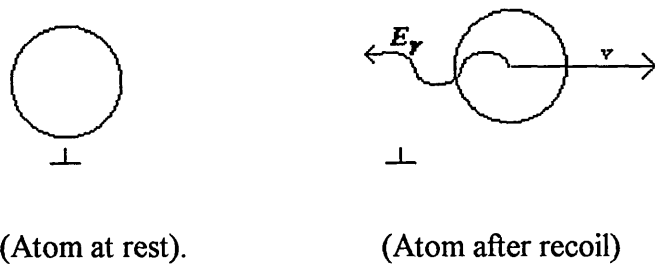
¹⁵⁴ R. L. Mössbauer, *Z. Physik*, **1958**, *151*, 124.

small to have any noticeable effect. With nuclear transitions however, the radiation energy is comparable to that required to recoil the atom. This can be represented by a simple model using mathematics. Consider an atom in the x plane. Assume that it is in the excited state. Its internal energy above the ground (0) state is therefore,

$$E = E_{ex} - E_0 \quad \text{Equation 1.1}$$

It also has some kinetic energy, $\frac{1}{2}mV_x^2$. The total energy of the nucleus above the ground state before emission is $E + \frac{1}{2}mV_x^2$. It then emits a γ -ray. Assuming the mass hasn't changed, the velocity of the atom must have, in accordance with the law of conservation of energy. Therefore, the atom now has an energy $\frac{1}{2}m(V_x + v)$.

Figure 1.4 Diagram showing atom before and after recoil.



velocity	V_x	$V_x + v$
energy	$E + \frac{1}{2}mV_x^2$	$E_\gamma + \frac{1}{2}m(V_x + v)^2$
momentum	$m V_x$	$m(V_x + v) + E_\gamma/c$

(E_γ is the energy of the γ -ray). v is a vector and so can be (and probably is) negative.

Also by the law of the conservation of energy,

$$E + \frac{1}{2}mV_x^2 = E_\gamma + \frac{1}{2}m(V_x + v)^2 \quad \text{Equation 1.2}$$

The difference between E and E_γ is the difference in energy between the excited and ground state of the atom δE . This may be written as,

$$\delta E = E - E_\gamma = \frac{1}{2}mv^2 + \frac{1}{2}mvV_x$$

$$= E_R + E_D$$

Equation 1.3

It is immediately apparent that the first term is dependent only on the velocity after emission, and hence on the amount of recoil of the atom ($= E_R$). This is an inherent property of the nucleus, and cannot be altered. The second term, however, is dependent on the velocity of the atom before emission. This is known as the Doppler-effect energy term, for obvious reasons ($= E_D$).

As the speeds involved are well below the speed of light, traditional mechanics can be used to give an idea of the random thermal energy possessed by the atom, and hence an indication of its speed. The random thermal energy of a perfect gas is $\frac{1}{2}kT$, where k is the Boltzmann constant and T is the absolute temperature. Therefore,

$$\frac{kT}{2} \approx E_k = \frac{m\bar{V}^2}{2}$$

This can be rearranged to give;

$$E_D = mv\sqrt{\bar{V}^2} = \sqrt{2E_k m v^2} = 2\sqrt{E_k E_R}$$

Equation 1.4

So, based on the above equation, when the atom emits a γ -ray, there will be a distribution of energies, displaced by E_R from E , and broadened by twice the geometric mean of the recoil energy and the average thermal energy, which is equal to the Doppler-effect energy.

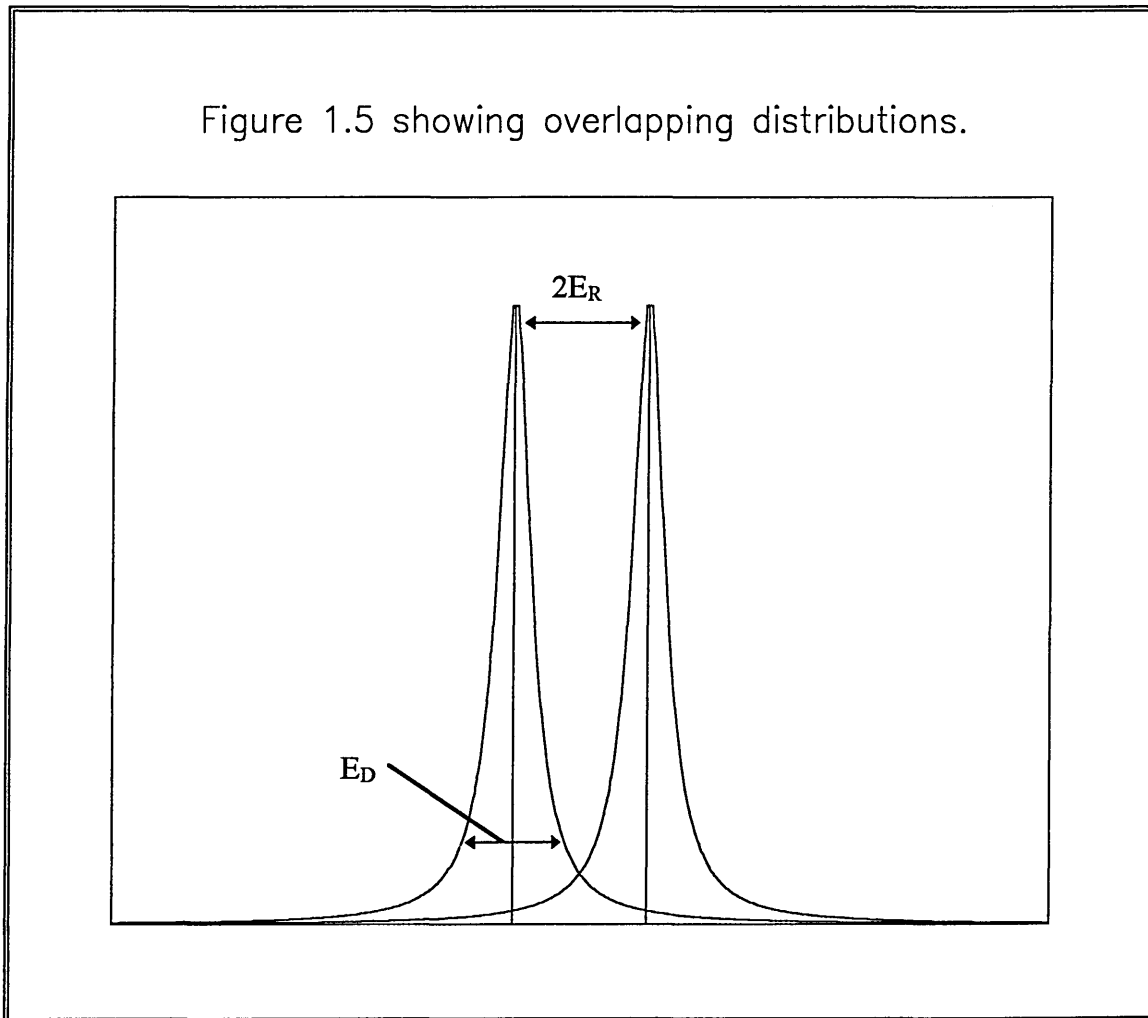
Now by the same arguments outlined above, it can be assumed that a nucleus absorbing a γ -ray will also recoil, but by the same amount in the opposite direction. Thus, there will be another distribution of energies broadened by E_D , and displaced from E in the opposite direction by E_R . This is shown diagrammatically in Figure 1.5.

Thus, in order for an atom to absorb a γ -ray and then re-emit it, there must be an overlap of the two distributions, implying that the Doppler-effect energy must be of the same order of magnitude as $2E_R$. This was first achieved by Moon¹⁵⁵ in 1950, using an ultracentrifuge to accelerate the sample to 1600 mph. Others have repeated the experiment using high temperatures or nuclear reactions to increase the Doppler broadening and increase the overlap of the distributions. Note that all these people are compensating for the recoil energy. This remained the case until 1957 when a young physicist named Rudolf Mössbauer appeared.

As far the author is aware, Mössbauer tried to increase the overlap by increasing the temperature. By increasing the temperature, the molecules have more energy and vibrate faster about their lattice positions, broadening the energy distributions and providing increased overlap. What was observed in fact, was a decrease, with a lower recoil free fraction at higher temperatures. From here it was recognised that it was not the high energy atoms that were causing the spectrum, but those with no energy.

¹⁵⁵ P. B. Moon, *Proc. Phys. Soc.*, 1950, 63, 1189.

Figure 1.5 Diagram of overlapping distributions $2E_R$ apart and broadened by E_D .



Mössbauer¹⁵⁴ reasoned that if the atom was part of a solid, then it was not the atom that would recoil, but the whole lattice. Even in a powder, a crystallite contains around 10^{15} atoms, reducing E_R by 10^{15} and making it negligible. By the same argument, E_D can also be considered negligible.

Mössbauer dutifully took his findings to his supervisor and told him his theory. His supervisor informed him that he was mistaken. Mössbauer persevered and published¹⁵⁴ his findings in a little known journal hoping his supervisor would not notice. Several

others did however. They repeated his experiments and came to the same conclusions. The phenomenon of resonant absorption followed by recoil free emission is thus attributed to Mössbauer, and gained him the Nobel prize at a later date.

1.5.2.1 Line-width and Resolution

One of the remarkable things about Mössbauer Spectroscopy is its incredible resolution. This is a consequence of the very narrow band of energies associated with the γ -ray, defined by the Heisenberg uncertainty principle. The ground state of a nuclear level has an infinite lifetime, and hence no uncertainty in energy. However, an excited state has a mean life (Δt) of a microsecond or less. For a γ -ray of energy ΔE

$$\Delta E \Delta t = \hbar \qquad \text{Equation 1.5}$$

This means that when the nucleus decays there will be a range of energies produced with a width at half-height (Γ), where

$$\Gamma = \hbar / \Delta t \qquad \text{Equation 1.6}$$

and $\Delta t = \ln 2 \times t_{1/2}$.

For all of the experiments herein ^{57}Fe was used. ^{57}Fe has a half-life $t_{1/2}$ of 97.7 ns. Working back, this gives a width at half height Γ of 4.67×10^{-9} eV. The resolution can be written as $\Gamma/\Delta E$. In the case of the Mössbauer effect, E_R and E_D are effectively eliminated. This indicates that for the 14.4 keV transition in ^{57}Fe , if thermal broadening could be avoided, a monochromaticity of 1 part in 10^{13} is theoretically possible. This

compares very favourably with such techniques as U.V.-visible (1 in 10^1), gas phase infra-red (1 in 10^3) and atomic line spectra (1 in 10^8).

1.5.2.2 Recoil Free Fraction

So far it has been seen that as long as the chemical binding energy is considerably greater than the free atom recoil energy (E_R), then the recoiling mass can be considered to be the whole crystal rather than that of the atom.

However, this argument ignores one important factor. The atom is not held rigidly on its lattice position, but is constantly vibrating about it. Fortunately, during the time of the nuclear decay, the mean displacement of the atom averages to zero. Therefore, a transfer of momentum to the atom is not possible, and any transfer of momentum to the random translational motion of the lattice is negligible. This leaves two processes by which the recoil energy could be dispersed. The first is by absorption of the recoil energy by the lattice vibrations, and the second is to emit a γ -photon.

In an Einstein solid, the vibrational energy of the lattice as a whole is quantised, so it can only change by discrete amounts, $0, \pm\hbar\omega, \pm 2\hbar\omega, etc.$ If $E_R < \hbar\omega$ then either zero or $\hbar\omega$ units of vibrational energy are transferred. Therefore, if a fraction, f , of γ -photons are emitted without transfer of recoil to lattice vibrations (zero phonon transitions), then a fraction $(1-f)$ will transfer one phonon, neglecting all higher multiples of $\hbar\omega$ to a first

approximation. Lipkin¹⁵⁶ has shown that if many emission processes are considered, the average energy transferred per event is exactly the free-atom recoil energy: or using the present model,

$$E_R = (1-f) \hbar\omega$$

which can be rearranged to give,

$$f = 1 - \frac{E_R}{\hbar\omega}$$

Equation 1.7

This fraction f , does not transfer any energy to the lattice vibrations, and all the energy is released in the γ -photon energy ($E=E_\gamma$).

This is still, however, a very simplistic model. A more realistic model would be to use a Debye model, where there are a range of frequencies that converge at a upper limit of ω_D . Fortunately, the lower frequencies which are dealt with here are difficult to excite, and similar to the Einstein model, otherwise the Mössbauer effect would not exist.

Thus far it is known that there is a finite probability of a γ -emitter emitting a γ -ray without recoil or thermal broadening, and that the line-width derives from the Heisenberg uncertainty principle. The question remains however, as to how much this finite probability actually is.

So far it has been seen that the recoil free fraction or probability of zero phonon events is related to three variables:

¹⁵⁶ H. J. Lipkin, *Ann. Phys.*, **1960**, *9*, 194.

- a) the free atom recoil energy
- b) the properties of the solid lattice
- c) the ambient temperature.

So, the smaller the γ -ray energy, the firmer the binding of the lattice, and the lower the temperature, the higher the proportion of zero phonon events (f) there are likely to be.

The forces acting within the nucleus are extremely short range whereas those holding the lattice together are of much longer range¹⁵³. Hence the nuclear decay is independent of the vibrational state and *vice versa*. The probability for recoilless emission can be written as¹⁵⁷,

$$f = e^{-k^2 \cdot x^2} \quad \text{Equation 1.8}$$

x is a random vibration vector. Therefore x^2 can be replaced by $\langle x^2 \rangle$, the component of the mean square vibrational amplitude of the emitting atom in the direction of the γ -ray.

Since $k^2 = 4\pi^2 / \lambda^2 = E_\gamma^2 / (\hbar c)^2$, where λ is the wavelength of the γ -ray,

$$f = \exp\left(\frac{-4\pi^2 \langle x^2 \rangle}{\lambda^2}\right) = \exp\left(\frac{E_\gamma^2 \langle x^2 \rangle}{(\hbar c)^2}\right) \quad \text{Equation 1.9}$$

Looking at equation 1.9 it is seen that the probability of zero-phonon emission decreases exponentially with the square of the γ -ray energy (this confirms what had been deduced qualitatively earlier). This indicates an upper limit on the value of E_γ that can

¹⁵⁷ N. N. Greenwood and T. C. Gibb, "Mössbauer Spectroscopy", Chapman and Hall, 1971, London, United Kingdom.

be used in the Mössbauer experiment (the highest transition energy for which a measurable Mössbauer effect has been reported is 155 keV for ^{188}Os). Equation 1.9 also shows that f increases exponentially with a decrease in $\langle x^2 \rangle$, which in turn depends on the firmness of the binding of the lattice, and on the ambient temperature. The displacement of the nucleus must be small with respect to the wavelength of the γ -ray. This explains why the Mössbauer effect is not visible in gases and non-viscous liquids. However, it does afford a valuable insight into the lattice dynamics of a solid.

In order to do so, however, a model of the vibrational modes within the solid is required. The simplest model is, as has been mentioned earlier, the Einstein model. This is rather too simplistic and will not be mentioned further. A better model, though still limited to a monatomic cubic solid, is the Debye model. The Debye model envisions a continuum of oscillator frequencies, ranging from zero upwards, to converge at a maximum frequency ω_D . The frequencies are distributed according to the following formula, $N(\omega) = \text{constant} \times \omega^2$. A characteristic temperature called the Debye temperature θ_D is defined as $\hbar \omega_D = k\theta_D$, and the average frequency is

$$\hbar \bar{\omega} = \frac{3\hbar\omega_D}{4}$$

The Debye temperature θ_D gives an indication of the approximate lattice properties, but it should be remembered that the values are grossly inadequate for most pure metals, let alone chemical compounds.

The Debye model leads to

$$k^2 \cdot x^2 = \frac{\hbar}{2M} \int_0^{\omega_D} \frac{N(\omega)}{\omega} \coth\left(\frac{\hbar\omega}{2kT}\right) d\omega$$

which can be written as,

$$f = \exp\left[\frac{-6E_R}{k\theta_D} \left\{ \frac{1}{4} + \left(\frac{T}{\theta_D}\right)^2 \int_0^{\theta_D/T} \frac{x}{e^x - 1} dx \right\}\right] \quad \text{Equation 1.10}$$

This is often written as $f = e^{-2W}$. The factor W is sometimes loosely called the Debye-Waller factor. The Debye-Waller factor was originally derived for X-ray scattering. The major difference is that X-ray scattering is fast compared to lattice vibrations, whereas the mean lifetime of a Mössbauer nucleus is long. At low temperatures where $T \ll \theta_D$, equation 1.12 approximates to

$$f = \exp\left[\frac{-E_R}{k\theta_D} \left\{ \frac{3}{2} + \frac{\pi^2 T^2}{\theta_D^2} \right\}\right] \quad T \ll \theta_D \quad \text{Equation 1.11}$$

and at absolute zero

$$f = \exp\left[\frac{-3E_R}{2k\theta_D}\right] \quad T = 0 \text{ K} \quad \text{Equation 1.12}$$

Finally, at the high temperature limit

$$f = \exp\left[\frac{-6E_R T}{k\theta_D^2}\right] \quad T \geq \frac{1}{2}\theta_D \quad \text{Equation 1.13}$$

The mechanism by which an atom can emit a γ -ray without recoil is now known. The same arguments can be used to explain how an atom absorbs one. In addition, an idea of how much of the sample is likely to experience resonant absorption / recoil free emission is also known.

1.5.2.3 Resonant Absorption Cross Section and Re-absorption

Take this a stage further. In order to perform a Mössbauer experiment, a radioactive emitter is used for a source, followed by subsequent recoil free absorption/emission by the absorbing material being studied. However, what would happen if the source material reabsorbed the γ -ray before it even reached the absorber? Alternatively, what happens if the absorber reabsorbs the γ -ray after it has emitted it? In order to answer these questions it is necessary to consider the resonant absorption cross-section of the material. Common sense dictates that the thicker the material is, the more likely it is to reabsorb the γ -ray, but this should be examined more closely. The preceding paragraph showed that the probability of recoilless emission is f_s . This radiation has a Heisenberg width at half-height of Γ_s , with a distribution of energy in accordance with the Breit-Wigner formula¹⁵⁸. This in turn shows that the number of transitions between $(E_\gamma - E)$ and $(E_\gamma - E + dE)$ follows a Lorentzian distribution defined by

$$N(E)dE = \frac{f_s \Gamma_s}{2\pi} \frac{dE}{(E - E_\gamma)^2 + \left(\frac{\Gamma_s}{2}\right)^2} \quad \text{Equation 1.14}$$

This is described diagrammatically in Figure 1.6. In a similar way, the resonant absorption cross section $\sigma(E)$ can be expressed as

$$\sigma(E) = \sigma_0 \frac{\left(\frac{\Gamma_a}{2}\right)^2}{(E - E_\gamma)^2 + \left(\frac{\Gamma_a}{2}\right)^2} \quad \text{Equation 1.15}$$

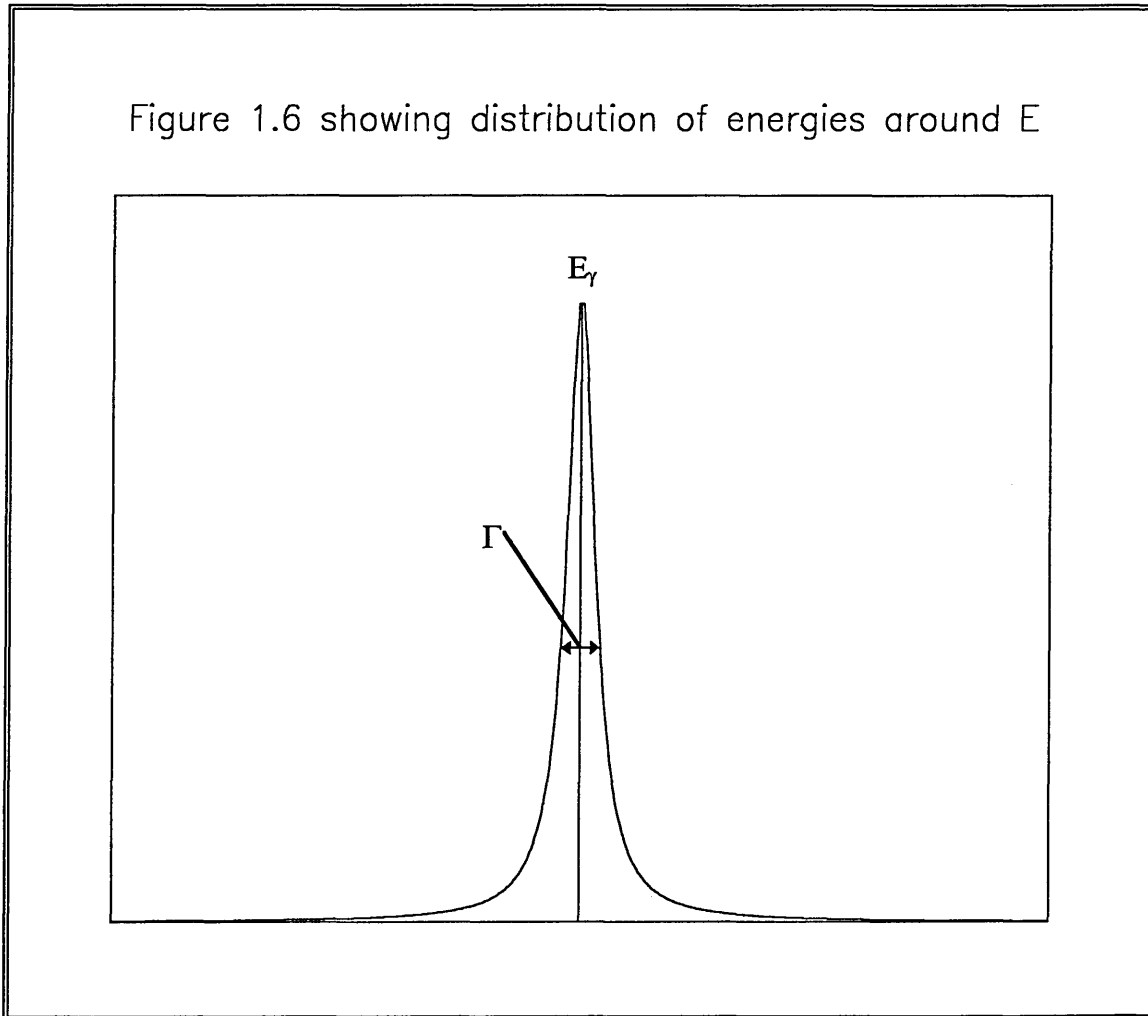
where Γ_a is the Heisenberg width at half-height of the absorption profile and σ_0 is the effective cross section given by

$$\sigma_0 = 2\pi\lambda^2 \left(\frac{2I_e + 1}{2I_g + 1} \right) \left(\frac{1}{1 + \alpha} \right)$$

Equation 1.16

where I_e and I_g are the nuclear spin quantum numbers of the excited and ground states, and α is the internal conversion coefficient of the γ -ray of wavelength λ .

Figure 1.6 Diagram of Lorentzian Line, E_γ with Heisenberg-width Γ .



(Note: Not all γ transitions produce a physically detectable γ -ray; a proportion eject electrons from the atomic orbitals, giving X-rays and these internal conversion electrons instead. The internal conversion coefficient of a γ -transition is defined as the ratio of the number of conversion electrons to the number of γ -ray photons emitted.). Equation 1.18

¹⁵⁸ G. Breit and E. Wigner, *Phys. Rev.*, 1936, 49, 519.

shows that a high absorption cross section requires that α has a low value. The resonant absorption process will also be in competition with other absorption processes such as photoelectric absorption, and it is important that the cross-section for nuclear resonance absorption should be higher than that for any other method of γ -ray attenuation. So, it is clear that the intensity of an emission-absorption resonance depends on three main properties:

- a) nuclear properties: the cross-section of γ -ray absorption and hence I_e , I_g , and α
- b) source properties: the recoil free fraction f_s and the Heisenberg width Γ_s
- c) absorber properties: the recoil free fraction for absorption f_a and the Heisenberg width Γ_a .

Unfortunately, a completely general evaluation of the problem is impossible, but useful results are obtained if it is assumed that both the source and the absorber have the same Heisenberg line-width ($\Gamma = \Gamma_s = \Gamma_a$). Using this assumption, Margulies and Ehrman¹⁵⁹ showed that the decrease in γ -transmission through a uniform resonant absorber which has a thickness tending towards zero (*i.e.* ideally thin) can be represented by,

$$I(\varepsilon) = \frac{\Gamma_r}{2\pi} \times \frac{1}{(\varepsilon - E_\gamma)^2 + (\Gamma_r/2)^2} \quad \text{Equation 1.17}$$

This was normalised so that $\int_0^\infty I(\varepsilon) d\varepsilon = 1$.

ε is the energy displacement between the source and absorber distribution maxima, Γ_r is the sum of the emission and absorption half-widths, *i.e.* $\Gamma_r = 2\Gamma$ and the distribution is still Lorentzian. If the absorber has an effective thickness $t = f_a n_a \alpha_a \sigma_0 t_a$, (where f_a is the

recoil free fraction of the absorber, n_a is the number of atoms of the element concerned per cm^3 in the absorber, α_a is the fractional abundance of the resonant isotope, σ_0 is the absorption cross section, and t_a is the thickness of the absorber in cm), the shape is still basically Lorentzian but will be broadened so that

$$\frac{\Gamma_r}{\Gamma} = 2.00 + 0.27t \quad 0 < t \leq 5 \quad \text{Equation 1.18}$$

and

$$\frac{\Gamma_r}{\Gamma} = 2.02 + 0.29t - 0.005t^2 \quad 4 \leq t \leq 10$$

By measuring Γ_r for a series of thickness', t , it is possible to obtain the true value of $\Gamma = \frac{1}{2}\Gamma_r (t \rightarrow 0)$.

So, if the source has a substantial recoil free fraction, and the emitted γ -rays pass through an absorber made of the same material, there will be a decrease in the transmission of the γ -rays on the other side due to their resonant re-absorption and subsequent re-emission over a 4π angle. This concludes the basic principles of the Mössbauer experiment.

¹⁵⁹ S. Margulies and J. R. Ehrman, *Nuclear Instr. Methods*, 1961, 12, 131.

1.5.3 Experimental

1.5.3.1 Source choice

Before starting a Mössbauer experiment a source of γ -rays is required. More importantly, a source of γ -rays that can easily be utilised. To start, take another look at the preceding section to see what sort of material is needed for the source.

First of all consider the energy of the γ -ray. Too little energy and the γ -ray will simply be absorbed into the surrounding matter. Too much energy, and the recoil free fraction (proportional to $\exp(-E_\gamma^2)$) falls to a very low value, and in addition could disrupt the surrounding matrix. This last consideration is also important for any preceding transitions of the excited nucleus. Moreover the absorption cross section σ_0 , which is proportional to $-E_\gamma^2$, and so also decreases rapidly as E increases. Ideally a γ -ray with an energy between 10 and 100 keV is required.

The first variable was the Heisenberg line-width. This is dependent on the half-life of the excited state. If the half-life of the excited state is too long, a very narrow band of energies will be produced, which is difficult to record accurately due to vibrations within the spectrometer. Alternatively, too short a half-life leads to a very broad range of energies, and a broad spectrum results with little or no fine structure. In practice, the optimal half-life lies somewhere between 1 and 100 ns. Still on the subject of half-life, the source should last months if not years in order to maximise consistency and minimise handling (unhealthy!). Therefore, the precursor to the excited state should have a long half-life.

The second variable considered was the recoil free fraction. In order to maximise the number of γ -rays, this should be as high as possible. The recoil free fraction depended on three main factors.

- 1) The free atom recoil energy (E_R). This should be as low as possible (usually $E_R < 6 \times 10^{-2}$ eV) in order to minimise the chance of a transfer of energy to lattice vibrations.
- 2) The properties of the solid lattice. The more rigidly the atom is held, the higher the recoil free fraction. This indicates that materials with a high value of θ_D (such as metals and oxides) are likely candidates.
- 3) The ambient temperature. Sources with a high θ_D are more likely to have a higher proportion of zero phonon events at room temperature. This eliminates the need to cool the source, minimising vibration and calibration complications.

The next variable to consider is the absorption cross section (σ_0). This should be as large as possible (generally $\sigma_0 > 0.06 \times 10^{-18}$ cm²) in order to maximise the number of γ -rays being released. In order for this to happen, the internal conversion coefficient α should be as small as possible, so as to favour the production of a γ -photon rather than a conversion electron. Also, in theory the γ -ray produced should be of as long a wavelength (λ) as possible, although in practice this is not necessary.

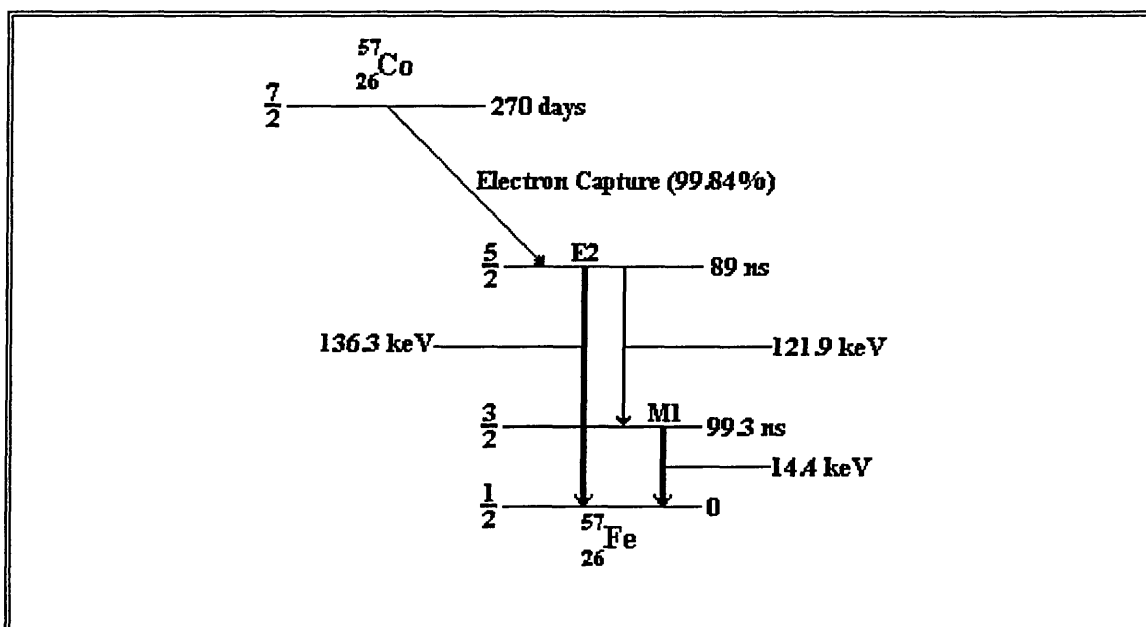
Other factors to consider include;

- a) the number of emission lines, as multiple lines lead to complicated spectra (1 is preferable),
- b) no appreciable quantity of the ground state isotope in the source material (as this increases the source line-width).

- c) Non-resonant scattering should be minimised. This is achieved either by careful choice of the other elements in the host matrix, or, in the case of a metal foil, by keeping the depth that the radioactive material diffuses into the foil as small as possible.
- d) Last, but far from least, the ground state isotope should be stable, and in a high natural abundance. This reduces the inconvenience (and cost) of having to prepare artificially enriched compounds.

In this project a foil of ^{57}Co in a rhodium matrix was used as the source. This source is readily available from commercial outlets at a reasonably low cost (a 30mCi source costs just over £1000 at the time of these experiments). ^{57}Co undergoes electron capture with 99.84% efficiency to give $^{57}\text{Fe}_{26}$ in an excited state. The half-life of this process is about 270 days, ensuring a reasonably long lived source. This then releases the energy in order to reach the ground state. 11% of the energy is lost as a 136.3 keV γ -ray, and 85% as a 121.9 keV γ -ray. The 121.9 keV γ -ray can then go on to give rise to a 14.4 keV γ -ray leaving the atom in its ground state. This is outlined in the diagram Figure 1.7. Of interest is the $3/2$ to $1/2$ transition which gives rise to the 14.4 keV γ -ray. This is within the 10-100 keV criterion discussed earlier. The half-life of 99.3 ns again matches the criterion of a value between 1 and 100 ns, giving rise to a Heisenberg line-width of 0.192 nm s^{-1} . The free atom recoil energy for Fe is $1.95 \times 10^{-3} \text{ eV}$ (at 300 K), which is well below the upper limit of $6 \times 10^{-2} \text{ eV}$. The absorption cross-section for iron is large with a value of $2.57 \times 10^{-18} \text{ cm}^2$ (greater than the $0.06 \times 10^{-18} \text{ cm}^2$ criterion). This is particularly useful as the internal conversion coefficient α is fairly large ($\alpha = 8.17$), which indicates that only 11% of the $3/2$ to $1/2$ transition actually emits a γ -ray.

Figure 1.7 Diagram showing γ -decay scheme for ^{57}Co .



The source gives rise to a single emission line preventing complex overlapping spectra. The ground state isotope ^{57}Fe has a natural abundance of just over 2% naturally. While this is not large, considering the large absorption cross section of iron, it does not require further enrichment artificially. The final reason that this source was used was that the compounds being studied contained iron.

1.5.3.2 Sample Preparation.

Sample preparation, in general terms, is extremely easy. The main problem lies in deciding how much sample to use. Too little sample and nothing is likely to be observed. Too much, and the spectrum will be broad, reducing both resolution and precision. In addition the transmission of the γ -rays also diminishes as a result of non-resonant scattering. It would appear that an optimum thickness is achievable, where resonance and transmission are maximised, and the line-width minimised. Margulies and Ehrman¹⁵⁹

showed that for a uniform resonant absorber and an ideally thin source, the transmission at the resonance maximum can be written as

$$T(0) = e^{-\mu_a t_a} \left\{ (1 - f_s) + f_s e^{\frac{1}{2} T_a} J_0\left(\frac{1}{2} i T_a\right) \right\} \quad \text{Equation 1.19}$$

where J_0 is the zero order Bessel function¹⁶⁰ and $t_a = f_a n_a a_a \sigma_0 t'_a$. They went on to show that the absorption of the final transmitted radiation can be represented as

$$\begin{aligned} \Delta T_0 &= e^{-\mu_a t_a} - T(0) \\ &= e^{-\mu_a t_a} f_s \left[1 - e^{\frac{1}{2} T_a} J_0\left(\frac{1}{2} i T_a\right) \right] \end{aligned} \quad \text{Equation 1.20}$$

If a plot of $\Delta T(0)$ is plotted versus t_a (where $\mu_a = 0.067$, $f_s = 0.7$, $a_a = 0.0219$, $\sigma_0 = 2.57 \times 10^{-18} \text{ cm}^2$), using values for f_a between 0 and 1.0, it quickly becomes apparent that the optimum value for $\Delta T(0)$ is about 10 mg cm^{-2} of total iron. This is the value that was used in calculating the amount of material to be used in all the experiments.

There was one other consideration in the preparation of the sample. If the sample was not ground thoroughly prior to use, a reduction in transmission, broadened half-widths, and orientation effects disrupted the spectrum. This can be demonstrated mathematically to be linked to particle size¹⁶¹.

$${}^{160} J_0(ix) = 1 + \left(\frac{x}{2}\right)^2 + \left(\frac{\left(\frac{x}{2}\right)^4}{1^2 \cdot 2^2}\right) + \left(\frac{\left(\frac{x}{2}\right)^6}{1^2 \cdot 2^2 \cdot 3^2}\right) + \dots \quad \text{Equation 1.20b}$$

¹⁶¹ Cotton, Wilkinson and Gaus, "Basic Inorganic Chemistry", pp44, reference 53, 1987, Wiley, New York, U. S. A.

1.5.3.3 Equipment.

1.5.3.3.1 Transducers

The chances of the source and absorber sharing the same nuclear energy gap is somewhat small. In addition, to observe hyperfine effects a range of energies is required. A means of varying the energy of the source to match that of the absorber is therefore needed. This is accomplished, somewhat ingeniously, by Doppler shifting the γ -rays of the source material. This requires a repetitive motion of small amplitude, which must be achieved with high reproducibility. A number of highly innovative and imaginative solutions have been found to this problem.

The earliest experiments involved the use of constant velocity drives. Sources have been mounted on numerous devices, from lathes and pendulums, to cams and spinning discs. One set-up even involved mounting the source on the piston of a V8 engine! However, the need to almost constantly supervise these instruments in order to change the velocity settings proved the downfall of most of these instruments.

It was de Benedetti¹⁵⁷ who pioneered the use of small transistorised, multi-channel analysers for Mössbauer Spectroscopy. The source is mounted on an electromechanical drive system (similar to a hi-fi loud speaker), which is fed a reference voltage wave-form from a servo-amplifier.

The electro-mechanical device incorporates two coils. One is fed the signal from the servo-amplifier, the other produces a signal proportional to the velocity of the drive, which is fed back into the servo-amplifier. The servo-amplifier compares the return signal with the original reference signal, and then minimises any discrepancies between them. The use of these electromechanical devices opened a new range of possibilities. By feeding different wave-forms to the transducer, different motions could be produced. In particular, the use of a triangular wave-form produced a constant acceleration of the source. This is the means by which most experiments are carried out to this day.

1.5.3.3.2 Counters

The next problem lies in detecting the γ -rays. There are four main types of counter.

For high energy γ -rays lithium-drifted germanium detectors provide an exceptionally high resolution spectrum. However, sensitivity is low, and resolution falls away quickly at lower energies. In addition they need to be kept at liquid nitrogen temperatures.

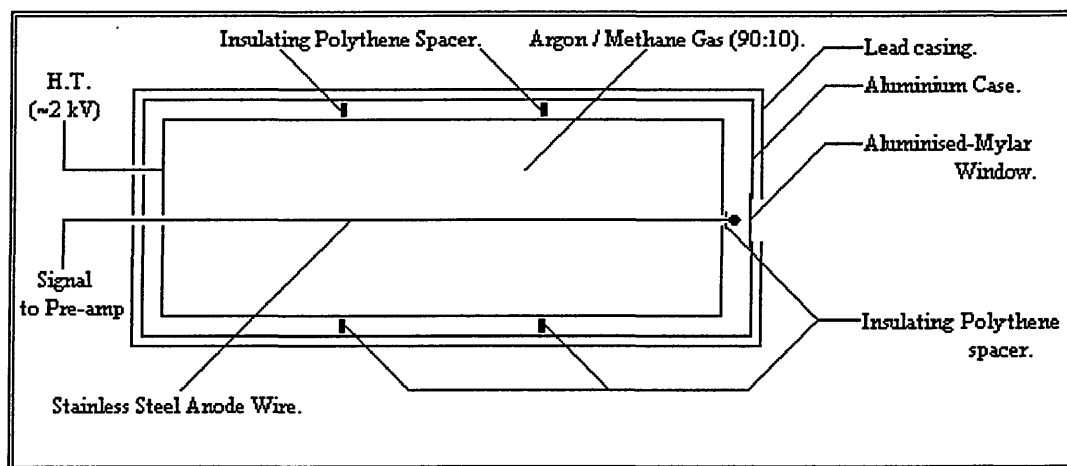
More frequently, scintillation-crystal type detectors such as NaI/Tl are often utilised. Yet again however, resolution falls away rapidly with the lower energy γ -rays.

A more efficient method is the use of a resonance scintillation counter¹⁶². A standard β -detection plastic scintillator is doped with the resonant absorber. This is insensitive to the non-resonant background of primary γ - and X-photons, but detects instead the secondary conversion electrons after γ -ray capture by the resonant nuclei. The main problem here is the necessity of preparing a new counter for each experiment.

In order to detect the lower energy γ -rays, a gas filled proportional counter is more commonly used. Although the efficiency and reliability are fairly low, the relatively high resolution at low energies, and its versatility have made it very popular. There are a number of theories concerning the design of proportional counters, although the most successful work appears to have been achieved on a trial and error basis.

The counters however have the same basic principle. Below is a diagram of the counter used in these experiments.

Figure 1.8 Diagram of a typical Proportional Counter.



¹⁶² L. Levy, L. Mitrani, and S. Ormandjiev, *Nuclear Instr. Methods*, 1964, 31, 233.

The counter is basically a hollow cylinder with a central anode wire, and a window transparent to γ -rays at one end. The cylinder is filled with an ionising gas to a little above atmospheric pressure. In order to detect the 14.4 keV γ -ray produced by ^{57}Fe , an argon / methane (90:10) mix is used. The γ - / X-rays enter the chamber and ionise the argon gas. The electrons produced accelerate away from the cathode tube ionising more gas, and releasing more electrons producing an avalanche effect. This reaches the anode wire (0 V) producing a pulse. The methane mops up any extra electrons generated, providing a sharp pulse. This is amplified by a pre-amp and then further amplified and integrated by a pulse amplifier. In some counters the anode wire is held at a positive voltage while the outer casing acts as the cathode. This has the disadvantage of needing to de-couple the signal before it can be used. This is done by feeding the pre-amp with the required bias voltage.

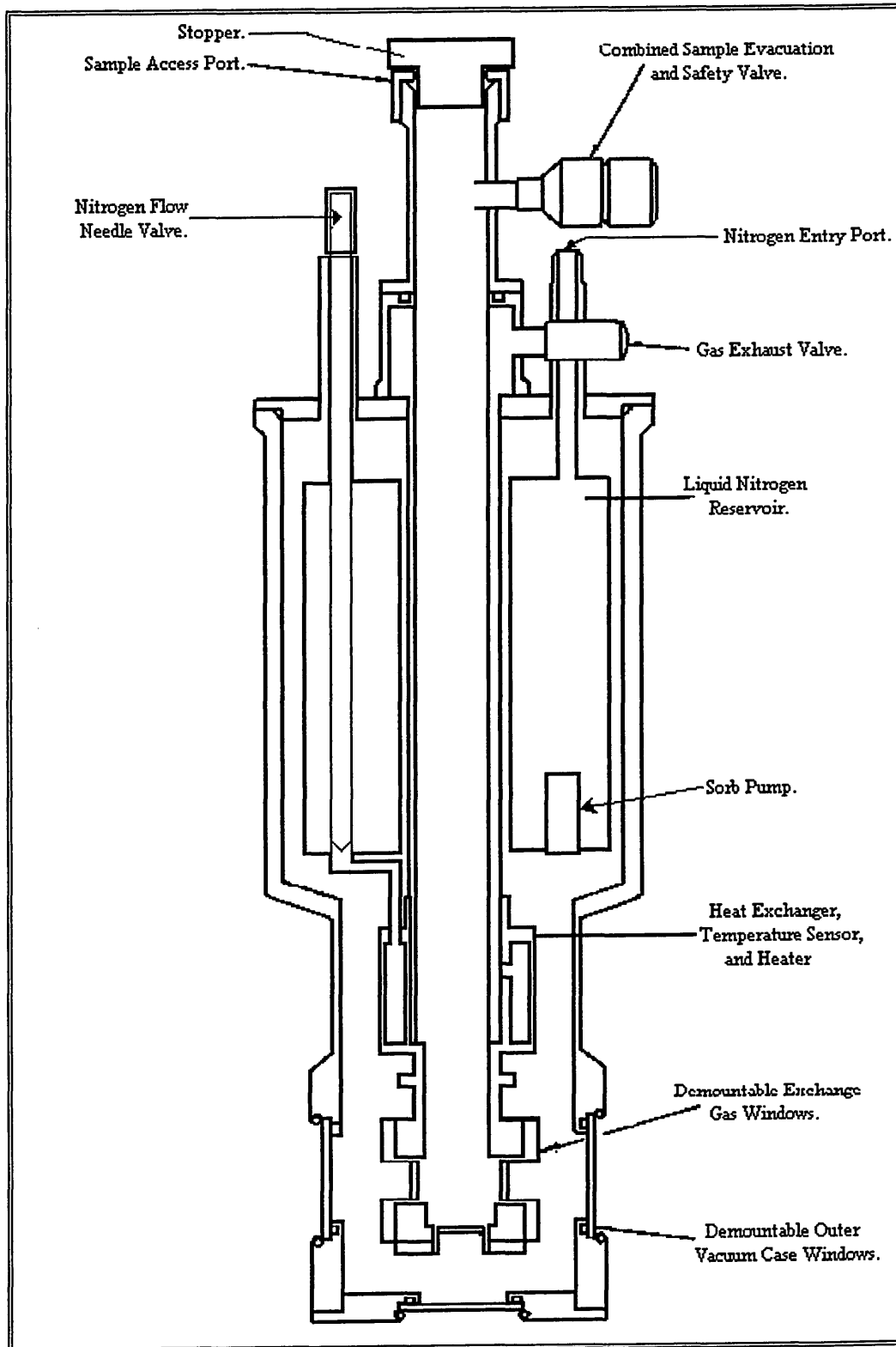
1.5.3.3.3 Cryogenics

In order to maximise the number of zero phonon emissions (the recoil free fraction), it is normal to cool the sample. In addition, the dependence of the spectra on temperature can frequently provide interesting information. Somewhat less frequently, the source is also cooled. This requires cryogenic equipment. Fortunately with ^{57}Fe , the source ^{57}Co is active enough at room temperature and only the sample needs to be cooled. Many commercial cryostats are available for this. There are two considerations however, which are peculiar to Mössbauer spectroscopy. The first of these, is the need for the path

between the source, absorber and detector to be transparent to the γ -rays. This is accomplished by the use of purified beryllium, aluminium or aluminised mylar. The second requisite, is the need to eliminate all vibration from the system. Any vibration will cause a Doppler broadening of the spectrum. This is achieved by a variety of methods, such as rubber mats, or the isolation of the sample from any moving parts. There are two main types of cryostat, both of which were used during the course of this work.

The simplest, the liquid cryostat, is outlined in Figure 1.9. This is basically a rather extrovert vacuum flask. The sample is placed in the central chamber and surrounded with the exchange gas. Since the present project involved working at liquid nitrogen temperatures, nitrogen gas was used. Tightly coiled around the bottom of the sample chamber is the heat exchanger. Here nitrogen drawn from the reservoir tank boils off cooling the chamber before it exits. The sample is thus at around 77 K, the boiling point of liquid nitrogen. In order to study compounds at temperatures above this, a heating coil is wrapped around the heat exchanger. A platinum thermocouple gives the temperature reading to within ± 2 K. The signal from the thermocouple is fed into a temperature controller, allowing it to adjust the power the heater requires to keep the sample at the desired temperature. There are no moving parts so there is no vibration to worry about. The only draw back in this design is the need to top up the nitrogen reservoir every other day.

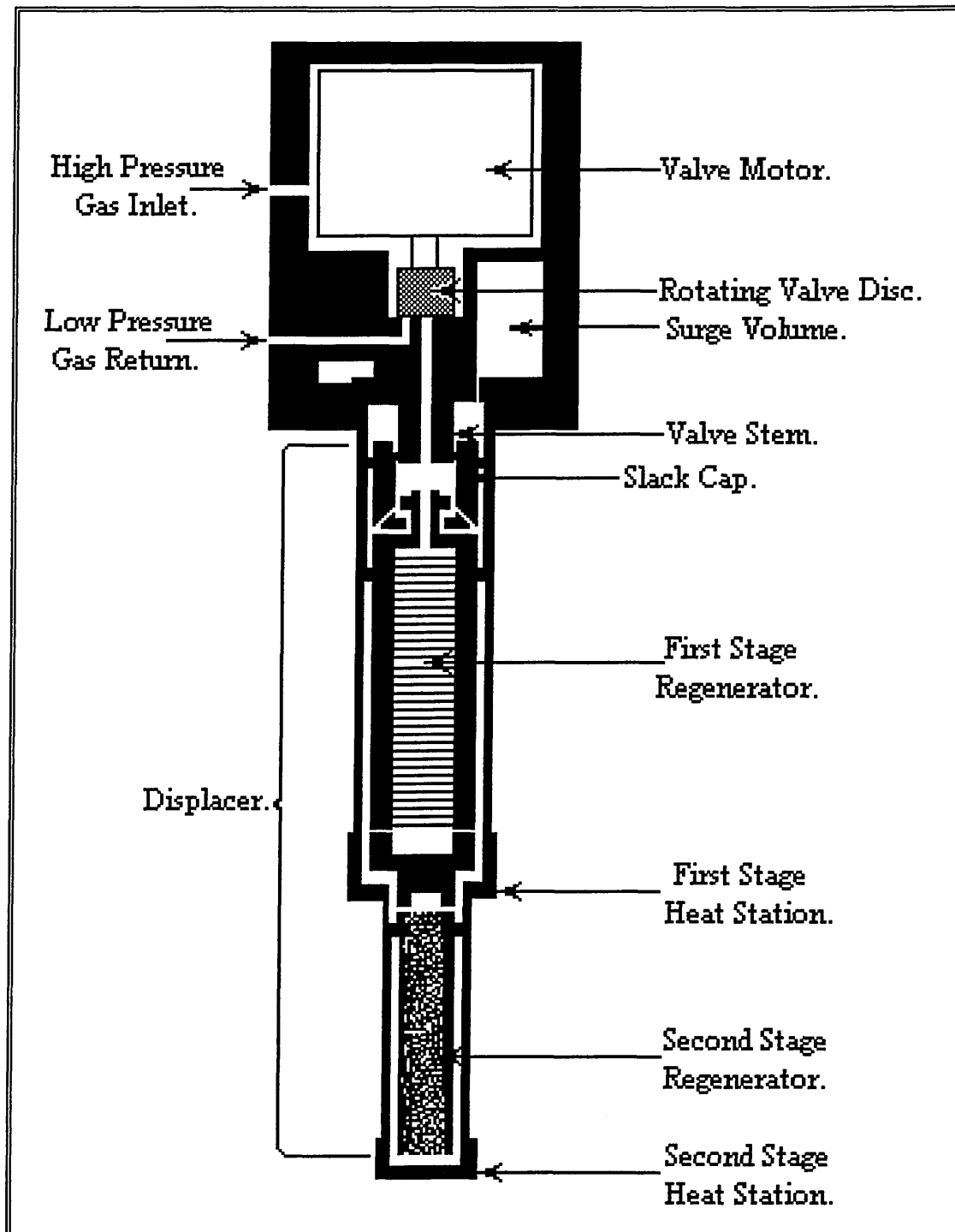
Figure 1.9 Diagram of Liquid Cryostat.



A rather more sophisticated design is the duplex cryostat system. This has the advantage of infrequent recharging and low maintenance. The overall principle is somewhat similar

to the domestic refrigerator. Gas is compressed, then allowed to expand adiabatically causing cooling. The gas is then recycled and the process starts again.

Figure 1.10 Schematic Diagram of the Expander Module for the Displex.



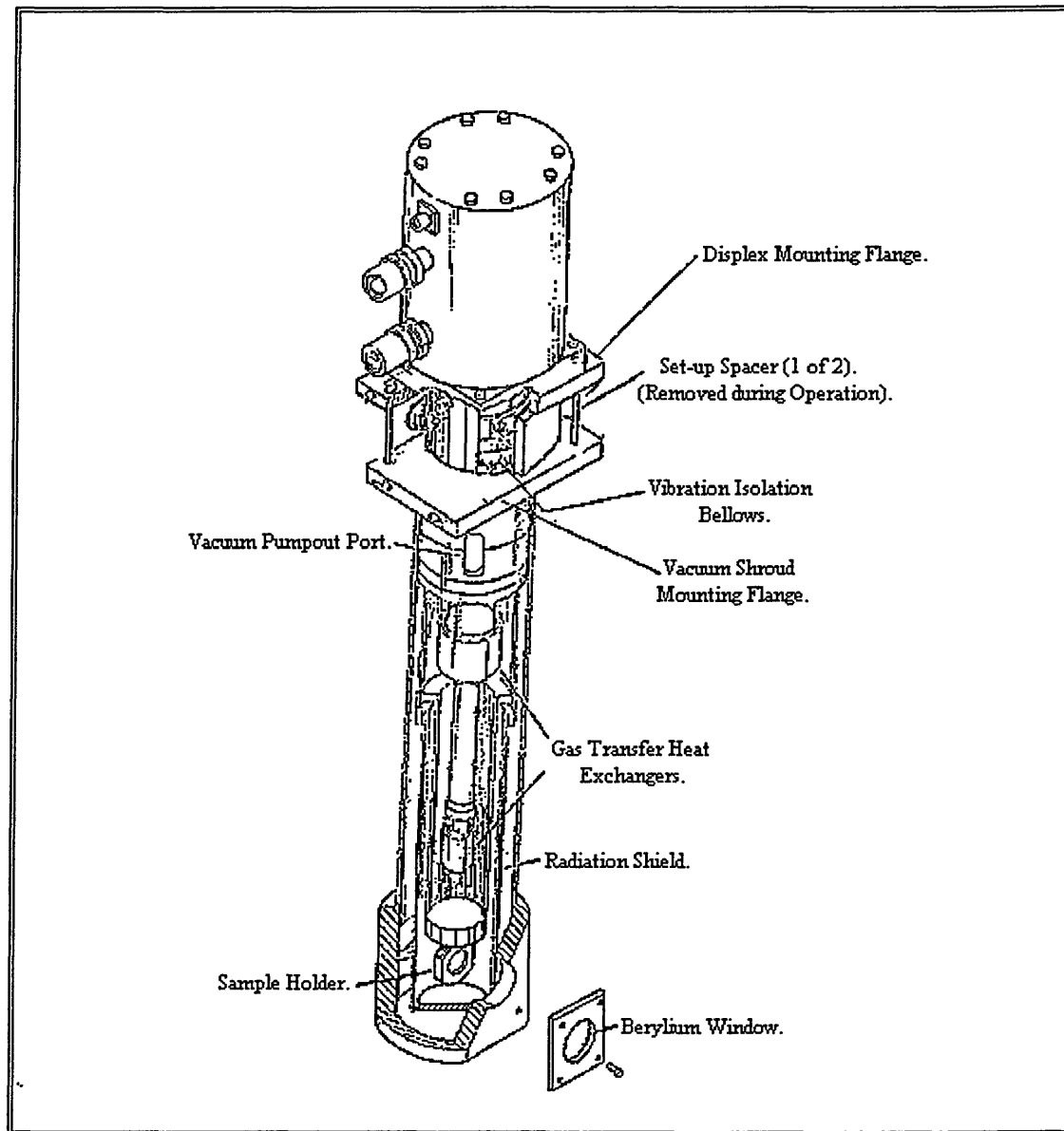
In this case an Air Products Compressor (1R02W) and Expander (DE202) were used, coupled with an Air Products temperature controller (DE3700). The compressor is of a fairly standard design and so will not be mentioned further. Suffice to say the compressor is charged and then switched on. The compressed gas is then pumped to the expander module.

The operation of the expander is worthy of note however. Once the compressed gas reaches the expander module, the inlet valve opens. The gas enters the first chamber via the cold regenerators, expanding and cooling. The inlet valve closes. Within this chamber is a piston type rod. As the gas enters, the rod is driven upwards forcing gas at the heat stations to expand and cool further. The exhaust valve now opens, and the rod drives back downwards. The gas expands once more cooling the regenerators ready for the new gas coming in. The gas exits back to the compressor and the process starts again. In this way, the gas is effectively cooled in three stages during one cycle, allowing temperatures as low as 6-10 K to be achieved.

Although efficient, this method produces a problem. The action of the rod driving up and down causes considerable vibration in the system. In order to overcome this, a second casing is placed around the cold finger, almost, but not quite touching. It is to the bottom of this casing that the sample is attached. The expander unit and sample casing are then mounted separately, joined only by a thin pair of neoprene latex bellows. Helium exchange gas is then introduced into the gap between the sample casing and the cold finger. Although this reduces efficiency by 3-4 K, it almost completely eliminates the vibration caused by the expander module.

Surrounding the sample casing is a radiation shield, and finally the vacuum shroud. The sample has to be kept under vacuum in order to prevent heat transfer from the outside world.

Figure 1.11 The Air Products Displex Cryostat.



Again a small note is needed here. The vacuum is provided by a diffusion pump complete with roughing line for fast change-over of samples. The pumps are mounted on rubber mats to prevent vibration. Now, at temperatures below 50 K air will start to condense on the sample casing, causing it to act as a cryo-pump. In the normal order of events, it

would be necessary to isolate the chamber from the pumps below 50 K, to prevent oil being sucked into the chamber. Fortunately, in this particular case the vacuum hose is so long and thin, it causes a considerable pressure gradient between the chamber and the pump, and so this is no longer necessary.

Wrapped around the bottom half of the sample casing is a heating element, with a gold / chromium alloy thermocouple attached to the base. These are connected to a temperature controller which keeps the sample to within $\pm 2\text{K}$ of the desired temperature. It is thus possible to study the sample at temperatures between 12 and 350K.

1.5.3.4 Acquiring a Spectrum.

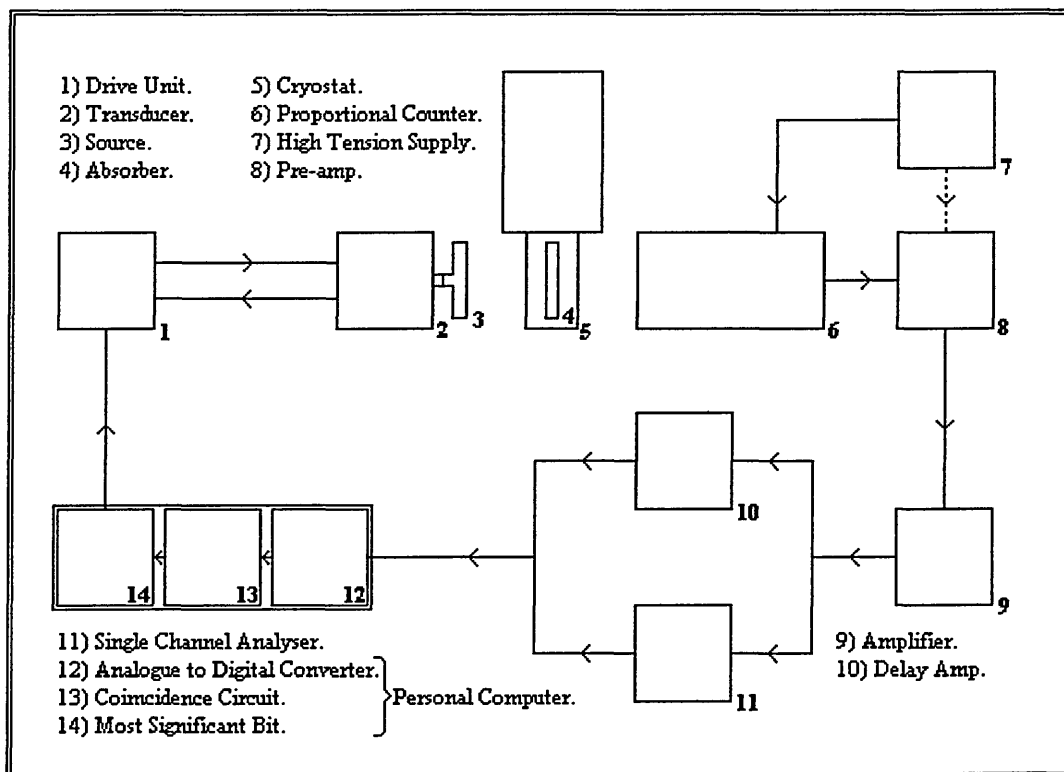
These days almost all data collection is done by computer. In this case a small PC (286) is equipped with an analogue to digital converter, and multi-channel analysing / scaling software (ACETM-MCS by EG&G-Ortec). The signal from the amplifier¹⁶³ is split into two, one half of which passes through a delay amplifier¹⁶⁴, and the other half of which passes through a single channel analyser¹⁶⁵ (SCA). This can occur either internally or externally to the computer.

¹⁶³ The signal from the counter initially passes through an Ortec 109PC pre-amplifier and then an Ortec 579A amplifier.

¹⁶⁴ Ortec 427A.

¹⁶⁵ Ortec 406A.

Figure 1.12 Schematic Diagram of the Mössbauer Laboratory.

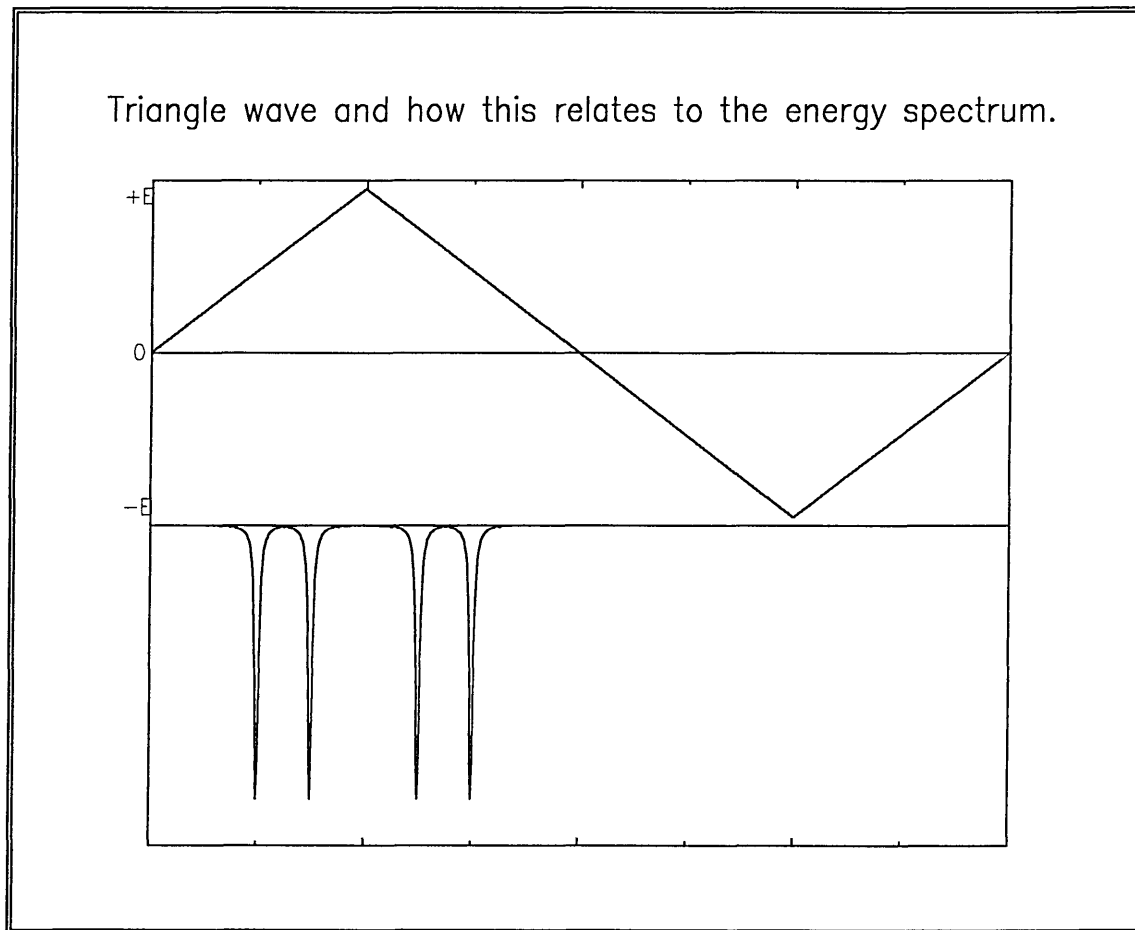


With the computer in multi-channel analysing mode a continuum of energies is displayed. The desired energy is then selected by means of the single channel analyser. The computer is then placed in multi-channel scaling mode, and a count is recorded when a pulse from the SCA and reference signal coincide. The advantage of this set-up is that the computer can also provide the signal sent to the drive unit¹⁶⁶, in order to control the movement of the transducer¹⁶⁷. This is all the equipment necessary to carry out a Mössbauer experiment. A typical arrangement (and in fact the one used), is outlined in Figure 1.12.

¹⁶⁶ Elscint MDR-N-5

¹⁶⁷ Elscint MVT4

Figure 1.13 Diagram of triangle wave and how this is related to energy.



As has been mentioned earlier, most spectrometers these days utilise constant acceleration drives. In order to achieve this a triangular wave-form, either from a signal generator or the PC, is fed to the transducer. In this way, a range of energies are swept from $E_{\gamma}-\delta E$ to $E_{\gamma}+\delta E$, and then back to $E_{\gamma}-\delta E$. If an absorber is placed between the source and detector, a lower count will be recorded at the energy which matches that of the nuclear energy gap of the absorber (see Figure 1.13). However, a close examination of Figure 1.13, shows that two spectra are in fact recorded, one on the forward sweep and then a mirror image spectrum on the reverse sweep. In order to overcome this, the finished spectrum is folded on itself using a simple minimisation routine. In this, a computer attempts to fold the spectrum ten channels either side of the middle channel.

The sum of the squared differences are then calculated, and the minimum value is considered to be the optimum position to fold the spectrum. This gives the completed Mössbauer spectrum.

1.5.3.4.1 Isomer Shift.

The position of the peak relative to 0 ($E\gamma$), is the amount by which the nuclear energy gap of the absorber nucleus differs from that of the source material. A smaller energy gap will show a resonance at a negative value, while a larger energy gap will show a resonance at a positive value. The difference in energy between the source and absorber nuclear energy gap is known as the chemical, or isomer shift (δ).

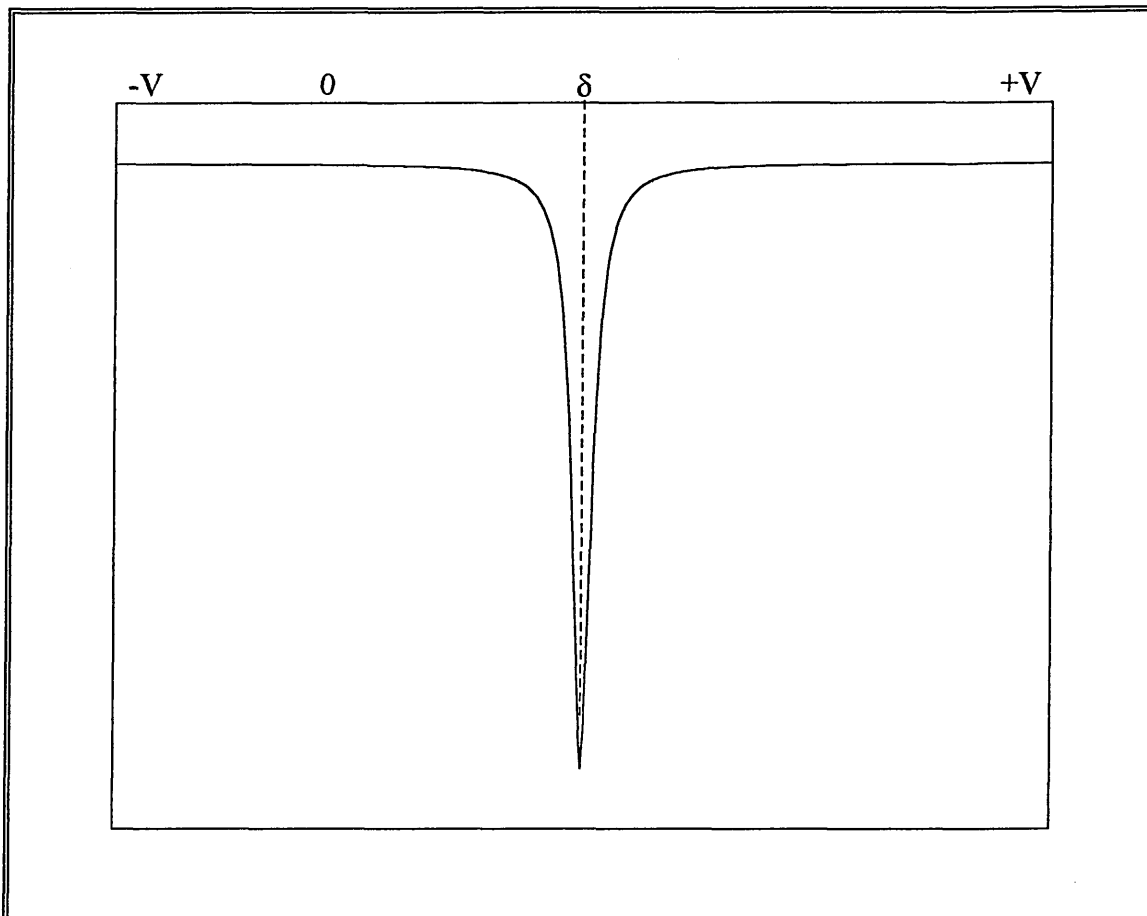
This arises because the 's' electrons have a finite probability of residing at the nucleus. The value of the isomer shift can be calculated mathematically by considering the Coulombic interaction between the nucleus and the 's' electrons.

The nucleus is assumed to be a point charge, with the 's' electron density given by Dirac theory. When simplified, this gives rise to an expression which is the product of a nuclear term and a chemical term. The nuclear term is constant for a given transition, so the equation can be reduced to

$$\delta = \text{constant} \times \left\{ |\psi_s(0)_A|^2 - |\psi_s(0)_B|^2 \right\} \quad \text{Equation 1.21}$$

A and B refer to the absorber and source respectively. $|\psi_s(0)|^2$ refers to the 's' electron density at the nucleus. This is sensitive to 'p', 'd', and 'f' electron screening effects, and also to covalency and bond formation.

Figure 1.14 Diagram Showing spectrum with isomer shift (δ).



So far only the effect of the chemical environment of the nucleus on the isomer shift (δ) has been discussed. However, the isomer shift is also affected by two other minor factors, temperature and pressure. Since all the experiments in this work were done at constant pressure it shall not be considered further. However, most of the work was carried out at different temperatures and so this will have to be considered. The existence of a relativistic temperature-dependant contribution to the isomer shift was pointed out

independently by both Pound and Rebka¹⁶⁸, and also by Josephson¹⁶⁹. As has been mentioned, the atom is vibrating about its lattice position at a rate of 10^{12} per second.

The lifetime of the excited state in the Mössbauer experiment is of the order of 10^{-7} of a second, so the average displacement is zero. However, there is a term in the Doppler shift which depends on v^2 , so that the mean value $\langle v^2 \rangle$ is non-zero. The relativistic equation¹⁷⁰ for the Doppler effect on an emitted photon gives the observed frequency f for a closing velocity v as

$$f = \nu \left(1 - \frac{v}{c}\right) \left(1 - \frac{v^2}{c^2}\right)^{-\frac{1}{2}}$$

Hence

$$f \cong \nu \left(1 - \frac{v}{c}\right) \left(1 + \frac{v^2}{2c^2}\right) \quad \text{Equation 1.22}$$

where ν is the frequency for a stationary system. The first-order term in velocity is a function of the velocity of the atom vibrating about its lattice site and will average to zero. The second-order term depends on v^2 however, and so is independent of direction leading to a non-zero value. This is commonly known as the Second Order Doppler Shift, and for a Mössbauer resonance can be written as

$$f = \nu \left(1 + \frac{\langle v^2 \rangle}{2c^2}\right)$$

The shift in the Mössbauer line is therefore given by

¹⁶⁸ R. V. Pound and G. A. Rebka, Jr, *Phys. Rev. Letters*, 1960, 4, 274.

¹⁶⁹ B. D. Josephson, *Phys. Rev. Letters*, 1960, 4, 341.

¹⁷⁰ W. G. V. Rosser, 'An Introduction to the Theory of Relativity', Butterworths, 1964, 114.

$$\frac{\delta E_\gamma}{E_\gamma} = \frac{\delta v}{v} = -\frac{\langle v^2 \rangle}{2c^2} \quad \text{Equation 1.23}$$

The kinetic energy per mole of the solid, $\frac{1}{2}M\langle v^2 \rangle$, can be related to the total energy of the solid per unit mass, U , ($\frac{1}{2}M\langle v^2 \rangle = \frac{1}{2}MU$) so that

$$\frac{\delta v}{v} = -\frac{U}{2c^2}$$

It is useful to consider the second order Doppler shift (SODS) in terms of lattice dynamics. The following is a simplification of a treatment used by Hazony¹⁷¹. A harmonic approximation is used, and the average energy associated with each atom is

$$\frac{1}{2}M\langle v^2 \rangle = 3\left(n_j + \frac{1}{2}\right)\hbar\omega_j \quad \text{Equation 1.24}$$

where $n_j = \left[\exp\left(\frac{\hbar\omega_j}{kT}\right) - 1 \right]^{-1}$ and ω_j is the oscillation frequency. If this is summed over all possible frequencies and modes of vibration

$$\frac{\delta v}{v} = -\frac{3}{2Mc^2} \sum_j A_j^2 \hbar\omega_j \left(\frac{1}{2} + n_j \right) \quad \text{Equation 1.25}$$

where the A_j^2 terms are weighting factors such that $\sum_j A_j^2 = 1$. M is the atomic mass of

the Mössbauer nuclide. The classical high temperature limit of this expression is

$$\frac{\delta v}{v} = -\frac{3}{2} \frac{RT}{Mc^2} \quad \text{Equation 1.26}$$

From the point of view of inter-comparison of chemical shifts, it is useful to consider the general equation as $T \rightarrow 0$. There is a zero-point motion term given by

¹⁷¹ Y. Hazony, *J. Chem. Phys.*, 1966, 45, 2664.

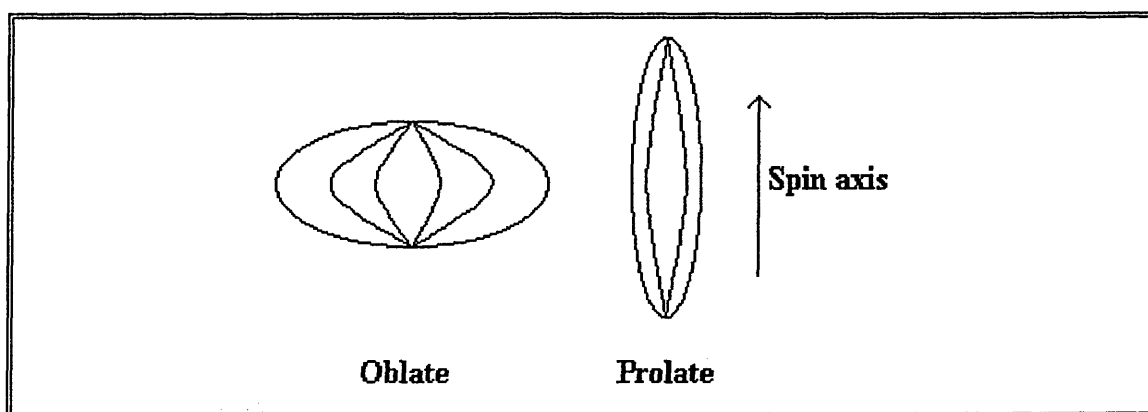
greater than $I = \frac{1}{2}$ then a non-symmetric charge distribution results. Hence it follows that if either or both of the nuclear states have a quadrupole moment, this will interact with electric field gradients in the vicinity. The magnitude of the charge deformation is described as the nuclear quadrupole moment, Q , and is given by

$$eQ = \int \rho r^2 (3 \cos^2 \theta - 1) d\tau \quad \text{Equation 1.30}$$

where e is the charge of the proton, ρ is the charge density in a volume element $d\tau$, which is at a distance r from the centre of the nucleus and making an included angle θ to the nuclear spin quantisation axis. The sign of Q depends on the shape of the deformation. A negative quadrupole moment indicates the nucleus is oblate or flattened along the spin axis, whereas a positive moment is prolate or elongated. In a chemically bonded atom, the electric charge distribution is rarely spherically symmetric, and so the electric field gradient at the nucleus is defined as the tensor

$$E_{ij} = -V_{ij} = -\left(\frac{\partial^2 V}{\partial x_i \partial x_j}\right)(x_i, x_j = x, y, z) \text{ where } V \text{ is the electrostatic potential.}$$

Figure 1.15 Diagram of Flat (Oblate) and Prolate (Elongated) Nucleus.



It is customary to define the axis system of the resonant atom such that $V_{zz} = eq$ is the maximum value of the field gradient. The orientation of the nuclear axis with respect to

$$\frac{\delta\nu_0}{\nu} = -\frac{3}{4} \frac{1}{Mc^2} \sum_j A_j^2 \hbar \omega_j \quad \text{Equation 1.27}$$

The magnitude of the zero-point motion will be dependent on the exact mode of vibration in the crystal, so that $\delta\nu_0/\nu$ will not in general be the same for all compounds.

If the Debye model is adopted, ω_j can have any frequency between 0 and ω_D with a probability of $9N\omega_j^2/\omega_D^3$, the average value of $\hbar\omega_j$ being given by $\frac{3}{4}\hbar\omega_D$. Hence

$$\frac{\delta\nu_0}{\nu} = -\frac{9}{16} \frac{\hbar\omega_D}{Mc^2} \quad \text{Equation 1.28}$$

or using the Debye temperature defined as $\hbar\omega_D = k\theta_D$

$$\frac{\delta\nu_0}{\nu} = -\frac{9}{16} \frac{k\theta_D}{Mc^2} \quad \text{Equation 1.29}$$

The zero-point motion term is proportional to the Debye temperature of the solid if this model is valid. Unfortunately, in the compounds studied here, the vibrational modes of the compounds are extremely complex and this theory falls apart rapidly. The final values obtained are wildly inaccurate, although a comparison of the relative magnitude can be made between similar compounds.

1.5.3.4.2 Quadrupole Splitting.

The vast majority of Mössbauer nuclei have a non-zero-spin, and of those, most have a half-integral spin. In addition, the spin of the excited state is invariably different to that of the ground state (selection rules in fact demand it). If the nucleus has a spin number

the principal axis, z , is quantised. There is an interaction energy between Q and eq which is different for each possible orientation of the nucleus.

The Laplace equation requires that the electric field gradient be a traceless tensor, i.e. the sum of the second derivatives of the electrostatic potential vanish

$$V_{zz} + V_{xx} + V_{yy} = 0 \quad \text{Equation 1.31}$$

Consequently only two independent parameters are needed to specify the electric field gradient completely, and the two which are usually chosen are V_{zz} and an asymmetry parameter η defined as

$$\eta = \frac{(V_{xx} - V_{yy})}{V_{zz}} \quad \text{Equation 1.32}$$

Using the convention that $|V_{zz}| > |V_{yy}| \geq |V_{xx}|$ ensures that $0 \leq \eta \leq 1$. The simplest case to consider is when the electric field gradient has axial symmetry, i.e. $V_{xx} = V_{yy}$ and $\eta = 0$.

The energy levels are then given directly by

$$E_Q = \frac{e^2 q Q}{4I(2I - 1)} [3I_z^2 - I(I + 1)] \quad \text{Equation 1.33}$$

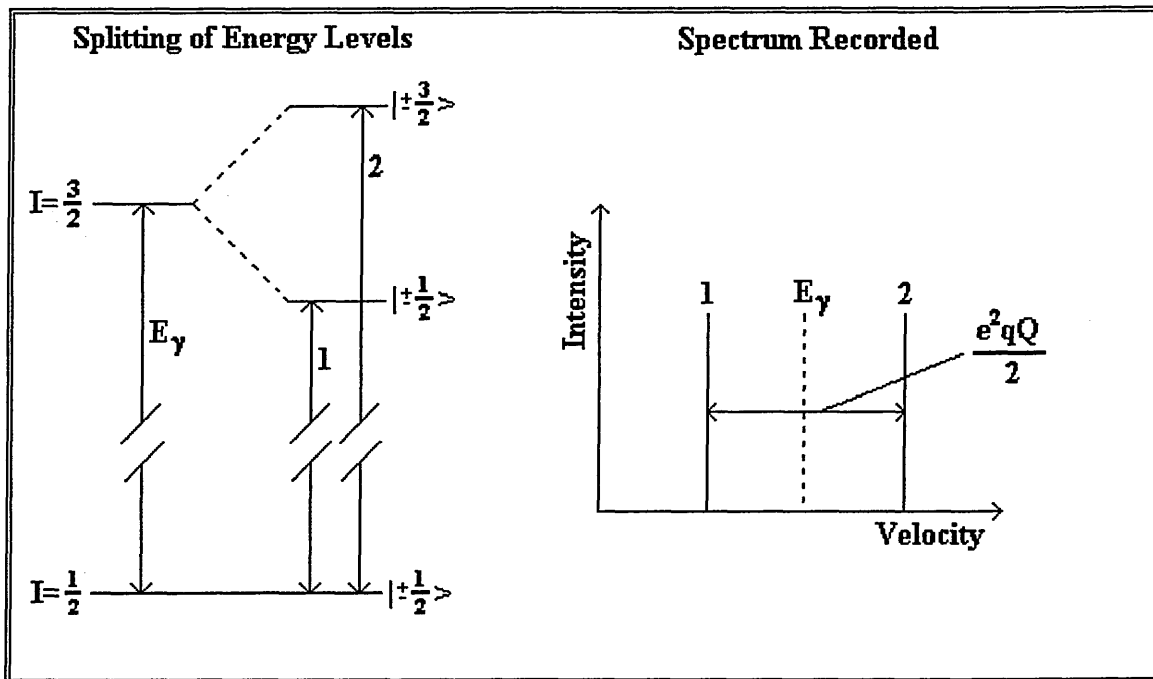
Instead of a single energy level there is now a series of Kramers' doublets identified by the $|I_z|$ quantum number. For $I = 1/2$ there is only one level, but for $I = 3/2$ there are two distinct eigenvalues of energy $+(e^2 q Q/4)$ (for $I_z = \pm 3/2$) and $-(e^2 q Q/4)$ (for $I_z = \pm 1/2$). In general, a Mössbauer transition occurs between two nuclear levels, each of which may have a nuclear spin and quadrupole moment. This means that both the ground-state and excited-state levels may show a quadrupole interaction. Because the energy separations due to these interactions are so small, all the levels connected with a given nuclear spin are equally populated at temperatures above 1 K. A change in the I_z quantum number is

allowed during the γ -ray transition, where $[(I_z)_e - (I_z)_g] = m$ is 0 or ± 1 . This means that for ^{57}Fe with $I = 3/2$, two transitions are possible arising from the $\{I = 3/2 \mid \pm 3/2 \rangle\}$ sub-levels to the unsplit $\{I = 1/2 \pm 1/2 \rangle\}$ level. The resultant spectrum consists of two lines of equal intensity, centred around the isomer shift (which is equal to the energy of the γ -ray transition without a quadrupole interaction), at a distance of $|e^2qQ/2|$ apart. A lack of axial symmetry in the electric field gradient introduces matrix elements which are off diagonal with $[(I_z)_e - (I_z)_g] = \pm 2$. For a $I = 3/2$ nucleus the eigenvalues become

$$E_Q = \frac{e^2qQ}{4I(2I-1)} [3I_z^2 - I(I+1)] \left(1 + \frac{\eta^2}{3}\right)^{\frac{1}{2}} \quad \text{Equation 1.34}$$

The magnitude of the quadrupole interaction is a product of two factors, eQ is a nuclear constant for the resonant isotope, while eq is a function of the chemical environment.

Figure 1.16 Diagram Showing Splitting of Energy Levels and Spectrum.



It should be noted that the electric field gradient, q , is the negative second derivative of the potential at the nucleus and of all the surrounding charge. It thus contains

contributions from both the valence electrons and the surrounding chemical environment. In general the valence part is the major contribution to the electric field gradient, unless the ion has a high intrinsic symmetry, such as high spin Fe^{3+} (d^5). In such cases, the charge and distribution of the counter-ions is the major contributor.

1.5.3.4.3 Hyperfine Splitting.

Although the magnetic hyperfine interaction does not really concern us, it does deserve a brief mention. An electric field gradient at the nucleus leads to a partial loss of degeneracy of the nuclear energy levels, which gives rise to a nuclear quadrupole interaction. A magnetic field at the nucleus leads to a complete loss of degeneracy of the nuclear levels, and produces the nuclear Zeeman effect¹⁷². The magnetic field can be either within the atom, or within the crystal, or as the result of an externally applied field. A general expression would be

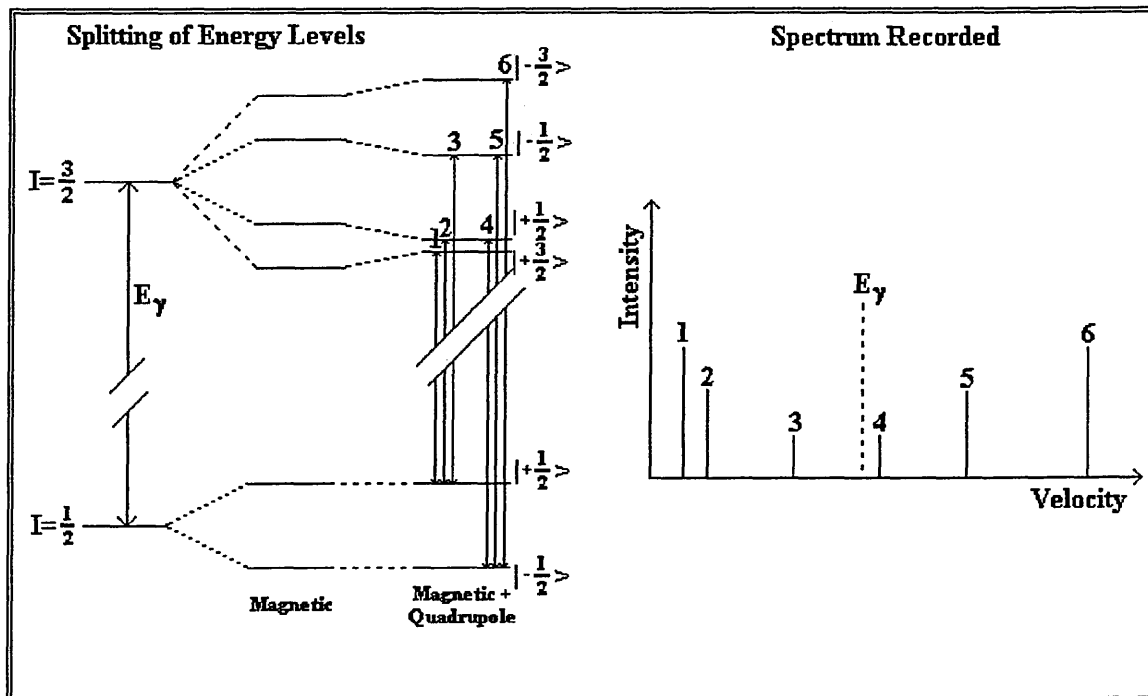
$$H = H_0 - DM + 4/3\pi M + H_S + H_L + H_D \quad \text{Equation 1.35}$$

H_0 refers to the external magnetic field. $-DM$ is the demagnetising field and $4/3\pi M$ is the Lorentz field (the coefficient being strictly applicable to cubic symmetry), but both are small. H_S arises as a result of an interaction of the nucleus with an imbalance in the 's'-electron spin density at the nucleus. This is sometimes referred to as the Fermi contact term. It may arise from intrinsic impairing of actual 's'-electrons, or as a result of polarisation effects on 's'-electrons. H_L arises if the orbital magnetic moment of the parent atom is non-zero. The final term, H_D , arises from the dipolar interaction of the

¹⁷² A. Abragam, 'The principles of Nuclear Magnetism', 1961, Clarendon Press, Oxford, UK.

nucleus with the spin moment of the atom. The sum of H_S , H_L and H_D is usually known as the internal magnetic field, and in most cases is the dominant contribution.

Figure 1.17 Diagram showing H, and H + Q effect on nuclear levels and spectrum.



At first glance it would appear that any compound containing unpaired electrons will show a magnetic hyperfine effect. However, the magnetic field contains a directional element, so if the spins that generate the magnetic field change direction (electronic spin relaxation) faster than the time of the Mössbauer experiment (10^7 s), the magnetic field averages to zero and nothing is seen. If the relaxation time is comparable to the time of the Mössbauer experiment, then a complex overlapping spectrum will be seen. If however the relaxation is slower than the time of the Mössbauer experiment, then a magnetic hyperfine interaction will be seen. For a $I = 3/2$ nucleus, this results in a six line spectrum, equally spaced around the isomer shift position. If a quadrupolar moment is present along with a magnetic moment at the nucleus, the nuclear energy levels are further separated by the requisite amount. This results in an asymmetry of the six line spectrum (see Figure 1.17).

1.5.3.4.4 Calibration of the Spectrum.

The next task is to calibrate the spectrum. This usually involves the use of a reference compound whose spectrum is well known. This was achieved by the use of enriched iron foil for high energy range spectra, and sodium nitroprusside in the case of low energy range spectra. Sodium nitroprusside has a single quadrupole spectrum which shows a constant splitting under normal laboratory conditions ($\Delta=1.705$ mm/s). Using this it is possible to work out how many channels there are per mm/s. This value can then be used to calibrate the unknown spectrum. A similar process is used with the enriched α -iron foil. The number of channels between lines 1 and 6, 2 and 5, and 3 and 4, are compared to the literature values¹⁷³ of 5.312 mm/s, 3.076 mm/s, and 0.841 mm/s respectively. The results are then averaged with a statistical weighting of 2:2:1 given to the differences between lines 1 and 6, 2 and 5, and 3 and 4, to give the final calibration constant. In this particular case an initial estimate of the line positions is fed into a computer program which automatically calculates the best fit based on a Lorentzian line, and then calculates the calibration constant. It should be noted that any values for the isomer shift obtained from spectra calibrated in this way, are by definition quoted as relative to the source used. In this case this is ⁵⁷Co. In order to try to standardise these values, most publications quote the isomer shifts relative to natural iron. This requires the addition of 0.11 mm/s to the isomer shift values obtained from the spectra quoted here.

¹⁷³ *Mössbauer Effect Reference Data Journal*, 1980, 3, 99.

1.5.3.5 Data analysis.

1.5.3.5.1 The Lorentzian Line.

Almost all data analysis is carried out using computers. In principle this allows far greater accuracy in the fitting and interpretation of spectra. A Mössbauer peak can be readily approximated to a Lorentzian curve or line. This is a remarkably simple function that for a single line defined by N points can be represented by;

$$N(i) = \frac{1}{\pi\Gamma\left(\left(\frac{i-\delta}{\Gamma}\right)^2\right)} \quad \text{Equation 1.36}$$

where i is the i 'th point, δ is the isomer shift at point i , and Γ is the half-width at half height of the line. This is then compared to the data points collected, and the parameters allowed to vary slightly. A minimisation routine is employed to determine the best fit. The programs used to fit the spectra in this work were written by Marc Dominic DeLuca of Sheffield Hallam University, and were based on a program written at UKAEA, Harwell, by Geoff Longworth and Ted Cranshaw¹⁷⁴. (These programs were then further modified to match more specific needs by the author). The fitting values are allowed to vary as determined by the user. The program then uses a hybrid non-linear least squares routine to produce a minimisation surface. The valley with the steepest descent determines the best fit, then the parameters are varied again within the routine from that point. This continues until a requisite number of attempts has been made. The user may then accept or change the parameters and the process is repeated until a reasonable fit is

¹⁷⁴ G. J. Longworth, "Mössbauer Spectroscopy Applied to Inorganic Chemistry", 1984, chapter 4, Plenum Press, New York, USA.

obtained. One problem with this system, is the possibility of local minima on the minimisation surface, which lead to erroneous values. This is more common with complex overlapping spectra, requiring the user to constrain most parameters and vary them manually.

1.5.3.5.2 The Fitting of Complex Spectra.

In a perfect world all spectra would consist of clearly resolved, symmetric Lorentzian curves. In practice however, this is not always the case. Orientation effects, magnetic relaxation, a Karyagin effect¹⁷⁵, or the presence of a large number of similar sites can lead to an asymmetric spectrum, with many of the lines of a Gaussian type character.

Selective orientation of the sample can affect the line intensities, as the intensity ratio is dependent on the angle between the electric field gradient axis and the direction of the γ -ray.

A magnetic relaxation effect could broaden and weaken the $\pm 3/2$ transition line more than the $\pm 1/2$ transition. This creates an asymmetry in the spectrum which becomes more pronounced at lower temperatures.

¹⁷⁵ S. V. Karyagin, *Proc. Acad. Sci. USSR, Phys. Chem. Soc.*, **1964**, *148*, 110-125.

The Karyagin effect is caused by anisotropy in the recoil free fraction of Mössbauer events. In other words, a difference in the mean square amplitude of molecular vibrations of the iron nucleus may exist so that Mössbauer transitions to the $m = \pm 3/2$ and $m = \pm 1/2$ states occur with different probabilities. This vibrational anisotropy increases as the temperature is raised, causing an increase in the asymmetry of the observed spectrum.

The last case is known as the Jahn-Teller effect. In effect, this gives rise to many overlapping spectra with very small differences in the hyperfine parameters. The fitting of these spectra is difficult, as the precise positioning of the overlapping spectra is often ambiguous. In addition, with very similar fitting parameters, the fitting program may assume the parameters are in fact identical, and merely fit one of the phases with a negative area. This is then offset by an excessively positive area for the other phases. In order to fit spectra of this type, a Poly-Quadrupole/Hyperfine (PQH) fitting routine is used. In this a linear relationship is assumed between the isomer shift and quadrupole splitting, where

$$\delta = csq + \varepsilon \cdot \Delta.$$

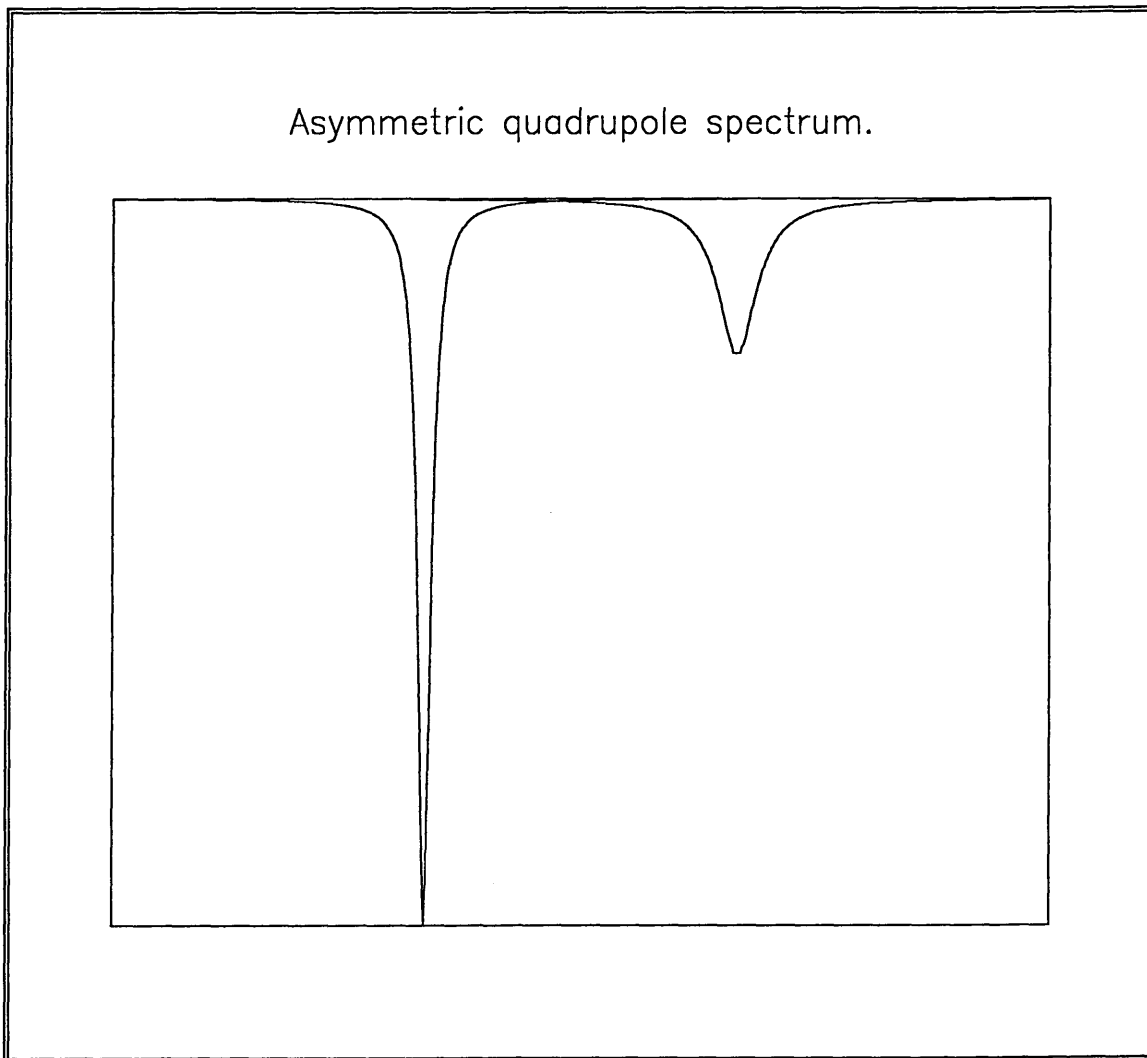
(δ = overall isomer shift of peak, csq = centre of the isomer shifts of the range of quadrupoles, ε = correlation coefficient for the range of quadrupoles, and Δ = the observed quadrupole splitting).

Using an algorithm developed by Philips, Twomey and Morup¹⁷⁶, the spectrum is divided up equally into a spread of quadrupole splittings between a maximum and minimum

¹⁷⁶ According to source code.

value defined by the user. The minimisation routine then calculates the relative area each quadrupole contributes to the overall spectrum. This can be represented as a probability of the molecule existing in that environment. Consider the spectrum shown in Figure 1.18.

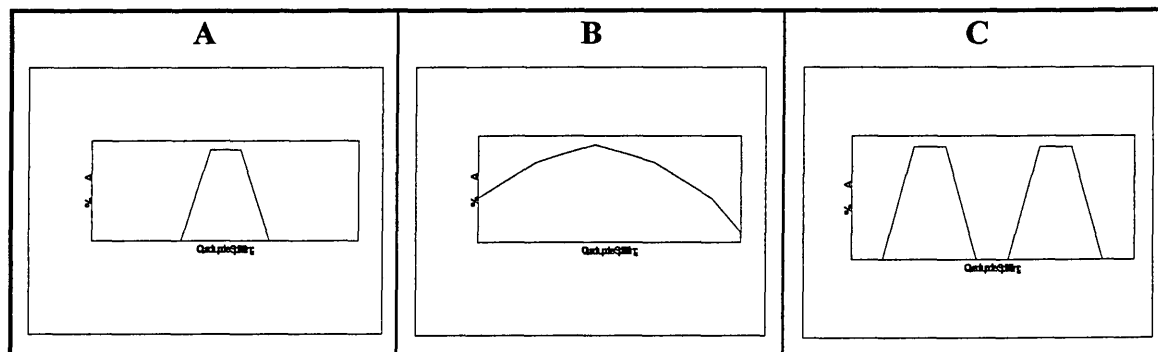
Figure 1.18 Asymmetric Quadrupole Spectrum.



Three possible results are outlined in Figure 1.19. In example a) there is only one distinct environment. Any asymmetry is due to orientation effects, magnetic relaxation, or a Karyagin effect. In b) there is a broad range of very similar environments (Jahn-Teller

effect). In example c) there are two distinct, separate environments. This information can then be used to refine the original fit obtained as necessary.

Figure 1.19 P. Q. fitting results plotted for A) One narrow environment, B) One broad environment, C) Two distinct environments.



Although an extremely useful tool, the fitting technique has its limits. In practice, a very careful selection of the fitting parameters has to be chosen, even as far as the number of quadrupoles to fit in the distribution per observed Quadrupole. Failure to do so causes the program to exceed the error threshold and fail almost immediately.

1.5.3.5.3 The Analysis of Variable Temperature Data; LNAT and ISODS.

If a number of spectra are collected at different temperatures, it is possible to gain further information about the material under study. The spectral area for each phase is proportional to its recoilless fraction. However, the relationship between the recoilless fraction and temperature is not so simple. In section 1.5.2.2 the recoilless fraction (f) was defined as

$$f = \exp \left[\frac{-6E_R}{k\theta_D} \left\{ \frac{1}{4} + \left(\frac{T}{\theta_D} \right)^2 \int_0^{\theta_D/T} \frac{x}{e^x - 1} dx \right\} \right] \quad \text{Equation 1.10}$$

where T = temperature, θ_D = the Debye temperature of the solid, E_R = the recoil energy, c = speed of light, k = the Boltzmann constant. The integral in this equation has no exact solution, but approximations can be made for the low and high temperature limits. As before, if $T \rightarrow 0$ then

$$f = \exp \left[\frac{-3E_R}{2k\theta_D} \right] \quad T = 0 \text{ K} \quad \text{Equation 1.12}$$

If however $T \geq \frac{1}{2}\theta_D$ then

$$f = \exp \left[\frac{-6E_R T}{k\theta_D^2} \right] \quad T \geq \frac{1}{2}\theta_D \quad \text{Equation 1.13}$$

For a thin absorber (Mössbauer thickness, t , less than or equal to 1 (see section 1.5.2.3))

where $t = f_a n x \sigma$, the area $A_t \propto t$, so

$$A = K (n x \sigma) f_a \quad \text{Equation 1.37}$$

where K is a constant, n = number of resonant nuclei/cm³, σ = the resonant cross section /cm², x = the actual thickness /cm. Returning to the approximation and rearranging, it is seen that for the low temperature limit

$$\ln A(T) = \ln K n x \sigma \cdot \left[\frac{-3E_R}{2k\theta_D} \right] = \text{a constant.} \quad \text{Equation 1.38}$$

and for the high temperature limit

$$\ln A(T) = \ln Knx\sigma \cdot \left[\frac{-3E_R}{k\theta_D} \right] + \ln Knx\sigma \cdot \left[\frac{-3E_R}{k\theta_D} \right] \cdot T \quad \text{Equation 1.39}$$

By measuring the area under the absorption peak at different temperatures and using equations (6) and (7), it is then possible to obtain a value for θ_D . If $\ln A$ is plotted against T , then the line produced will be flat where it intercepts the y axis, then slowly bend to give a straight line of gradient $(-3E_R/k\theta_D)$. In practice the line will bend again towards the high temperature limit due to anharmonicity in the lattice. Alternatively, this is done using a program originally written by Gavin Williams of Sheffield Hallam University, based on the Levenberg-Marquant algorithm. In this the normalised areas, together with the respective temperatures, are used to evaluate the Debye integral (see equation 1.10) numerically. This gives the Debye Temperature (θ_D), and the recoilless fraction at 291K. A least squares minimisation routine then compares the theoretical and experimental values to give a goodness of fit approximation.

A similar process is performed on the isomer shift data. Looking back to section 1.9.3.4.1, it is seen that the isomer shift is shifted from its expected position by vibration within the solid according to the following equation,

$$\frac{\delta\nu_0}{\nu} = -\frac{9}{16} \frac{k\theta_D}{Mc^2} \quad \text{Equation 1.29}$$

where $\theta_D = \frac{\hbar\omega_D}{k}$. Using a program written by E. Vanderberge¹⁷⁷, the experimental isomer shifts and temperatures are fitted using a least squares minimisation routine to the theoretical values. Once again a value for θ_D is produced, together with a value for the

¹⁷⁷ See source code.

intrinsic isomer shift for the compound. The program is somewhat limited, as a value for the recoiling mass (M) is difficult to predict, and in addition the complex vibrational modes within the compounds studied leads to gross inaccuracies in θ_D . However, it does permit comparison of θ_D for different compounds.

1.5.3.6 Information available from experiment

1.5.3.6.1 Oxidation state

To a first approximation, the oxidation state of a compound can be readily correlated to its isomer shift. In section 1.5.3.4.1 it was shown that the isomer shift depends on the 's'-electron density at the nucleus. Bonding has little effect on the inner 's'-electron density and so has little effect on the isomer shift. However, the outermost 's'-electrons are very sensitive to the shielding effects of valence 'p'-, 'd'- and 'f'-electrons, and therefore so is the isomer shift. In section 1.5.3.4.1 it was seen that the isomer shift could be expressed as

$$\delta = \text{constant} \times \left\{ |\psi_s(0)_A|^2 - |\psi_s(0)_B|^2 \right\} \quad \text{Equation 1.21}$$

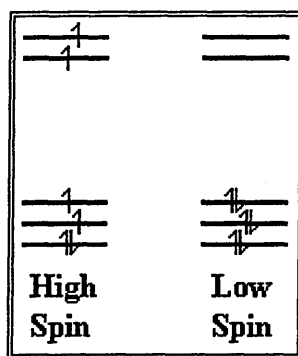
For ^{57}Fe the constant has a negative value. Therefore, any factors leading to a reduction in the 's' electron density at the nucleus will lead to a more positive isomer shift relative to the source. For instance, oxidation of Fe^{2+} to Fe^{3+} leads to a reduction in 'd' electron density. The decreased shielding experienced by the nucleus leads to an increase in 's' electron density and a less positive isomer shift is seen. Typically Fe(II) compounds have a large isomer shift ($>0.5 \text{ mm s}^{-1}$), whilst Fe(III) compounds have small isomer shifts ($0-0.5 \text{ mm s}^{-1}$). Similarly, the introduction of electron-withdrawing groups around the iron

will lead to a reduction in 's' electron density leading to a more positive isomer shift. The more electronegative the ligands the more positive the isomer shift.

1.5.3.6.2 Local environment

Information concerning the local environment can be deduced from the quadrupole splitting of the compound under consideration. In section 1.5.3.4.2 it was seen that the quadrupole splitting arose due to an electric field gradient across the nucleus. This is mainly dependent on the oxidation state and electronic configuration of the atom. It is also dependent to some extent on the charge, polarity and arrangement of molecules around the resonant atom. In the first instance, an idea of the origin of the electric field gradient can be gained from considering the shape of the molecule / ion and using crystal field theory¹⁷⁸. For instance, consider Fe(II) (d^6) in an octahedral environment.

Figure 1.20 Diagram showing different electronic configurations for Fe(II).



For the high spin species there will be a considerable electric field gradient across the nucleus and hence a quadrupole interaction is likely to be observed. For the low spin

¹⁷⁸ Cotton, Wilkinson, and Gaus, "Basic Inorganic Chemistry", 1987, Second Edition, Wiley, UK.

species however the charge is balanced and so no electric field gradient will be observed across the nucleus. No quadrupole interaction will be seen in the Mössbauer spectrum. Surrounding ligands will also have an affect. The less symmetric the balance of charge around the nucleus, the bigger the quadrupole splitting. An octahedral complex with identical ligands will not give rise to quadrupole interaction. Asymmetry resulting from replacing one or more of the ligands will increase the quadrupole splitting. The greater the difference in electronegativity of the ligands the greater the quadrupole splitting. Less symmetric arrangements of ligands, tetrahedral for instance, will tend to give a lower quadrupole splitting.

Information can also be acquired from variable temperature studies. For instance, while studying organo-tin complexes supported on montmorillonite, Breen *et al.*¹⁷⁹ observed a change in gradient in the *ln* Area vs. temperature data around 210 K. This was attributed to the melting of the interlayer layer which left the organo-tin molecules with greater vibrational freedom. A similar change in gradient was also observed by Hendrickson *et al.* when studying valence electron de-trapping phenomena in biferrocenium salts¹⁸⁰. The change in gradient was found to coincide with the start of the valence electron de-trapping. They discovered that the change in gradient was caused by oscillation of the counter ion which started at this temperature. This produced a less rigid lattice and also led to a more symmetric environment around the biferrocenium cation. This in turn allowed the transfer of an electron between the iron centres. The phase transition was subsequently confirmed by scanning differential calorimetry.

¹⁷⁹ C. Breen, K. C. Molloy, and K. Quill, *Clay. Min*, **1992**, *27*, 445-455.

¹⁸⁰ T-Y. Dong, D. N. Hendrickson, K. Iwai, M. J. Cohn, S. J. Geib, A. L. Rheingold, H. Sano, I. Motoyama, and S. Nakashima, *J. Am. Chem. Soc.*, **1985**, *107*, 7996-8008.

1.5.3.6.3 More Complicated Spectra.

So far an attempt to correlate the electronic and molecular structure of a compound to its Mössbauer Spectrum has been made. However, in practice this is not always immediately apparent. In order to observe a hyperfine interaction the effect must last longer than the Larmor frequency, which for iron is approximately 100ns^{157} . This is quite long at an electronic level, which can lead to complications. For instance, imagine a molecule with a quadrupole splitting Q . If the molecule rotates at a speed so great that the electric field gradient is averaged out over the time of the experiment, then no quadrupole will be seen in the spectrum, *i.e.* $Q(\text{observed}) = 0$.

Alternatively, consider two atoms with different oxidation states, but able to transfer an electron between them. At low transfer rates ($\ll 10^7\text{ s}^{-1}$), both of the resonances due to each oxidation state will be seen. At transfer rates similar to that of the lifetime of the excited state ($\approx 10^7\text{ s}^{-1}$), both resonances will be seen, but also an average resonance. At high transfer rates ($\gg 10^7\text{ s}^{-1}$), only the average resonance will be seen. This process is known as valence electron de-trapping (see section 1.4.3). In the above processes it is also wise to scrutinise the line-widths. If the resonances start to broaden, this implies that the process involves the resonant atom directly. If the line-widths remain the same, then it implies that it involves some indirect process surrounding the resonant atom.

1.6 Other Techniques

1.6.1 Ultra-Violet Spectrometry (U.V.)

Measurements were made using a Hitachi U-2000 double beam UV-spectrometer, with cells of path-length 1 cm. Although of limited use in our work, Ultra-Violet spectrometry gives us an indication of how much compound has exchanged with the clay.

1.6.2 C, H, N Analysis

CHN analysis was carried out by Brunel University. The figures provide not only confirmation that the compound synthesised was the one desired, but also exchange ratios for the clay contact experiments, and an internal check that the molecule had not decomposed upon entering the clay.

1.6.3 X-Ray Fluorescence Spectrometry (XRF).

X-Ray fluorescence spectrometry is another technique which is not particularly well known. In an effort to enlighten those unfamiliar with the technique, a quick summary follows.

In principle XRF is the same as many other spectrometric techniques. A sample is exposed to incident radiation, the intensity of the scattered radiation is measured, and then compared to a standard calibration curve to give a measure of the material present. In the first instance, the sample needs to be in a form suitable to introduce into the spectrometer. In the present case this was achieved by fusing the dried sample with lithium borate (typically 1 g: 9 g) to form a glass bead. The radiation used is a continuum of X-rays. The sample is bombarded with x-rays and the fluorescent radiation measured. The detector scans through a range of angles, and the elements present are identified by their characteristic wavelengths (As the d-spacings for the dispersion crystals are known, the wavelength is related to the angle the radiation is detected at). The intensity of each element is then compared with a suitable calibration curve collected earlier for that element. In practice almost everything is controlled by a PC, and analysis takes a matter of minutes.

1.6.4 Variable Temperature Infra-Red Spectroscopy (VT-IR).

Spectra were recorded of a 5 mg, 15 mm diameter disc, using a 200 times KBr dilution of sample pressed at 10 tons pressure for 2 minutes. Spectra were initially recorded using a Perkin-Elmer 783, and later an ATI Mattson Genesis series FTIR, over the range 200-4000 cm^{-1} with a resolution of 2.0 cm^{-1} . In the variable temperature experiments, the discs were heated under vacuum in 50°C increments, and left to stabilise for 15 minutes prior to recording the spectrum. (When studying clays, VT-IR removes most of the interlayer water, permitting observation of the bands which may otherwise have been obscured).

1.6.5 Thermogravimetric Analysis.

Thermogravimetric analysis was performed using a Mettler M3 balance/TG50 furnace, connected to a Mettler TC10A processor. Samples (typically 5-10mg) , were heated from 25-800°C, at a rate of 20 °C/min, in a dynamic atmosphere of dry N₂ gas flowing at 20 ml/min. Although somewhat ambiguous, the technique is useful where there is a distinct weight loss, such as a cyclopentadienyl ring, or as a fingerprint for a specific compound.

1.6.6 Thermal Desorption Mass Spectroscopy (TD-MS)

TD-MS was carried out on a Viglen Trio Mass Spectrometer. The sample, (*ca.* 1mg), was placed on the probe and inserted directly into the mass spectrometer. The probe was heated from 50-750°C, at a rate of 20°C min⁻¹, and then cooled from 750-50°C at a rate of 250°C min⁻¹. The total collection time is theoretically 37.8 minutes, 35 minutes of which corresponds to the heating phase. The total number of scans is approximately 1320. The spectra are therefore composed of a heating phase of 1-1224 scans, where there are 1.75 scans/°C, and a cooling phase from 1224-1320 scans, where there are 0.14 scans/°C. The computer software controlling the experiment is not very efficient however, and the total experiment time is actually 46 minutes. This lag is due to the time it takes the data to be read and stored by the processor. This does not have much affect on the recorded temperatures, although the heating rate can be assumed to have a discrepancy of up to 20%. Therefore it must be remembered when comparing with other

dynamic techniques (such as thermogravimetric analysis), that compounds may decompose somewhat faster than predicted. This technique is still extremely useful however. Not only does it give an idea of a stability of the products, but it also allows identification of the breakdown products.

1.6.7 Variable Temperature X-Ray Diffraction (VT-XRD).

VT-XRD of partially orientated clay on glass slides and also of powder samples, was accomplished using a Philips PW1050/25 goniometer, with a Philips PW2236/20 cobalt tube operating at 40 kV, 40 mA. The beam was passed through a nickel filter and was detected by a Philips PW1965/30 detector connected to an IBM compatible personal computer. This scanned between $2-50^{\circ} 2\theta$, counting for 1 second in $0.02^{\circ} 2\theta$ increments. A heating stage manufactured according to Brown¹⁸¹ was used to heat the samples in the temperature range 20-400°C. By studying the d-spacings at different temperatures, it is possible to determine if and how the molecule has successfully inserted between the layers of the clay. In addition it is also possible to get an idea of how thermally stable the inserted molecule is.

¹⁸¹ G. Brown, B. Edwards, E. G. Ormerod and A. H. Weir, *Clay Minerals*, 1972, 9, 407.

1.7 The project

1.7.1 N, N - dimethylaminomethylferrocene on clay.

Previous work by Breen *et al.*¹⁸² on the uptake of organo-metallic compounds onto clay, had shown that a high loading was difficult to achieve and by no means predictable. The first part of the project was to try to find a means to maximise the uptake of the organo-metallic compound onto the clay. The clay used was chosen because of the low iron content, but there is still a small amount which can cause problems with the higher temperature Mössbauer spectra, especially if the exchanged material is only present in small amounts. Breen *et al.*¹⁸² had achieved a loading of about 40% while studying the uptake of the tricarbonyl(η^5 -2,4-dimethylcyclohexadienyl)iron⁺ and tricarbonyl(η^5 -2-methoxycyclohexadienyl)iron⁺ cations onto the montmorillonite Westone-L. Following on this work, Westone-L was exchanged with the unsubstituted cation, tricarbonyl(η^5 -cyclohexadienyl)iron⁺. However only 7% of the cation was exchanged. Although this cation has approximately the same size, shape and charge as those before, it is obvious that the factors affecting uptake are finely balanced. As an attempt to study biferrocenes within the clay was to be tried later on, it was decided to try contacting ferrocene with the clay. This attempt failed with no observable exchange at all. It was noticed at this stage that the exchange process seemed to favour compounds with substituted rings. Breen *et al.*¹⁸² had noted that the tricarbonyl(η^5 -2-methoxy-cyclohexadienyl)iron⁺ was more firmly anchored in the clay, and tentatively suggested that the methoxy group may be interacting with the hydroxyl groups in the aluminosilicate sheet of the clay. In order

¹⁸² C. Breen, J. S. Brookes, S. Forder, A. Maggs, G. Marshall, and G. R. Stephenson, *J. Materials Chemistry*, 1995, 5(1), 97-104.

to take advantage of this, an attempt to exchange the clay with N, N, -dimethylamino-methylferrocene (A) was made. The decision to use A was arrived at after a lot of careful thought. Firstly it was hoped that the side chain would behave similarly to the methoxy group used before, able to interact with the aluminosilicate lattice, and possibly be trapped in a hole surrounding the main anchoring site. Secondly, the amine functionality has the ability to protonate to form a charged side-chain. It was anticipated that this might help displace the sodium ions in the clay, enabling an even higher exchange ratio.

1.7.2 Biferrocene/Biferrocenium on clay

The first stage of this part of the project was to see if the biferrocene could be incorporated into the clay in a manner similar to that of A. If successful, the second stage involves seeing if the molecule could be oxidised up in situ, or alternatively oxidised and then contacted with the clay afterwards. These materials are difficult to produce in large amounts, so excess CEC and multiple contacts are not a viable option. In addition, each biferrocenium has two amine groups capable of being protonated, giving a possible overall charge of +3. In practice this could reduce the exchange ratio by a third, so the first option of oxidising up in situ would be preferred. The second stage of this part of the project, was to investigate the effect of incorporating the molecule into the clay. As has been mentioned in section 1.4, the extreme sensitivity of the biferrocenium cation to its local environment has been an exciting area of research lately. In the work of Hendrickson *et al.*¹⁸⁰, they synthesised a number of different compounds, varying the anion or solvent molecules present and then compared them. This can cause problems as different crystal structures, defects, different ionic radii *etc.* can complicate direct

comparisons. In our work the clay should act as a consistent “dilute” anion, which can absorb differing amounts of solvent, which can then be directly compared.

1.7.3 Synthesis and Heat treatments of A-APWL

An area of ever expanding interest is that of heterogeneous catalysis. The requirements in the synthesis of such catalysts have been mentioned elsewhere (see section 1.3.2). In an effort to achieve this, an attempt to introduce the molecule into aluminium pillared Westone-L was made. When pillaring a clay, the exchange capacity is greatly reduced by the migration of protons into the intralaminar spaces. The use of a base can restore the exchange capacity however. Using A, it was hoped that the molecule would be drawn into the cavities in the structure formed by the pillaring, by forming the protonated species *in situ*. After characterisation to ensure the molecule is within the cavity and not just residing on the clay surface, the molecule is heated until it decomposes. It is hoped that this will leave discrete iron particles dispersed throughout the pillared matrix, residing in the main cavities formed by the pillaring of the clay. Careful study of the breakdown products in an order to elucidate the iron species formed, should give us an idea of how suitable the material is likely to be as a catalyst.

1.7.4 Glossary of Terms.

Many of the compounds used in this project have somewhat long winded names. In an effort to reduce tedious reading (and typing), the following abbreviations have been used.

Na-WL	Sodium Exchanged Westone-L
HWL	Acid exchanged Westone-L
APWL	Aluminium Pillared Westone-L
A	N, N-dimethylaminomethylferrocene
AA	2,2''-bis[(dimethylamino)methyl]biferrocene
AA'	2,5''''-bis[(dimethylamino)methyl]biferrocene
AA ⁺	2,2''-bis[(dimethylamino)methyl]biferrocenium
AH	ferrocenylmethyldimethylammonium
A-WL	Product of contact of A + Na-WL
AH-WL	Product of contact of AHCl + Na-WL
A-HWL	Product of contact of A + HWL
A-H-WL	Product of contact of A + H ⁺ + Na-WL
A-APWL	Product of contact of A + APWL
AA-HWL	Product of 3 hr contact of AA + HWL
AA-HWL(48)	48 hr contact of AA + HWL
AA ⁺ -HWL	Product of iodine oxidation of AA-HWL
⁺ AA-HWL	Product of contact of AA ⁺ + HWL

2. N, N-dimethylaminomethylferrocene on Westone-L.

2.1 Experimental Methods.

2.1.1 Materials.

Clay. The clay used in all the experiments was the montmorillonite **Westone-L** from Texas, supplied by ECC International, which was found to have a cation exchange capacity (CEC) of 91meq/100g. **N,N-dimethylaminomethylferrocene** and **AlCl₃.6H₂O** were supplied by Aldrich Chemicals. **NaOH** was supplied by BDH Chemicals.

2.1.2 Preparation.

2.1.2.1 Sodium Exchanged Westone-L

This was produced by a three step process. First the raw Westone-L was sedimented to remove heavy particles such as quartz and iron oxide. Secondly, the lighter clay fraction (nominally $< 2 \mu\text{m}$ particle size¹⁸³) was contacted (three times) with aqueous 1M NaCl, and finally washed, by repeated suspension in deionised water followed by centrifugation and removal of supernatant, until a residual conductivity of less than 50 μS was achieved. This is hereafter referred to as Na-WL.

¹⁸³ Stokes' Law for a particle of radius a falling with a terminal velocity v , through a liquid medium of viscosity ω can be written as $F = 6av\omega$, where F is the force on the particle. For a spherical particle of density η , this can be re-written as $t = (9/2)\omega(d/\eta g a^2)$, where t is the time in seconds, g is the acceleration due to gravity (9.8 m s^{-2}), and d is the distance in metres. So, if $t > 16$ hours, $\omega = 10^{-3} \text{ Kg m}^{-1} \text{ s}^{-2}$ (20°C), $d = 0.1 \text{ m}$, then the particles obtained will have a radius $a < 1.4 \mu\text{m}$.

2.1.2.2 Acid Exchanged Westone-L

Na-WL was contacted with aqueous 1 M sulphuric acid for two hours at 20 °C, followed by washing, as for the Na-WL above. This will subsequently be referred to as H-WL.

2.1.2.3 (ferrocenylmethyl)dimethylammonium chloride

1 g (4.12 mmol) of N,N-dimethylaminomethylferrocene was added drop-wise with stirring to 50 ml of 1M HCl. This was evaporated (in vacuo) to give a green solid. Recrystallisation from CHCl₃/Et₂O gave long golden brown crystals in 87% yield. C, H, N, analysis: theory C=55.85, H=6.49, N=5.01; found C=55.59, H=6.40, N=5.02.

2.1.3 Exchange Procedures.

2.1.3.1 The intercalation of (ferrocenylmethyl)dimethylammonium into Westone-L.

METHOD (1). N,N-dimethylaminomethylferrocene (1 g, 2 CEC, 4.12 mmol) was suspended in 50 ml deionised water, and 5 ml of 1 M HCl (an excess) added drop-wise with stirring to give a solution of (ferrocenylmethyl)dimethylammonium-chloride. 1 g of ground Na-WL powder (dried at 120°C) was then added and the resulting suspension left to stir overnight. The clay was isolated by centrifugation and the process repeated twice more. Finally, the product (referred to as A-H-WL) was washed with deionised water (5x 120 ml), and air dried at room temperature.

METHOD (2). N,N-dimethylaminomethylferrocene (1 g, 2 CEC, 4.12 mmol) was dissolved in 50 ml of methanol and 1g of H-WL (dried at 120°C) added. The resulting suspension was left to stir overnight, centrifuged and finally washed with methanol (5x120 ml). The product (referred to as A-HWL) was then air dried at room temperature.

METHOD (3). (ferrocenylmethyl)dimethylammonium chloride (2.8 g, 1.0 CEC) was dissolved in 50 ml of deionised water, and 1 g of powdered Na-WL (dried at 120°C) added. The suspension was then left to stir for 8 hours. The clay was isolated and the process repeated twice more. The product was then washed (5x120 ml de-ionised water) as above. The product is hereafter referred to as AH-WL. C, H, N, analysis; Theory: 100% exchange C = 14.2, found 11.0, equivalent to 80% exchange).

2.1.3.2 Intercalation of N,N-Dimethylaminomethylferrocene into Na-WL.

N,N-dimethylaminomethylferrocene (3 g, 3 CEC, 12.46 mmol) was suspended in 100 ml of deionised water, and 1 g of powdered Na-WL (dried at 120°C) was added. The suspension was left to stir for 6 hours at 25°C. The clay was then isolated by centrifugation and the process repeated twice more. The final product (hereafter referred to as A-WL) was then washed (3 x 120 ml H₂O, 3 x 120 ml MeOH, 1x120 ml H₂O) in the normal manner.

2.1.4 Adsorption Isotherms.

20 ml methanolic solutions of N,N-dimethylaminomethylferrocene / (ferrocenyl-methyl)dimethylammonium chloride in the range 0-3 CEC were prepared, and the absorption at 435 nm, characteristic of N,N-dimethylaminomethylferrocene measured.

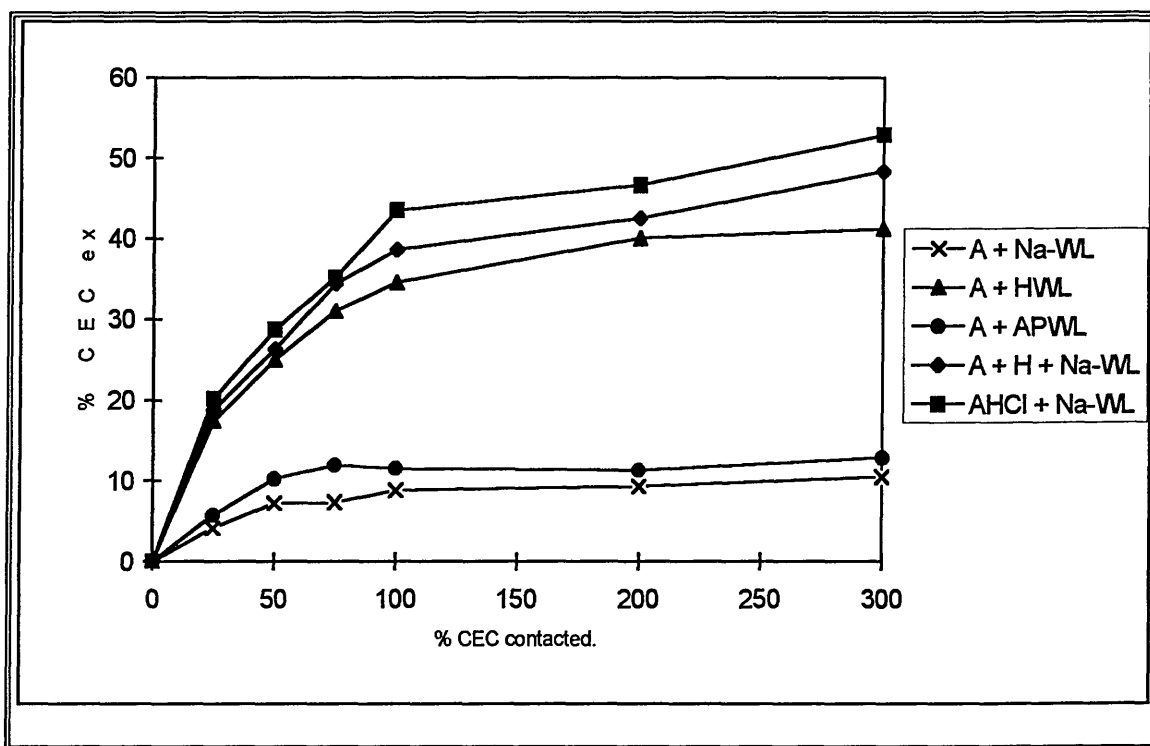
0.1 g of clay dried at 120°C was then added and the suspensions shaken overnight. These were then centrifuged, and the absorption of the supernatant measured.

2.2 Results and Discussion.

2.2.1 Adsorption Isotherms

The results for the adsorption of *N,N*-dimethylaminoferrocene (A) and (ferrocenylmethyl)dimethylammonium chloride (AH^+Cl^-) onto Westone-L are shown in Figure 2.1 and Table 2.1.

Figure 2.1 Adsorption Isotherms for different contact methods.



Contact of *N,N*-dimethylaminomethylferrocene with Na-WL (A + Na-WL) proved of little success, giving an uptake equal to only 10% exchange of the CEC. This lack of success was attributed to a combination of two distinct factors. Firstly, incomplete separation of the layers due to the solvent, methanol; and secondly there was little to favour incorporation of a neutral species between the layers. In the first instance there was little choice as the neutral compound was only sparingly soluble in water. Synthesis

of the hydrochloride salt followed by contact with the clay (AHCl + Na-WL) in methanol proved successful yielding 53% exchange. It was however expensive in material, with 20% being lost during the conversion of A to AHCl. Thus an attempt to produce the acid salt in situ, by addition of acid to the methanolic solutions, followed by contact with the clay (A + H + Na-WL) was undertaken. This would be very important for future work as the biferrocenes are difficult to produce in large amounts. This approach proved successful giving 48% exchange. In the final experiment of the series, the N,N-dimethylaminomethylferrocene was contacted with an acid clay (A + H-WL). Exchange was successful although the loading was still only about 45% of the theoretical value. Based upon these results, the upper limit for exchange in methanol is about 50 % (see Table 2.1).

Table 2.1 Upper limits of exchange achieved by contacting in methanol.

Method of contact.	Maximum exchange observed in suspension (%)
<i>A + Na-WL</i>	10
<i>AH⁺Cl + Na-WL</i>	53
<i>A + H⁺ + Na-WL</i>	48
<i>A + H-WL</i>	45

This is in stark contrast to the incorporation of ferrocene in dehydrated zeolites where 90 % exchange is achieved in under three minutes⁸⁸.

2.2.2 X-Ray Fluorescence

XRF provided details of the extent of the exchange in centrifuged and dried samples. In calculating the % exchange shown in Table 2.2, two assumptions were made. Firstly, that no iron was lost by volatilisation during either the drying process, or during the fusing of the bead. Secondly, it was assumed that the iron content of the clay was already 0.35 %, although figures have been known as high as 0.5 %. The figures for the amount of iron exchanged are based on a univalent iron species. The theoretical value for the Na content of the clay, if completely exchanged is 2.09 %, assuming the CEC to be equal to 91meq/100g. The value of 1.85% is at first a mystery. However, it was found that after passage through an ion exchange column, the water is *ca.* pH 5. It is possible therefore, that protons may well have displaced some of the sodium during the washing of the clay. The theoretical value for 100% exchange, based on an Fe⁺ species is 5.1% although together with the 0.5% initially present this gives a final value of 5.6%. It is immediately apparent that the Na and Fe values do not agree. There are three possible explanations for this. One, some of the organoiron species has oxidised during the exchange process and so is now doubly charged. This would displace two sodium ions instead of one per inserted molecule.

Table 2.2 Summary of XRF results for each exchange method.

Compound	% Fe	% Na	% exchange	% Na displaced
<i>Na-WL</i>	0.36	1.85	-	-
<i>H-WL</i>	0.43	0.09	-	94
<i>APWL</i>	0.41	0.03	-	100
<i>AH-WL</i>	3.42	0.47	50	76
<i>A-H-WL*</i>	4.09	0.12	73	94
<i>A-HWL</i>	3.37	0.08	59	92
<i>A-WL*</i>	3.26	0.67	57	68

A = N,N-dimethylaminomethylferrocene, AH = (ferrocenylmethyl)dimethylammonium.

* Contacted three times with the clay.

Two, where water is the exchange solvent, it is possible that protons may have displaced some of the sodium (see Table 2.2). Three, the assumption that no iron was volatilised during the fusing of the bead was incorrect. The anomalously high value for the direct contact of A with the sodium clay (A-WL) is the result of three separate contacts in water. It is proposed that there were sufficient protons present during this process, to protonate enough A to promote exchange. Interestingly, the AH-Cl contact with Na-WL only gave 50% of the total CEC exchanged, based on Fe (see Table 2.2). However, the C, H, N analysis (see section 2.3.1) gave a figure of 80% of the CEC exchanged, which is in good agreement with the % exchange based on the sodium displaced (76%). This would seem to indicate that some of the iron has in fact been volatilised during the manufacture of the bead. However, thermal desorption mass spectrometry would be needed to confirm this. It should be noted that both the XRF and CHN figures seem to give higher exchange than had been predicted from the isotherm data. However, the solvent used for the preparation of most of the above samples was water - not methanol, as in the isotherm experiments, and so no direct comparison between the two techniques would be valid. In addition, in some instances more than one contact was utilised in the sample preparation.

2.2.3 Infra-Red Spectroscopy

Infra-red spectroscopy provided little information in the characterisation of these compounds. (Ferrocenylmethyl)dimethylammonium chloride (AHCl) had absorption bands at 2940 and 2641 assigned to aliphatic C-H stretches, and another band characteristic of hydrogen strongly hydrogen bonded to nitrogen, at 2463 cm^{-1} . It also showed further absorptions between 1400-1500 cm^{-1} attributed to the cyclopentadienyl rings. After introduction into the clay, most of these bands were overlaid by absorptions from either adsorbed interlayer water, or absorptions from the aluminosilicate lattice. However, weak absorptions were just visible at 3136 and 2694 cm^{-1} corresponding to the C-H stretches, and further bands at 1472 and 1410 cm^{-1} corresponding to stretches within the cyclopentadienyl rings. The problem of the water swamping other possible absorptions present was removed by heating the disc in situ. Unfortunately this did not provide any further information.

2.2.4 Thermogravimetric Analysis

The derivative thermogram of Na-WL (Figure 2.2) shows that the desorption of physisorbed water was essentially complete by 100°C, with dehydroxylation of the structure reaching a maximum at 660°C¹⁸⁴. A further small weight loss was occasionally visible at 480°C in some of the samples tested. This was attributed to a kaolinite impurity.

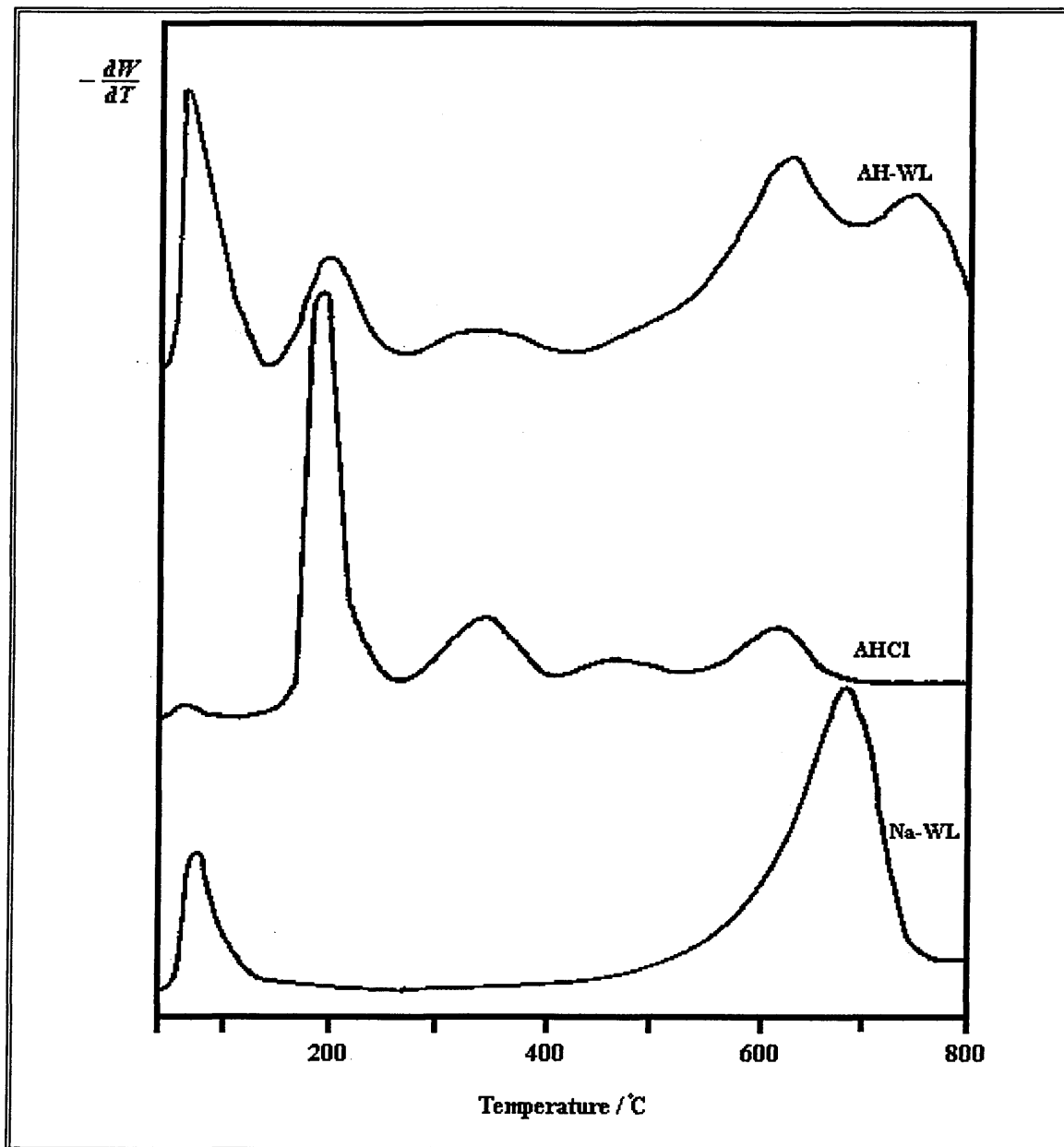
The liquid N,N-dimethylaminomethylferrocene (A) boils at 200°C and so little information about its decomposition was gained. The corresponding ammonium salt (AHCl) decomposed at ca. 200°C with an associated weight loss of 27%. This was followed by further weight losses of 15%, 9.4% and 14.5% at 350°C, 460°C and 610°C, respectively (Figure 2.2). Although little information can be gleaned from this without the use of mass spectrometry, it provides a useful fingerprint for the protonated moiety. The fingerprint of the (ferrocenylmethyl)dimethylammonium cation was sharply defined in the traces obtained of (ferrocenylmethyl)dimethylammonium-WL.

In the trace of (ferrocenylmethyl)dimethylammonium-WL (Figure 2.2), the characteristic sharp weight loss at 200°C was clearly visible. In addition there was clear evidence of those occurring at 350°C and 610°C being present. There was however a new peak around 740°C, which has approximately twice the weight loss of the 200°C peak. This could possibly be caused by carbon from the decomposed organic fragments being lost as

¹⁸⁴ C. Breen, J. J. Flynn, and G. M. B. Parkes, *Clay Min.*, **1993**, *28*, 123-137.

CO₂, although it is difficult to confirm the origin of this weight loss without the use of mass spectrometry. However, this does indicate that the decomposition pathway in the clay may well occur by a different mechanism.

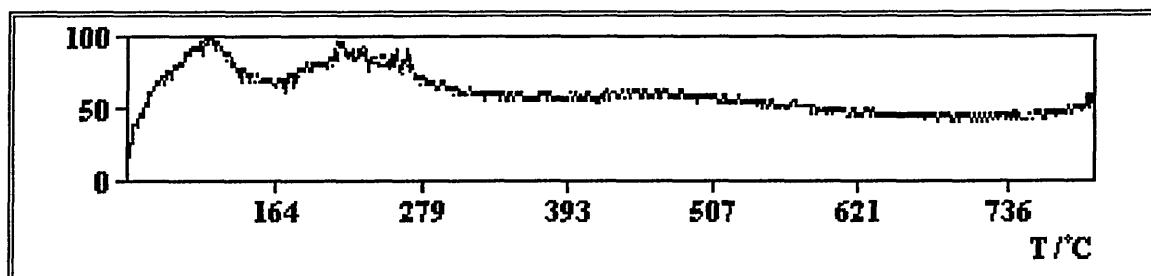
Figure 2.2 Derivative thermogram traces for the samples indicated.



2.2.5 Thermal Desorption Mass Spectroscopy.

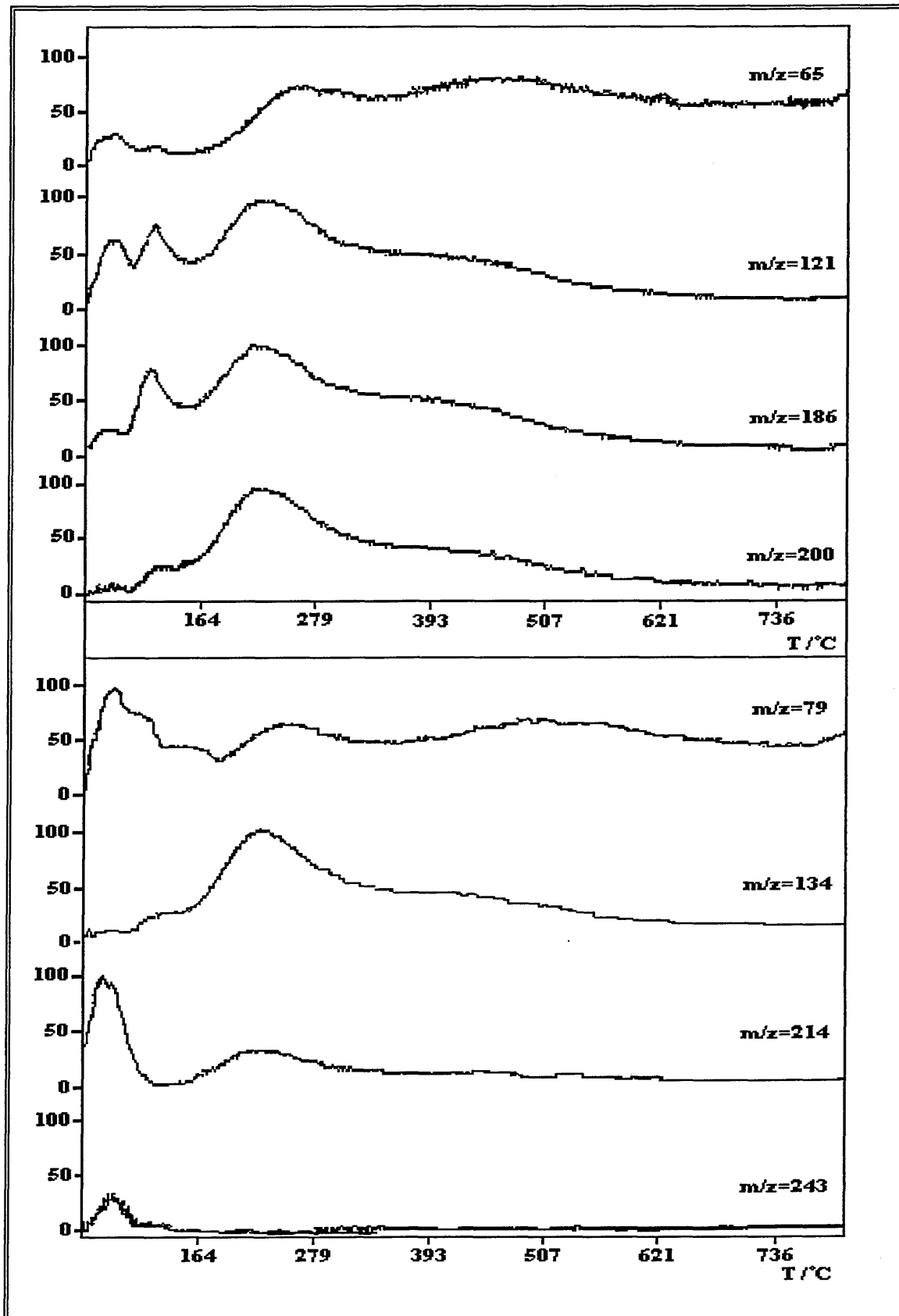
The total ion current (TIC) for the AH-WL samples (Figure 2.3) showed two broad features at approximately 110 and 215°C, although the TIC remained high throughout.

Figure 2.3 TIC for AH-WL.



Closer examination of the single ion chromatograms in Figure 2.4 revealed that the 110°C peak had a shoulder at approximately 70°C. The shoulder was of very low intensity, exhibiting fragments of $m/z = 65, 79, 121,$ and 186 . A very small amount of $m/z = 214$ was also detected. ($m/z 243 = \text{CpFeCpCH}_2\text{NMe}_2$ (Cp = cyclopentadienyl, Me = methyl), $214 = \text{CpFeCpCH}_2\text{NH}$, $200 = \text{CpFeCpCH}_3$, $186 = \text{CpFeCp}$, $134 = \text{FeCpCH}_2$, $121 = \text{FeCp}$, $79 = \text{CpCH}_3$, Cp = 65). These fragments are consistent with loss of an entire (ferrocenylmethyl)dimethylammonium molecule, possibly from surface exchange sites on the clay. The 110°C peak itself was mainly comprised of fragments with $m/z = 121$ and 186 , although fragments with $m/z = 65$ and 200 are also visible. These are consistent with the loss of ferrocene, possibly from the edge sites of the clay. These edge sites exhibit a high Lewis acidity (see section 1.2.3), which is conducive to formation of a ferrocene and dimethylammonium radical (see section 1.2.6). A simple electron transfer followed by a proton abstraction from the abundant water nearby, would then lead to a ferrocene ion and a dimethylammonium cation.

Figure 2.4 Thermal Desorption Mass Spectra for AH-WL



The loss of iron containing fragments in both the 70 and 110°C peaks, confirmed earlier suspicions (see section 2.2.2) that iron had been volatilised during the manufacture of the bead for XRF. This is in direct contradiction to the behaviour observed both by Breen *et al.*¹⁸² with the half-sandwich tricarbonyl-iron compounds supported on montmorillonite, and also by Borvornwattanont *et al.*³³ with the ferrocenium-zeolite-Y composite. It is interesting to note that no fragments corresponding to the ammonium side chain are apparent. This would seem to indicate a strong interaction between the ammonium group and the clay.

The major loss occurred at 215°C. Fragments of m/z 65, 79, 121, 134, 186, 200, and 214 were recorded. This agrees closely with the decomposition temperature observed in the derivative thermograms of AHCl and AH-WL (see section 2.2.4). Further heating resulted in a sharp decrease in the ion current due to fragments of $m/z = 121, 134, 186,$ and 200, although the ion current due to fragments $m/z = 65$ and 79 decreased slightly before increasing to a higher level than before. The current due to fragment $m/z = 214$ is no longer visible. It would appear that at least two decomposition routes are in operation. The first, peaking at around 215°C is due to the straightforward decomposition of the AH ion, resulting in a loss of some iron⁺ and ammonium⁺ containing fragments. However, a further decomposition process peaking at approximately 480°C, in which the cyclopentadienyl rings are lost, and the iron⁺ and ammonium⁺ containing fragments remain on the clay, dominates at higher temperatures. This second process is similar to that observed by Borvornwattanont *et al.*³³. (Note that the kaolinite impurity mentioned in section 2.2.4 was in too small a quantity to be responsible for the 480°C “peak”).

2.2.6 Variable Temperature X-Ray Diffraction

VTXRD gives the first real indication that the exchanged molecule was present within the interlayer. Na-WL has a typical d_{001} -spacing of *ca.* 1.25nm at room temperature and average humidity, which collapses around 55°C to *ca.* 0.96nm (see section 1.2.2 and Figure 2.5). The decrease in d_{001} -spacing in the Na-WL, was caused by the loss of the loosely bound water from the interlayer, together with water from the sodium ions hydration spheres. When a large molecule such as (ferrocenylmethyl)dimethyl-ammonium is inserted, the interlayer spacing increases. However, as noted for other swelling lattices such as the vanadylphosphate series mentioned earlier¹⁸⁵, (see section 1.1.2.3.2), the increase in spacing here is typically 0.1-0.2 nm less than that expected from the insertion of the organoiron species. In addition, these organometallic molecules are not hydrated to the same extent as the Na⁺ ion, and so the spacing remains relatively constant until the molecule itself decomposes. The (ferrocenylmethyl)dimethyl-ammonium cation is estimated to have a perpendicular height of *ca.* 0.7 nm, with a width of *ca.* 0.6 nm for the unsubstituted ring, and a length *ca.* 0.8 nm for the ring together with side chain^{185,186}. Considering the uncertainty in the increase of the d_{001} -spacing of swelling lattices, this makes conclusions regarding the orientation of the molecule somewhat difficult. However, the observed d_{001} -spacing for AH-WL of 1.55 nm, indicates that the molecule may well lie with the cyclopentadienyl rings perpendicular to the silicate layers with the side chain accommodated in the interlamellar space, thus making no contribution to the layer expansion. Taking the (ferrocenylmethyl)dimethylammonium cation as roughly

¹⁸⁵ G. Matsubatahi, S. Ohta, and S. Okanu, *Inorganica Chimica Acta*, **1991**, *184*, 47-52.

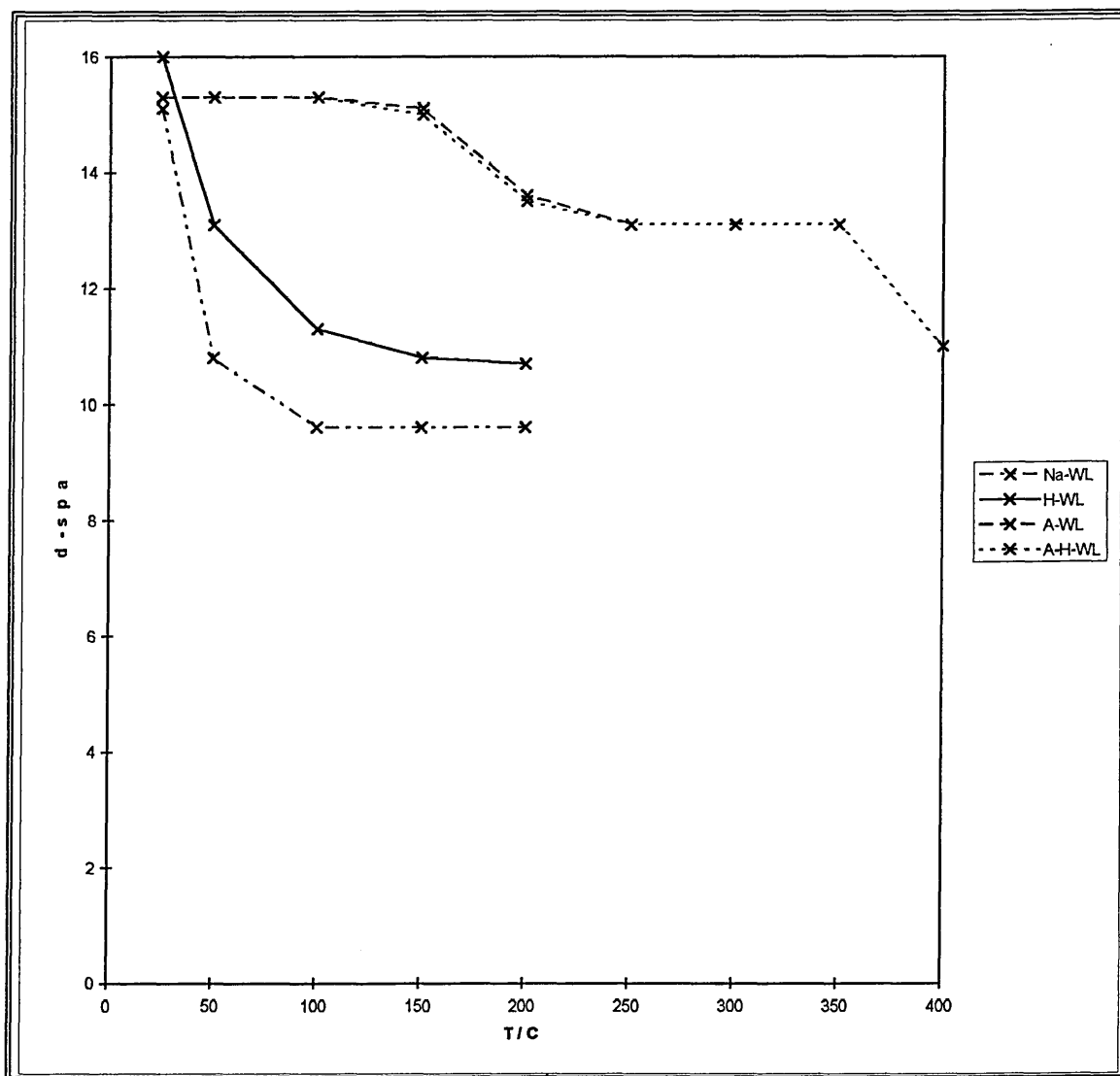
¹⁸⁶ K. Chatakondy, C. Formstone, M. Green, D. O'Hare, J. Twyman, and P. Wireman, *J. Mater. Chem.*, **1991**, *1(2)*, 205-212.

spherical with a diameter of *ca.* 0.7nm¹⁸⁷, the predicted increase in the d_{001} -spacing agrees well with that observed (Figure 2.5). It is interesting to note that in contrast to the present study, when A was incorporated into α -SnP from aqueous solution, a bilayer of the protonated amine formed in the interlayer space¹⁸⁸. Similarly, a bilayer was also formed on the intercalation of $\text{FcCH}_2\text{CH}_2^{15}\text{NH}_2$ into both α -ZrP and MoO_3 . Large increases in d_{001} -spacing, *i.e.* layer expansion, were also observed when ferrocenylalkylammonium iodides were incorporated between the layers of VOPO_4 . In the latter case the length of the alkyl bridging unit influenced both the layer spacing and the extent to which the ferrocene moiety was oxidised⁶².

(Ferrocenylmethyl)dimethylammonium-WL has a spacing of 1.55 nm which remains essentially constant until 200°C, whereupon it collapses to 1.3nm. The decrease in d_{001} -spacing seen in Figure 2.5, coincides with the first major weight loss seen during the TGA experiment (see section 2.2.4), and also with the major decomposition peak in the TD-MS at 215°C (see section 2.2.5). Furthermore, if the inserted molecule had not exchanged uniformly, but only onto edge sites for instance, then above 60°C the domains which contain the sodium ions would have collapsed. This would produce a separate higher angle peak on the XRD trace. It is immediately apparent from Figure 2.6 that the (ferrocenylmethyl)dimethylammonium-WL trace shows no sign of any peaks corresponding to such a sodium ion domain, and so although only 80% exchange was achieved, the XRD data suggests that the organometallic molecule was uniformly dispersed throughout the layers.

¹⁸⁷ S. Okanu and G. Matsubayashi, *J. Chem. Soc. Dalton Trans.*, 1992, 2441-2445.

Figure 2.5 XRD d-spacing vs. T

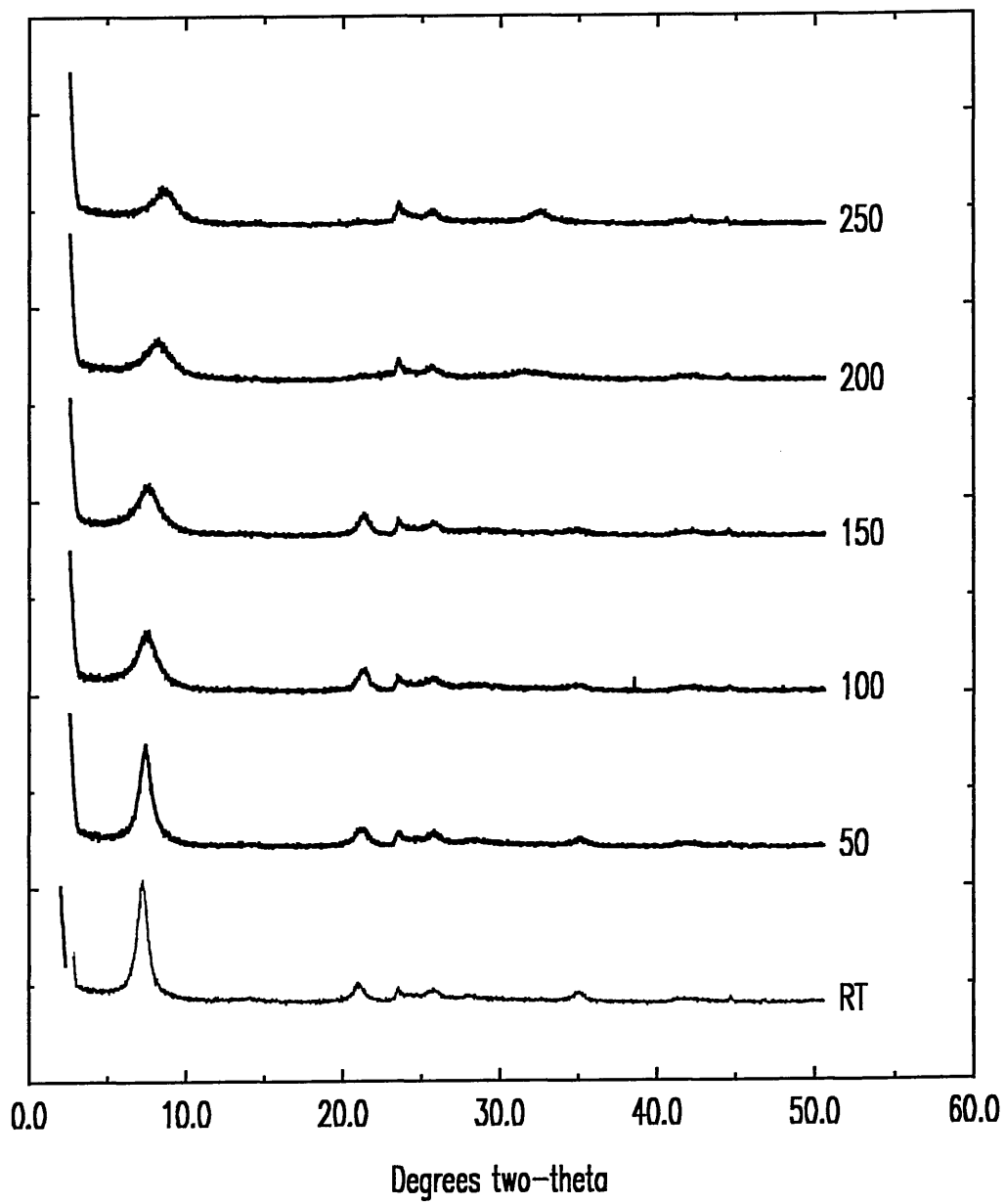


It should be noted here that uncertainty in the measurement of the d-spacing may be quite high ($\pm 0.05\text{nm}$). This is due to the very low angle of the incident beam. A very small difference in the thickness of the film on the glass slide could have quite a dramatic effect on the d-spacing. This will not however affect comparisons within each set of temperature data.

¹⁸⁸ E. Rodriguez-Castellon, A. Jiminez-Lopez, M. Martinez-Lara and L. Moreno-Real, *J. Inclusion Phenom.*, 1987, 6, 335-342.

Figure 2.6 A-WL VT-XRD

VTXRD of AH-WL



Although between 150-200 °C the d-spacing for (ferrocenylmethyl)dimethyl-ammonium-WL (see Figure 2.5 and Figure 2.6) collapses from 1.6 nm to 1.3 nm, it does not reach the 0.96 nm spacing characteristic of a completely collapsed clay. This indicates that something was left between the layers, most likely an iron oxide of some kind. This reinforces the observation, that only a minor amount of iron was lost by volatilisation (see section 2.2.5), during the manufacture of the bead for x-ray fluorescence spectrometry.

2.2.7 Variable Temperature Mössbauer Spectroscopy

N,N-dimethylaminomethylferrocene (A) is a liquid. Although it is possible to obtain a spectrum by freezing the sample, it is not clear how well this would relate to the intercalated state, especially at temperatures above the melting point of A. Therefore, in order to understand the behaviour of the species before intercalation, an alternative had to be found. Utilising the amine group functionality, the hydrochloride salt, which is a solid, was prepared and a variable temperature Mössbauer study performed. The spectrum consisted of a single, symmetric doublet with a quadrupole splitting (Δ) of 2.34 ± 0.02 mm/s, which remained constant between 15-300 K. The isomer shift (δ) exhibited a typical second order Doppler shift effect, with a shift from ^{57}Co in a rhodium matrix, of 0.41 ± 0.02 mm/s at 15 K, which fell steadily to a final value of 0.34 mm/s at 300 K (see Table 2.3).

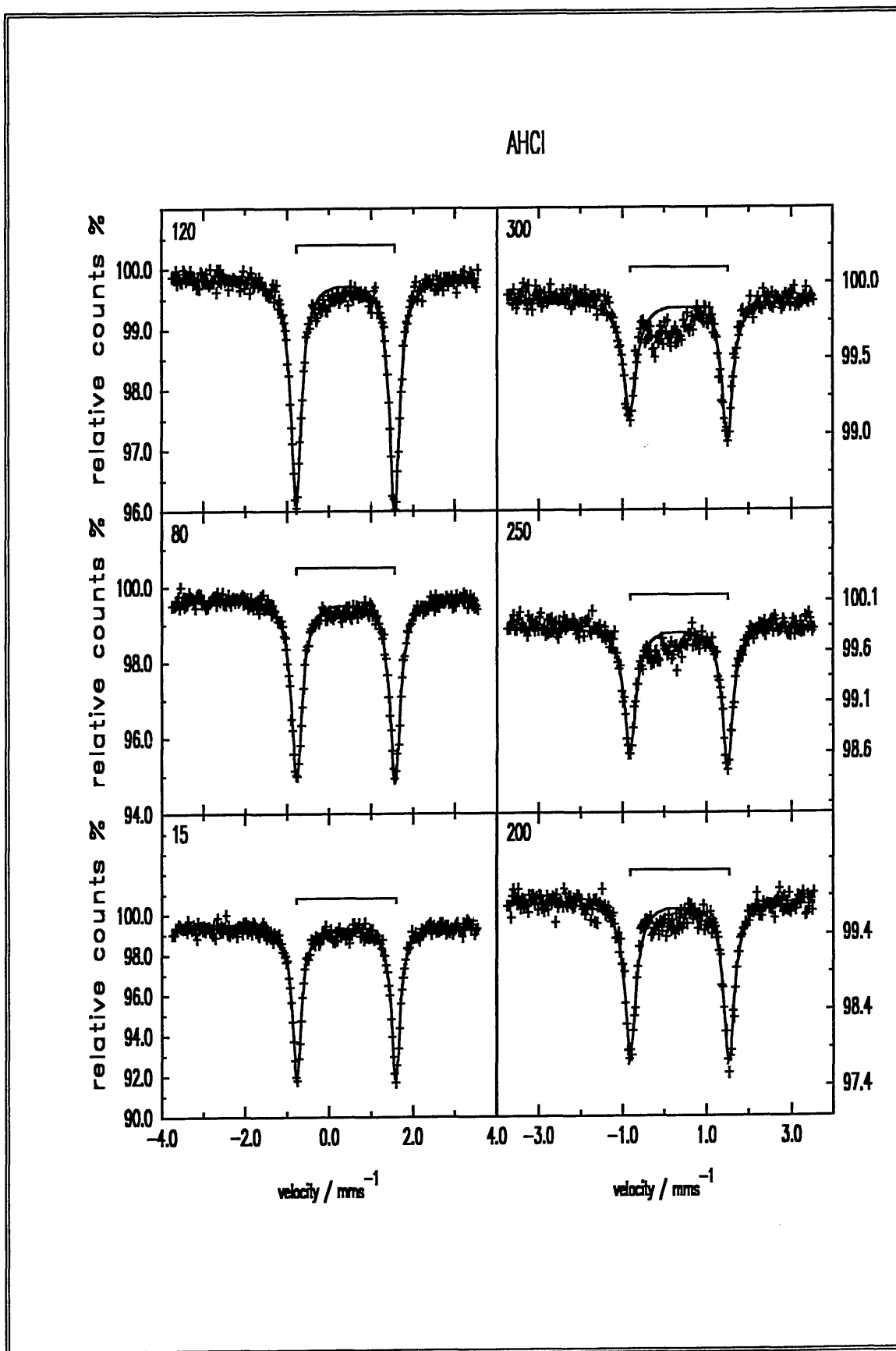
Table 2.3 Least squares fitting parameters for AHCl.

T K	δ mm/s	Δ mm/s	$\Gamma(l)$ mm/s	$\Gamma(r)$ mm/s	Norm. Area	χ^2
15	0.41	2.36	0.26	0.26	2.041	0.504
33	0.41	2.36	0.26	0.26	1.888	0.772
50	0.41	2.36	0.28	0.28	1.817	1.074
80	0.40	2.34	0.32	0.30	1.564	0.663
100	0.40	2.34	0.28	0.28	1.350	1.065
120	0.39	2.34	0.32	0.30	1.214	0.872
140	0.39	2.34	0.30	0.28	1.045	0.810
160	0.39	2.34	0.34	0.32	0.934	0.934
200	0.36	2.34	0.34	0.32	0.698	0.698
250	0.34	2.32	0.36	0.32	0.455	0.975
300	0.34	2.32	0.36	0.32	0.300	1.060

Errors: $T = \pm 2$ K, $\delta = \pm 0.02$ mm/s, $\Delta = 0.02$ mm/s, $\Gamma = 0.02$ mm/s.

The total counts for each phase, *i.e.* the area under each phase in the spectrum, are divided by the background count (obtained by averaging the first and last five data points of the spectrum), to give the normalised area for that phase.

Figure 2.7 Variable Temperature Mössbauer Spectra of AHCl



Subsequent analysis of the normalised area/temperature data (Figure 2.9) gave a Debye temperature (θ_D) of 144 ± 5 K and a recoil free fraction (f_{291}) of 0.14 ± 0.02 using an effective recoiling mass of 57 amu. This rather low θ_D is typical of organometallic compounds. In the present case this was heightened by the increased vibrational freedom, allowed by the large difference in size between the large organoiron cation and small chloride anion. The width of the peaks at half height (Γ) varied from 0.26 mm/s at 15 K to 0.32 mm/s at 300 K. This broadening is caused by increased vibration within the lattice as the solid is warmed. The slight asymmetry in the spectrum at higher temperatures is most likely due to the Karyagin effect (see section 1.5.3.5.2).

The results (see Table 2.4, Table 2.5, Table 2.6, and Table 2.7) for the species intercalated into Westone-L, show that the method of insertion did not affect either the isomer shift or the quadrupole splitting of the intercalated molecule.

Table 2.4 Least squares fitting parameters for AH-WL

T K	Phase	δ mm/s	Δ mm/s	$\Gamma(l)$ mm/s	$\Gamma(r)$ mm/s	Norm. Area	% Area	χ^2
15	Fe ²⁺	0.43	2.42	0.28	0.30	0.933	81	0.604
80	Fe ²⁺	0.42	2.42	0.28	0.30	0.687	75	0.582
160	Fe ²⁺	0.39	2.41	0.24	0.26	0.387	61	0.572
240	Fe ²⁺	0.36	2.41	0.24	0.28	0.233	49	0.540
300	Fe ²⁺	0.32	2.40	0.26	0.28	0.134	40	0.607
15	Fe ³⁺	0.33	0.82	0.48	0.48	0.054	5	0.604
80	Fe ³⁺	0.33	0.82	0.48	0.48	0.066	7	0.582
160	Fe ³⁺	0.29	0.84	0.48	0.48	0.071	11	0.572
240	Fe ³⁺	0.29	0.90	0.46	0.46	0.031	7	0.540
300	Fe ³⁺	0.30	0.99	0.40	0.40	0.021	6	0.607
15	Fe ⁰	0.24		0.96		0.175	15	0.604
80	Fe ⁰	0.24		0.96		0.169	18	0.582
160	Fe ⁰	0.24		0.98		0.174	28	0.572
240	Fe ⁰	0.24		1.00		0.202	44	0.540
300	Fe ⁰	0.23		0.96		0.178	54	0.607

Errors: T = ± 2 K, $\delta = \pm 0.02$ mm/s, $\Delta = 0.02$ mm/s, $\Gamma = 0.02$ mm/s.

Fe²⁺ = Iron(II) present in the ferrocene unit of the inserted molecule.

Fe³⁺ = Iron(III) present in the clay from isomorphous substitution.

Fe⁰ = Iron(0) present in the graphite sample holder.

Figure 2.8 Mössbauer Spectra of A-H-WL.

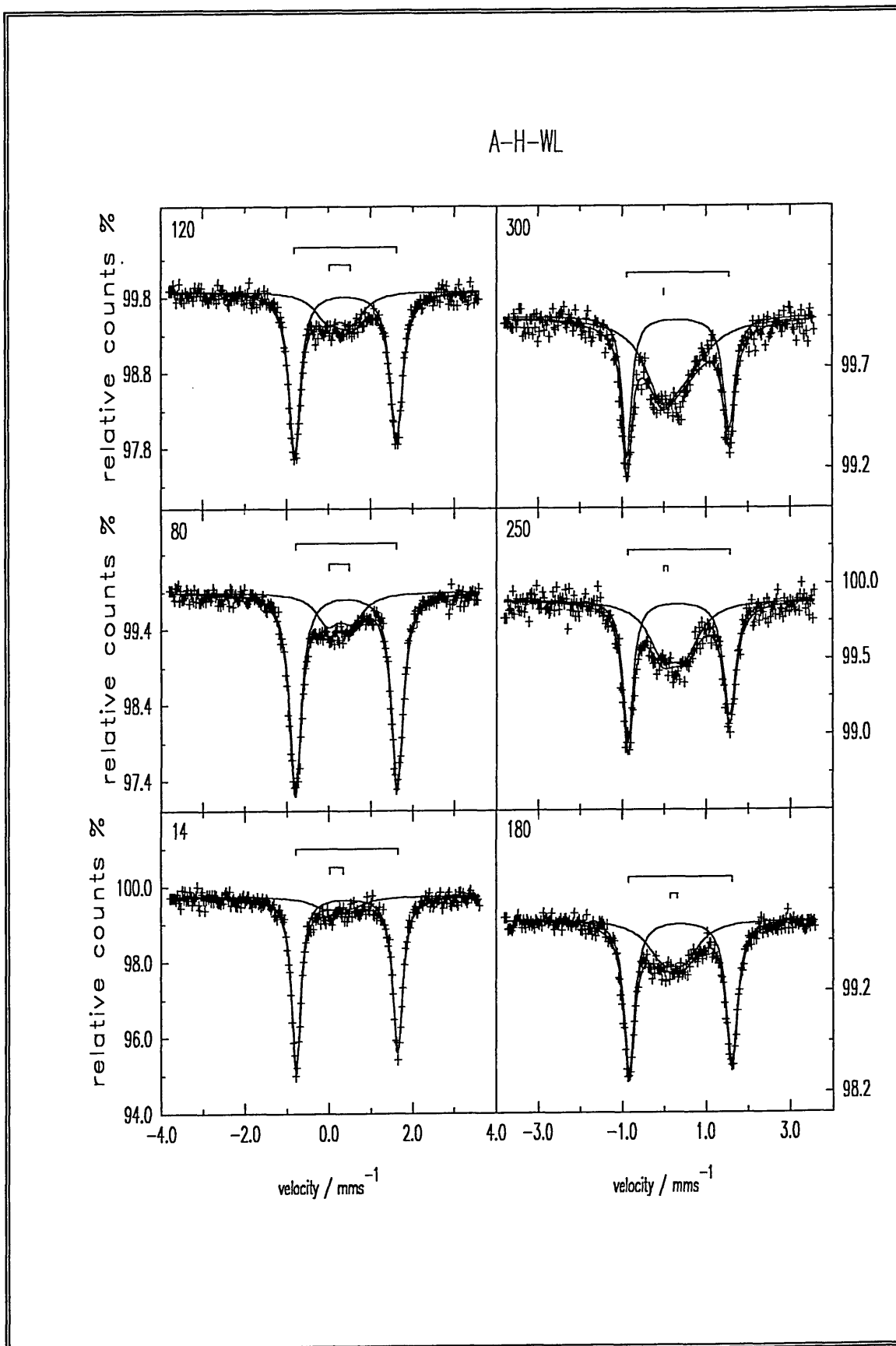


Figure 2.9 Log Area vs. Temperature Graphs.

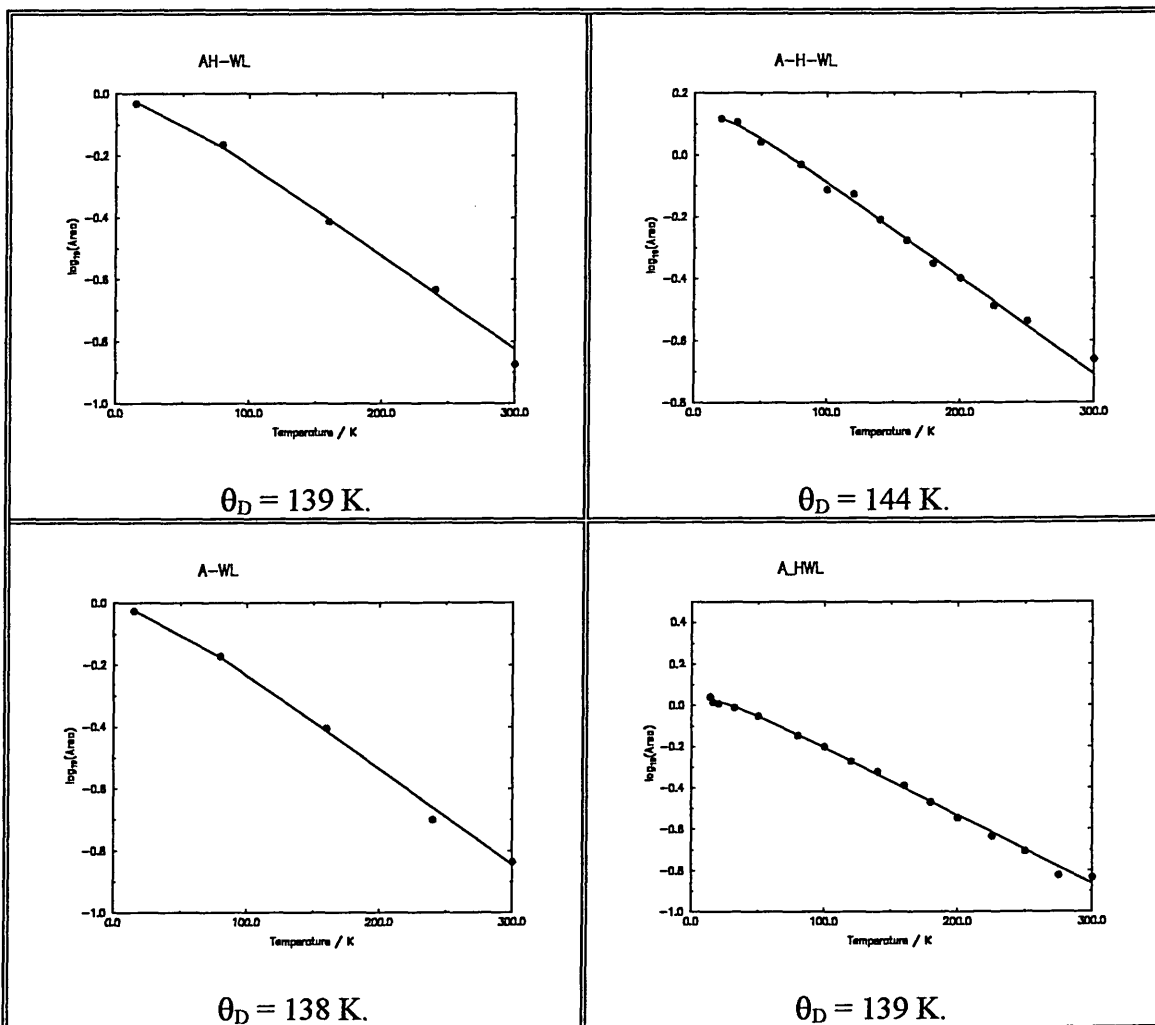


Table 2.5 showing least squares fitting parameters for A-HWL

T K	Phase	δ mm/s	Δ mm/s	$\Gamma(l)$ mm/s	$\Gamma(r)$ mm/s	Norm. Area	% Area	χ^2
14	Fe ²⁺	0.43	2.44	0.28	0.30	1.103	82	0.540
16	Fe ²⁺	0.43	2.44	0.28	0.30	1.041	80	0.622
20	Fe ²⁺	0.43	2.42	0.28	0.32	1.022	79	0.697
32	Fe ²⁺	0.42	2.44	0.26	0.30	0.980	78	0.923
50	Fe ²⁺	0.42	2.44	0.28	0.30	0.890	75	0.557
80	Fe ²⁺	0.42	2.44	0.28	0.32	0.716	73	0.543
100	Fe ²⁺	0.41	2.42	0.28	0.32	0.632	71	0.618
120	Fe ²⁺	0.41	2.42	0.28	0.30	0.537	66	0.543
140	Fe ²⁺	0.40	2.44	0.28	0.32	0.478	63	0.555
160	Fe ²⁺	0.39	2.42	0.26	0.30	0.410	59	0.708
180	Fe ²⁺	0.38	2.44	0.26	0.30	0.341	56	0.531
200	Fe ²⁺	0.37	2.44	0.26	0.30	0.286	52	0.582
225	Fe ²⁺	0.36	2.44	0.26	0.32	0.233	47	0.566
250	Fe ²⁺	0.35	2.44	0.32	0.34	0.197	42	0.605
275	Fe ²⁺	0.33	2.44	0.28	0.34	0.151	36	0.584
300	Fe ²⁺	0.34	2.46	0.26	0.32	0.147	37	0.661
14	Fe ³⁺	0.22	0.54	0.90	0.96	0.236	18	0.540
16	Fe ³⁺	0.24	0.58	0.98	0.96	0.261	20	0.622
20	Fe ³⁺	0.24	0.58	0.96	1.10	0.263	21	0.697
32	Fe ³⁺	0.23	0.54	0.96	1.14	0.270	22	0.923
50	Fe ³⁺	0.23	0.54	0.96	1.22	0.289	25	0.557
80	Fe ³⁺	0.23	0.54	0.96	1.22	0.267	27	0.543
100	Fe ³⁺	0.23	0.54	0.94	1.22	0.263	29	0.618
120	Fe ³⁺	0.23	0.54	0.94	1.22	0.270	34	0.543
140	Fe ³⁺	0.23	0.56	0.94	1.40	0.281	37	0.555
160	Fe ³⁺	0.23	0.56	0.94	1.38	0.287	41	0.708
180	Fe ³⁺	0.23	0.56	0.94	1.38	0.272	44	0.531
200	Fe ³⁺	0.23	0.56	0.94	1.38	0.269	48	0.582
225	Fe ³⁺	0.23	0.56	0.94	1.38	0.265	53	0.566
250	Fe ³⁺	0.23	0.58	0.94	1.42	0.272	58	0.605
275	Fe ³⁺	0.22	0.56	0.94	1.48	0.265	64	0.584
300	Fe ³⁺	0.23	0.60	0.96	1.38	0.253	63	0.661

Errors: T = ± 2 K, $\delta = \pm 0.02$ mm/s, $\Delta = 0.02$ mm/s, $\Gamma = 0.02$ mm/s.

Fe²⁺ = Iron(II) present in the ferrocene unit of the inserted molecule.

Fe³⁺ = Iron(III) present in the clay from isomorphous substitution.

All of the intercalated samples showed a large outer doublet attributable to the Fe(II) of the ferrocene unit, and a broader, ill defined absorption of smaller quadrupole value between the arms of this doublet (Figure 2.8). As can be seen from Table 2.4, Table 2.5, Table 2.6, and Table 2.7, the hyperfine parameters do not vary significantly from those obtained for the acid chloride salt (Table 2.3). This indicates that no substantial changes, such as oxidation, have occurred within the organoiron cation.

Table 2.6 Least squares fitting parameters for A-H-WL

T K	Phase	δ mm/s	Δ mm/s	$\Gamma(l)$ mm/s	$\Gamma(r)$ mm/s	Norm. Area	% Area	χ^2
14	Fe ²⁺	0.43	2.44	0.26	0.30	1.241	84	0.544
14	Fe ²⁺	0.43	2.46	0.28	0.28	1.259	84	0.645
16	Fe ²⁺	0.43	2.46	0.30	0.32	1.295	84	0.464
20	Fe ²⁺	0.43	2.46	0.32	0.34	1.313	85	0.946
32	Fe ²⁺	0.43	2.46	0.34	0.36	1.282	84	0.855
50	Fe ²⁺	0.42	2.44	0.30	0.32	1.104	81	0.653
80	Fe ²⁺	0.42	2.42	0.34	0.34	0.934	79	0.756
100	Fe ²⁺	0.43	2.46	0.28	0.30	0.774	66	0.559
120	Fe ²⁺	0.41	2.40	0.34	0.36	0.749	74	0.664
140	Fe ²⁺	0.41	2.46	0.30	0.32	0.619	68	0.607
160	Fe ²⁺	0.39	2.44	0.30	0.34	0.530	74	0.641
180	Fe ²⁺	0.39	2.46	0.32	0.34	0.448	62	0.474
200	Fe ²⁺	0.38	2.44	0.30	0.34	0.401	61	0.716
225	Fe ²⁺	0.37	2.46	0.24	0.28	0.326	53	0.663
250	Fe ²⁺	0.35	2.42	0.30	0.36	0.291	52	0.603
300	Fe ²⁺	0.33	2.44	0.30	0.34	0.219	46	0.728
14	Fe ³⁺	0.23	0.60	0.72	0.88	0.228	16	0.544
14	Fe ³⁺	0.23	0.56	0.92	0.92	0.247	16	0.645
16	Fe ³⁺	0.21	0.60	0.84	0.90	0.251	16	0.464
20	Fe ³⁺	0.23	0.54	0.90	0.90	0.240	15	0.946
32	Fe ³⁺	0.24	0.54	0.90	0.90	0.245	16	0.855
50	Fe ³⁺	0.27	0.60	0.72	0.88	0.266	19	0.653
80	Fe ³⁺	0.26	0.58	0.64	0.70	0.254	21	0.756
100	Fe ³⁺	0.36	0.52	1.06	1.08	0.377	33	0.559
120	Fe ³⁺	0.27	0.58	0.70	0.70	0.261	26	0.664
140	Fe ³⁺	0.21	0.52	0.88	0.82	0.289	32	0.607
160	Fe ³⁺	0.26	0.56	0.74	0.72	0.259	26	0.641
180	Fe ³⁺	0.22	0.48	0.88	0.88	0.296	38	0.474
200	Fe ³⁺	0.26	0.56	0.74	0.78	0.260	39	0.716
225	Fe ³⁺	0.22	0.48	0.94	0.98	0.293	47	0.663
250	Fe ³⁺	0.24	0.54	0.84	0.86	0.266	48	0.603
300	Fe ³⁺	0.19	0.52	0.82	0.86	0.254	54	0.728

Errors: T = ± 2 K, $\delta = \pm 0.02$ mm/s, $\Delta = 0.02$ mm/s, $\Gamma = 0.02$ mm/s.

Fe²⁺ = Iron(II) present in the ferrocene unit of the inserted molecule.

Fe³⁺ = Iron(III) present in the clay from isomorphous substitution.

Furthermore, it may be inferred from the similar quadrupole splittings and isomer shifts, that the interlayer separation of the clay merely expanded to accommodate the (ferrocenylmethyl)dimethylammonium cation, with no detectable distortion in the orientation of the cyclopentadienyl rings or the oxidation state of the iron centre. Calculations on the effect of tilting the rings, has shown that a 9° tilt in the cyclopentadienyl rings, reduces the isomer shift by 0.02mm/s, and the quadrupole

splitting by 0.11mm/s^{189} . Considering the expansion in the d-spacing of the clay was 0.1 nm less than may have been expected (see section 2.2.6), this observation seems remarkable, although it is consistent with similar work by Breen *et al.*¹⁸² on the introduction of half sandwich organoiron compounds into Westone-L.

Table 2.7 Least squares fitting parameters for A-WL

T K	Phase	δ mm/s	Δ mm/s	$\Gamma(l)$ mm/s	$\Gamma(r)$ mm/s	Norm. Area	% Area	χ^2
15	Fe ²⁺	0.42	2.42	0.26	0.27	0.946	83	0.563
80	Fe ²⁺	0.41	2.42	0.26	0.26	0.675	77	0.588
160	Fe ²⁺	0.39	2.40	0.26	0.27	0.395	68	0.508
240	Fe ²⁺	0.38	2.40	0.26	0.31	0.200	55	0.537
300	Fe ²⁺	0.33	2.38	0.32	0.34	0.146	46	0.550
15	Fe ³⁺	0.25	0.80	0.48	0.48	0.127	11	0.563
80	Fe ³⁺	0.28	0.80	0.48	0.48	0.134	15	0.588
160	Fe ³⁺	0.28	0.82	0.48	0.48	0.130	22	0.508
240	Fe ³⁺	0.22	0.86	0.48	0.48	0.114	31	0.537
300	Fe ³⁺	0.16	0.86	0.48	0.48	0.117	37	0.550
15	Fe ⁰	0.25	-	0.40		0.067	6	0.563
80	Fe ⁰	0.25	-	0.40		0.064	7	0.588
160	Fe ⁰	0.25	-	0.40		0.055	10	0.508
240	Fe ⁰	0.19	-	0.40		0.053	14	0.537
300	Fe ⁰	0.16	-	0.40		0.056	17	0.550

Errors: T = ± 2 K, $\delta = \pm 0.02$ mm/s, $\Delta = 0.02$ mm/s, $\Gamma = 0.02$ mm/s.

Fe²⁺ = Iron(II) atom of the ferrocene unit in the inserted molecule.

Fe³⁺ = Iron(III) present in the clay from isomorphous substitution.

Fe⁰ = Iron present in graphite sample holder.

The broad, ill defined absorption, seen between the (ferrocenylmethyl)dimethylammonium doublet, was composed of a smaller broad doublet, corresponding to the Fe(III) present in the clay which arises due to isomorphous substitution, and a broad singlet, characteristic of Fe(0), which apparently is added as particles to the graphite rod from which the sample holders were made. The purpose of this iron is to aid machining of the rod. It is present in very low concentrations, and is not normally visible. Unfortunately, due to the low iron content of the materials under study and a higher than normal concentration of Fe(0) in the holder, the absorption became significant (Figure

¹⁸⁹ J. S. Brookes, C. M. Care, and S. Plimley, *Hyperfine Interactions*, 1984, 20, 151-167.

2.8). It should be noted that the presence of this iron was not intentional. Indeed, until the present work its presence was unknown to the author. The broadness of the Fe(III) doublet indicates that the iron present in the clay was in a variety of sites. Although the iron already present on the clay was of very low concentration (0.35% w/w), it is bound tightly within the lattice, and the recoil free fraction was relatively unaffected by temperature. This means that as the temperature was increased, the absorption made a steadily more significant contribution to the overall spectrum. (Figure 2.8), because the recoil free fraction of the organoiron compound decreased rapidly with temperature.

The intercalation of the (ferrocenylmethyl)dimethylammonium cation into Westone-L, gave a Debye temperature (θ_D) of 140 K (see Table 2.4, Table 2.5, Table 2.6, Table 2.7, Table 4.1, Table 2.8, and Figure 2.9) with a recoil free fraction at 291 K (f_{291}) of 0.13 for the inserted species. This was very similar to the acid chloride salt (AHCl) where $\theta_D = 144 \text{ K} \pm 5 \text{ K}$ and $f_{291} = 0.14 \pm 0.02$. This indicates that the molecule was in a very similar pseudo-cubic environment. Interestingly, this was not what Breen *et al.*¹⁸² observed with the organoiron half sandwich compounds. The half sandwich cations, tricarbonyl(η^5 -2,4-dimethylcyclohexadienyl)iron(1+), and tricarbonyl(η^5 -2-methoxycyclohexadienyl)iron(1+), typically gave a Debye temperature 30 K lower when intercalated into the clay, than when incorporated in a PF_6^- lattice. This was ascribed to the cations being less tightly bound when sandwiched between the layers of the clay, than when locked within the anionic lattice. The similar Debye temperature obtained for the intercalated (ferrocenylmethyl)dimethylammonium cation, might tentatively be due to, a) an interaction between the protonated amine group and the silicate lattice, b) the locking of the ammonium group in one of the surrounding ditrigonal holes, or c) the half sandwich

compounds were more rigidly held in the salt as the anions were of similar size. In this case the ferrocene molecule can thus be viewed as having moved from one fairly free environment to another. The second suggestion (b) agrees well with the suggestion in section 2.2.6, that the molecule is parallel to the layers, with the side chain in the same plane. Another argument for the similar Debye temperature, could be a restriction of movement of the molecule by the freezing of the surrounding interlayer water molecules. This however seems unlikely. Other work by Simopoulos *et al.*¹⁹⁰ on organotin compounds intercalated into montmorillonites, showed an elbow near 210 K in the log Area vs. Temperature data. They observed that the value of the gradient of the line increased considerably at this temperature, although linearity was retained. This was attributed to the melting of the interlayer water. Collisions with the interlayer water increased the mean square displacement of the tin nuclei, which in turn reduced the recoil free fraction. This was verified by the disappearance of this elbow when the samples were dehydrated in vacuum before collecting the VT-¹¹⁹Sn Mössbauer data. The lack of this elbow in our data (see Figure 2.9) may be attributed to two factors. Firstly, the hydrophobic nature of the ferrocene centre, means that the water molecules are only weakly associated with the iron nuclei. Hence, the onset of motion in the water molecules is unlikely to have any significant affect on the iron nuclei. This agrees well with similar Mössbauer studies carried out by Molloy *et al.*⁸⁹, on the intercalation of N-methyl-3-(triphenylstannyl)pyridinium onto montmorillonite. Secondly, when mounted within the cryostat the samples were in a vacuum. The samples were then cooled, and spectra recorded from 12K to room temperature. Hence, the samples may well have been “freeze dried” by the time the experiment commenced. Similar studies on unsubstituted ferrocene incorporated into AlPO₄-5 and AlPO₄-8 have shown that the ferrocene has

¹⁹⁰ A. Simopoulos, D. Petridis, A. Kostikas, and N. Gangas, *Hyperfine Interactions*, **1988**, *41*, 843-848.

almost complete three-dimensional freedom at room temperature¹⁹¹. This averages the electric field gradient across the ferrocene molecule during the life-time of the excited state, and hence a singlet is seen in the Mössbauer spectrum. The ferrocene molecule is essentially spherical, with an effective diameter of 0.7 nm which is somewhat smaller than the 0.78 nm channel width in the AlPO₄ channels allowing the molecule to rotate. In the present case a doublet was observed at all temperatures. This indicates that either no reorientation process is taking place, or that any reorientation process is occurring much slower than the sampling time of the Mössbauer experiment (see section 1.5.3.6.3). As has been mentioned previously (see section 2.2.6) the interlayer spacing is *ca.* 0.1 nm smaller than would be expected on inserting AH⁺ into clay. This leaves little room for the organometallic to rotate. In addition the bulky side chain on AH⁺ is likely to inhibit rotation within the interlayer. The influence of bulky side-chains on the freedom of organoiron compounds has been noted previously¹⁸².

Once again there was evidence of increasing asymmetry in the spectrum at higher temperatures. This again could possibly be attributed to the Karyagin effect. A similar effect has been noticed for bis(fulvalene)diiron¹⁹².

The Debye temperatures and recoil free fractions from the various methods of insertion of the (ferrocenylmethyl)dimethylammonium cation are summarised in Table 2.8.

¹⁹¹ A. Lund, D. G. Nicholson, R. V. Parish and J. P. Wright, *Acta Chem. Scand.*, **1994**, *4*, 1723-1729.

¹⁹² C. LeVanda, K. Bechaard, D. O. Cowan, U. T. Muella-Westerhoff, P. Eilbracht, G. A. Candela, and R. L. Collins, *J. Am. Chem. Soc.*, **1976**, *98(11)*, 3183-3187.

Table 2.8 showing summary of θ_D and f_{291} values for the variable temperature experiments performed.

Compound	θ_D	f_{291}
<i>AH-CI</i>	144	0.143
<i>AH-WL</i>	139	0.128
<i>A-H-WL</i>	144	0.147
<i>A-HWL</i>	139	0.125
<i>A-WL</i>	138	0.123
<i>(A-APWL)</i>	(118)	(0.057)

Errors: $\theta_D = \pm 5$ K, $f_{291} = 0.02$.

2.3 Conclusions.

The hydrochloride salt (ferrocenylmethyl)dimethylammonium chloride has been prepared and characterised by a variety of techniques. VT-Mössbauer data indicated that no reorientation processes were in effect and that the molecule had a Debye temperature of 144 ± 5 K and a recoil free fraction at 291 K of 0.14 ± 0.02 .

In addition, the (ferrocenylmethyl)dimethylammonium cation has been intercalated into the montmorillonite Westone-L by several different methods. By a combination of techniques, it has been shown that the cation occupies 80% of the exchange sites, that it is most likely orientated with the cyclopentadienyl rings perpendicular to the silicate layers, with no discernible distortion of the cyclopentadienyl rings. The cation is very probably in a site similar in environment to that found in the chloride salt. Moreover, it appears that the decomposition of the supported complex, in contrast to the half-sandwich compounds studied by Breen *et al.*¹⁸², involves the volatilisation of iron below 350°C. Above 350°C the decomposition occurs by a different mechanism, with the loss of the cyclopentadienyl rings and the retention of the iron on the clay. Once again VT-Mössbauer data showed that reorientation processes are evident and that the inserted molecule gave a Debye temperature of 140 K. In addition the molecule was not affected by the melting of the interlayer water.

2.4 Future Work.

In this project, the (ferrocenylmethyl)dimethylammonium cation has been intercalated into the montmorillonite Westone-L, with a maximum of 80% of the total CEC exchanged (= AH-WL). Intercalation did not affect any of the Mössbauer fitting parameters.

The use of Raman spectroscopy may provide information which was not available using infra-red spectroscopy. In Raman spectroscopy the bands due to the aluminosilicate lattice of the clay appear as two sharp peaks. This is in stark contrast to the broad feature seen in infra-red spectroscopy, and means that bands from the intercalated molecule may be visible.

The use of EXAFS may provide further information on the position and orientation of the molecule within the clay interlayer.

Information on the factors effecting intercalation may be obtained by varying the length of the carbon side-chain in the amine functionality of the substituted ferrocene. Using the techniques utilised in this study and by comparing the amount incorporated, the means of predicting and maximising the uptake of organometallics onto the clay may be achieved.

The materials studied here may have applications as a clay modified electrode. Since clays are low cost, with high thermal stability and offer resistance to extreme chemical

conditions, the use of impregnated clays in order to modify electrode surfaces has been widespread¹⁹³.

Alternatively, AH-WL could be used in solid state batteries for overcharge protection. The compound A has in fact already been suggested for this very purpose for use in lithium batteries¹⁹⁴.

¹⁹³ M. T. Carter and A. J. Bard, *J. Electroanal. Chem.*, **1987**, *229*, 191-214.

¹⁹⁴ M. N. Golovin, D. P. Wilkinson, J. T. Dudley, D. Holonko, and S. Woo, *J. Electrochem. Soc.*, **1992**, *139(1)*, 5-10.

3. Biferrocene / biferrocenium on clay.

The study of factors affecting electron transfer between metal complexes in solution and within biological processes has been ongoing for many years now¹⁴⁴. Some of the most revealing work in recent years has been carried out by Hendrickson *et al.*, by using various substituted biferrocenium complexes as a model¹⁴⁹. By systematically varying the ring substituent, anion and solvent molecules in the crystal structure, it was discovered that the rate and temperature of the onset of valence electron de-trapping (VEDT) was extremely sensitive to the immediate environment around the biferrocenium cation. So sensitive is this effect, that different isomorphs of the same material were found to exhibit VEDT at different temperatures. As changing the anion or solvent molecule has an impact on the crystal structure, a means of eliminating one or more variables was necessary. An attempt to intercalate a biferrocenium compound between the layers of a clay was thus attempted. The clay acts as a dilute anion with no distinct cluster of charge. In addition the layers of the clay act as an insulator, effectively screening the biferrocenium molecules from each other. Further, the clay is able to reversibly absorb differing amounts of solvent. A direct means of studying the effect of solvent on VEDT within the biferrocenium molecule should now be possible. It was with this thought in mind that the following study was undertaken.

3.1 Experimental

3.1.1 Materials.

N,N-dimethylaminomethylferrocene, butyllithium, anhydrous cobalt(II)chloride, and the **Brockmann Grade II alumina** were supplied by Aldrich Chemicals. **Tetrahydrofuran,** supplied by Aldrich, was distilled over potassium using benzophenone as an indicator. **Benzene, diethyl-ether, methanol and petroleum-ether** (b.p.40-60°C) were supplied by BDH chemicals. The **acid clay** used was the same as prepared earlier (see section 2.1.2.2).

3.1.2 Compound Preparation.

3.1.2.1 2,2'' - and 2,5'' - bis[(dimethylamino)methyl]biferrocene

This was based on the method of Booth *et al.*¹⁹⁵. [(Dimethylamino)methyl]ferrocene (4.86 g, 0.02 mol) was dissolved in dry tetrahydrofuran (100 ml), and n-butyllithium (0.03 mol) in hexane was added. After stirring for 3 hours at room temperature a solid bright orange precipitate is seen. The mixture was then cooled to -80 °C, and anhydrous cobalt(II)chloride was added. The mixture was stirred for 1 hour at -80 °C, and then left stirring overnight to warm to room temperature. The mixture was quenched by the addition of water, and then made basic with an excess of 1 M sodium hydroxide. The

¹⁹⁵ D. J. Booth, G. Marr, and B. Rockett, *J. Organometallic Chem.*, 1971, 227.

black suspension resulting was extracted repeatedly with benzene, and the extracts dried over anhydrous magnesium sulphate. This was then evaporated to low bulk and chromatographed on alumina in benzene / light petroleum ether. Diethylether / light petroleum ether eluted the 2,5''-bis[(dimethylamino)methyl]-biferrocene (AA') (1.5 g, 31% yield). Diethylether eluted the starting material (1.9 g). Finally, methanol / diethylether eluted the 2,2'' - bis[(dimethylamino)methyl]-biferrocene (AA) (1.2 g, 25% yield). C, H, N analysis: theory; C = 64.49, H = 6.66, N = 5.78; found C = 64.39, H = 6.71, N = 5.66.

3.1.2.2 [2,2'' - bis[(dimethylammonium)methyl]biferrocene] Westone-L.

2,2'' - bis[(dimethylamino)methyl]biferrocene (0.2 g, 1 CEC, 0.41 mmol) was dissolved in 50 ml tetrahydrofuran / methanol and 0.5 g of HWL (dried 120 °C) was added. The resulting suspension was left to stir for 3 hours, then centrifuged and the supernatant removed. The residue was then washed with petroleum ether (3 x 50 ml), diethylether (1 x 50 ml), and finally methanol (3 x 50 ml). C, H, N analysis: theory (100% exchange of +2 species) C = 12.1, H = 1.25, N = 1.09; found C = 9.10, H = 1.25, N = 0.81. This is consistent with 75 % exchange of the total CEC. The product (referred to as AA-HWL) was split into two equal parts, one half of which was left to dry in air at room temperature, and the other half which was contacted once again with the supernatant for a further 45 hours. This was isolated, washed as before, and left to dry in air at room temperature. This second product is referred to as AA-HWL(48).

3.1.2.3 [2,2'' - bis[(dimethylammonium)methyl]biferrocenium]-HWL.

Iodine (0.01 g, 0.09 mmol) was dissolved in 30 ml of hexane and [2,2'' - bis[(dimethylammonium)methyl]biferrocene]-HWL (AA-HWL) (0.1 g) added. The resulting suspension was left to stir for 12 hours, then centrifuged, washed (3 x 50 ml hexane, 1 x 50 ml diethylether, 3 x 50 ml methanol), and then left to dry in air at room temperature. The product will be referred to as AA⁺-HWL.

3.2 Results and Discussion.

3.2.1 Infra-Red Spectroscopy.

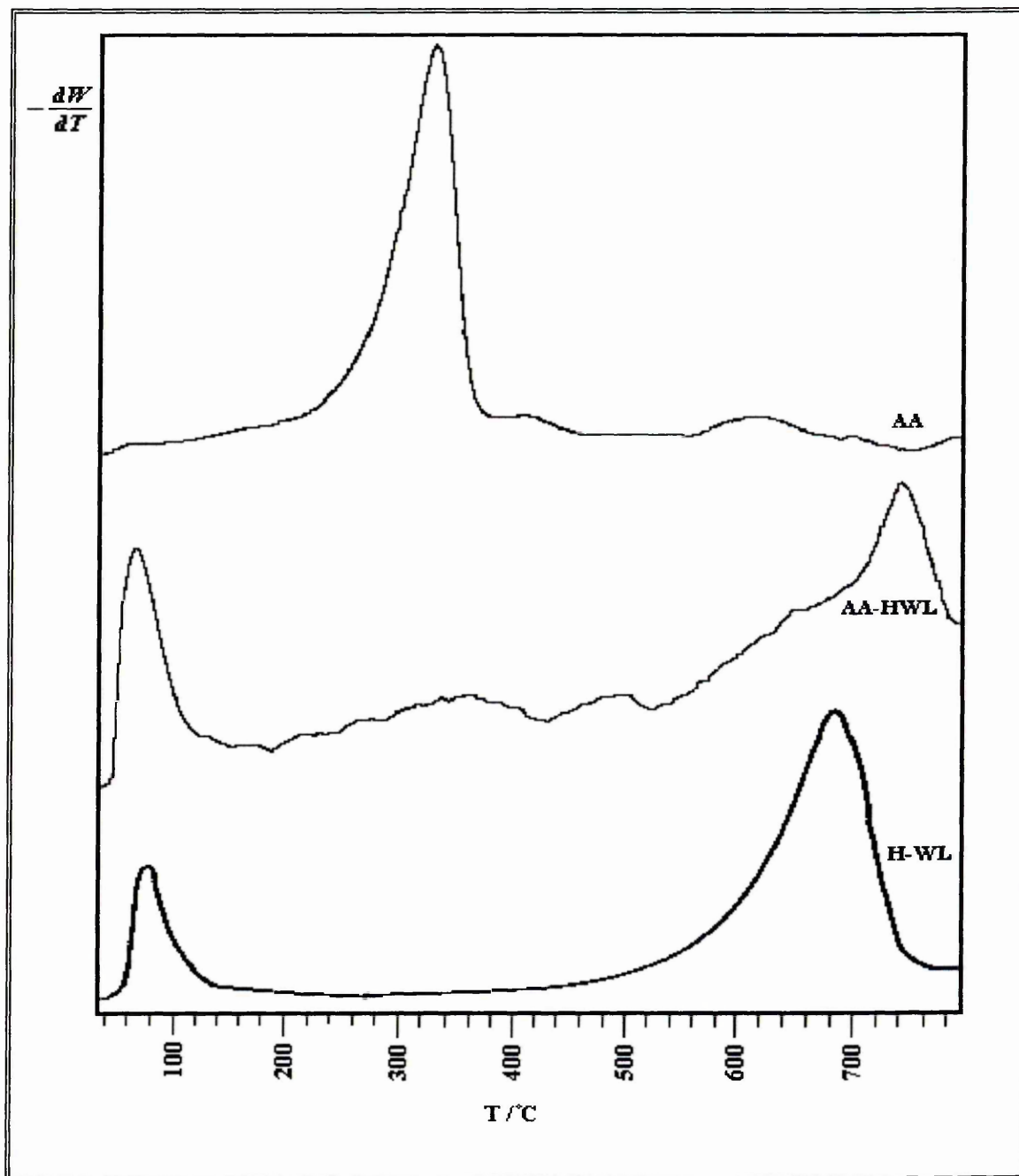
Infra-red spectroscopy proved of little use in identifying the products. Ferrocene has a C-H stretch at 815 cm^{-1} . This shifts to 851 cm^{-1} in ferrocenium triiodide, providing a useful insight into the oxidation state of the molecule. The compound AA exhibited two strong C-H stretches at 801 and 818 cm^{-1} . Typically, with biferrocenium compounds one of the bands shifts to around 845 cm^{-1} . This gives an immediate indication of the oxidation state of the compound, potentially allowing an important insight into the interaction of the molecule upon intercalation into the clay. Unfortunately, in this case these bands are totally obscured by the overlying aluminosilicate bands which swamp the whole spectrum in this region. There should be a symmetric ring-metal-ring Raman active stretch in this spectral region, which could be useful since the aluminosilicate region is very sharp and unobtrusive in the raman spectrum. Unfortunately, the opportunity to test this has not arisen at the present time.

3.2.2 Thermogravimetric Analysis.

The derivative thermogram of AA (see Figure 3.1) exhibited a maximum at 330°C , corresponding to 74 % of the total weight lost. A smaller weight loss, associated with 9 % of the total weight loss, was also observed at 620°C . These weight losses cannot be

equated to the loss of any specific fragments, but does show that the molecule decomposes above 300 °C in a nitrogen atmosphere.

Figure 3.1 Derivative thermograms of AA, HWL, AA-HWL.



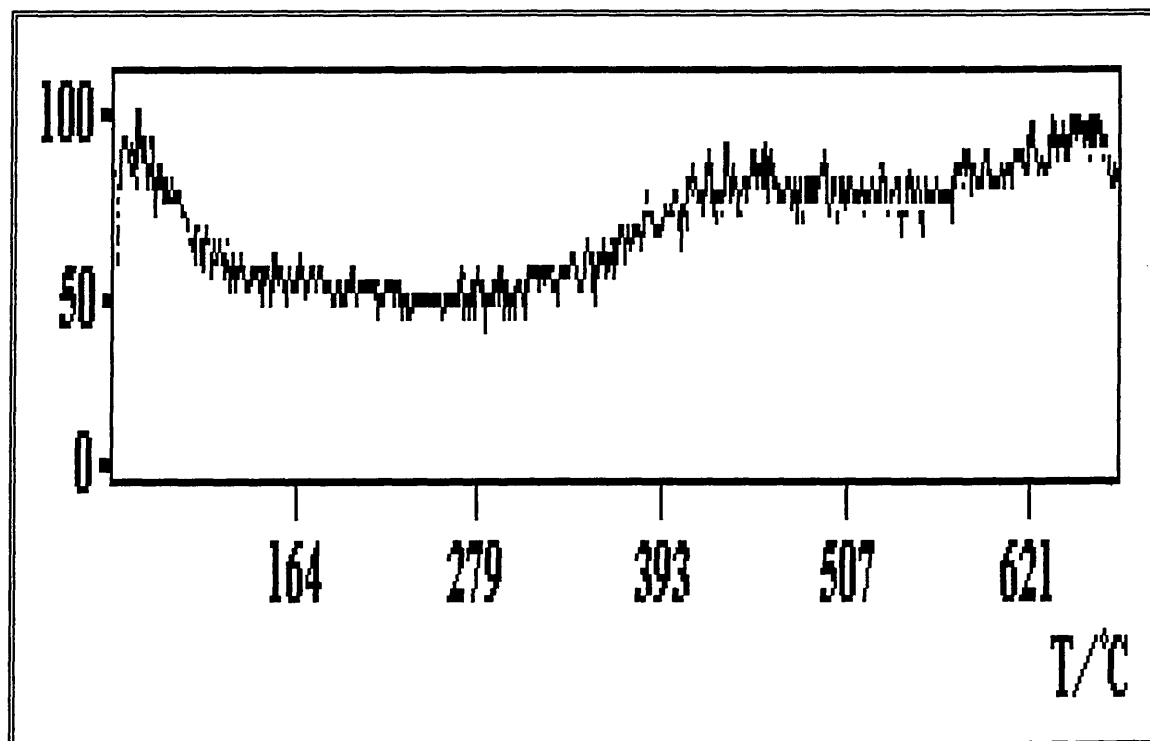
The derivative thermogram for AA-HWL shows the desorption of physisorbed water below 100°C¹⁸⁴, as observed for H-WL (Figure 3.1) but after this there was little fine

structure. The derivative thermogram suggested a weight loss beginning at 190 °C, peaking at 360 °C and then tailing away towards 430 °C. 20 % of the overall weight loss occurred over this range. This is broadly consistent with the major weight loss seen with AA. Above 430 °C, the derivative thermogram once again rises, peaking at 480 °C, and then diminishing towards 520 °C. A further 9 % was lost in this range. This amount is too large to be attributed to the kaolinite impurity alone. At 520 °C the major loss corresponding to 55 % of the overall weight loss started to occur. There was some evidence of a shoulder at 650°C before the derivative thermogram peaked at 740 °C, and then fell sharply away. It is interesting to note that this peak was also present in the AH-WL sample. Again it is difficult to establish the source of this weight loss without mass spectrometry, but it does suggest that as with A, AA may also decompose by a different route when supported on the clay.

3.2.3 Thermal Desorption Mass Spectroscopy.

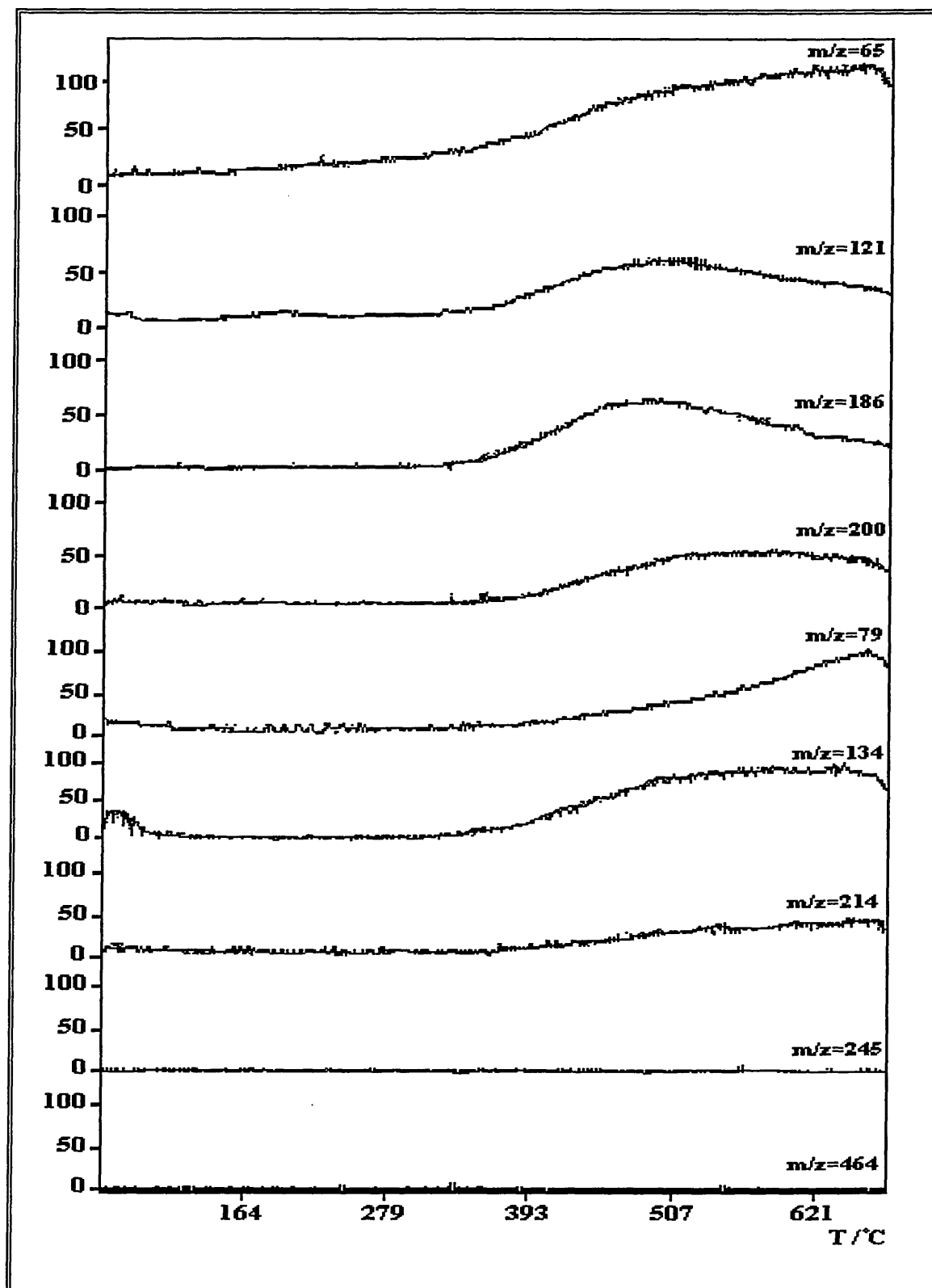
The total ion current for the AA-HWL sample remained relatively constant throughout the temperature range (Figure 3.2). The TIC was comprised of three main features. The first was a sharp peak around 75°C, which was caused by the loss of physisorbed solvent (methanol/THF) and water from the interlayer of the clay. Two further features were visible. The first started at 280°C, reached a maximum at 450°C, and then fell away until 490°C. The second began at 490°C, peaked at 660°C, and diminished towards 690°C. Beneath the second peak (maximum 430°C), fragments of $m/z = 65$, 121 and 186 were abundant, although fragments of $m/z = 79$, 134, and 200 were also present in small quantities(Figure 3.3).

Figure 3.2 TIC for AA-HWL



A very small amount of $m/z = 214$ was also detected. ($m/z 243 = \text{CpFeCpCH}_2\text{NMe}_2$ (Cp = cyclopentadienyl, Me = methyl), $214 = \text{CpFeCpCH}_2\text{NH}$, $200 = \text{CpFeCpCH}_3$, $186 = \text{CpFeCp}$, $134 = \text{FeCpCH}_2$, $121 = \text{FeCp}$, $79 = \text{CpCH}_3$, Cp = 65). Once again it is clear that ferrocene was being lost from the interlayer as it had been with the AH-WL samples (see section 2.2.5). As has been mentioned before (see section 2.2.5) this is in direct contradiction to previous work by both Breen *et al.*¹⁸² on iron tricarbonyls supported on montmorillonite and Borvornwattanont *et al.*³³ on the ferrocenium-zeolite-Y composite. In general the results agree favourably with those obtained from thermogravimetric analysis. It should be noted at this stage that the TD-MS was carried out *in vacuo* whereas the TGA was carried out under a dynamic atmosphere of nitrogen gas.

Figure 3.3 Thermal Desorption Mass Spectra for AA and AA-HWL



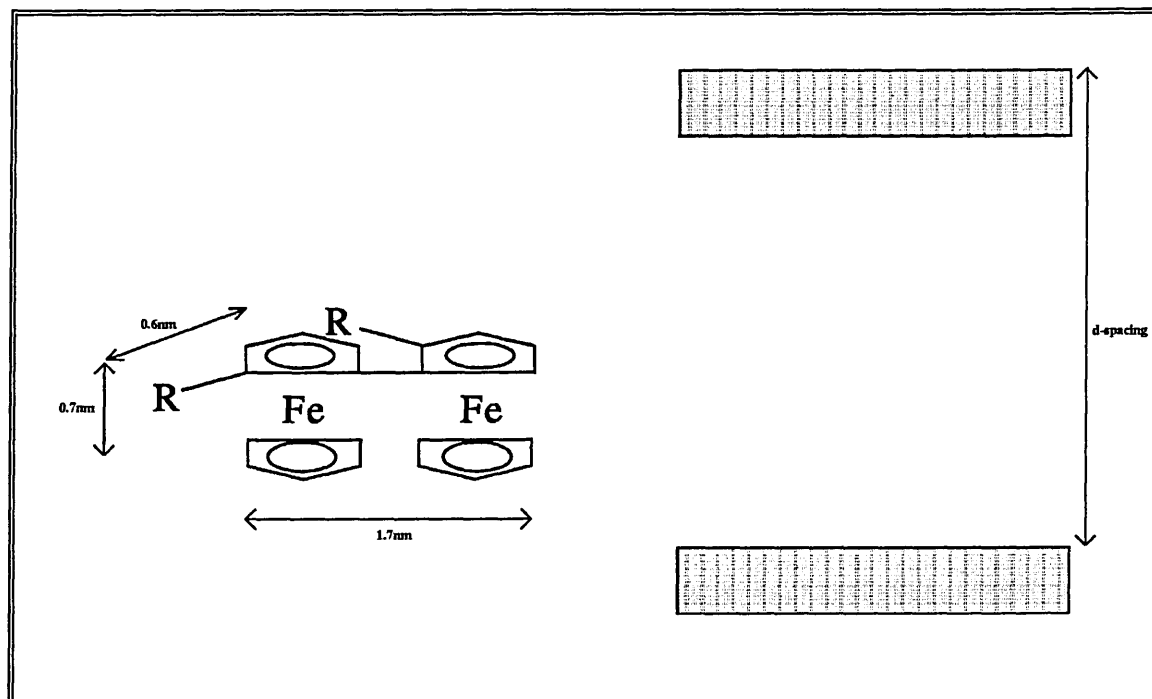
As with the AH-WL samples, further heating above 490°C led to a decrease in the ion current due to fragments $m/z = 121$ and 186 , with an increase in the ion current from fragments of $m/z = 65$ and 79 . A small amount of $m/z = 134$ and a trace of $m/z = 214$ were also detected. This behaviour continued until 660°C where a decrease in all fragment intensities was observed. It would appear that as with the AH-WL samples, at least two decomposition processes are in operation. The first dominating below 490°C involves the loss of fragments containing iron. The second dominates above 490°C during which the iron remains on the clay and only organic fragments are lost. Once again (see section 2.2.5) there was no sign of fragments from the ammonium side chain being lost throughout the temperature range. This indicates a strong interaction between the ammonium side chain and the clay lattice.

3.2.4 Variable Temperature X-Ray Diffraction.

As noted earlier (see section 1.2.2), Na-WL has a d_{001} -spacing of 1.25nm at 25°C, which collapses at temperatures near 55°C to yield a spacing of 0.95nm. The room temperature scan of AAHWL exhibited a d-spacing of 1.65 nm, indicating that the molecule AA was indeed residing within the interlayer. Molecular modelling using Microsoft Chemwindows indicated that the molecule AA had dimensions of 0.7nm ring-ring, 0.6nm ring depth, and 1.7nm width from amine to amine (see Figure 3.4). As seen in section 2.2.6 swelling lattices present a measure of uncertainty when attempting to correlate the

increase in the interlayer distance with the dimensions of the guest molecule¹⁹⁶. With clays the interlayer distance is typically 0.1-0.2 nm less than the predicted increase.

Figure 3.4 Diagram of AA and d_{001} -spacing.

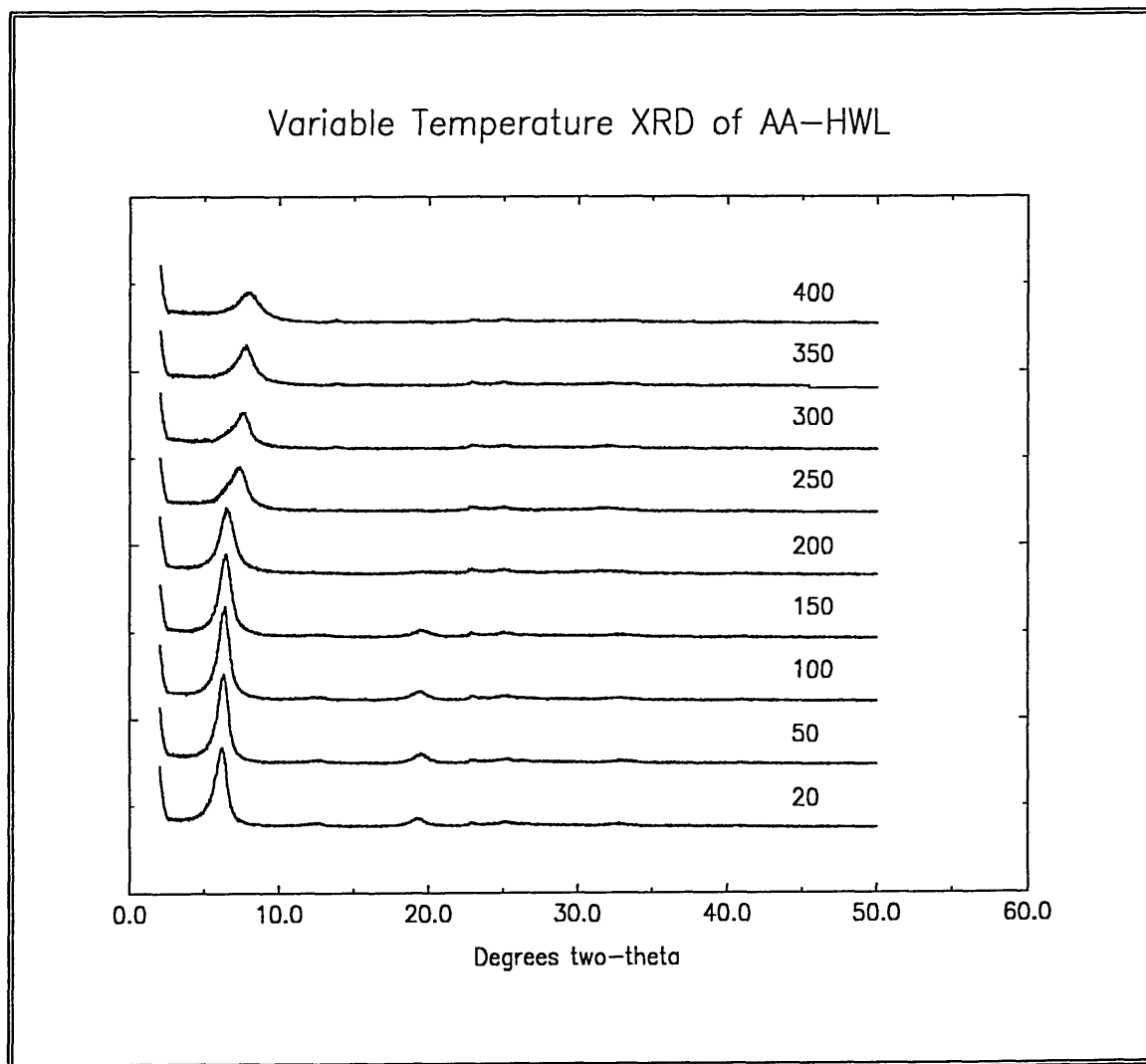


The observed interlayer distance of 1.65 nm is therefore consistent with the molecule being orientated with the cyclopentadienyl rings perpendicular and the long axis of the molecule parallel to the interlayer sheet. This is in agreement with the work by Hendrickson *et al.* on the diethylbiferrocenium - SWY-1 montmorillonite clay composite¹⁵². This conforms with the assumed orientation of AH^+ in AH-WL discussed in section 2, and agrees well with other work by Okuno *et al.* on the intercalation of biferrocenes into $VOPO_4$ and V_2O_5 ¹⁹⁷. This is in accord with the majority of ferrocene intercalates, which produce a single layer of ferrocene molecules sandwiched between

¹⁹⁶ F. Farzenah and T. J. Pinnavaia, *Inorganic Chemistry*, **1983**, *22*, 2210-2216.

the layers of the host, although bilayers have been observed by O'Hare *et al.*⁶³ with MoO₃ and Zr(HPO₄)₂. However, the possibility that the molecule lies with the rings parallel to the interlayer sheet cannot be discounted (see Figure 3.4). At a temperature of 250°C the spacing decreased to 1.41 nm, after which it slowly decreased to 1.29 nm at 400°C (Figure 3.5).

Figure 3.5 Variable Temperature XRD spectra for AA-HWL



Considering both the TGA and TD-MS measurements were carried out under dynamic conditions, whereas in this case the compound is held for a long period of time at an

¹⁹⁷ S. Okuno and G-E. Matsubayashi, *Chem. Lett.*, **1993**, 799-802.

elevated temperature, this is in good agreement with the TGA / TD-MS measurements which show a gradual weight loss from 200°C onwards (see section 3.2.2 and 3.2.3).

The diffraction profiles in Figure 3.5 provide no evidence of a peak corresponding to a fully collapsed spacing which would indicate that all the organometallic component had been lost. This indicates that not only is the molecule between the layers, but that it may also be homogeneously distributed throughout the interlayer.

Table 3.1 Peak Index of VT-XRD of AA-HWL

T /°C	Peak	2θ /°	I / %	d /nm	h	k	l	Assignment
20	1	06.22	100	16.49	0	0	1	AA-HWL
20	2	12.37	8	8.31	0	0	2	AA-HWL
20	3	19.28	15	5.35	0	0	3	AA-HWL
20	4	22.93	8	4.50	0	0	1	Opaline Silica
20	6	32.62	7	3.19	0	0	6	AA-HWL
50	1	6.32	100	16.28	0	0	1	AA-HWL
50	2	12.66	8	8.12	0	0	2	AA-HWL
50	3	19.47	14	5.29	0	0	3	AA-HWL
50	4	23.02	8	4.49	0	0	1	Opaline Silica
50	6	32.91	7	3.16	0	0	6	AA-HWL
100	1	6.42	100	16.00	0	0	1	AA-HWL
100	2	12.75	8	8.06	0	0	2	AA-HWL
100	3	19.47	13	5.29	0	0	3	AA-HWL
100	4	23.02	8	4.49	0	0	1	Opaline Silica
100	6	32.62	5	3.19	0	0	6	AA-HWL
150	1	6.42	100	16.00	0	0	1	AA-HWL
150	2	12.56	9	8.18	0	0	2	AA-HWL
150	3	19.38	13	5.32	0	0	3	AA-HWL
150	4	22.93	9	4.50	0	0	1	Opaline Silica
150	6	33.10	7	3.14	0	0	6	AA-HWL
200	1	6.51	100	15.76	0	0	1	AA-HWL
200	3	19.57	9	5.27	0	0	3	AA-HWL
200	4	23.02	12	4.49	0	0	1	Opaline Silica
200	6	31.38	10	3.31	0	0	6	AA-HWL
250	1	7.18	100	14.29	0	0	1	AA-HWL
250	2	12.18	13	8.44	0	0	2	AA-HWL
250	3	19.28	11	5.35	0	0	3	AA-HWL
250	4	23.12	16	4.47	0	0	1	Opaline Silica
250	6	31.76	15	3.27	0	0	6	AA-HWL
300	1	7.66	100	13.39	0	0	1	AA-HWL
300	2	13.81	14	7.45	0	0	2	AA-HWL
300	4	22.93	17	4.50	0	0	1	Opaline Silica
300	6	32.05	15	3.24	0	0	6	AA-HWL
350	1	7.95	100	12.93	0	0	1	AA-HWL
350	2	13.90	16	7.40	0	0	2	AA-HWL
350	3	18.70	12	5.51	0	0	3	AA-HWL
350	4	22.93	5	4.50	0	0	1	Opaline Silica
350	6	31.95	18	3.25	0	0	6	AA-HWL

3.2.5 Variable Temperature Mössbauer Spectroscopy.

3.2.5.1 2,2''-bis[(dimethylammonium)methyl]biferrocene.

The Mössbauer spectrum of 2,2''-bis[(dimethylammonium)methyl]biferrocene consisted of a single doublet ($\Delta = 2.36 \pm 0.02$ mm/s) which remained constant between 15 and 300 K (see Table 3.2). The isomer shift exhibited a standard second order Doppler shift effect, with a value of 0.41 ± 0.02 mm/s at 15 K decreasing to 0.33 ± 0.02 mm/s at 300 K. Analysis of the normalised spectral areas led to a Debye temperature (θ_D) of 172 ± 5 K, and a recoil free fraction at 291K (f_{291}) of 0.26 ± 0.02 . The Debye temperature was higher than that observed in the chloride salt of N,N-dimethylaminomethylferrocene ($\theta_D = 144 \pm 5$ K), indicating that the lattice in the 2,2''-bis[(dimethylammonium)methyl]-biferrocene is more rigid. The half-widths of the doublet increase from 0.23 mm/s at 15 K to 0.25 mm/s at 300K. This is due to increased vibration within the solid as the temperature is raised. These values are typical for this type of material and agree well with similar work published by Hendrickson *et al.*¹⁸⁰ on other biferrocenes and biferrocenium salts. Unfortunately a complete comparison is not possible due to a lack of published low temperature data (*i.e.* below 120 K).

Figure 3.6 VT-Mössbauer spectra of AA.

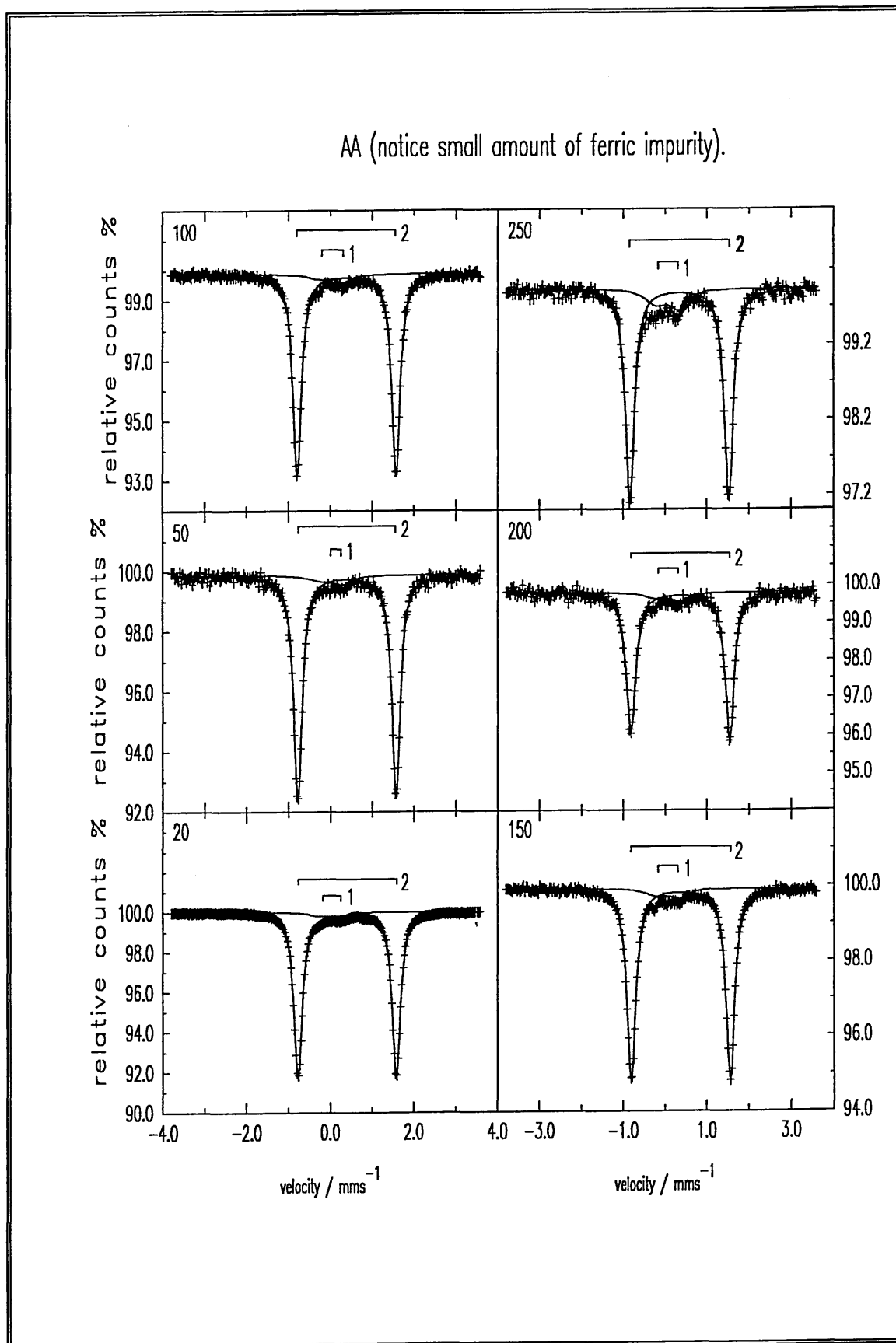


Table 3.2 Fitting parameters for AA

T (K)	Phase	δ (mm/s)	Δ (mm/s)	Γ_1 (mm/s)	Γ_2 (mm/s)	Norm. Area	% Area	χ^2
16	Fe ³⁺	0.03	0.50	0.60	0.48	0.124	05.69	2.4
16	Fe ²⁺	0.41	2.35	0.23	0.23	2.048	94.31	2.4
55	Fe ³⁺	0.03	0.30	0.76	0.48	0.133	06.69	0.5
55	Fe ²⁺	0.40	2.35	0.23	0.24	1.855	93.31	0.5
100	Fe ³⁺	0.05	0.56	0.66	0.48	0.120	06.68	0.6
100	Fe ²⁺	0.39	2.36	0.24	0.24	1.683	93.32	0.6
150	Fe ³⁺	0.06	0.55	0.65	0.48	0.123	06.68	0.6
150	Fe ²⁺	0.38	2.37	0.25	0.25	1.340	93.32	0.6
200	Fe ³⁺	0.06	0.55	0.65	0.48	0.108	9.22	0.4
200	Fe ²⁺	0.36	2.36	0.27	0.26	1.059	90.78	0.4
250	Fe ³⁺	0.06	0.55	0.64	0.51	0.133	15.09	0.6
250	Fe ²⁺	0.34	2.37	0.25	0.25	0.750	84.91	0.6
300	Fe ³⁺	0.04	0.47	0.50	0.36	0.105	16.46	0.7
300	Fe ²⁺	0.33	2.35	0.25	0.24	0.535	83.54	0.7

Errors: T = ± 2 K, $\delta = \pm 0.02$ mm/s, $\Delta = \pm 0.02$ mm/s, $\Gamma = \pm 0.02$ mm/s.

Fe³⁺ = A ferric impurity.

Fe²⁺ = Iron (II) in biferrocene.

3.2.5.2 Mössbauer spectra of AA-HWL, AA-HWL(48) and AA⁺-HWL

The Mössbauer spectra of AA-HWL, AA-HWL(48) and AA⁺-HWL appear at first to consist of two “nested” doublets. A sharp outer doublet characteristic of AA, and a broad inner doublet consistent with HWL. However, subsequent fitting proved more complex. A close examination of the spectra revealed that the intensity of the biferrocene peaks had decreased from the AA-HWL spectra to the AA-HWL(48) and AA⁺-HWL spectra. It was considered that some of the biferrocene may have oxidised during the contact time with the clay, so a third doublet, with the fitting parameters of ($\delta_{16K} = 0.34$ mm/s, $\Delta=1.17$ mm/s), was introduced. As the reduction in the intensity of the biferrocene doublet was most pronounced for the AA⁺-HWL sample, the fitting was first performed using these data sets in order to reduce possible errors. The fitted values were then taken and an attempt to fit the AA-HWL(48) and AA-HWL spectra was attempted.

Figure 3.7 Spectra of A) AA-HWL, B) AA-HWL(48) and C) AA⁺-HWL.

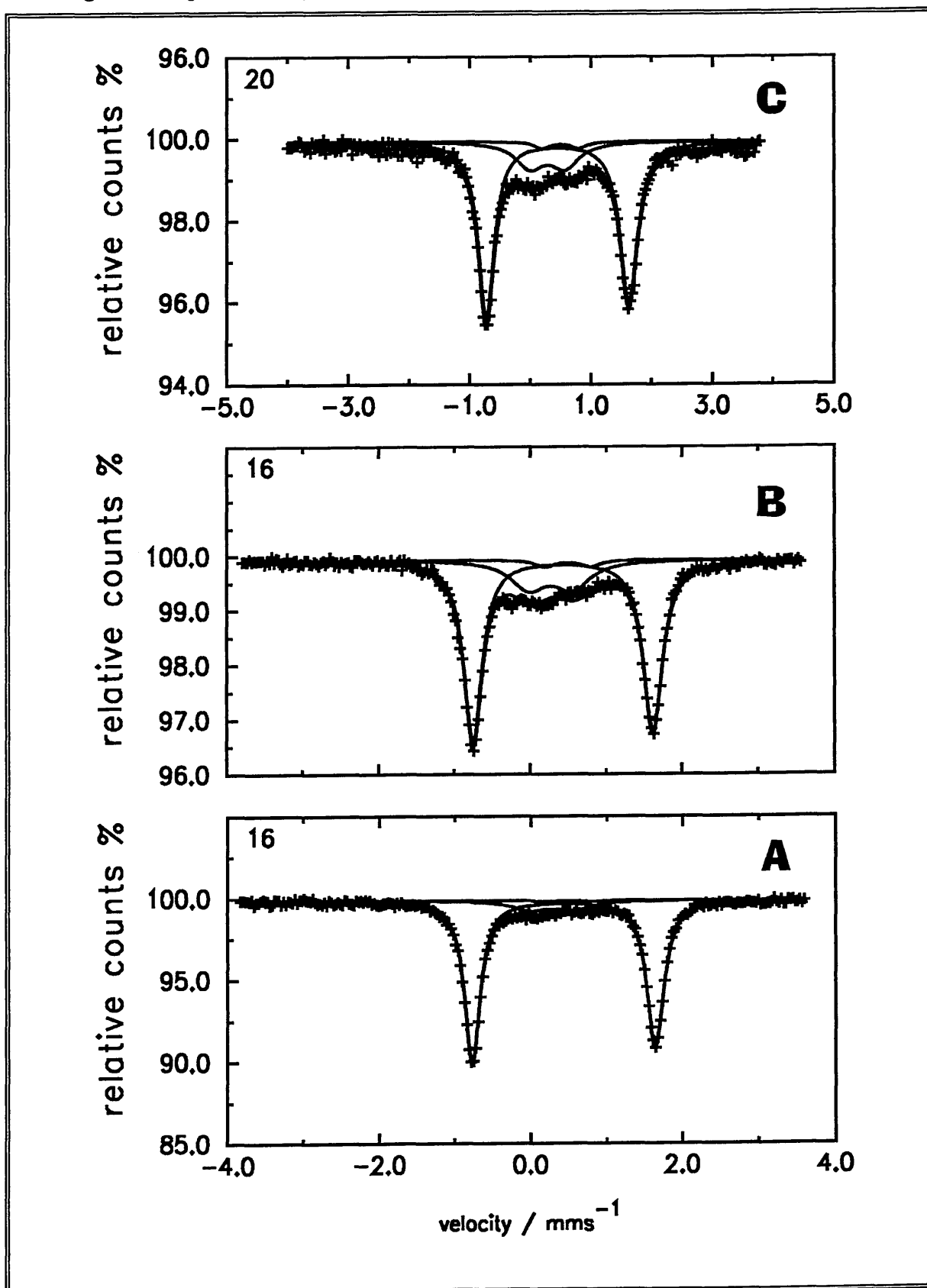


Table 3.3 AA⁺-HWL fitting parameters for 3 phase model.

T (K)	Phase	δ (mm/s)	Δ (mm/s)	Γ_l (mm/s)	Γ_r (mm/s)	Norm. Area	% Area	χ^2
16	Fe ³⁺ (i)	0.29	0.58	0.56	0.56	0.368	20.81	0.7
16	Fe ²⁺	0.45	2.35	0.32	0.35	1.362	77.11	0.7
16	Fe ³⁺	0.34	1.17	0.32	0.32	0.037	02.08	0.7
100	Fe ³⁺ (i)	0.30	0.58	0.56	0.56	0.360	28.44	0.5
100	Fe ²⁺	0.43	2.34	0.32	0.37	0.882	69.64	0.5
100	Fe ³⁺	0.34	1.17	0.32	0.32	0.024	01.90	0.5
150	Fe ³⁺ (i)	0.30	0.58	0.56	0.56	0.367	33.52	0.6
150	Fe ²⁺	0.42	2.32	0.38	0.41	0.709	64.74	0.6
150	Fe ³⁺	0.34	1.17	0.32	0.32	0.019	01.74	0.6
200	Fe ³⁺ (i)	0.28	0.58	0.56	0.56	0.344	38.74	0.7
200	Fe ²⁺	0.40	2.31	0.38	0.42	0.530	59.68	0.7
200	Fe ³⁺	0.36	1.17	0.32	0.32	0.014	01.58	0.7
250	Fe ³⁺ (i)	0.25	0.58	0.56	0.56	0.277	46.71	0.6
250	Fe ²⁺	0.36	2.31	0.39	0.43	0.325	54.75	0.6
250	Fe ³⁺	0.37	1.17	0.32	0.32	0.009	01.46	0.6
$\theta_D(\text{Clay})=286\text{K}$, $f_{291}(\text{Clay})=0.61$		$\theta_D(\text{AA})=149\text{K}$, $f_{291}(\text{AA})=0.17$			$\theta_D(\text{Fe}^{3+})=170\text{K}$, $f_{291}(\text{Fe}^{3+})=0.25$			

Errors: T = ± 2 K, $\delta = \pm 0.02$ mm/s, $\Delta = \pm 0.02$ mm/s, $\Gamma = \pm 0.02$ mm/s, $\theta_D = \pm 5$ K, $f_{291} = 0.02$.

Fe³⁺ (i) = Inorganic iron present in the clay.

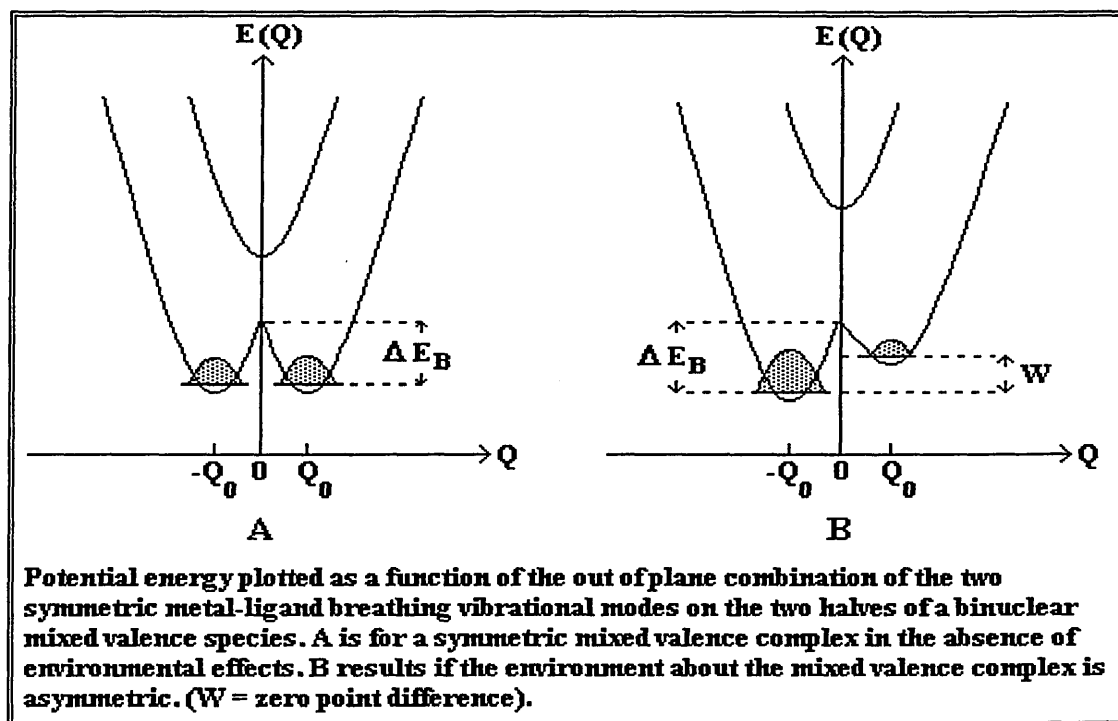
Fe²⁺ = Iron(II) biferrocene/biferrocenium molecules.

Fe³⁺ = Iron(III) in the biferrocenium molecules.

It was noticed that the Debye temperature of the extra phase was characteristic of an organometallic compound ($\theta_D = 170$ K), rather than that of an inorganic salt (Typically > 300 K), and that although the fit worked well for the lower temperatures, it became increasingly erroneous at higher temperatures. This indicated that the biferrocene had not decomposed during the contact with the clay, but had merely oxidised to biferrocenium. This is in good agreement with both the TGA, TD-MS and XRD data (see sections 3.2.2, 3.2.3, 3.2.4 respectively), which showed that the compound was stable in the interlayer up to 200°C. In order to account for this high temperature discrepancy, a fourth doublet was added, this time characteristic of a charge averaged biferrocenium species ($\delta_{300\text{K}} = 0.37\text{mm/s}$, $\Delta = 1.22$ mm/s). The transfer of an electron between the two iron centres above a certain temperature is known as valence electron de-trapping (VEDT), and has been studied extensively by both Hendrickson, Dong and co-workers¹⁸⁰. At this stage there were a number of ways of fitting the observed spectra.

VEDT proceeds by one of three scenarios (see section 1.4.3). Hendrickson notes that each iron atom sits in a potential energy well defined by the local environment.

Figure 3.8 Potential well diagrams.



The symmetry of the environment surrounding the biferrrocene molecule affects the depth of these potential energy wells. In scenario one, the difference in the depth of the wells is of a similar magnitude to the random thermal energy available in the crystal (kT). If the transfer is initially slower than the time scale of the Mössbauer experiment (*i.e.* $<10^7 \text{ s}^{-1}$), then only two resonances, one for iron(II) and one for iron(III) will be seen. As the temperature is raised, some of the molecules gain enough energy to be able to transfer an electron. If the transfer occurs at a rate comparable to the time scale of the Mössbauer experiment (*i.e.* $\sim 10^7 \text{ s}^{-1}$), then an additional resonance characteristic of iron(2.5) will also be seen. In this case a broadening of all the resonances will also be observed. Any further rise in temperature leads to an increase in the number of molecules transferring an electron, and also the electron transfer rate. This causes the iron(2.5) resonance to grow at the expense of the iron(II) and iron(III) resonances.

In scenario two, a change occurs within the crystal which alters the shape of the potential wells. This could be caused by the onset of motion of a counter ion or solvate molecule. This produces a more symmetric environment around the molecule. As the symmetry of the environment around each iron centre becomes similar, a mirror like, double well type potential is produced, and the likelihood of the transfer of an electron between the two centres increases. As the temperature is increased the motion of the counter ion or solvate molecule increases, and so in turn does the intramolecular electron transfer (vibronic coupling). In this model, if the transfer is comparable to the Mössbauer experiment time-scale, the Fe(II) and Fe(III) resonances simply move towards each other, until they finally merge to form an average resonance. At no stage is there any line broadening. This type of de-trapping is sometimes referred to as “fusion” type de-trapping, and has been observed in compounds such as 1', 1''-dibenzylbiferrocenium hexafluorophosphate¹⁵⁰.

In scenario three there is once again some change within the solid as in scenario two. However, in this case it is restricted to small domains within the solid. As the temperature is raised these domains become larger and larger, until finally the whole solid is affected. In this case, the resonances due to the Fe(II) and Fe(III) will be present, and if the electron transfer in the ‘changed’ domains is greater than 10^7 Hz, a further average resonance representing the valence de-trapped domains will be seen. This average resonance will increase in intensity as the temperature increases, while the intensity of the Fe(II) and Fe(III) resonances decreases. Eventually only the average resonance will be present. Again, no line broadening is seen. This type of de-trapping is

sometimes referred to as “domain” de-trapping, and has been observed in compounds such as 1', 1'''-dibenzylbiferrocenium triiodide¹⁴⁹.

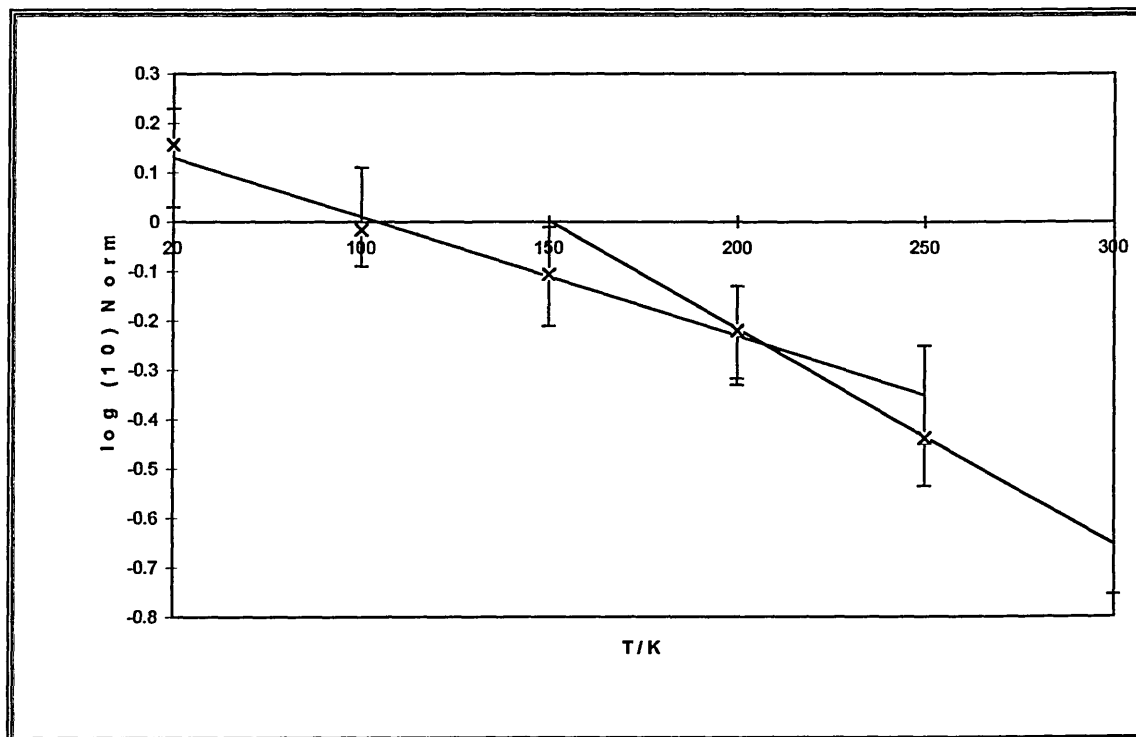
In this present case the problem was compounded by the broad Fe³⁺ doublet (arising from the clay) overlying the central area of the spectrum. Under this resonance it is almost impossible to fit any precise features, making the temperature range at which any de-trapping starts almost impossible to determine. A close inspection of the fit, the normalised areas and finally the spectral intensities was needed to solve the puzzle. A close examination of the normalised area temperature data for the organometallic phase in the AA⁺-HWL spectra revealed an “elbow” in the data around 200 K (see Figure 3.9), where the data switched from one type of straight line behaviour to another. This has been seen by several groups who have attributed its cause to a number of different reasons. Pertinent to this study is the observation of Hendrickson *et al.*¹⁸⁰ While studying the biferrocenium, compounds they also noticed a break from the standard straight line behaviour in the normalised area vs. temperature data as the compound de-trapped. This was a direct result of a phase transition producing a “softer” lattice, whilst also inducing the valence electron de-trapping. This argument was backed up by both differential scanning calorimetry (D.S.C.) and variable temperature electron paramagnetic resonance (V.T.E.P.R.) measurements¹⁹⁸.

However, once again the problem herein was compounded by the physiochemical characteristics of the clay. A similar elbow in the normalised area temperature data had

¹⁹⁸ R. J. Webb, P. M. Hagen, R. J. Wittebort, M. Sorai, and D. N. Hendrickson, *Inorg. Chem.*, **1992**, *32*, 1791-1801.

been observed by both Breen *et al.*⁸⁹ and Simopoulos *et al.*¹⁹⁰ whilst studying organotin cations exchanged on montmorillonite, and more interestingly, around the same temperature observed here.

Figure 3.9 LNAT plot for AA⁺-HWL organometallic phase.



Their conclusion was that the molecule gained a degree of freedom as the interlayer water melted. This left a softer lattice, thus producing a second region of straight line behaviour from the point the interlayer water melted. It should be noted here that this behaviour was not seen in the monomer N,N-dimethylaminomethylferrocene (see section 2.2.7). It should be noted here that a third possibility also exists. Whilst studying polyvinylferrocenes Plimley *et al.*¹⁹⁹ noted a similar deviation from straight line behaviour. It was concluded that this was caused by an anharmonic bending mode within the molecule. However this behaviour was not observed in AA. It was therefore possible that any or indeed all of these possibilities could be contributing to the elbow in Figure

¹⁹⁹ S. Plimley, G. C. Corfield, J. S. Brooks, and C. M. Care, *Hyperfine Interactions*, 1984, 20, 151-167.

3.9. An attempt was therefore made to fit the spectra using scenario two (“fusion” de-trapping) with the assumption that the de-trapping occurred after 200K. This produced a good fit (see Table 3.4, Table 3.5, and Table 3.6), and a subsequent analysis of the normalised spectral areas yielded a Debye temperature of 343 K for the clay, and 147 K for the organometallic phases. As a concluding check, the ratio of Fe(II,II) to Fe (II,III) was compared. Assuming the two systems have similar Debye temperatures, this ratio should be constant throughout the temperature range. When calculated the relative areas of the biferrocene/biferrocenium were reasonably constant (AA-HWL = 55 ± 3 , AA-HWL(48) = 8 ± 3 and AA⁺-HWL = 6 ± 2) indicating that the “fusion” model was theoretically consistent.

Table 3.4 AA-HWL fitting parameters for “fusion” de-trapping.

T (K)	Phase	δ (mm/s)	Δ (mm/s)	Γ_1 (mm/s)	Γ_r (mm/s)	Norm. Area	% Area	χ^2
16	Fe ³⁺ (i)	0.27	0.58	0.56	0.56	0.315	10.88	0.8
16	Fe ²⁺	0.44	2.41	0.24	0.27	2.555	88.32	0.8
16	Fe ³⁺	0.49	0.60	0.32	0.32	0.023	00.79	0.8
50	Fe ³⁺ (i)	0.27	0.58	0.56	0.56	0.330	12.92	1.6
50	Fe ²⁺	0.43	2.41	0.25	0.27	2.203	86.30	1.6
50	Fe ³⁺	0.49	0.60	0.32	0.32	0.02	00.78	1.6
100	Fe ³⁺ (i)	0.26	0.58	0.56	0.56	0.322	16.94	1.1
100	Fe ²⁺	0.42	2.40	0.24	0.27	1.574	82.33	1.1
100	Fe ³⁺	0.49	0.60	0.32	0.32	0.028	01.48	1.1
150	Fe ³⁺ (i)	0.26	0.58	0.56	0.56	0.308	21.11	0.8
150	Fe ²⁺	0.41	2.39	0.24	0.28	1.132	77.50	0.8
150	Fe ³⁺	0.47	0.60	0.32	0.32	0.020	01.40	0.8
200	Fe ³⁺ (i)	0.23	0.58	0.56	0.56	0.303	27.40	1.1
200	Fe ²⁺	0.39	2.38	0.24	0.27	0.789	71.31	1.1
200	Fe ^{(2+x)+}	0.38	1.51	0.32	0.32	0.007	00.64	1.1
200	Fe ^{(3-x)+}	0.40	1.07	0.32	0.32	0.007	00.64	1.1
250	Fe ³⁺ (i)	0.23	0.58	0.56	0.56	0.281	33.21	1.0
250	Fe ²⁺	0.36	2.38	0.25	0.28	0.555	65.61	1.0
250	Fe ^{2.5+}	0.37	1.22	0.32	0.32	0.010	01.18	1.0
300	Fe ³⁺ (i)	0.18	0.58	0.56	0.56	0.284	40.13	0.9
300	Fe ²⁺	0.34	2.38	0.26	0.28	0.417	58.81	0.9
300	Fe ^{2.5+}	0.34	1.22	0.32	0.32	0.008	01.06	0.9
θ_D (Clay) = 480 K, f_{291} (Clay) = 0.83				θ_D (Biferrocene) = 139 K, f_{291} (Biferrocene) = 0.13				

Errors: T = ± 2 K, $\delta = \pm 0.02$ mm/s, $\Delta = \pm 0.02$ mm/s, $\Gamma = \pm 0.02$ mm/s, $\theta_D = \pm 5$ K, $f_{291} = \pm 0.02$.

Fe³⁺ (i) = Inorganic iron present in the clay.

Fe³⁺ = Iron(III) in the biferrocenium molecules.

Fe^{(2+x)+} = Partially de-trapped Fe²⁺

Fe²⁺ = Iron(II) biferrocene/biferrocenium molecules.

Fe^{2.5+} = Charge averaged iron(2.5) in the biferrocenium molecules.

Fe^{(3-x)+} = Partially de-trapped Fe³⁺

Table 3.5 AA-HWL(48) fitting parameters for “fusion” de-trapping.

T (K)	Phase	δ (mm/s)	Δ (mm/s)	Γ_l (mm/s)	Γ_r (mm/s)	Norm. Area	% Area	χ^2
16	Fe ³⁺ (i)	0.27	0.58	0.56	0.56	0.298	21.93	1.1
16	Fe ²⁺	0.43	2.37	0.29	0.30	1.019	74.94	1.1
16	Fe ³⁺	0.49	0.60	0.32	0.32	0.042	03.13	1.1
100	Fe ³⁺ (i)	0.22	0.58	0.56	0.56	0.316	31.06	1.1
100	Fe ²⁺	0.42	2.36	0.30	0.32	0.649	63.66	1.1
100	Fe ³⁺	0.46	0.60	0.32	0.32	0.054	05.28	1.1
150	Fe ³⁺ (i)	0.23	0.58	0.56	0.56	0.296	37.59	2.1
150	Fe ²⁺	0.40	2.37	0.30	0.31	0.452	57.52	2.1
150	Fe ³⁺	0.43	0.60	0.32	0.32	0.038	04.89	2.1
200	Fe ³⁺ (i)	0.25	0.58	0.56	0.56	0.286	43.48	1.7
200	Fe ²⁺	0.39	2.37	0.31	0.32	0.343	52.17	1.7
200	Fe ³⁺	0.40	0.60	0.32	0.32	0.029	04.35	1.7
250	Fe ³⁺ (i)	0.23	0.58	0.56	0.56	0.273	50.71	1.1
250	Fe ²⁺	0.36	2.35	0.33	0.32	0.245	45.51	1.1
250	Fe ^{2.5+}	0.37	1.22	0.32	0.32	0.020	03.78	1.1
300	Fe ³⁺ (i)	0.18	0.58	0.56	0.56	0.270	57.87	1.4
300	Fe ²⁺	0.33	2.35	0.33	0.34	0.182	38.90	1.4
300	Fe ^{2.5+}	0.34	1.22	0.32	0.32	0.015	03.23	1.4
θ_D (Clay) = 449 K, f_{291} (Clay) = 0.81				θ_D (Biferrocene) = 142 K, f_{291} (Biferrocene) = 0.14				

Errors: T = ± 2 K, $\delta = \pm 0.02$ mm/s, $\Delta = \pm 0.02$ mm/s, $\Gamma = \pm 0.02$ mm/s, $\theta_D = \pm 5$ K, $f_{291} = \pm 0.02$.

Fe³⁺ (i) = Inorganic iron present in the clay.

Fe²⁺ = Iron(II) biferrocene/biferrocenium molecules.

Fe³⁺ = Iron(III) in the biferrocenium molecules.

Fe^{2.5+} = Charge averaged iron(2.5) in the biferrocenium molecules.

Table 3.6 AA⁺-HWL fitting parameters for “fusion” de-trapping.

T (K)	Phase	δ (mm/s)	Δ (mm/s)	Γ_l (mm/s)	Γ_r (mm/s)	Norm. Area	% Area	χ^2
16	Fe ³⁺ (i)	0.28	0.58	0.56	0.56	0.337	19.20	0.6
16	Fe ²⁺	0.45	2.35	0.32	0.35	1.368	77.84	0.6
16	Fe ³⁺	0.49	0.60	0.32	0.32	0.052	02.96	0.6
100	Fe ³⁺ (i)	0.26	0.58	0.56	0.56	0.344	26.88	0.6
100	Fe ²⁺	0.43	2.34	0.32	0.37	0.872	68.01	0.6
100	Fe ³⁺	0.46	0.60	0.32	0.32	0.065	05.11	0.6
150	Fe ³⁺ (i)	0.28	0.58	0.56	0.56	0.323	29.67	0.7
150	Fe ²⁺	0.42	2.32	0.38	0.41	0.711	65.28	0.7
150	Fe ³⁺	0.43	0.60	0.32	0.32	0.055	05.04	0.7
200	Fe ³⁺ (i)	0.27	0.58	0.56	0.56	0.314	33.46	0.7
200	Fe ²⁺	0.39	2.31	0.38	0.42	0.533	60.28	0.7
200	Fe ³⁺	0.40	0.60	0.32	0.32	0.038	04.26	0.7
250	Fe ³⁺ (i)	0.21	0.58	0.60	0.60	0.268	44.59	0.6
250	Fe ²⁺	0.36	2.31	0.35	0.39	0.295	49.08	0.6
250	Fe ^{2.5+}	0.37	1.22	0.32	0.32	0.038	06.32	0.6
θ_D (Clay) = 343 K, f_{291} (Clay) = 0.70				θ_D (Biferrocene) = 147 K, f_{291} (Biferrocene) = 0.16				

Errors: T = ± 2 K, $\delta = \pm 0.02$ mm/s, $\Delta = \pm 0.02$ mm/s, $\Gamma = \pm 0.02$ mm/s, $\theta_D = \pm 5$ K, $f_{291} = \pm 0.02$.

Fe³⁺ (i) = Inorganic iron present in the clay.

Fe²⁺ = Iron(II) biferrocene/biferrocenium molecules.

Fe³⁺ = Iron(III) in the biferrocenium molecules.

Fe^{2.5+} = Charge averaged iron(2.5) in the biferrocenium molecules.

An attempt to fit the data using scenario three (“domain” de-trapping) was then attempted, with the assumption that de-trapping again occurred at 200 K. Reasonable fits were again obtained, and the normalised area temperature data appeared to be consistent with an inorganic clay phase and three organometallic phases (see Table 3.7, Table 3.8, and Table 3.9). A close inspection of the biferrocene/biferrocenium ratio indicated that this model could also be considered consistent, although more scatter was observed in the biferrocene/biferrocenium ratio than for the “fusion” type de-trapping constant (AA-HWL = 40 ± 14 , AA-HWL(48) = 8 ± 4 and AA⁺-HWL = 7 ± 3). The increased scatter is most likely a consequence of the fitting routine. More consistent values could be produced if the areas of the phases were fixed. The phase areas in this case are of a similar magnitude to the spectral noise making precise fitting difficult.

Table 3.7 AA-HWL fitting parameters for “Domain” de-trapping.

T (K)	Phase	δ (mm/s)	Δ (mm/s)	Γ_1 (mm/s)	Γ_r (mm/s)	Norm. Area	% Area	χ^2
16	Fe ³⁺ (i)	0.23	0.58	0.56	0.56	0.302	10.44	0.8
16	Fe ²⁺	0.44	2.41	0.24	0.27	2.554	88.24	0.8
16	Fe ³⁺	0.50	0.60	0.32	0.32	0.038	01.32	0.8
50	Fe ³⁺ (i)	0.23	0.58	0.56	0.56	0.302	11.81	1.4
50	Fe ²⁺	0.43	2.41	0.25	0.27	2.203	86.23	1.4
50	Fe ³⁺	0.49	0.60	0.32	0.32	0.050	01.96	1.4
100	Fe ³⁺ (i)	0.21	0.58	0.56	0.56	0.264	13.68	1.0
100	Fe ²⁺	0.42	2.40	0.24	0.27	1.582	81.94	1.0
100	Fe ³⁺	0.48	0.60	0.32	0.32	0.085	04.38	1.0
150	Fe ³⁺ (i)	0.22	0.58	0.56	0.56	0.268	18.33	0.7
150	Fe ²⁺	0.41	2.39	0.24	0.28	1.135	77.59	0.7
150	Fe ³⁺	0.47	0.60	0.32	0.32	0.059	04.09	0.7
200	Fe ³⁺ (i)	0.20	0.58	0.56	0.56	0.262	23.50	0.8
200	Fe ²⁺	0.39	2.38	0.24	0.27	0.787	70.63	0.8
200	Fe ³⁺	0.46	0.60	0.32	0.32	0.065	05.87	0.8
250	Fe ³⁺ (i)	0.20	0.58	0.56	0.56	0.247	28.99	0.8
250	Fe ²⁺	0.36	2.38	0.25	0.28	0.554	65.03	0.8
250	Fe ^{2.5+}	0.37	1.26	0.32	0.32	0.030	03.51	0.8
250	Fe ³⁺	0.41	0.60	0.32	0.32	0.021	02.47	0.8
300	Fe ³⁺ (i)	0.17	0.58	0.56	0.56	0.248	35.23	0.9
300	Fe ²⁺	0.34	2.38	0.26	0.28	0.422	59.90	0.9
300	Fe ^{2.5+}	0.34	1.26	0.32	0.32	0.034	04.87	0.9
θ_D (Clay) = 283 K, f_{291} (Clay) = 0.60				θ_D (Biferrocene) = 151 K, f_{291} (Biferrocene) = 0.18				

Errors: T = ± 2 K, δ = ± 0.02 mm/s, Δ = ± 0.02 mm/s, Γ = ± 0.02 mm/s, θ_D = ± 5 K, f_{291} = ± 0.02 .

Fe³⁺ (i) = Inorganic iron present in the clay.

Fe²⁺ = Iron(II) biferrocene/biferrocenium molecules.

Fe³⁺ = Iron(III) in the biferrocenium molecules.

Fe^{2.5+} = Charge averaged iron(2.5) in the biferrocenium molecules.

Table 3.8 AA-HWL(48) fitting parameters for “domain” de-trapping.

T (K)	Phase	δ (mm/s)	Δ (mm/s)	Γ_l (mm/s)	Γ_r (mm/s)	Norm. Area	% Area	χ^2
16	Fe ³⁺ (i)	0.27	0.58	0.56	0.56	0.298	21.93	1.1
16	Fe ²⁺	0.43	2.37	0.29	0.30	1.019	74.94	1.1
16	Fe ³⁺	0.49	0.60	0.32	0.32	0.042	03.13	1.1
100	Fe ³⁺ (i)	0.26	0.58	0.56	0.56	0.277	27.48	1.1
100	Fe ²⁺	0.42	2.36	0.30	0.32	0.659	65.27	1.1
100	Fe ³⁺	0.49	0.60	0.32	0.32	0.074	07.26	1.1
150	Fe ³⁺ (i)	0.26	0.58	0.56	0.56	0.266	33.96	2.0
150	Fe ²⁺	0.40	2.37	0.30	0.31	0.460	58.72	2.0
150	Fe ³⁺	0.47	0.60	0.32	0.32	0.057	07.32	2.0
200	Fe ³⁺ (i)	0.25	0.58	0.56	0.56	0.263	39.87	1.5
200	Fe ²⁺	0.39	2.37	0.31	0.32	0.346	52.50	1.5
200	Fe ^{2.5+}	0.40	1.26	0.32	0.32	0.026	04.02	1.5
200	Fe ³⁺	0.45	0.60	0.32	0.32	0.024	03.61	1.5
250	Fe ³⁺ (i)	0.23	0.58	0.56	0.56	0.271	50.21	1.1
250	Fe ²⁺	0.36	2.35	0.33	0.32	0.244	45.35	1.1
250	Fe ^{2.5+}	0.37	0.74	0.32	0.32	0.024	04.44	1.1
300	Fe ³⁺ (i)	0.18	0.58	0.56	0.56	0.267	57.01	1.4
300	Fe ²⁺	0.33	2.35	0.33	0.34	0.181	38.67	1.4
300	Fe ^{2.5+}	0.34	1.22	0.32	0.32	0.020	04.32	1.4
θ_D (Clay) = 535 K, f_{291} (Clay) = 0.86				θ_D (Biferrocene) = 149 K, f_{291} (Biferrocene) = 0.17				

Errors: T = \pm 2 K, δ = \pm 0.02 mm/s, Δ = \pm 0.02 mm/s, Γ = \pm 0.02 mm/s, θ_D = \pm 5 K, f_{291} = \pm 0.02.

Fe³⁺(i) = Inorganic iron present in the clay.

Fe²⁺ = Iron(II) biferrocene/biferrocenium molecules.

Fe³⁺ = Iron(III) in the biferrocenium molecules.

Fe^{2.5+} = Charge averaged iron(2.5) in the biferrocenium molecules.

Table 3.9 AA⁺-HWL fitting parameters for “domain” de-trapping.

T (K)	Phase	δ (mm/s)	Δ (mm/s)	Γ_l (mm/s)	Γ_r (mm/s)	Norm. Area	% Area	χ^2
20	Fe ³⁺ (i)	0.27	0.58	0.56	0.56	0.323	18.39	0.6
20	Fe ²⁺	0.45	2.35	0.32	0.35	1.368	77.80	0.6
20	Fe ³⁺	0.51	0.60	0.32	0.32	0.067	03.82	0.6
100	Fe ³⁺ (i)	0.26	0.58	0.56	0.56	0.304	23.93	0.5
100	Fe ²⁺	0.43	2.34	0.32	0.37	0.882	69.41	0.5
100	Fe ³⁺	0.49	0.62	0.32	0.32	0.084	06.66	0.5
150	Fe ³⁺ (i)	0.27	0.58	0.56	0.56	0.311	28.45	0.6
150	Fe ²⁺	0.42	2.32	0.38	0.41	0.711	65.02	0.6
150	Fe ³⁺	0.47	0.60	0.32	0.32	0.072	06.52	0.6
200	Fe ³⁺ (i)	0.25	0.58	0.56	0.56	0.282	31.80	0.7
200	Fe ²⁺	0.40	2.31	0.38	0.42	0.535	60.42	0.7
200	Fe ^{2.5+}	0.40	1.26	0.32	0.32	0.036	04.09	0.7
200	Fe ³⁺	0.46	0.60	0.32	0.32	0.033	03.69	0.7
250	Fe ³⁺ (i)	0.23	0.58	0.56	0.56	0.229	38.56	0.6
250	Fe ²⁺	0.36	2.31	0.39	0.43	0.325	54.64	0.6
250	Fe ^{2.5+}	0.37	1.22	0.32	0.32	0.040	06.81	0.6
θ_D (Clay) = 299 K, f_{291} (Clay) = 0.63				θ_D (Biferrocene) = 153 K, f_{291} (Biferrocene) = 0.18				

Errors: T = \pm 2 K, δ = \pm 0.02 mm/s, Δ = \pm 0.02 mm/s, Γ = \pm 0.02 mm/s, θ_D = \pm 5 K, f_{291} = \pm 0.02.

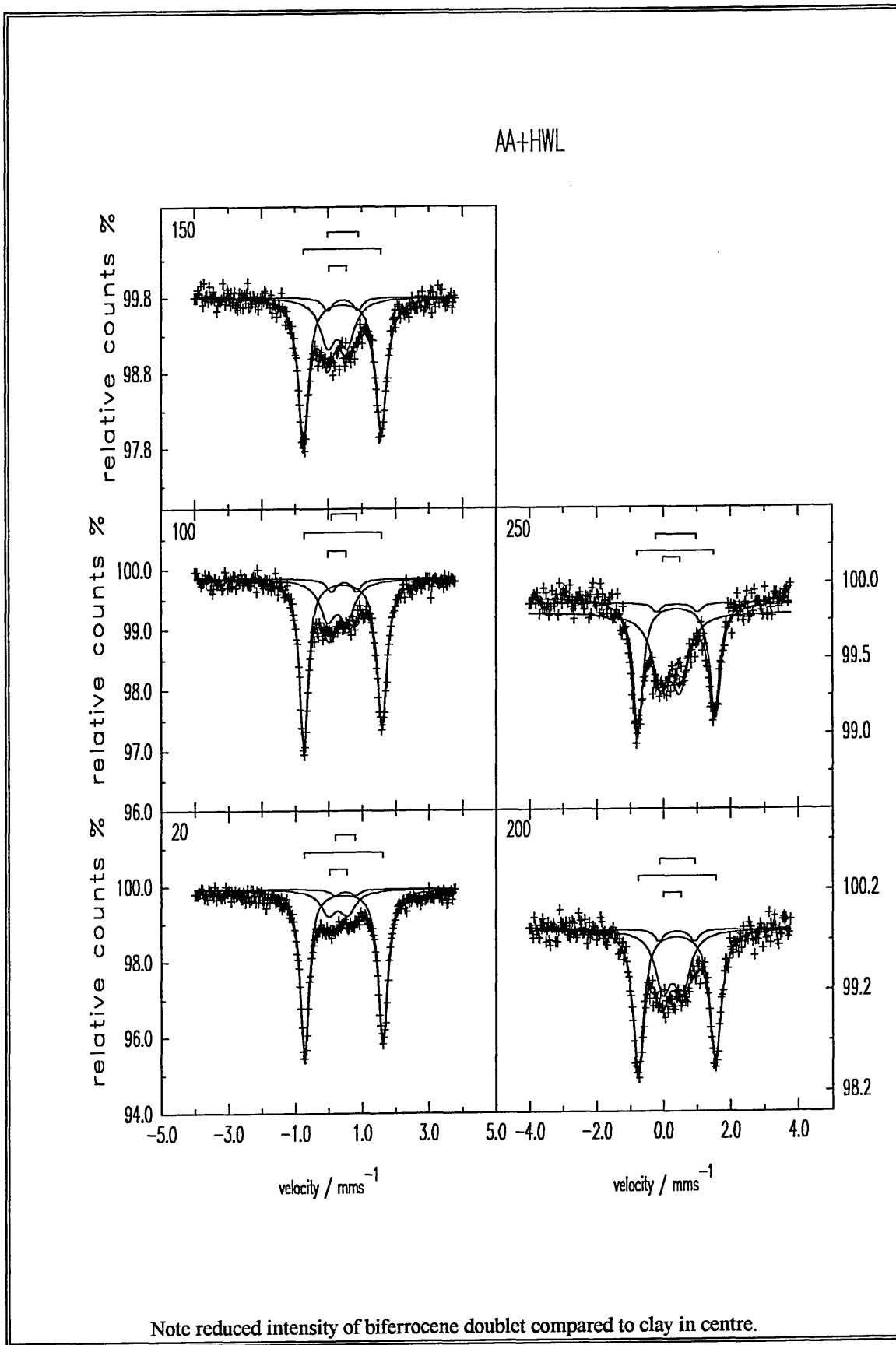
Fe³⁺(i) = Inorganic iron present in the clay.

Fe²⁺ = Iron(II) biferrocene/biferrocenium molecules.

Fe³⁺ = Iron(III) in the biferrocenium molecules.

Fe^{2.5+} = Charge averaged iron(2.5) in the biferrocenium molecules.

Figure 3.10 AA⁺-HWL Spectra fitted using "domain" de-trapping model.



It should be noted that Hendrickson *et al.* observed this “domain” type de-trapping when studying the diethylbiferrocenium - SWy-1 montmorillonite clay composite¹⁵². The de-trapping in that case started around 125 K, 75 K earlier than the present case. In addition only 76 % of the diethylbiferrocenium - SWy-1 montmorillonite had de-trapped by 300 K. Unfortunately the diagrams of the spectra and a complete listing of the fitting parameters were never published. This makes comparisons somewhat subjective.

In order to cover every eventuality the lower temperature spectra (below 200K) were also fitted with charge-averaged doublets. Although a reasonable fit was obtained, the biferrocene/biferrocenium ratios were not consistent and after repeated analysis of the areas and intensities, it was concluded that the solid most likely started de-trapping around 200 K. From the limited evidence available, it seems likely that this continued until near 250 K where only the average Fe(2.5) peak was justifiable. Unfortunately this effect was not noticed until after the experiment had concluded and so a complete investigation was not possible.

It is possible that the onset of the VEDT was a direct result of the melting of the interlayer water. The onset of motion of the water molecules could produce a more symmetric environment around the biferrocene molecule. Furthermore, it is conceivable that there may be some sort of vibronic coupling between the water molecules and the biferrocene, possibly through the amine functionality. It should be noted however that due to the nature of the spectra, it is possible that a combination of the models described above may be in effect. The clay peak obscures all sharp features, and the fitted areas are very small. The amount of scatter present in the background count makes any definite

conclusions difficult to justify. It is also possible that within the sample, there were a range of environments, some of which de-trapped at low temperatures, for instance around 100 K and some of which de-trapped at higher temperatures, say around 250 K. Fitting as any one distinct model may therefore be erroneous.

To conclude, the materials studied consisted of an outer doublet due to the biferrocene. Within this was a broad doublet caused by Fe(III) in the clay and two to three further doublets attributed to the oxidation of biferrocene to biferrocenium, and the subsequent de-trapping of the biferrocenium was observed to occur between 200 and 250 K. Considering the nature of these materials and previous work by Hendrickson *et al.* on diethylbiferrocenium - SWy-1 montmorillonite¹⁵², it is thought that the “domain” de-trapping model was most probable, despite the fact that the “fusion” type de-trapping scenario provided a fit with greater internal integrity. Analysis of the biferrocene / biferrocenium ratios indicated that 2 % of AA had oxidised to AA⁺ during the 3 hour contact with HWL in suspension. 11 % of AA had oxidised after 48 hours contact with the clay in suspension. Contact of AA-HWL with iodine solution for 3 hours resulted in a 16 % conversion of AA to AA⁺.

The organometallic intercalate was finally found to have a Debye temperature (θ_D) of 150 ± 5 K. This is 20 K less than that observed for the biferrocene. This indicates that the molecule resides in a less rigid environment when intercalated into Westone-L. This mimics the behaviour of the half-sandwich iron tricarbonyl compounds studied by Breen *et al.*¹⁸² which typically saw a reduction of 20-30 K in the Debye Temperature upon intercalation. The quadrupole splittings and isomer shifts indicate that significant

distortion of the cyclopentadienyl rings has not occurred. Previous work by Brooks *et al.*¹⁸⁹ on polyvinylferrocenes has shown that a 9° tilt in the cyclopentadienyl rings results in a reduction of the isomer shift by 0.02 mm/s and the quadrupole splitting by 1.11 mm/s¹⁸⁹.

As can be seen from Table 3.2 to Table 3.6 no such reduction in either quadrupole splitting or isomer shift occurs. A slight increase in asymmetry in the spectra with temperature is discernible, although whether this is a result of the regions of the material selectively de-trapping (e.g. surface exchange sites), or a Karyagin effect is difficult to determine.

3.3 Conclusions.

2, 2''-bis[(dimethylamino)methyl]biferrocene has been intercalated into the montmorillonite Westone-L. It has been shown that the cation accounts for 75% of the C.E.C. of the clay, and that the molecule most probably lies with the rings perpendicular to the silicate sheet. There was no indication of any distortion of the cyclopentadienyl rings upon intercalation. The Debye temperature (θ_D) for the intercalate was 150 ± 5 K. This is 20 K less than that observed for 2, 2''-bis[(dimethyl-amino)methyl]biferrocene ($\theta_D = 170$ K), indicating that the molecule resides in a less rigid environment when intercalated into the clay. This reflects the trend observed by Breen *et al.* when intercalating half-sandwich irontricarbonyl compounds into Westone-L¹⁸².

If the contact time of the biferrocene with the clay is extended, partial oxidation (*ca.* 11%) of the biferrocene to biferrocenium occurs. Contact of the biferrocene intercalated with iodine results in *ca.* 16 % oxidation to biferrocene. The biferrocenium intercalate exhibited valence electron de-trapping above 200 K, until by 250 K only a single charge averaged (Fe(2.5)) resonance was seen in the Mössbauer spectrum. It is possible that the de-trapping was occurring by either the "fusion" or "domain" fashion, although most likely the latter.

Thermal decomposition of 2, 2''-bis[(dimethylamino)methyl]biferrocene under nitrogen shows two major weight losses as identified by maxima in the derivative thermogram at 330 and 620°C. The intercalate also shows signs of weight loss in these regions (360°C and 650°C), but also shows an extra peak in the derivative thermogram at 480°C.

Thermal desorption mass spectroscopy indicates that two decomposition processes are in operation. The first dominates up to 430°C and involves the loss of ferrocene fragments. This is in contradiction to the work of Breen *et al.* with the half-sandwich iron tricarbonyl compounds on Westone-L¹⁸², and also of Borvornwattanont *et al.* on the ferrocene-zeolite composite³³ but is in accord with the work on A on WL and APWL (see chapters 2 and 4). The second decomposition process dominates above 490°C and involves the loss of cyclopentadienyl rings from the intercalate.

3.4 Future Work.

A number of further studies could be considered necessary to complete this work. Firstly, Raman spectroscopy could provide information where infra-red spectroscopy was of little help. For instance, the aluminosilicate bands in the Raman spectrum of the clay are very sharp and so do not interfere with other bands in that region of the spectrum. In addition a further Mössbauer study utilising data collected between 200 and 250 K is needed to obtain a clearer picture of the de-trapping process.

The use of XPS could provide more accurate information on the proportion of biferrocene that was oxidised on contact with the clay. In addition, it is possible that the use of EXAFS may provide information on the position and alignment of the biferrocene molecule within the interlayer.

An attempt to produce AA^+ and subsequent characterisation, especially by Mössbauer spectroscopy is urgently required. Moreover, an attempt to intercalate AA^+ into H-WL should also be seriously considered, although a high occupation of the exchange capacity is not likely.

The insertion of AA into a synthetic, non-iron containing clay would be worth attempting. This would remove the complication of the underlying iron phase in the Mössbauer spectra, allowing more accurate and precise fitting. This could be followed by the doping of the sample with specific amounts of water into the interlayer to see how

this affected the temperature at which valence electron de-trapping occurred. In addition, the use of different solvents to dope the biferrocene-clay composite could provide further information on the factors affecting valence electron de-trapping phenomena.

Cun²⁰⁰ has reported the synthesis of biferrocene Schiff base complexes with varying lengths of polyunsaturated bridges. By oxidising and then intercalating these compounds into clays, the electron transfer between the two iron centres can be fully investigated. This would provide information on the interactions between the bimetallic species and the supporting lattice, which in turn may prove useful in the future design of two dimensional conducting materials. For instance, if successful, it is possible that these studies could lead to a two dimensional super-conducting material.

²⁰⁰ L. Cun, P. Xin, and Y. Zeng, *Synth. React. Inorg. Met.-Org. Chem.*, **1990**, *20(9)*, 1231-1239.

4. The Synthesis and Heat treatments of A-APWL.

There has been a considerable amount of work lately attempting to disperse catalysts on a solid support. This has numerous advantages from ease of separation of products to the ability to work at elevated temperatures¹¹⁵. Some of the most important industrial catalysts require iron particles dispersed on a porous solid matrix. The most successful attempts to produce such materials have involved the exchange of zeolites with organoiron compounds, followed by calcination in order to remove the organic part and leave finely divided iron particles behind⁸⁸.

Pillared clays have a thermal stability comparable to zeolites, and in addition can be easily manufactured with larger cavity sizes making them preferable hosts. During the production of a pillared clay, protons are released into the aluminosilicate sheet. Following the success of the exchange of an acid montmorillonite with A (see section 2), it was thought that the same technique could provide an organoiron containing pillared clay. The protons would hopefully be drawn out from the aluminosilicate sheet and anchor the organoiron compound within the cavities. As the organoiron compound is of comparable size to the cavity, only one molecule could reside in each cavity. This could ensure that the iron was finely dispersed throughout the solid on calcination. The high porosity of the material should prevent reduction of the iron to the zero oxidation state, making it ideal for the reduction of hydrogen sulfide from reducing gas mixtures²⁰¹. As the final iron concentration was likely to be very dilute, the use of Mössbauer spectroscopy would be vital in characterisation of the finished products.

²⁰¹ J. W. Geus, *Applied Catal.*, 1986, 25, 313-333.

4.1 Experimental.

4.1.1 Materials.

Clay. The clay used in all the experiments was the montmorillonite **Westone-L** from Texas, supplied by ECC International, which was found to have a cation exchange capacity (CEC) of 91meq/100g. **N,N-dimethylaminomethylferrocene** and **AlCl₃.6H₂O** were supplied by Aldrich Chemicals. **NaOH** was supplied by BDH Chemicals.

4.1.2 Sample Preparation.

4.1.2.1 Sodium Exchanged Westone-L.

This was produced by a three step process. First the raw Westone-L was sedimented to remove heavy particles such as quartz and iron oxide. Secondly, the lighter clay fraction (nominally < 2 μm particle size¹⁸³) was contacted (three times) with aqueous 1M NaCl, and finally washed, by repeated suspension in deionised water followed by centrifugation and removal of supernatant, until a residual conductivity of less than 50 μS was achieved. This is hereafter referred to as Na-WL.

4.1.2.2 Pillaring of Westone-L.

This was achieved using a method described by Schoonheydt et al.²⁰². Na-WL was suspended in 100 ml of water and left to stir for 6 hours. An aqueous solution of NaOH (17 ml, 0.4 M) was added drop-wise at 1 ml / minute to an aqueous solution of $\text{AlCl}_3 \cdot 6\text{H}_2\text{O}$ (17 ml, 0.2 M, 10 CEC) with vigorous stirring. The resulting solution was refluxed for 3 hours and then added drop-wise (8 ml / minute) to the Na-WL suspension. This was left to stir for 12 hours, and then washed with de-ionised water until the conductivity of the supernatant fell below 30 μS . The clay was then calcined at 500°C for 1 hour. This yields aluminium pillared Westone-L (abbreviated to APWL) with an interlayer spacing of 1.8-1.9 nm.

4.1.2.3 Insertion of N,N-Dimethylaminomethylferrocene into APWL.

N,N-dimethylaminomethylferrocene (1 g, 2 CEC, 4.12 mmol) was dissolved in 50 ml of methanol and 1 g of the pillared clay (dried at 120°C) added. The suspension was left to stir overnight, washed (5 x 120 ml methanol), and collected in the normal manner. The product is hereafter referred to as A-APWL. C, H, N analysis: Theory; (based on 100% exchange in the original Westone-L. The pillared clay will have a much reduced CEC which unfortunately is not known). C = 14.2. Found C = 4.2, (equivalent to 29% exchange). XRF found 1.95 % iron, equivalent to 22 % exchange.

²⁰² R. Schoonheydt, J. Van Den Eynde, and W. Stone, *Clay and Clay Minerals*, 1993, 41(5), 598-607.

4.1.2.4 Heat Treatment of A-APWL in Air.

80 mg of A-APWL powder was ground, then pressed to give a disc of diameter 1.5 cm and 0.25 cm thickness. This gives an approximate Mössbauer thickness of 0.2. The sample was placed in a closed furnace at the appropriate temperature for a 1 hour period, cooled and a Mössbauer spectrum recorded at 80K. The sample was then returned to the furnace for treatment at the next temperature. Spectra were recorded after treatment of the sample at 20, 100, 200, 300, 400, 500, and 600°C.

4.1.2.5 Heat Treatment of A-APWL in Nitrogen.

A disc of A-APWL (prepared as above) was placed in a flow of dry, oxygen free, nitrogen gas, at a flow rate of ~50 ml / min for 20 minutes. The sample was then moved into the body of a tube furnace and the nitrogen flow rate reduced to ca. 5 ml / min. The sample was left for 1 hour at the required temperature, before being removed from the body of the furnace, and left to cool under nitrogen at the end of the tube. A Mössbauer spectrum was then recorded at 80 K. The sample was then returned to the furnace, as before, for the next heat treatment. Spectra (80 K) were collected after the sample had been heated to 20, 100, 200, 300, 400, 500, and 600°C.

4.1.2.6 Heat Treatment of A-APWL in Hydrogen.

A disc of A-APWL was prepared as above. This was then cut to give a square (1 cm²), to allow the sample to fit into the apparatus used for the hydrogen treatment. The hydrogen was purified by passage through a Pd membrane held at 400°C. The sample was placed in a flow of dry, oxygen free, nitrogen gas (ca. 5 ml / min) within the glass sample chamber for 15 minutes. The gas was then switched to hydrogen and maintained at a flow rate of 5 ml / min for a further 45 minutes. The sample was heated to the required temperature by means of a coil wrapped around the sample chamber, and left for one hour. (The time required to reach 600°C and stabilise was approximately 10 minutes, although considerably less time was required at the lower treatment temperatures. Cooling was more rapid, typically 5 minutes). The sample was cooled under hydrogen to room temperature. Nitrogen was then blown over the sample during its removal and transfer to a dewar of liquid nitrogen. Mössbauer spectra (80 K) were recorded after treatment of the sample at 20, 150, 350, and 600°C.

4.1.2.7 Heat treatment of Na-WL and APWL.

A sample of Na-WL and APWL was placed in a furnace at 600°C in air in order to determine if any structural changes occurred. An 80 K Mössbauer spectrum was recorded of the original sample and also of the heat treated sample in order to determine any differences in the structural iron of the clay.

4.2 Results and Discussion.

4.2.1 XRF and CHN Analysis.

The molecule N,N-dimethylaminomethylferrocene was incorporated into APWL at a level equivalent to 29% of the CEC of the original clay, as determined by C, H, N analysis. XRF analysis only gave an exchange of 22%. This lower value from XRF analysis has been observed before (see section 2.2.2), in the exchange of A into Westone-L. In that case the lower reading from the XRF experiment was caused by the loss of iron-containing fragments during the manufacture of the bead for analysis (see section 1.6.3). The low loading of the A-APWL compared to the AH-WL (see section 2.2.2) was a combination of two factors. Firstly, when the pillared clay is calcined, the CEC is not completely regenerated²⁰². Secondly, it is possible that the outer exchange sites became filled first. The inserted molecule may then become anchored, preventing the diffusion of further molecules into the structure.

4.2.2 Infra-Red Spectroscopy.

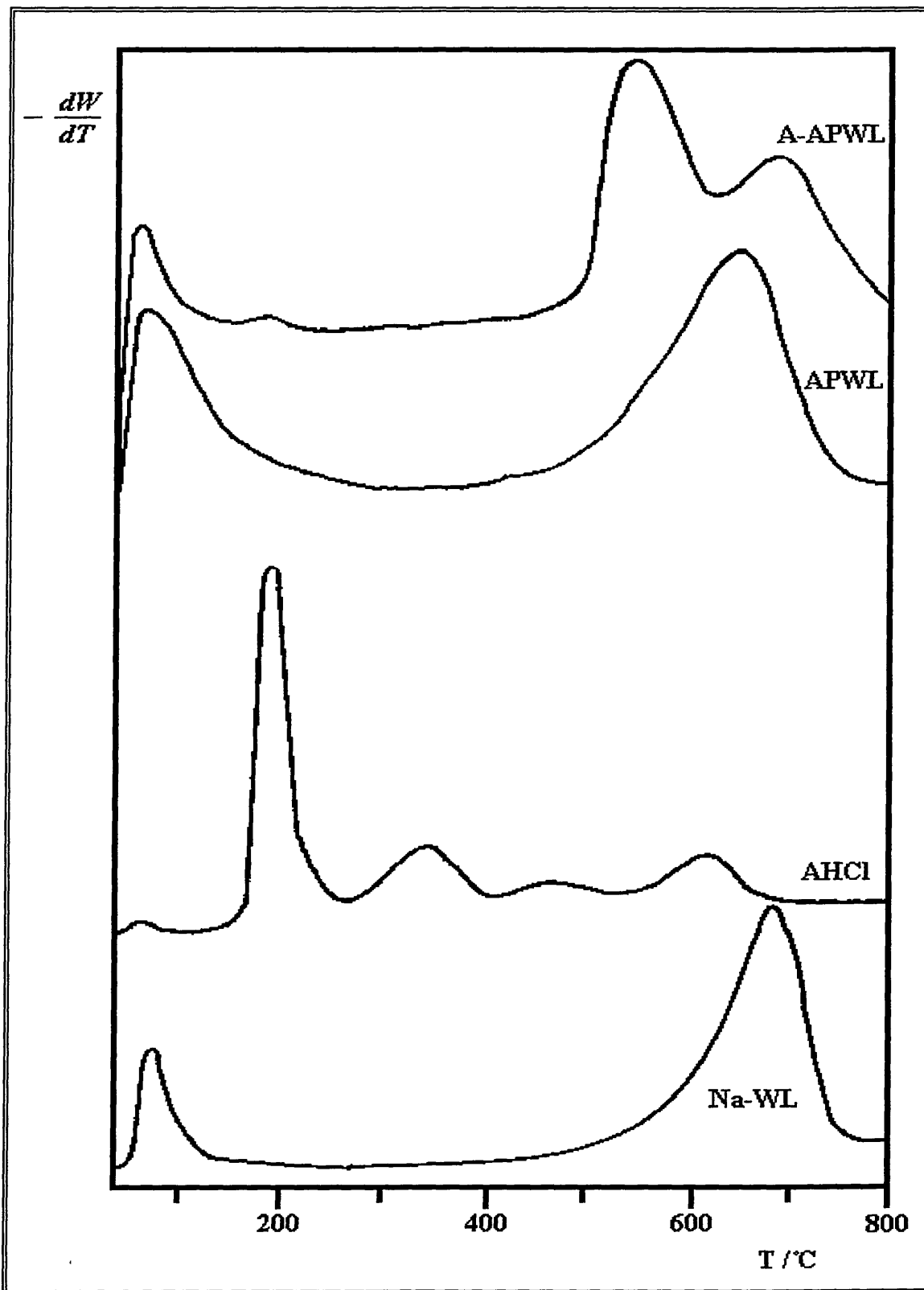
The infra-red spectrum of A-APWL showed a weak absorption at 1472 cm⁻¹ characteristic of a cyclopentadienyl ring. In addition the lattice OH stretch at 3620 cm⁻¹ present in APWL has moved to 3647 cm⁻¹. This shift to a higher frequency indicates a stronger bond. This is most likely due to the inserted molecule causing a more hydrophobic environment around the lattice OH. Further bands however, were obscured by absorptions from internal physisorbed water within the pillared lattice, and also by the aluminosilicate bands from the clay.

4.2.3 Thermogravimetric Analysis.

Thermogravimetric analysis showed a large weight loss accounting for 43% of the total weight lost (*ca.* 8% of the initial mass) at 550°C, in addition to the usual bands at 60 and 660°C expected from a pillared clay (see Figure 4.1).

The 60°C peak arises from the loss of solvent (methanol) from the exchange procedure, and also from physisorbed water within the pillared lattice. The 660°C peak is due to dehydroxylation of the silicate lattice¹⁸⁴. The origin of the peak at 550°C is difficult to establish without the use of mass spectroscopy, but could indicate an enhanced stability of *ca.* 300°C for the major weight loss, compared to that seen for the (ferrocenylmethyl)dimethylammonium-WL (see section 2.2.4). This suggests that the molecule decomposes by a different mechanism when supported on the pillared clay compared to when intercalated in the non-pillared clay (see section 2.2.4). However, it is more likely that the weight loss is caused by the oxidation of coke from the decomposition of the organic part of the molecule to CO₂. This has been observed with alkyltrimethylammonium exchanged smectites at 660°C.

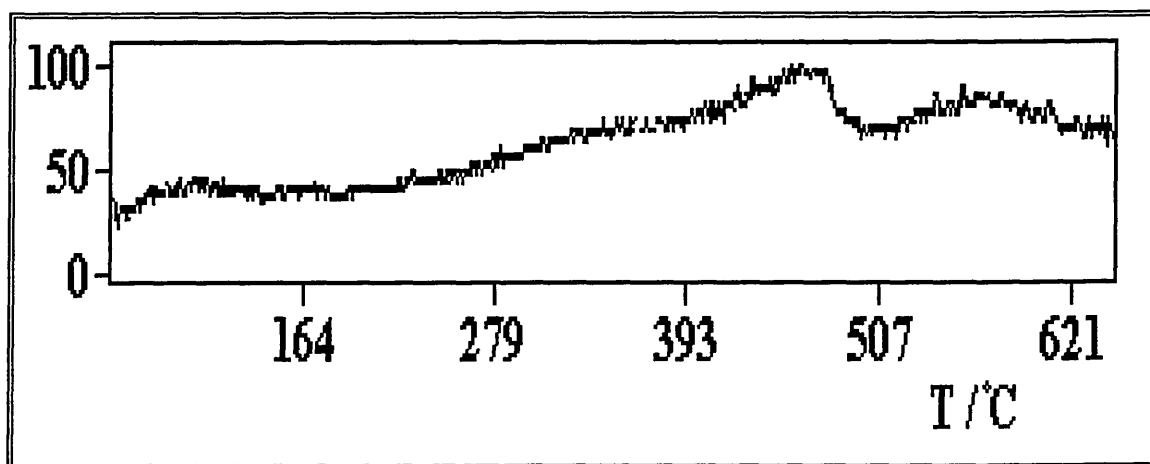
Figure 4.1 Derivative Thermograms for Na-WL, AHCl, APWL and A-APWL.



4.2.4 Thermal Desorption Mass Spectroscopy.

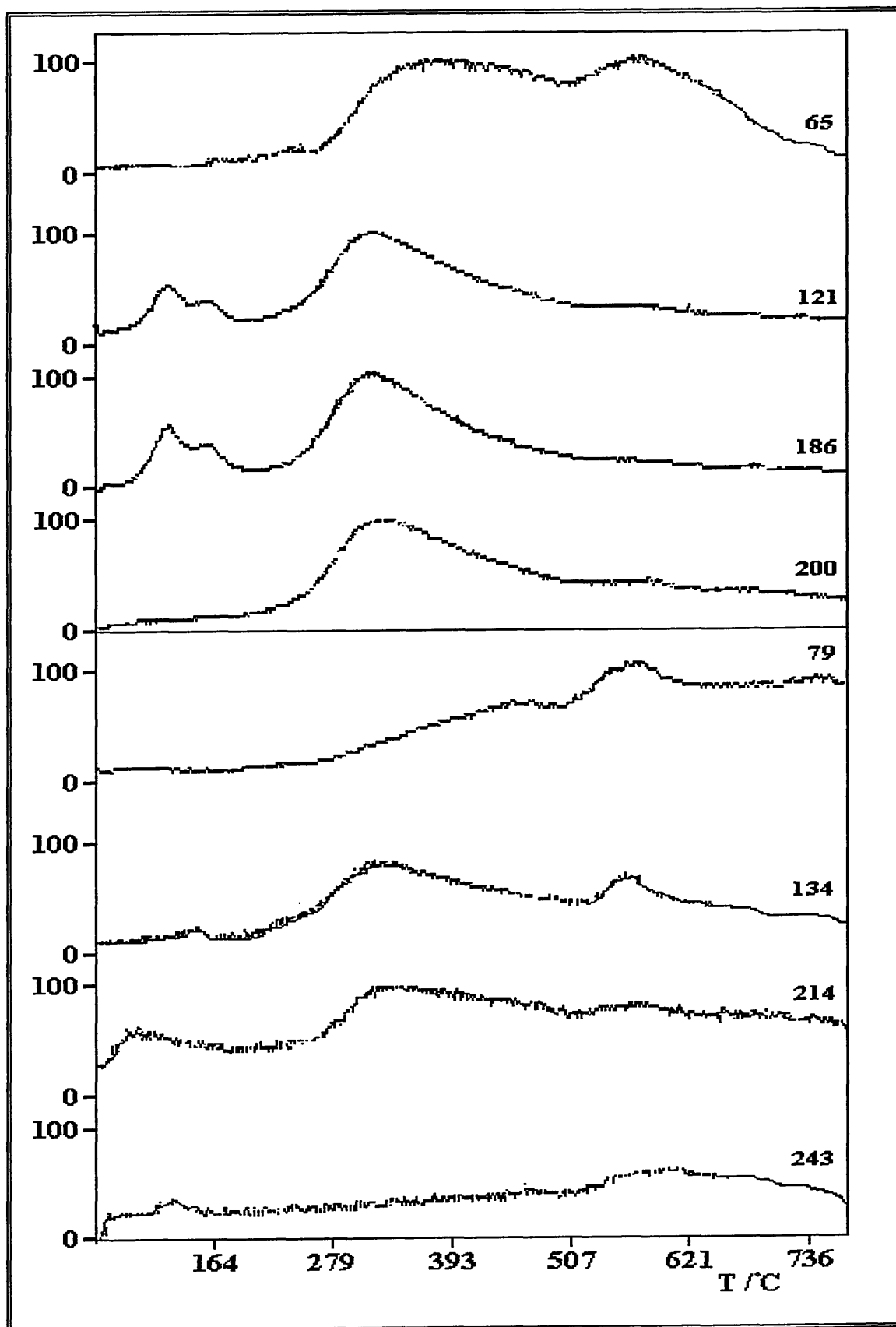
The decomposition of A-APWL is characterised by three main phases. Around 120°C there was a small peak in the TIC, concurrent with the loss of ferrocene and its daughter fragments. It is likely that this is lost from edge sites since there was only a very small amount and it was desorbed over a short temperature interval. Interestingly, no side chain fragments were observed at this stage.

Figure 4.2 TIC for A-APWL.



At 280°C the major peak in the TIC began, with fragments of $m/z = 200, 186, 121,$ and 134 being lost. ($m/z 243 = \text{CpFeCpCH}_2\text{NMe}_2$ (Cp = cyclopentadienyl, Me = methyl), $214 = \text{CpFeCpCH}_2\text{NH}$, $200 = \text{CpFeCpCH}_3$, $186 = \text{CpFeCp}$, $134 = \text{FeCpCH}_2$, $121 = \text{FeCp}$, $79 = \text{CpCH}_3$, Cp = 65). The loss of ferrocene maximised at 310°C, although the TIC was still rising at this stage, until by 500°C the loss of ferrocene had finished. It is likely that most of this ferrocene was from edge sites. As has been mentioned before (see 2.2.5) these sites exhibit a high Lewis acidity which is conducive to the formation of a ferrocene and dimethylammonium radical.

Figure 4.3 TD-MS Spectra of A-APWL.



A simple electron transfer and proton abstraction from the abundant water nearby would then lead to a ferrocene ion and dimethylammonium cation. This behaviour is in contradiction to that observed by both Breen *et al.*¹⁸² on the iron tricarbonyl compounds supported on Montmorillonite, and also by Borvornwattanont *et al.*³³ with the ferrocenium- zeolite-Y composite.

By 470°C the TIC maximised, and then began to drop. The major portion of the TIC in this region was due to ring fragments, although some iron-containing fragments were still being de-sorbed. As with the AH-WL and AA-HWL samples there was no evidence of the loss of any amine-containing fragments. This indicates a strong interaction between the amine group and the pillared clay lattice. By 500°C no fragments containing iron were visible, and only ring fragments were de-sorbed.

At 550°C, there was a small increase in the ion current as amine and ring fragments were lost, but there were still no fragments containing iron. This suggests that a different decomposition mechanism may come into operation above 550°C.

4.2.5 X-Ray Diffraction.

The pillared clay has alumina pillars propping the layers apart. Therefore the interlayer spacing of the pillared clay is constant regardless of the inserted molecule. In addition the spacing is not dependant on temperature. This is reflected in the XRD trace obtained of the pillared clay, which provided little information except that the APWL exhibited a

constant spacing of 1.85 nm. No extra peaks due to the inserted cation were seen, indicating that A was not in a powder form mixed with the APWL.

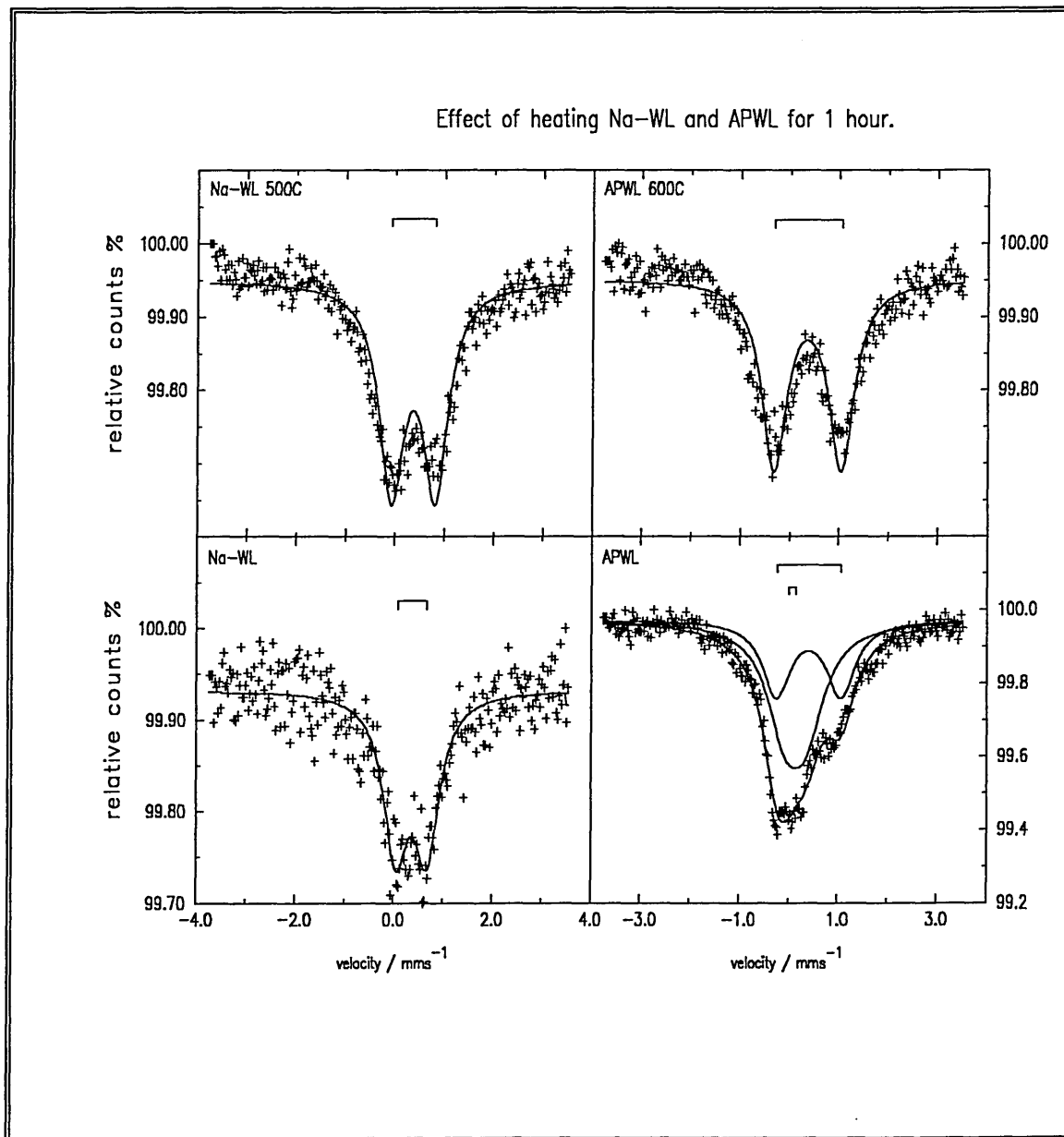
4.2.6 Mössbauer Spectroscopy.

4.2.6.1 APWL

The clay Westone-L exhibits a Mössbauer spectrum which contains a single broad doublet ($\delta = 0.36 \pm 0.02$ mm/s, $\Delta = 0.32 \pm 0.02$ mm/s). This is caused by high spin, octahedrally co-ordinated iron(III) in the clay structure. The broadness is caused by iron nuclei in number of very similar but not identical sites. Heating in air for 1 hour at 500°C had little effect on these parameters. After contact with the pillaring solution, drying in air, and subsequent firing at 500°C for 1 hour, an even broader, unsymmetrical resonance was observed. Various interpretations of the data were considered, but after much deliberation, was finally fitted as two nested overlapping doublets, with fitting parameters Q(outer), $\delta = 0.28$ mm/s, $\Delta = 1.28$ mm/s, and Q(inner), $\delta = 0.18$ mm/s, $\Delta = 0.56$ mm/s. It has been shown that the aluminium tetrahedra invert at the point at which the pillar meets the clay sheet²⁰³. This inversion will leave a defect in the clay sheet and the proximity of this defect to the iron centre will influence the amount to which the Mössbauer spectrum is affected.

²⁰³ D. Plee, F. Borg, L. Gatineau, and J. J. Fripiat, *J. Am. Chem. Soc.*, **1985**, *107*, 2362-2369.

Figure 4.4 Spectra of WL, WL(500), APWL, APWL(600).

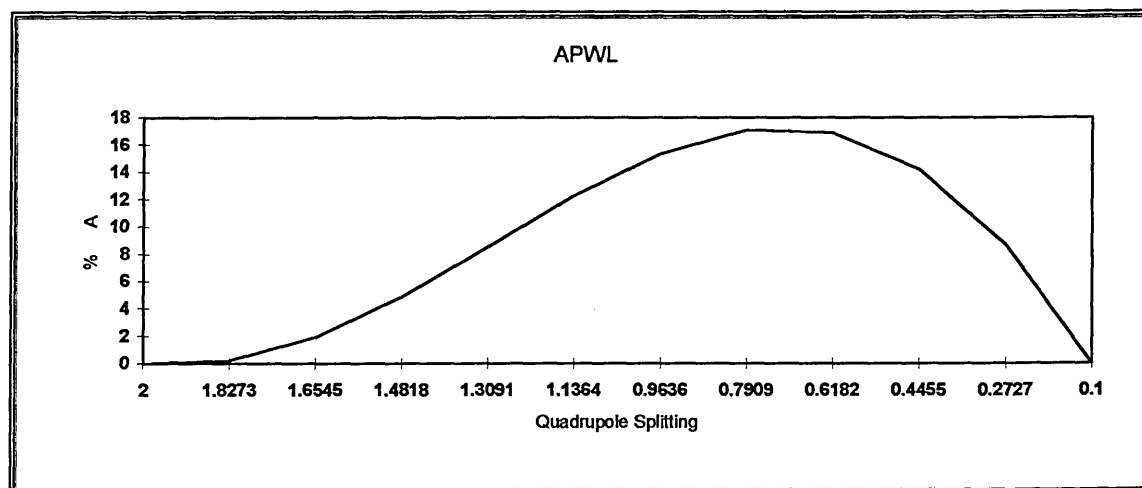


If the defect was two or three atoms away, it is unlikely that any change would be observed in the spectrum. However, if the inversion was next to the iron centre, a considerable change in the Mössbauer spectrum would be expected²⁰⁴.

²⁰⁴ M. F. de Jesus-Filho, M. A. Gonçalves, J. C. Bosch-Neto, and V. K. Garg, *Hyperfine Interactions*, 1992, 70, 961-964.

In an attempt to clarify the origin of the broad asymmetric resonance seen, a poly-quadrupole fitting routine was utilised. In this, a range of quadrupole splittings are used to fit the spectrum. The relative areas of the phases represent the probability of the iron residing in that environment.

Figure 4.5 PQH plot of % Area vs. QS for APWL.



The plot of % Area vs. QS (Figure 4.5), shows that only one “distinct” iron site was found. However, the broadness of the plot indicates a wide range of similar sites. This reflects the diverse array of iron sites produced by the varying proximity of the defect to the iron centres. The two doublets quoted in the fit therefore represent the extremes of a wide range of similar sites. Further heating of APWL to 500°C for 1 hour in air, led to the regeneration of a single doublet. The fitting parameters were however, different to those observed for the original clay ($\delta=0.36 \pm 0.02$ mm/s , $\Delta = 1.37 \pm 0.02$ mm/s). The larger quadrupole splitting indicated that the system had reorganised to give a more symmetric environment around the iron centres than was present in the original clay. The smaller half-width shows that the distribution of iron centres was now more uniform. As far as the author is aware, this is the first time that this behaviour has been observed. It

would be interesting to see MASNMR of the samples to see if the defects exist. Work by Roch *et al.*²⁰⁵ using MASNMR on montmorillonite, has shown that above 550°C there is an increase in the amount of tetrahedral and pentahedral aluminium sites. Other work (Schoonheydt *et al.*²⁰²) has shown that during the pillaring process, protons are released into the aluminosilicate layer. Under these conditions it is not unreasonable to assume that some measure of dehydroxylation may well be occurring, possibly within the aluminosilicate layer itself, leaving a more uniform crystalline aluminosilicate sheet behind. This would account for the lower than expected number of protons in the pillared clay observed by Schoonheydt *et al.*²⁰².

²⁰⁵ G. Roch, M. E. Smith, and S. Drachman, *Abstract from Mineralogical Society spring 1996 Meeting, 1996*, "Investigation of thermal transformations of clay minerals by ²⁷Al and ²⁹Si solid-state nuclear magnetic resonance".

4.2.6.2 A-APWL

The Mössbauer spectrum contained two doublets as observed with (ferrocenylmethyl)-dimethylammonium-WL. It consisted of a large outer doublet characteristic of A, and a smaller broad resonance distinctive of the APWL.

Table 4.1 showing least squares fitting parameters for A-APWL.

T K	Phase	δ mm/s	Δ mm/s	Γ_l mm/s	Γ_r mm/s	Norm. Area	% Area	χ^2
14	Fe ³⁺	0.18	0.56	0.60	0.60	0.130	16.01	0.7
14	Fe ³⁺	0.28	1.28	0.60	0.60	0.058	7.10	0.7
14	Fe ²⁺	0.43	2.43	0.37	0.37	0.624	76.89	0.7
25	Fe ³⁺	0.17	0.56	0.60	0.60	0.124	15.92	0.7
25	Fe ³⁺	0.28	1.28	0.60	0.60	0.076	9.67	0.7
25	Fe ²⁺	0.43	2.43	0.37	0.37	0.581	74.41	0.7
50	Fe ³⁺	0.17	0.56	0.62	0.62	0.142	21.19	0.6
50	Fe ³⁺	0.28	1.28	0.60	0.60	0.081	12.10	0.6
50	Fe ²⁺	0.43	2.43	0.32	0.34	0.448	66.71	0.6
80	Fe ³⁺	0.16	0.36	0.64	0.64	0.117	22.53	0.7
80	Fe ³⁺	0.28	1.28	0.64	0.64	0.085	16.31	0.7
80	Fe ²⁺	0.42	2.42	0.40	0.40	0.318	61.17	0.7
100	Fe ³⁺	0.17	0.56	0.60	0.60	0.123	23.76	0.6
100	Fe ³⁺	0.29	1.28	0.62	0.62	0.103	19.89	0.6
100	Fe ²⁺	0.41	2.44	0.39	0.39	0.292	56.35	0.6
140	Fe ³⁺	0.16	0.56	0.64	0.64	0.122	29.77	0.5
140	Fe ³⁺	0.29	1.28	0.64	0.64	0.086	21.07	0.5
140	Fe ²⁺	0.41	2.40	0.46	0.46	0.201	49.16	0.5
180	Fe ³⁺	0.16	0.56	0.64	0.64	0.118	35.15	0.7
180	Fe ³⁺	0.28	1.28	0.62	0.62	0.086	25.53	0.7
180	Fe ²⁺	0.39	2.40	0.38	0.34	0.132	39.32	0.7
220	Fe ³⁺	0.16	0.56	0.68	0.68	0.107	39.34	0.6
220	Fe ³⁺	0.28	1.28	0.68	0.68	0.083	30.63	0.6
220	Fe ²⁺	0.42	2.42	0.40	0.40	0.082	30.03	0.6
250	Fe ³⁺	0.16	0.56	0.68	0.68	0.105	43.26	0.8
250	Fe ³⁺	0.28	1.28	0.66	0.66	0.070	29.02	0.8
250	Fe ²⁺	0.37	2.44	0.39	0.42	0.067	27.71	0.8
300	Fe ³⁺	0.16	0.38	0.68	0.68	0.111	50.73	0.6
300	Fe ³⁺	0.28	1.28	0.66	0.66	0.072	32.93	0.6
300	Fe ²⁺	0.37	2.44	0.44	0.42	0.036	16.34	0.6

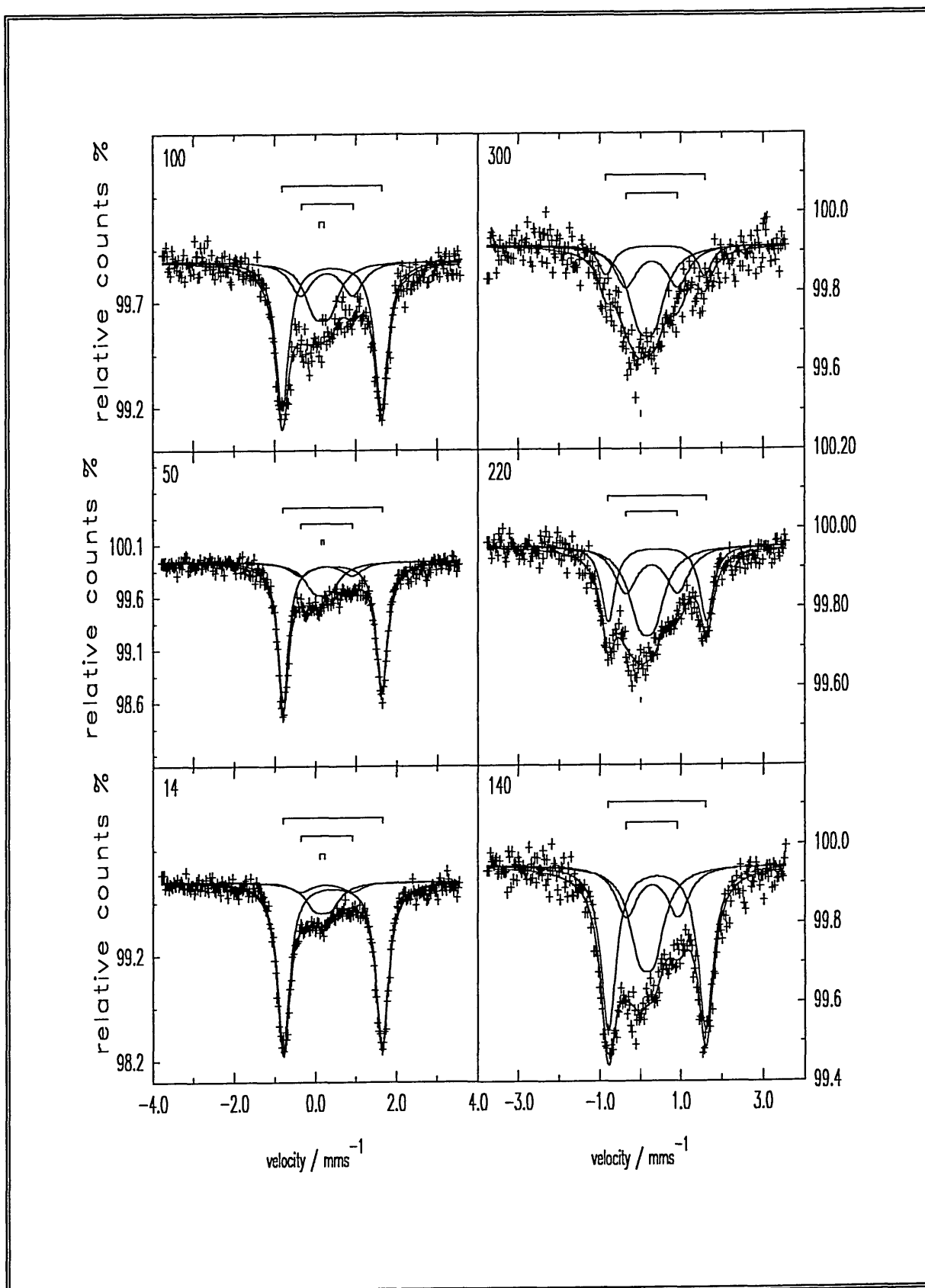
Errors: T = ± 2 K, $\delta = \pm 0.02$ mm/s, $\Delta = \pm 0.02$ mm/s, $\Gamma = \pm 0.02$ mm/s

Fe³⁺ = Iron(III) present in the clay from isomorphous substitution.

Fe²⁺ = Iron(II) present in the ferrocene unit of the inserted molecule.

As with AH⁺-WL (section 2.2.7), the insertion of A into the pillared clay made little difference to the fitting parameters (see Table 4.1), which indicated that it may again be the protonated species present.

Figure 4.6 A-APWL Spectra.



This is likely as strong bases such as A have been shown to entice the protons generated during the pillaring process from out of the aluminosilicate sheet. Variable temperature Mössbauer spectroscopy revealed that the Debye temperature of A-APWL was much lower than that observed with the AH-WL samples. A-APWL was found to have a Debye temperature (θ_D) of 113 ± 5 K (compare $\theta_D(\text{AH-WL}) = 140 \pm 5$ K), with a correspondingly lower recoil free fraction, $f_{291} = 0.05 \pm 0.02$ ($f_{291}(\text{AH-WL}) = 0.13 \pm 0.02$). This indicated that the molecule was much less tightly bound, consistent with the molecule enjoying considerable freedom in the large pores of APWL which are similar to the cages found in a zeolite.

Figure 4.7 LNAT plot for A-APWL Fe^{2+}

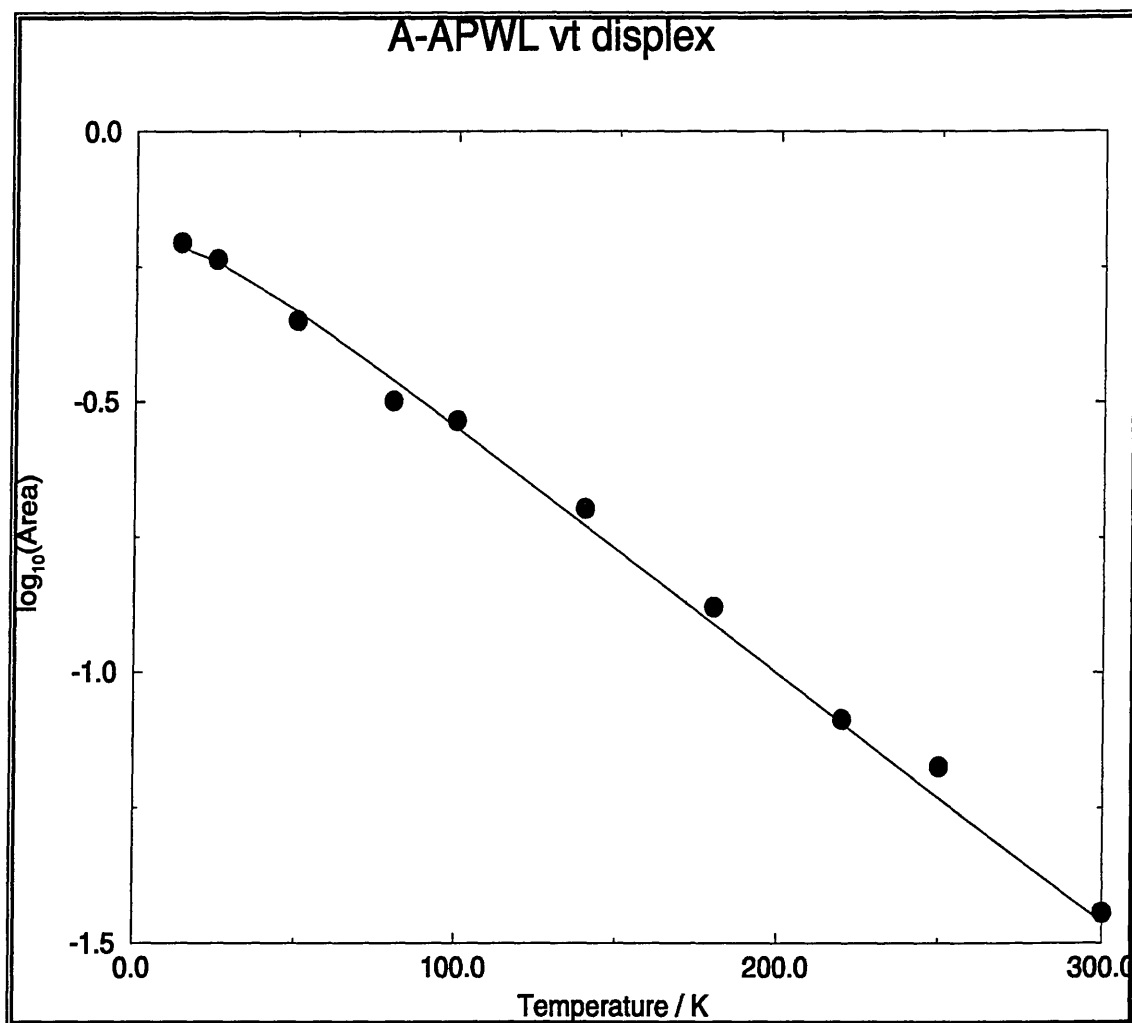
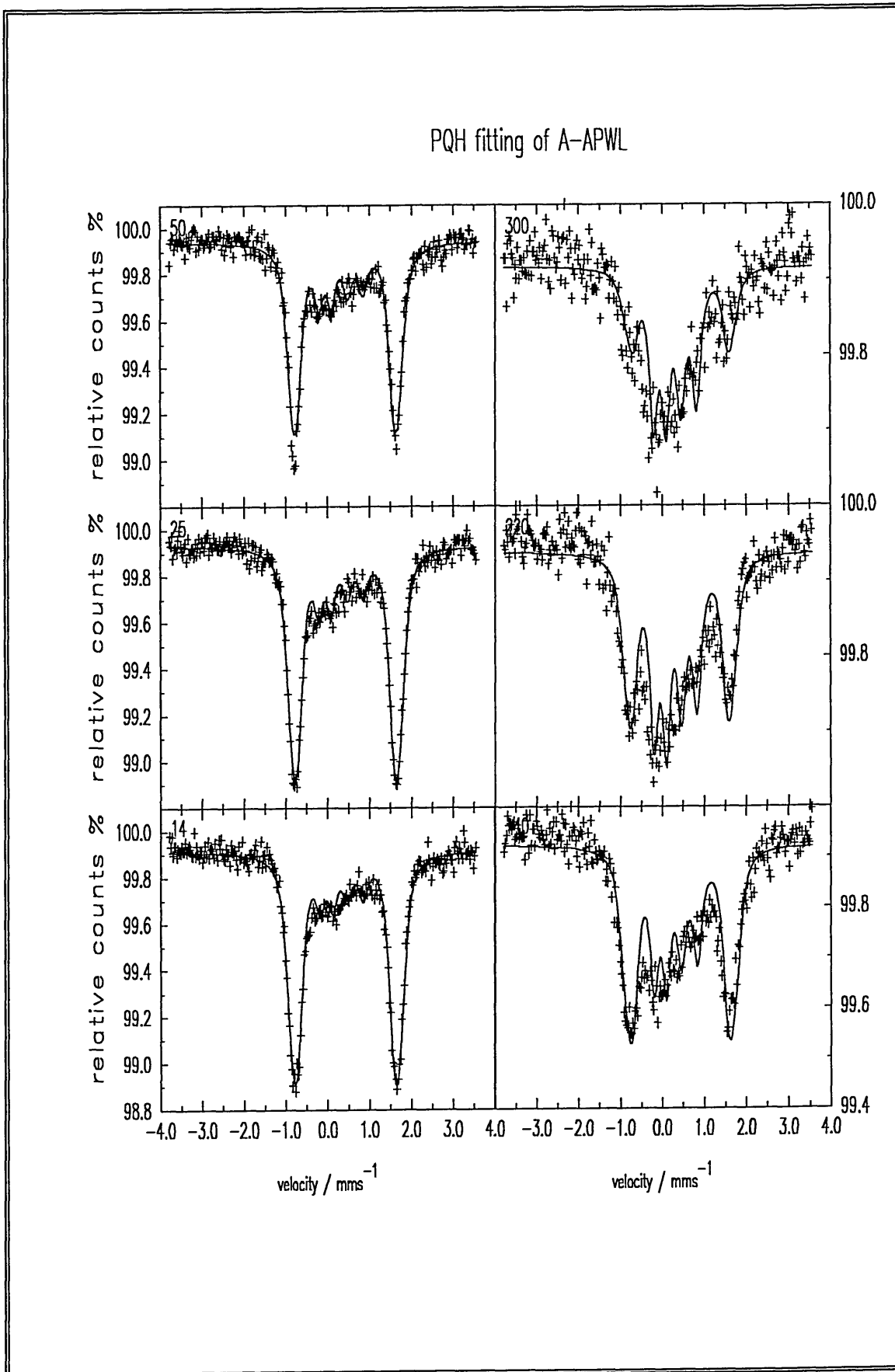
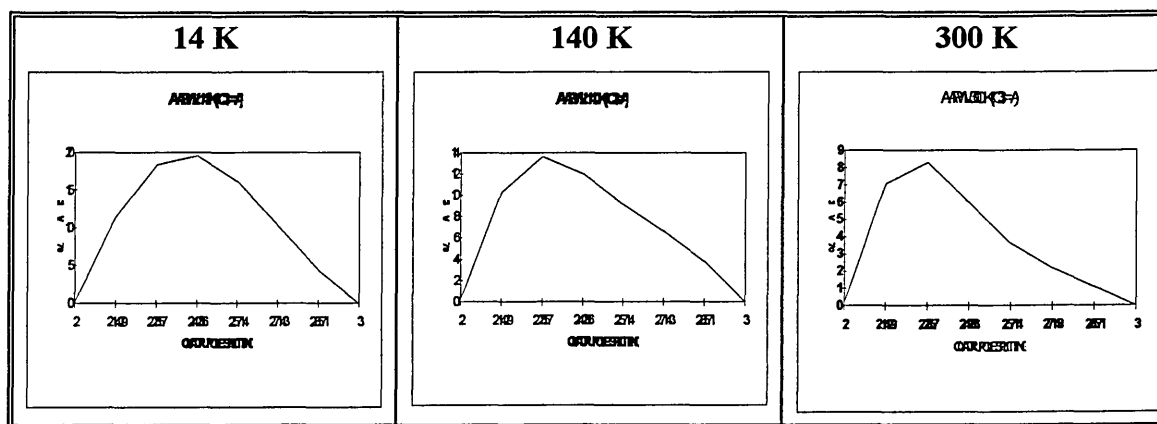


Figure 4.8 Diagram Showing PQH fitted spectra.



The line-widths for A were somewhat larger than those seen in either AHCl or AH-WL (see section 2.2.7), suggesting that the inserted molecule could reside in more than one type of site. Therefore an attempt to fit the spectra using a polyquadrupole routine was attempted. The results are shown diagrammatically in Figure 4.9 and the resultant spectra are shown in Figure 4.8. Figure 4.9 clearly shows that there was only one distinct iron(II) environment which supports the fitting routine used above.

Figure 4.9 PQH plots of % Area vs. QS for A in A-APWL.



It should be noted that whereas a zeolite consists of distinct cages linked together, a pillared clay basically has an open plan interlayer space with the supporting pillars randomly distributed throughout. The large line-widths are therefore a result of either the molecule's environment, *i.e.* the molecule is free to vibrate, or the micro-crystalline nature of the material.

4.2.6.3 Fitting of Mössbauer spectra for heated samples.

The spectra of the heat treated samples tended to be extremely broad doublets, composed of one or more overlapping phases. Precise fitting was difficult and interpretation was very challenging. In the fitting parameters quoted, the number of phases has been kept to a minimum, whilst at the same time maintaining chemical integrity. For instance, the insertion of a tetrahedral iron (iii) phase may have improved the fit, but such a phase would not likely be produced in a reducing atmosphere of hydrogen gas at 600°C. In assigning the phases guidelines were formulated using the extensive literature available for Fe-exchanged zeolites and used in assigning the phases. These are summarised in Table 4.2.

Table 4.2 Summary of Mössbauer parameters for iron in different co-ordination geometry's.

Isomer Shift	Quadrupole Splitting	Assignment
0.5 - 0.8	0.4 - 0.8	Fe (II) T _d ^{206, 207, 129, 208, 209}
0.5 - 1.4	1.7 - 3.3	Fe (II) O _h ^{206, 207, 129, 208, 210, 211, 212, 213, 214, 215}
0.1 - 0.3	0.7 - 1.8	Fe (III) T _d ^{206, 207}
0.3 - 0.7	0.5 - 1.3	Fe (III) O _h ^{206, 207, 208, 213, 214, 215, 216, 217}

²⁰⁶ A. Mulaba-Bafubiani, J. Helsen, A. Maes, and G. Langouche, *Hyperfine Interactions*, **1992**, *70*, 1049-1052.

²⁰⁷ K. Lázár, A. M. Szelezcky, G. Vorbeck, R. Fricke, A. Vondrova, and J. Cejka, *J. Radioanalytical and Nuclear Chemistry*, **1995**, *190(2)*, 407-411.

²⁰⁸ M. Petrera, A. Gennaro, P. Gherardi, G. Gubitosa, and N. Pernicone, *J. Chem. Soc., Faraday Trans. 1*, **1984**, *80*, 709-720.

²⁰⁹ W. N. Deglass, R. L. Garten, and M. Boudart, *J. Chem. Phys*, **1969**, *50*, 4603-4610.

²¹⁰ W. N. Deglass, R. L. Garten, and M. Boudart, *J. Phys. Chem.*, **1969**, *73*, 2970-2977.

²¹¹ Z. Gao and L. V. C. Rees, *Zeolites*, **1982**, *2*, 205-214.

²¹² B. L. Dickson and L. V. C. Rees, *J. Chem. Soc., Faraday Trans. 1*, **1974**, *70*, 2051.

²¹³ R. Schmidt, M. D. Amiridis, J. A. Dumesic, L. M. Zelewski, and W. S. Millman, *J. Phys. Chem.*, **1992**, *96*, 8142-8149.

²¹⁴ V. Luca and C. M. Cardile, *Clay Miner.*, **1989**, *24*, 555-560.

²¹⁵ B. A. Goodman, *Clay Miner.*, **1987**, *22*, 36-41.

²¹⁶ C. M. Cardile and I. W. M. Brown, *Clay Miner.*, **1988**, *23*, 13-18.

²¹⁷ I. Rozenson and A. Heller-Kallai, *Inorg. Chem.*, **1978**, *26*, 173-178.

Clearly several of these assignments overlap. It was therefore necessary to consider the conditions under which the material was formed. In an oxidising atmosphere, reduction was unlikely. Similarly, in a reducing atmosphere, oxidation was unlikely. Finally, the environment of the starting material was considered. In A-APWL, the complex resides in a large cavity similar to the super-cage in a zeolite. The lower symmetry tetrahedral species quoted in Table 4.2 were found in narrow channels within the zeolites, coordinated to the framework oxygen atoms. The higher symmetry complexes occurred in the super-cages where more space was available. It is probable therefore, that the decomposition products of A-APWL would tend towards octahedral symmetry, assuming that there was no migration or agglomeration of the iron.

4.2.6.3.1 Sample Heat Treated in Air.

Heating at 100°C for 1 hour in air resulted in little change in the spectrum (see Figure 4.10), although the relative area of A decreased from 81 to 73% of the total spectral area. This is in good agreement with the TD-MS results which showed that no side chain fragments were lost, but a small amount of ferrocene was volatilised at this temperature.

After heating to 200°C for 1 hour in air, the spectrum changed dramatically. The greater part of the spectral area arose from a new doublet with parameters, $\delta = 0.34 \pm 0.02$ mm/s, and $\Delta = 1.17 \pm 0.02$ mm/s. This could be assigned to either octahedral high spin iron(III), or possibly tetrahedral high spin iron(III) (see Table 4.2). Considering the initial complex A was assumed to be in a large cavity, the tetrahedral species seems unlikely.

Table 4.3 Least squares fitting parameters for air heat treated sample.

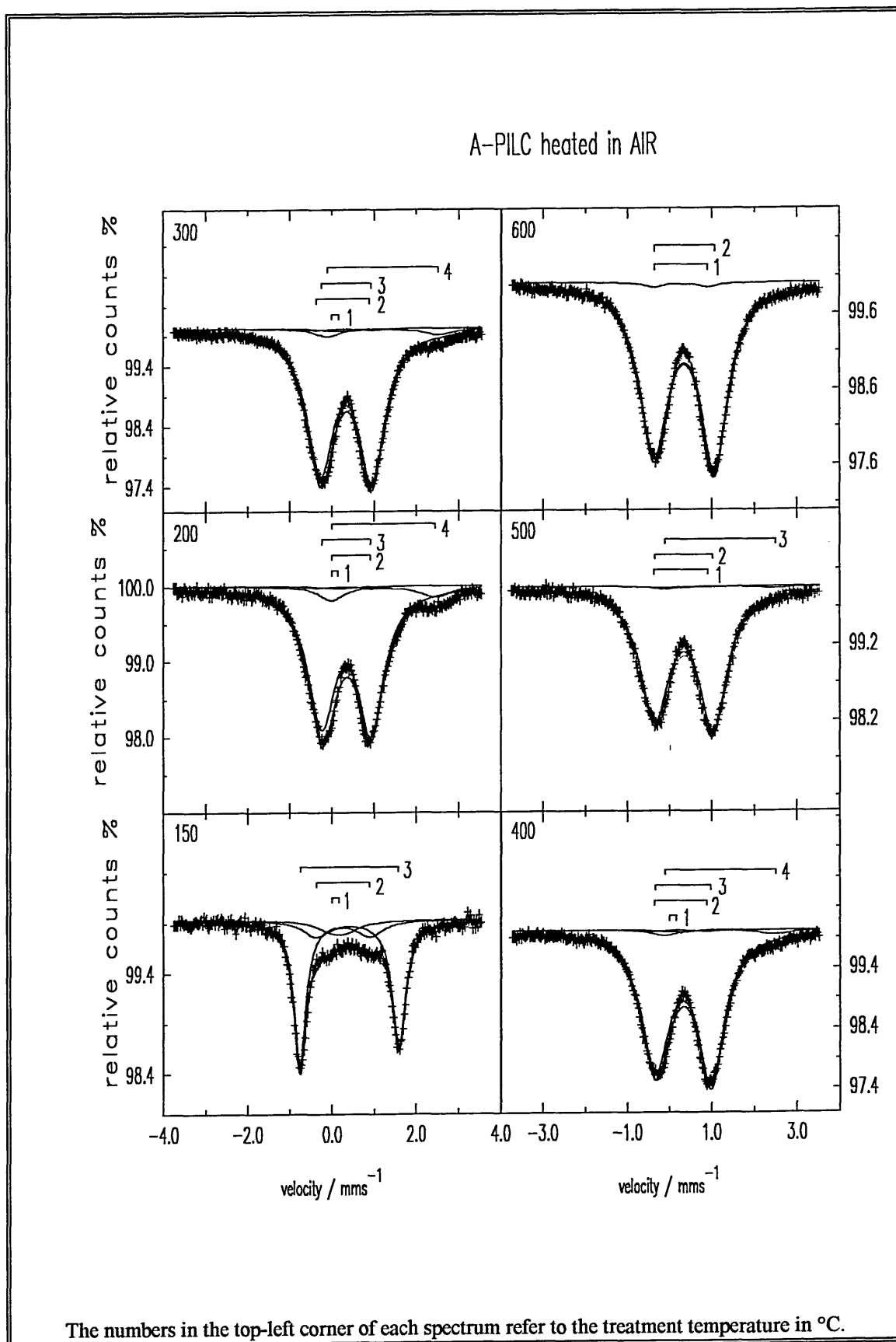
T (C)	Phase	δ (mm/s)	Δ (mm/s)	Γ_1 (mm/s)	Γ_r (mm/s)	Norm. Area	% Area	χ^2
100	APWL	0.17	0.36	0.78	0.78	0.073	10.13	0.001
100	APWL	0.26	1.28	0.73	0.73	0.122	17.05	0.001
100	A	0.41	2.34	0.35	0.39	0.522	72.82	0.001
200	APWL	0.16	0.37	0.84	0.84	0.015	00.94	0.003
200	APWL	0.27	1.28	0.69	0.69	0.015	00.94	0.003
200	Fe ^{III} O _h	0.34	1.17	0.78	0.74	1.460	89.62	0.003
200	Fe ^{II} O _h	1.21	2.45	0.70	0.88	0.138	08.49	0.003
300	APWL	0.16	0.37	0.84	0.84	0.020	00.98	0.004
300	APWL	0.27	1.28	0.69	0.69	0.020	00.98	0.004
300	Fe ^{III} O _h	0.34	1.22	0.77	0.77	1.872	93.14	0.004
300	Fe ^{II} O _h	1.20	2.63	0.70	0.88	0.099	04.90	0.004
400	APWL	0.16	0.37	0.84	0.84	0.020	01.00	0.004
400	APWL	0.27	1.28	0.69	0.69	0.020	01.00	0.004
400	Fe ^{III} O _h	0.33	1.32	0.82	0.75	1.928	94.53	0.004
400	Fe ^{II} O _h	1.19	2.61	0.70	0.88	0.071	03.48	0.004
500	APWL	0.16	0.37	0.84	0.84	0.016	01.01	0.003
500	APWL	0.27	1.28	0.69	0.69	0.016	01.01	0.003
500	Fe ^{III} O _h	0.34	1.39	0.84	0.77	1.510	95.96	0.003
500	Fe ^{II} O _h	1.19	2.61	0.70	0.44	0.032	02.02	0.003
600	APWL	0.27	1.28	0.61	0.61	0.040	02.00	0.004
600	Fe ^{III} O _h	0.35	1.43	0.83	0.76	1.941	98.00	0.004

Errors: $T = \pm 2$ K, $\delta = \pm 0.02$ mm/s, $\Delta = \pm 0.02$ mm/s, $\Gamma = \pm 0.02$ mm/s

The isomer shift does indeed seem to indicate an octahedral species, although it is possibly distorted. This has been observed for both structural iron in reduced charge montmorillonites²⁰⁶, and also in iron-exchanged zeolites²⁰⁸. In addition, a further new doublet (parameters, $\delta = 1.21 \pm 0.02$ mm/s, $\Delta = 2.45 \pm 0.02$ mm/s) appeared. This was characteristic of a high spin octahedral iron(II) species (see Table 4.2), similar to the species found in the ferrous ion-exchanged NH₄-A zeolites²¹¹.

No evidence of A can be found. This decomposition was in good agreement with that observed in the TGA and TD-MS data which indicated a significant loss of intercalated material around 200°C.

Figure 4.10 Diagram showing 80 K spectra of samples heated in air.

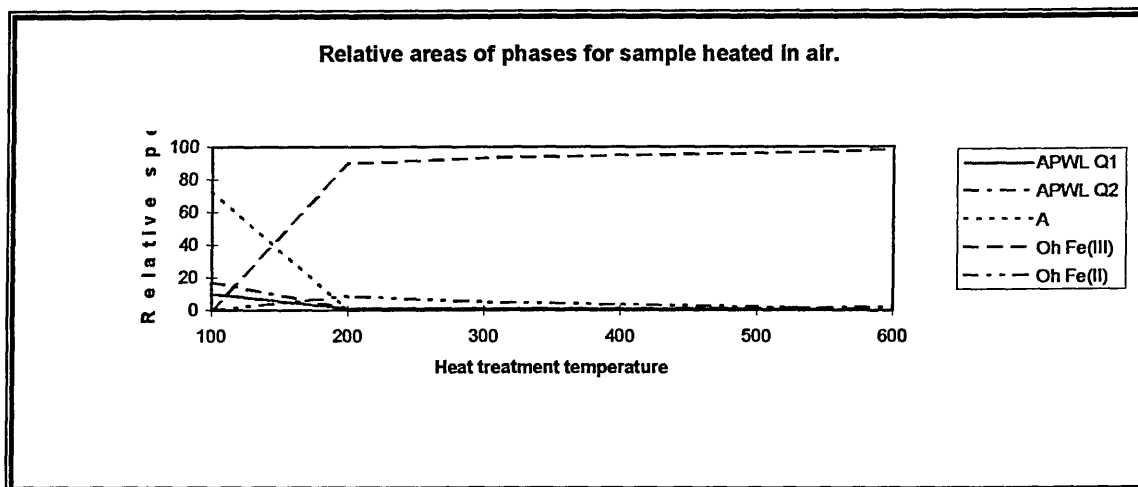


The numbers in the top-left corner of each spectrum refer to the treatment temperature in °C.

The APWL resonance slowly reverted to a single doublet (see earlier), although this was lost under the area of the new iron(III) peak. The area of the iron(II) phase was reduced at higher temperatures until by 600°C it was no longer present. This indicates the rate limiting step in the oxidation process was possibly dependent on the diffusion of oxygen into the matrix.

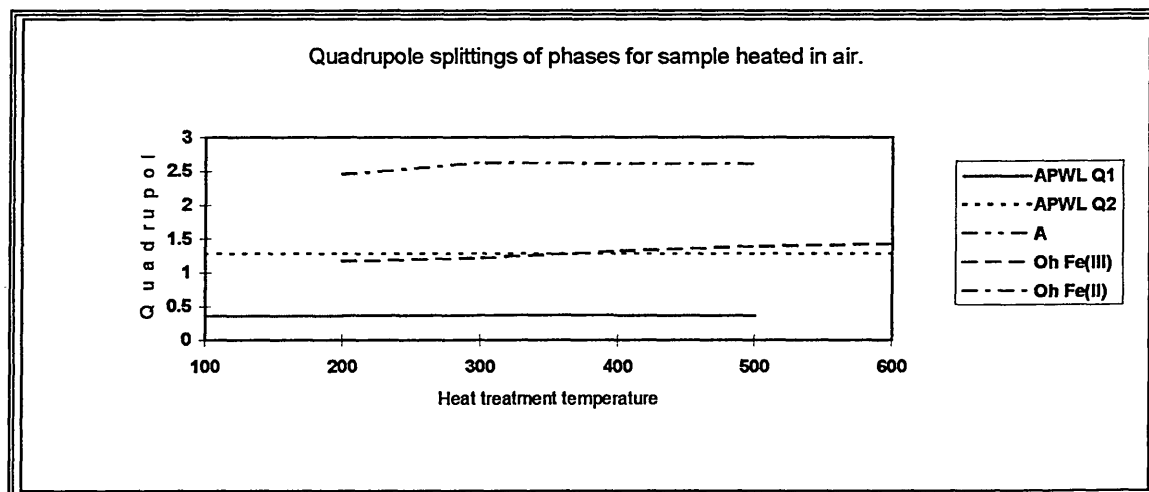
The isomer shift of the component phases remained constant within experimental error. The quadrupole splitting of the two new phases however, showed a slight increase as the treatment temperature was increased.

Figure 4.11 Relative Areas of phases for Sample Treated in Air.



According to TD-MS no nitrogen containing fragments were lost. In addition, unlike the work by Borvornwattanont *et al.*³³ using EXAFS on $(\text{COT})\text{Fe}(\text{CO})_3$ supported on the H-Y zeolite, there was at no time justification for including a half-sandwich iron species in the Mössbauer fitting routine. This suggested that both cyclopentadienyl rings split off leaving both the iron and the amine side-chain behind.

Figure 4.12 QS vs. HT for Sample Heated in Air.



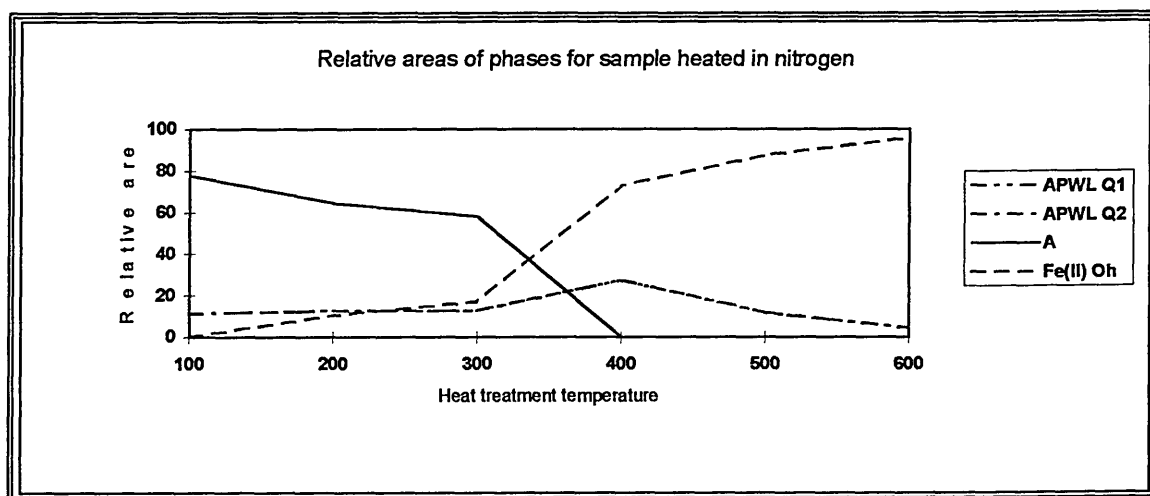
It is possible that if the iron species was co-ordinated to the oxygens of the clay sheet or alumina pillar, the residual amine species could reduce the effective charge from the lattice, causing a greater contribution from the other ligands to the electric field gradient across the iron nucleus. A similar effect has been seen by Rees *et al.* when heating the ferrous ion-exchanged NH_4 -zeolite A composite²¹¹. This is consistent with a high spin octahedral iron(III) complex co-ordinated trigonally to three lattice oxygens, and also to three $\text{H}_2\text{O} / ^-\text{OH}$.

It should be noted that Lund *et al.*⁴⁸ observed no clustering of iron atoms during the thermal decomposition of ferrocene on AlPO_5 . Instead the iron atoms were shown to reside in the double six-rings of the twelve ring channel system. This agrees favourably with the interpretation stated above.

4.2.6.3.2 Sample heat treated in nitrogen.

Treatment at 100°C in nitrogen again had little effect on the Mössbauer spectrum (Figure 4.14). The area of A was again reduced indicating the volatilisation of iron in some form, although no decomposition of the compound was evident. This was consistent with the TD-MS data which showed a loss of ferrocene at this temperature. After treatment at 200°C there was evidence of decomposition in the Mössbauer spectrum. A new doublet ($\delta = 1.11 \text{ mm/s}$, $\Delta = 2.88 \text{ mm/s}$) was observed. These parameters indicate a high spin iron(II) species in an octahedral environment (see Table 4.2). A similar species has been observed during the thermal decomposition of an iron dipyriddy complex supported on zeolites X and Y, and also with the Fe-ZSM-5 zeolite composite²⁰⁸.

Figure 4.13 Relative Areas of Phases for Sample Heated in Nitrogen.



The doublet arising from A still represents the major component in the spectrum however, which suggests a different decomposition mechanism to that observed for the samples heat-treated in air. Heating to 300°C caused the new doublet ($\delta = 1.11 \pm 0.02 \text{ mm/s}$, $\Delta = 2.88 \pm 0.02 \text{ mm/s}$) to grow at the expense of that for A. By 400°C there was

no spectral evidence for the original organometallic species, A. The pillared clay doublet was now transformed (see section 4.2.6.1), and was present as a single doublet ($\delta = 0.38$ mm/s, $\Delta = 1.36$ mm/s). Further heating caused the high spin octahedral iron(II) to grow in intensity at the expense of the other components.

Table 4.4 Least squares fitting parameters for sample heated in nitrogen.

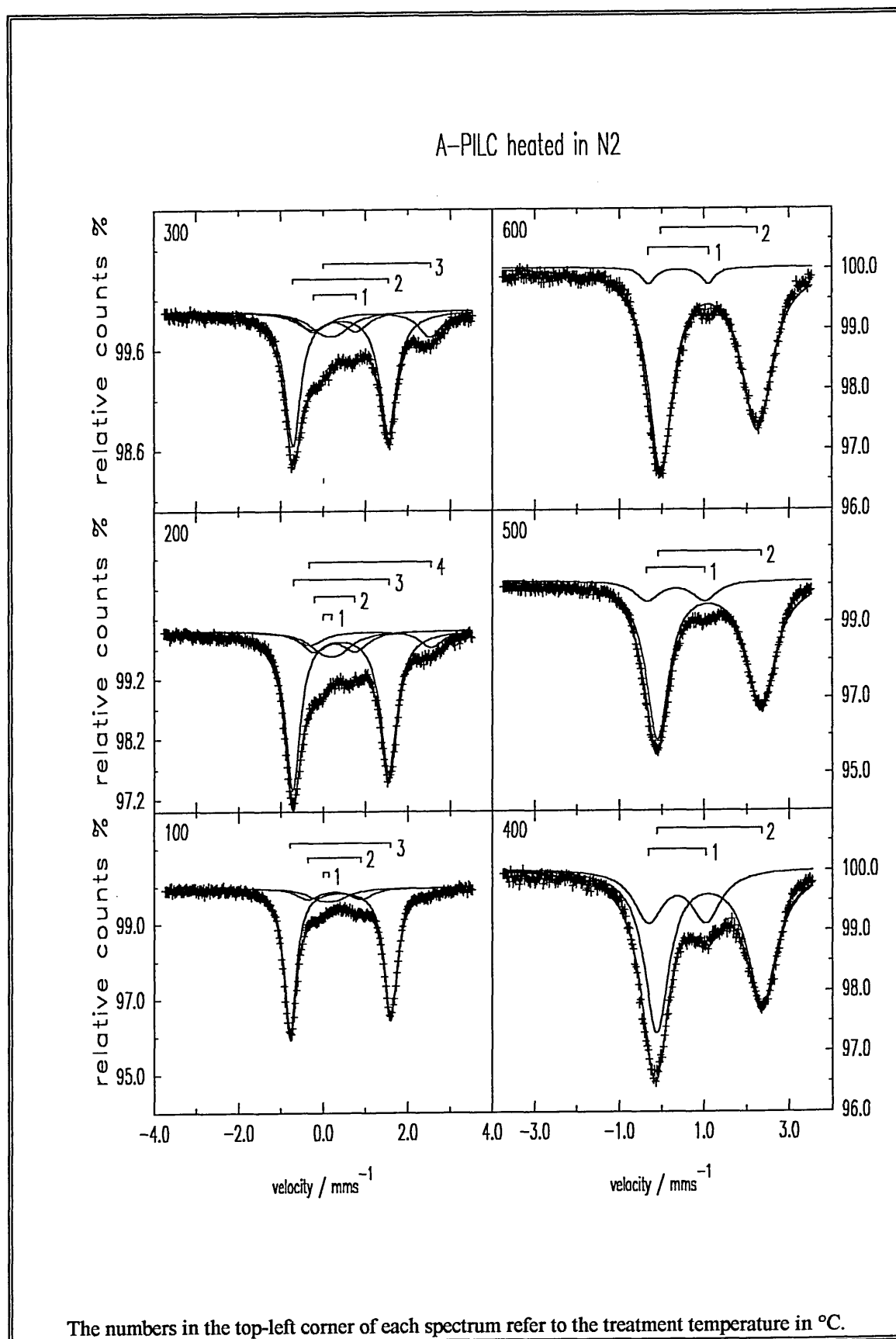
T (C)	Phase	δ (mm/s)	Δ (mm/s)	Γ_1 (mm/s)	Γ_r (mm/s)	Norm. Area	% Area	χ^2
100	APWL	0.13	0.35	0.86	0.86	0.20	11.09	0.003
100	APWL	0.27	1.26	0.64	0.64	0.20	11.20	0.003
100	A	0.41	2.37	0.34	0.38	1.40	77.72	0.003
200	APWL	0.19	0.36	0.86	0.86	0.23	12.36	0.003
200	APWL	0.27	0.98	0.69	0.69	0.23	12.61	0.003
200	A	0.42	2.26	0.43	0.47	1.19	64.66	0.003
200	Fe ^{II} O _h	1.11	2.89	0.77	0.64	0.19	10.38	0.003
300	APWL	0.18	0.36	0.86	0.86	0.14	12.53	0.002
300	APWL	0.27	1.02	0.67	0.67	0.14	12.54	0.002
300	A	0.42	2.25	0.44	0.46	0.63	58.01	0.002
300	Fe ^{II} O _h	1.15	2.77	0.93	0.66	0.18	16.92	0.002
400	APWL	0.38	1.36	0.84	0.84	0.75	27.33	0.005
400	Fe ^{II} O _h	1.13	2.48	0.70	0.84	2.00	72.67	0.005
500	APWL	0.34	1.37	0.70	0.70	0.39	11.70	0.006
500	Fe ^{II} O _h	1.12	2.44	0.66	0.82	2.94	88.30	0.006
600	APWL	0.40	1.41	0.38	0.38	0.11	04.33	0.005
600	Fe ^{II} O _h	1.12	2.27	0.70	0.69	2.45	95.67	0.005

Errors: $T = \pm 2$ K, $\delta = \pm 0.02$ mm/s, $\Delta = \pm 0.02$ mm/s, $\Gamma = \pm 0.02$ mm/s

The isomer shifts of the phases were unaffected by the heat treatments. However, the quadrupole splitting values for A and the new iron(II) phase fell steadily with higher temperature treatments (Figure 4.15).

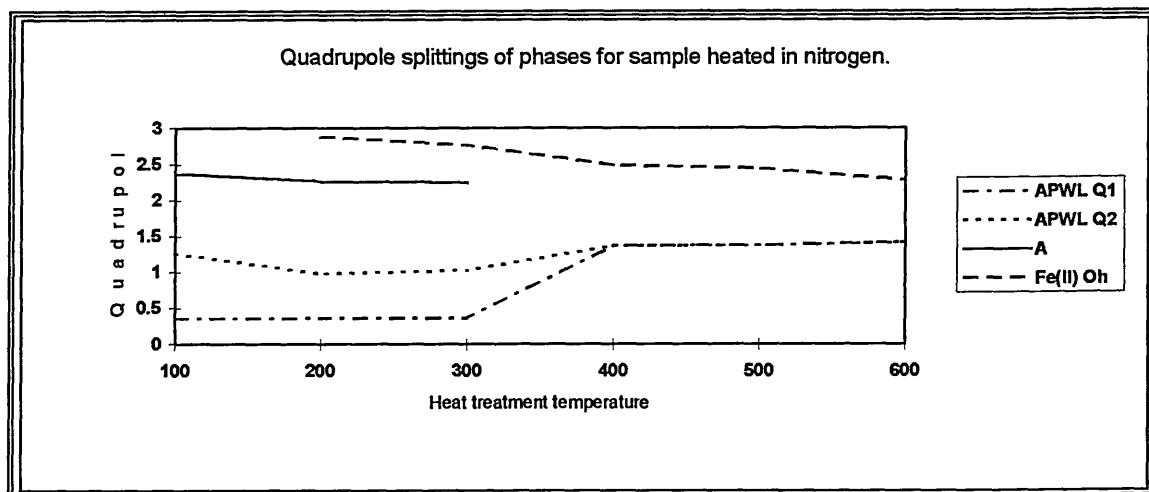
The same phenomenon was observed by Rees *et al.* when studying the ferrous exchanged NH₄-zeolite-A composite²¹¹.

Figure 4.14 Diagram showing 80 K spectra of the sample heated in nitrogen.



They concluded that this was caused by dehydration of the cavity, which led to a more asymmetric environment around the complexes and hence a smaller quadrupole splitting was observed.

Figure 4.15 QS vs. T for Sample Heated in Nitrogen.



The effect was less for A because the distance between the water molecules and the iron nucleus was much greater. This greatly reduces the polarising effect of the water molecules and hence their contribution to the electric field gradient across the iron nucleus. In addition the cyclopentadienyl rings are hydrophobic which again prevents the interaction of water with the iron nucleus.

4.2.6.3.3 Samples Heat Treated in Hydrogen.

Treatment at 150°C gave rise to a new peak with fitting parameters $\delta = 1.07 \pm 0.02$ mm/s and $\Delta = 2.89 \pm 0.02$ mm/s (see Table 4.5, Figure 4.16). This was assigned to high spin iron(II) in an octahedral environment, similar to that which occurred in the samples

heat-treated in nitrogen. The doublet arising from A was still the major phase however (75%).

Further heating to 350°C caused a reduction in the spectral area of A, and an increase in the area of the high-spin, octahedrally co-ordinated iron(II) component.

By 600°C there was no evidence for A. The spectral area was dominated by the high spin octahedral iron(II), although a further new peak with least squares fitting parameters, $\delta = 0.52 \pm 0.02$ mm/s, $\Delta = 1.90 \pm 0.02$ mm/s had appeared, contributing ~20% to the total area. This again was characteristic of high spin iron(II) (see Table 4.2), although the lower quadrupole splitting indicates that the species resided in a less symmetric environment than the first high spin octahedral iron(II) component. This was most likely formed by the reduction of one or more of the trigonally co-ordinated iron(II) - lattice oxygen bonds of the first high spin octahedral iron(II) species parameters. It follows therefore that further heating at 600°C under hydrogen should lead to a single isolated iron(II) species with no direct chemical attachment to the clay lattice. If the process was then continued further, a physisorbed iron(O) species could possibly result. It should be noted however, that a report by Anderson *et al.* stated that zeolites exchanged with iron cannot be reduced below the ferrous state without the use of hydrogen/ammonia mixtures, or hydrogen spill-over from platinum metal²¹⁸.

²¹⁸ Y. Y. Huang and J. R. Anderson, *J. Catal.*, 1975, 40, 143-150.

Figure 4.16 Diagram showing spectra of the sample heated in hydrogen.

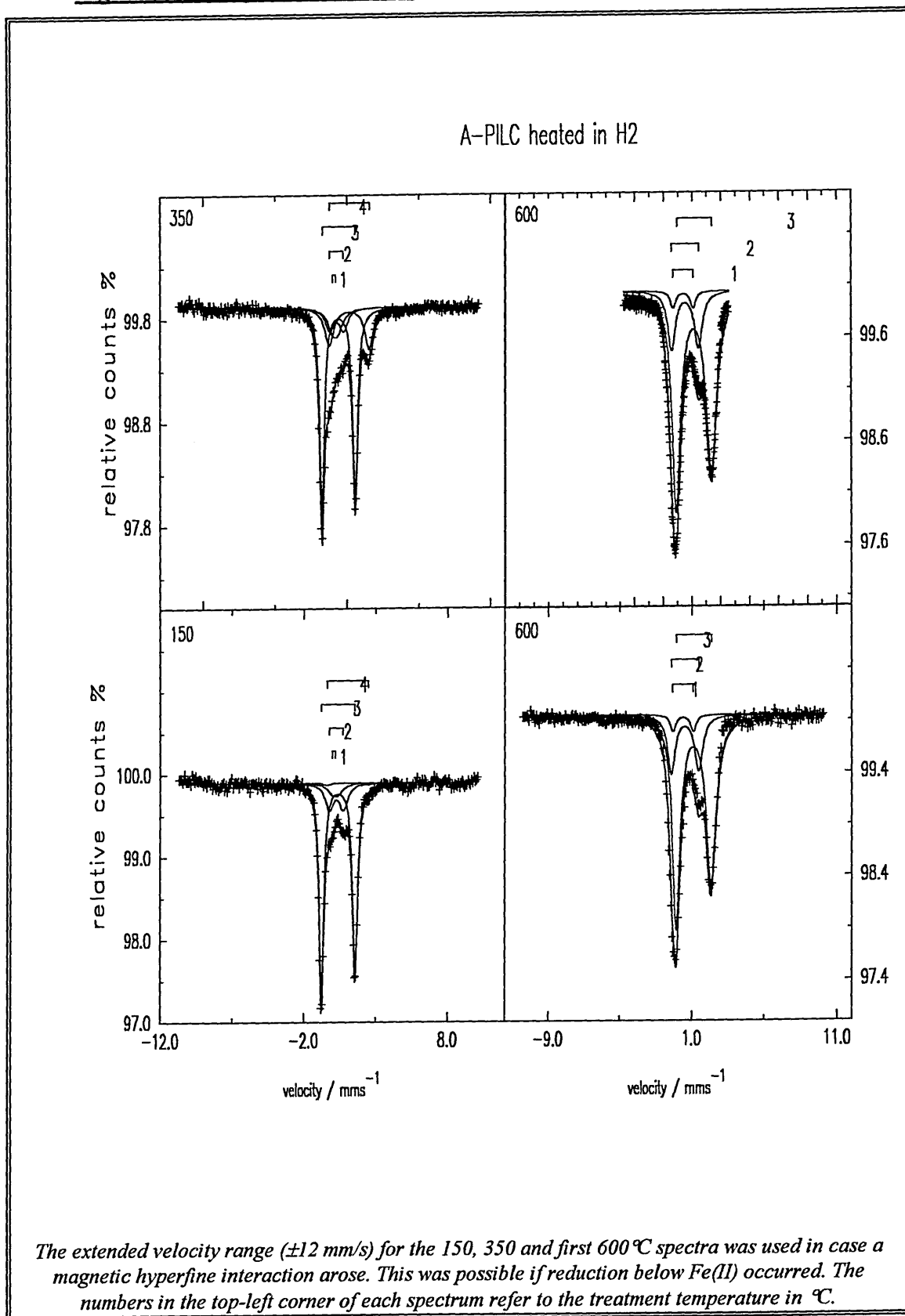


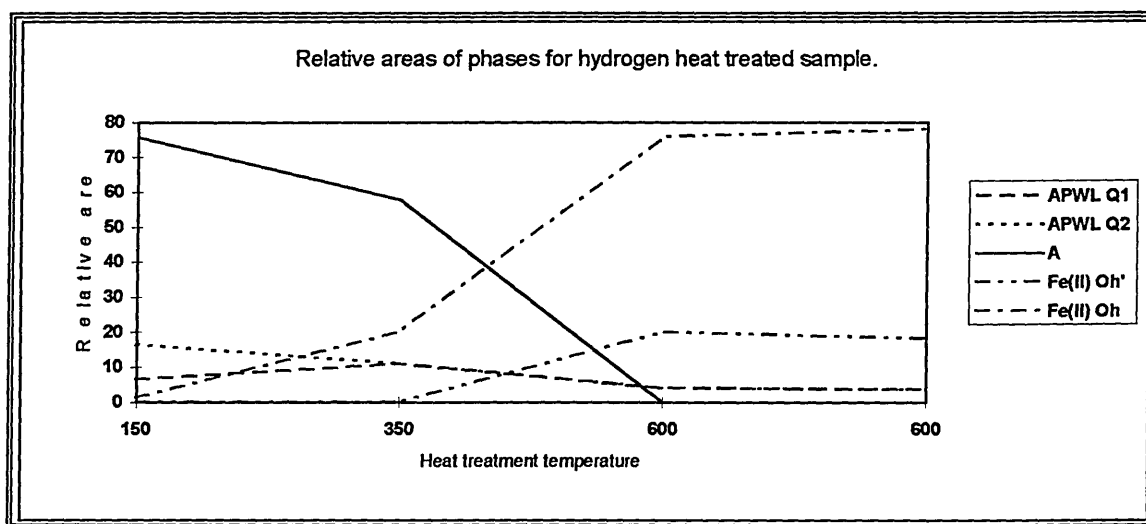
Table 4.5 Least squares fitting parameters for sample heated in hydrogen.

T (C)	Phase	δ (mm/s)	Δ (mm/s)	Γ_1 (mm/s)	Γ_r (mm/s)	Norm. Area	% Area	χ^2
150	APWL	0.19	0.36	0.86	0.86	0.032	06.53	0.001
150	APWL	0.27	0.98	0.69	0.69	0.080	16.50	0.001
150	A	0.41	2.34	0.36	0.41	0.366	75.75	0.001
150	Fe ^{II} O _h	1.07	2.89	0.64	0.67	0.006	01.22	0.001
350	APWL	0.19	0.36	0.86	0.86	0.056	10.99	0.001
350	APWL	0.27	0.98	0.69	0.69	0.056	10.99	0.001
350	A	0.41	2.32	0.38	0.42	0.293	57.85	0.001
350	Fe ^{II} O _h	1.15	2.77	0.75	0.69	0.102	20.17	0.001
600	APWL	0.40	1.41	0.44	0.44	0.027	04.01	0.001
600	Fe ^{II} O _h	0.52	1.90	0.63	0.66	0.133	20.07	0.001
600	Fe ^{II} O _h	1.13	2.41	0.66	0.82	0.501	75.91	0.001
600*	APWL	0.40	1.41	0.44	0.44	0.076	03.65	0.004
600*	Fe ^{II} O _h	0.53	1.89	0.63	0.66	0.380	18.25	0.004
600*	Fe ^{II} O _h	1.15	2.44	0.73	0.89	1.627	78.10	0.004

* Spectrum velocity range +/- 4 mm/s as opposed to +/- 12 mm/s.

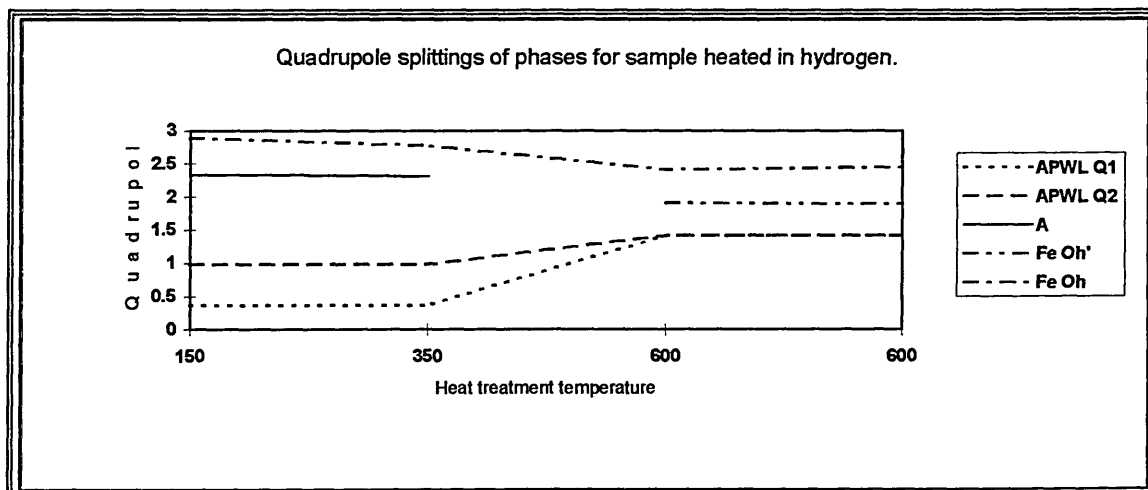
Errors: $T = \pm 2 K$, $\delta = \pm 0.02 \text{ mm/s}$, $\Delta = \pm 0.02 \text{ mm/s}$, $\Gamma = \pm 0.02 \text{ mm/s}$

Figure 4.17 Relative Areas of Sample heated in Hydrogen.



If some agglomeration had occurred this could also prevent further reduction. Small particles contain a large number of crystallographic planes, hence most of the particle has a layer of oxygen which could prevent the hydrogen from being adsorbed. Note that by 600°C the APWL was once again represented by a single doublet ($\delta = 0.40 \pm 0.02 \text{ mm/s}$, $\Delta = 1.41 \pm 0.02 \text{ mm/s}$).

Figure 4.18 QS vs. T for Sample Heated in Hydrogen.



The isomer shifts and quadrupole splittings of the phases did not vary significantly, apart from the more symmetric high spin iron(II) species. This showed a steady decrease of the quadrupole splitting energy which, as with the sample heated in nitrogen (see 4.2.6.3.2), was again attributed to dehydration of the cavity. This increased the asymmetry around the iron species leading to a decrease in the observed quadrupole splitting. This was seen earlier for the A-APWL sample heat treated in nitrogen, and also by Rees *et al.*²¹¹ in the ferrous exchanged NH_4 -A zeolite.

Author's note.

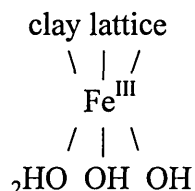
Thought a little extra explanation might help on the theories regarding the *slight* change in quadrupole splittings observed in this section.

Both theories are based on the same assumption. The observed quadrupole splitting (Q_{observed}) is made up of two parts; a valence electron contribution (Q_{valence}) and a surrounding contribution (Q_{surround}). *i.e.*

$$Q_{\text{observed}} = Q_{\text{valence}} + Q_{\text{surround}}$$

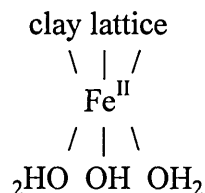
Assume both are the same sign, and also that the clay has a charge of about 0.3⁻ versus the 2.7⁻ from the other ligands. Yes, it's hard to believe but bear with it...

Air sample.



The thought here was that the amine species might dissociate letting protons migrate into the clay lattice. This would reduce the effective charge on the clay lattice further causing a larger Q_{surround} and hence a larger Q_{observed} . A later thought (after submission) was that, "hey, the air sample was grey after heating whereas the other two were black. Wonder if all the nitrogen and hydrocarbon were lost as NO_2 , CO_2 and H_2O ?". The driving force for the dissociation reaction?

N_2 and H_2 samples.



Here the idea was that a proton was hopping between the OH / H_2O molecules very fast (quicker than the Lamorr frequency). As water was lost from *around* the complex, the residual amine species (the sample was black so presumably it's all still there somewhere. Decomposed mind you, but there), could have an affect on the complex. This could be one of three things. A simple distortion of the complex would lower Q_{valence} (but also isomer shift). The amine could polarise the surrounding water distorting the charge and therefore lower Q_{surround} (unlikely to make much difference). Alternatively, the amine could polarise the OH / H_2O groups enough to slow down the proton hopping below the Lamorr frequency. This would effectively show a less symmetric species and hence a lower Q_{surround} (and so a lower Q_{observed}).

Dr J. C. E. Hamer, 29/04/1998.

4.3 Conclusions.

The molecule *N,N*-dimethylaminomethylferrocene has been inserted into aluminium pillared Westone-L and characterised. It was apparent that the molecule had exchanged up to 30% of the total cation exchange capacity, and that the inserted molecule was much less tightly bound than in either the acid chloride salt, or the non-pillared clay. This is consistent with the molecule residing within a large cavity. There was however no sign of a reorientation process. Yet again the decomposition of the supported complex involved the volatilisation of iron below 350°C.

The sample heat treated in air began to decompose at 200°C, probably by a mechanism involving molecular oxygen, to give a high spin iron(III) in a distorted octahedral environment. This was possibly co-ordinated trigonally to three lattice oxygens and also to three water / hydroxyl groups. On treatment at higher temperatures the quadrupole splitting showed a slight increase. This was tentatively attributed to amine fragments reducing the lattice contribution to the electric field gradient across the iron(III) nucleus.

The sample heated in nitrogen started to decompose at 200°C, although the process continued up to 400°C leaving a high spin octahedrally co-ordinated iron(II) species. This was believed to be co-ordinated trigonally to three lattice oxygen, and also to three water / hydroxyl molecules.

Heat treatment of A-APWL in hydrogen gave spectra similar to those observed in the nitrogen heated samples. Decomposition was evident at 150°C and continued through to

350°C, leading to high spin iron(II) in an octahedral environment. Further heating at 600°C led to the reduction of one or more of the iron(II) - lattice oxygen bonds, leading to a second high spin iron(II) species, with a less symmetric co-ordination sphere than the first. It is possible that further reduction could lead to an isolated iron(II) species. This is likely to have catalytic properties, such as the removal of hydrogen sulfide from reducing gas mixtures²⁰¹.

On heating, there was a slight decrease in the quadrupole splitting for the octahedral iron(II) in the samples heated under nitrogen and hydrogen, which was ascribed to dehydration of the cavity causing a more asymmetric environment around the coordinated iron species.

4.4 Future Work.

There is a considerable amount of work needed on these materials. Initially MASNMR of the APWL should give an insight into the change in the Mössbauer spectrum before and after the pillaring and the heat treatments.

It would be interesting to see if further heating of the sample heat treated in hydrogen produced any further changes in the Mössbauer spectrum. In addition the effect of using a hydrogen / ammonia mixture as the reducing gas would again be intriguing.

Moreover, EXAFS and possibly XPS of the heat treated samples should give a clearer picture of the ligands and immediate environment surrounding the iron nuclei. In addition the use of TEM (Transmission Electron Microscopy) may elucidate whether any migration or agglomeration of the iron nuclei has occurred.

The samples heat treated in hydrogen show all the requirements necessary to act as a catalyst in the reduction of hydrogen sulfide from reducing gas mixtures. A test of its suitability as a catalyst is definitely needed as this is of great importance in industry.

Work by Lee²¹⁹ has produced mixed metal pillared clays. Insertion of N,N-dimethylaminoferrocene into iron/aluminium pillared clays together with variable

²¹⁹ W. Lee and B. J. Tartarchuk, *Hyperfine Interactions*, 1988, 41, 661-664.

temperature Mössbauer spectroscopy could elucidate the electronic interactions between pillar and inserted molecule.

Furthermore, the introduction of other metallocenes or catalytically active molecules into the aluminium pillared and mixed-metal pillared clays, followed by the use of the spectroscopic techniques mentioned above, could provide a valuable insight into the interactions between host and guest in composite materials and catalysts.

In addition, by varying the pillaring conditions and hence the pillar height, it may be possible to produce a heterogeneous catalyst which favours a specific reactant or product molecule.

One other consideration is the use of A-APWL in solid state batteries for overcharge protection. The molecule A has already been suggested for use in rechargeable lithium batteries for this specific use¹⁹⁴.

5. Conclusions.

(Ferrocenylmethyl)dimethylammonium chloride has been synthesised and characterised by a variety of techniques. Variable temperature Mössbauer spectroscopy indicated that no reorientation effects were in effect between 12 and 300 K, and that the molecule had a Debye temperature of 144 ± 5 K with corresponding recoilless fraction at 291 K of 0.14 ± 0.02 .

The (ferrocenylmethyl)dimethylammonium cation has been intercalated into the montmorillonite Westone-L by a variety of different methods. The cation was shown to occupy 80 % of the total exchange capacity of the clay, and that the molecule was most likely orientated with the cyclopentadienyl rings perpendicular to the silicate layers with no discernible distortion of the cyclopentadienyl rings. Once again variable temperature Mössbauer spectroscopy revealed that no reorientation effects were in operation between 12 and 300 K, and that the intercalated cation exhibited a Debye temperature of 140 ± 5 K ($f_{291} = 0.13 \pm 0.02$). This suggests that the cation resides in an environment similar to that found in the hydrochloride salt. In contrast to the work by Molloy *et al.*⁸⁹ on organotin compounds on clay, the cation was unaffected by the melting of the interlayer water. In addition close examination of the intercalated Mössbauer spectra revealed a Karayagin effect above 80 K. Thermal decomposition of the intercalated cation involved the volatilisation of iron below 350°C, which contrasts to the behaviour observed by Breen *et al.*¹⁸² on the decomposition of half-sandwich tricarbonyl iron compounds on montmorillonite clay. Above 350°C the decomposition occurred by a different mechanism, with loss of the cyclopentadienyl rings and the retention of iron on the clay.

Variable-temperature XRD showed that the d_{001} -spacing of 1.55 nm, decreased at 200°C to give a d_{001} -spacing of 1.3 nm. This confirmed that some sort of complex, probably an iron oxide, remained within the interlayer after the inserted molecule had decomposed.

Based on the intercalation of the (ferrocenylmethyl)dimethylammonium into acid Westone-L, 2, 2''-bis[(dimethylamino)methyl]biferrocene was successfully intercalated into acid exchanged Westone-L. This saved valuable material which would have been lost synthesising and recrystallising the acid salt of the biferrocene. The cation was shown to occupy 75 % of the total CEC of the clay. As with the intercalated (ferrocenylmethyl)dimethylammonium cation the molecule most likely resides with the cyclopentadienyl rings perpendicular to the silicate sheet with no discernible distortion of the cyclopentadienyl rings. Variable temperature Mössbauer spectroscopy indicated a Debye temperature of 150 ± 5 K ($f_{291} = 0.17 \pm 0.02$) for the intercalated molecule. This was 20 K lower than that observed for 2, 2''-bis[(dimethylamino)methyl]biferrocene consistent with the molecule residing in a less rigid environment. This reflects the trend observed by Breen *et al.*¹⁸² on the intercalation of half-sandwich tricarbonyliron compounds on montmorillonite. Once again close examination of the Mössbauer spectra revealed a slight Karyagin effect.

During the three hour contact of the biferrocene with the acid Westone-L, *ca.* 2 % of the biferrocene supported on the clay was oxidised to biferrocenium. A 45 hour extension of the contact time of the biferrocene with the clay resulted in further oxidation (*ca.* 11 %) to biferrocenium. Contact of iodine with a suspension of the intercalated biferrocene resulted in *ca.* 16 % oxidation to biferrocene. The biferrocenium intercalate exhibited

valence electron de-trapping above 200 K until by 250 K only a single charge averaged doublet was observed. The de-trapping was most likely occurring in small domains to start with, which then spread throughout the material as the temperature was raised.

Thermal decomposition of the biferrocene under nitrogen revealed two major weight losses at 330 and 620 °C as identified by maxima in the derivative thermogram. Similar decomposition of the intercalate revealed an extra peak in the derivative thermogram at 480°C. Studies utilising thermal desorption mass spectroscopy, indicated that as with the (ferrocenylmethyl)dimethylammonium intercalate, two different decomposition mechanisms were in effect. The first involving the loss of ferrocene dominated up to 430°C. The second, involving the loss of the cyclopentadienyl rings whilst retaining the iron on the clay, dominated above this temperature. Variable-temperature XRD indicated a d_{001} -spacing of 1.65 nm at room temperature which collapsed to 1.41 nm at 250°C, after which it slowly decreased to 1.29 nm at 400°C. This confirms that some sort of species, probably an iron oxide, was left within the interlayer after the intercalated molecule had decomposed:

The molecule N, N-dimethylaminomethylferrocene was successfully intercalated into aluminium pillared Westone-L. The molecule occupied 30 % of the total CEC of the original clay. The inserted molecule was found to have a Debye temperature of 113 ± 5 K ($f_{291} = 0.05 \pm 0.02$) as determined by variable temperature Mössbauer spectroscopy. This is consistent with the molecule residing in a much less rigid environment than that found in either the chloride salt or Westone-L intercalate. Although residing in a much less rigid environment, there was still no indication of a reorientation process. This may

be due to strong interactions between the ammonium side group and the aluminosilicate lattice. As with the (ferrocenylmethyl)dimethylammonium and biferrocene Westone-L intercalates, decomposition of the inserted molecule involved the loss of iron below 350°C.

When heated in air the inserted molecule decomposed above 200°C giving rise to high spin iron(III) in a distorted octahedral environment. This was possibly co-ordinated trigonally to three silicate lattice oxygens and also trigonally to three water / hydroxy groups. Further heating led to a slight rise in the quadrupole splitting of the new species. This was tentatively ascribed to amine fragments reducing the lattice contribution to the electric field gradient across the iron nucleus.

Heating the sample in nitrogen again resulted in decomposition above 200°C, although this continued up to 400°C. The resulting species was characteristic of high spin octahedrally co-ordinated iron(II). This was also believed to be trigonally co-ordinated to three silicate lattice oxygens and also trigonally to three hydroxy / water molecules.

Heat treatment in hydrogen showed that decomposition was evident at 150°C. This continued through to 350°C, leading to high spin iron(II) in an octahedral environment. This also was believed to be trigonally co-ordinated to three silicate lattice oxygen atoms and trigonally to three hydroxyl / water molecules. Further heating at 600°C led to a second high spin iron(II) species with a less symmetric co-ordination sphere than the first. This is believed to be caused by the reduction of one or more of the iron(II)- silicate

lattice bonds. It is possible that further reduction at this temperature could lead to an isolated physisorbed iron (II) species within the pillared clay gallery. This is likely to have catalytic properties such as the removal of hydrogen sulfide from reducing gas mixtures²¹¹.

On heating there was a slight decrease in quadrupole splitting for the octahedral iron(II) in the samples heated under nitrogen and hydrogen. This was ascribed to dehydration of the cavity causing a more symmetric environment around the co-ordinated iron species.

6. Table of Equations.

$E = E_{EX} - E_0$	EQUATION 1.1	43
$E + \frac{1}{2}MV_x^2 = E_\gamma + \frac{1}{2}M(V_x + V)^2$	EQUATION 1.2	43
$= E_R + E_D$	EQUATION 1.3	44
$E_D = mv\sqrt{V^2} = \sqrt{2E_R}mv^2 = 2\sqrt{E_k}E_R$	EQUATION 1.4	44
$\Delta E \Delta t = \hbar$	EQUATION 1.5	47
$\Gamma = \hbar / \Delta T$	EQUATION 1.6	47
$f = 1 - \frac{E_R}{E}$	EQUATION 1.7	49
$F = E^{-k^2 x^2} \hbar \omega$	EQUATION 1.8	50
$f = \exp\left(\frac{-4\pi^2 \langle x^2 \rangle}{\lambda^2}\right) = \exp\left(\frac{E_\gamma^2 \langle x^2 \rangle}{(\hbar c)^2}\right)$	EQUATION 1.9	50
$f = \exp\left[\frac{-6E_R}{k\theta_D} \left\{ \frac{1}{4} + \left(\frac{T}{\theta_D}\right)^2 \int_0^{\theta_D/T} \frac{x}{e^x - 1} dx \right\}\right]$	EQUATION 1.10	52
$f = \exp\left[\frac{-E_R}{k\theta_D} \left\{ \frac{3}{2} + \frac{\pi^2 T^2}{\theta_D^2} \right\}\right]$	$T \ll \theta_D$ EQUATION 1.11	52
$f = \exp\left[\frac{-3E_R}{2k\theta_D}\right]$	$T = 0$ K EQUATION 1.12	52
$f = \exp\left[\frac{-6E_R T}{k\theta_D^2}\right]$	$T \geq \frac{1}{2}\theta_D$ EQUATION 1.13	52
$N(E)dE = \frac{f_s \Gamma_s}{2\pi} \frac{dE}{(E - E_\gamma)^2 + \left(\frac{\Gamma_s}{2}\right)^2}$	EQUATION 1.14	53
$\sigma(E) = \sigma_0 \frac{\left(\frac{\Gamma_a}{2}\right)^2}{(E - E_\gamma)^2 + \left(\frac{\Gamma_a}{2}\right)^2}$	EQUATION 1.15	53
$\sigma_0 = 2\pi\lambda^2 \left(\frac{2I_e + 1}{2I_g + 1}\right) \left(\frac{1}{1 + \alpha}\right)$	EQUATION 1.16	54
$I(\varepsilon) = \frac{\Gamma_r}{2\pi} \times \frac{1}{(\varepsilon - E_\gamma)^2 + (\Gamma_r/2)^2}$	EQUATION 1.17	55
$\frac{\Gamma_r}{\Gamma} = 2.00 + 0.27t \quad 0 < T \leq 5$	EQUATION 1.18	56
$T(0) = e^{-\mu a} \left\{ (1 - f_s) + f_s e^{\frac{1}{2}T a} J_0\left(\frac{1}{2}i T a\right) \right\}$	EQUATION 1.19	61
$= e^{-\mu a} f_s \left[1 - e^{\frac{1}{2}T a} J_0\left(\frac{1}{2}i T a\right) \right]$	EQUATION 1.20	61
$\delta = \text{constant} \times \{ \psi_s(0)_A ^2 - \psi_s(0)_B ^2 \}$	EQUATION 1.21	74
$f \cong v \left(1 - \frac{v}{c}\right) \left(1 + \frac{v^2}{2c^2}\right)$	EQUATION 1.22	76

$\frac{\delta E_\gamma}{E_\gamma} = \frac{\delta v}{v} = -\frac{\langle v^2 \rangle}{2c^2}$	EQUATION 1.23.....	77
$\frac{1}{2} M \langle v^2 \rangle = 3 \left(n_j + \frac{1}{2} \right) \hbar \omega_j$	EQUATION 1.24.....	77
$\frac{\delta v}{v} = -\frac{3}{2Mc^2} \sum_j A_j^2 \hbar \omega_j \left(\frac{1}{2} + n_j \right)$	EQUATION 1.25.....	77
$\frac{\delta v}{v} = -\frac{3}{2} \frac{RT}{Mc^2}$	EQUATION 1.26.....	77
$\frac{\delta v_0}{v} = -\frac{3}{4} \frac{1}{Mc^2} \sum_j A_j^2 \hbar \omega_j$	EQUATION 1.27.....	78
$\frac{\delta v_0}{v} = -\frac{9}{16} \frac{\hbar \omega_D}{Mc^2}$	EQUATION 1.28.....	78
$\frac{\delta v_0}{v} = -\frac{9}{16} \frac{k\theta_D}{Mc^2}$	EQUATION 1.29.....	78
$eQ = \int \rho r^2 (3 \cos^2 \theta - 1) d\tau$	EQUATION 1.30.....	79
$V_{ZZ} + V_{XX} + V_{YY} = 0$	EQUATION 1.31.....	80
$\eta = \frac{(V_{xx} - V_{yy})}{V_{zz}}$	EQUATION 1.32.....	80
$E_Q = \frac{e^2 q Q}{4I(2I-1)} [3I_z^2 - I(I+1)]$	EQUATION 1.33.....	80
$E_Q = \frac{e^2 q Q}{4I(2I-1)} [3I_z^2 - I(I+1)] \left(1 + \frac{\eta^2}{3} \right)^{\frac{1}{2}}$	EQUATION 1.34.....	81
$H = H_0 - DM + 4/3 \pi M + H_S + H_L + H_D$	EQUATION 1.35.....	82
$N(i) = \frac{1}{\pi \Gamma \left(\left(\frac{i-\delta}{\Gamma} \right)^2 \right)}$	EQUATION 1.36.....	85
$A = K (NX\sigma) F_A$	EQUATION 1.37.....	90
$\ln A(T) = \ln Knx\sigma \cdot \left[\frac{-3E_R}{2k\theta_D} \right] = \text{a constant.}$	EQUATION 1.38.....	90
$\ln A(T) = \ln Knx\sigma \cdot \left[\frac{-3E_R}{k\theta_D} \right] + \ln Knx\sigma \cdot \left[\frac{-3E_R}{k\theta_D} \right] \cdot T$	EQUATION 1.39.....	91
160. EQUATION 9.40.....		223

7. Table of Figures.

FIGURE 1.1 THE STRUCTURE OF MONTMORILLONITE.....	21
FIGURE 1.2 DIAGRAM SHOWING VEDT TYPE II.....	39
FIGURE 1.3 DIAGRAM SHOWING DE-TRAPPING TYPE III.....	40
FIGURE 1.4 DIAGRAM SHOWING ATOM BEFORE AND AFTER RECOIL.....	43
FIGURE 1.5 DIAGRAM OF OVERLAPPING DISTRIBUTIONS $2E_R$ APART AND BROADENED BY E_D	46
FIGURE 1.6 DIAGRAM OF LORENTZIAN LINE, E_γ WITH HEISENBERG-WIDTH Γ	54
FIGURE 1.7 DIAGRAM SHOWING γ -DECAY SCHEME FOR ^{57}CO	60
FIGURE 1.8 DIAGRAM OF A TYPICAL PROPORTIONAL COUNTER.....	64
FIGURE 1.9 DIAGRAM OF LIQUID CRYOSTAT.....	67
FIGURE 1.10 SCHEMATIC DIAGRAM OF THE EXPANDER MODULE FOR THE DISPLEX.....	68
FIGURE 1.11 THE AIR PRODUCTS DISPLEX CRYOSTAT.....	70
FIGURE 1.12 SCHEMATIC DIAGRAM OF THE MÖSSBAUER LABORATORY.....	72
FIGURE 1.13 DIAGRAM OF TRIANGLE WAVE AND HOW THIS IS RELATED TO ENERGY.....	73
FIGURE 1.14 DIAGRAM SHOWING SPECTRUM WITH ISOMER SHIFT (δ).....	75
FIGURE 1.15 DIAGRAM OF FLAT (OBLATE) AND PROLATE (ELONGATED) NUCLEUS.....	79
FIGURE 1.16 DIAGRAM SHOWING SPLITTING OF ENERGY LEVELS AND SPECTRUM.....	81
FIGURE 1.17 DIAGRAM SHOWING H, AND H + Q EFFECT ON NUCLEAR LEVELS AND SPECTRUM.....	83
FIGURE 1.18 ASYMMETRIC QUADRUPOLE SPECTRUM.....	88
FIGURE 1.19 P, Q, FITTING RESULTS PLOTTED FOR A) ONE NARROW ENVIRONMENT, B) ONE BROAD ENVIRONMENT, C) TWO DISTINCT ENVIRONMENTS.....	89
FIGURE 1.20 DIAGRAM SHOWING DIFFERENT ELECTRONIC CONFIGURATIONS FOR Fe(II)	93
FIGURE 2.1 ADSORPTION ISOTHERMS FOR DIFFERENT CONTACT METHODS.....	108
FIGURE 2.2 DERIVATIVE THERMOGRAM TRACES FOR THE SAMPLES INDICATED.....	114
FIGURE 2.3 TIC FOR AH-WL.....	115
FIGURE 2.4 THERMAL DESORPTION MASS SPECTRA FOR AH-WL.....	116
FIGURE 2.5 XRD D-SPACING VS. T.....	120
FIGURE 2.6 A-WL VT-XRD.....	121
FIGURE 2.7 VARIABLE TEMPERATURE MÖSSBAUER SPECTRA OF AHCL.....	124
FIGURE 2.8 MÖSSBAUER SPECTRA OF A-H-WL.....	126
FIGURE 2.9 LOG AREA VS. TEMPERATURE GRAPHS.....	127
FIGURE 3.1 DERIVATIVE THERMOGRAMS OF AA, HWL, AA-HWL.....	143
FIGURE 3.2 TIC FOR AA-HWL.....	145
FIGURE 3.3 THERMAL DESORPTION MASS SPECTRA FOR AA AND AA-HWL.....	146
FIGURE 3.4 DIAGRAM OF AA AND D_{001} -SPACING.....	148
FIGURE 3.5 VARIABLE TEMPERATURE XRD SPECTRA FOR AA-HWL.....	149
FIGURE 3.6 VT-MÖSSBAUER SPECTRA OF AA.....	152
FIGURE 3.7 SPECTRA OF A) AA-HWL, B) AA-HWL(48) AND C) AA^+ -HWL.....	154
FIGURE 3.8 POTENTIAL WELL DIAGRAMS.....	156
FIGURE 3.9 LNAT PLOT FOR AA^+ -HWL ORGANOMETALLIC PHASE.....	160
FIGURE 3.10 AA^+ -HWL SPECTRA FITTED USING "DOMAIN" DE-TRAPPING MODEL.....	164
FIGURE 4.1 DERIVATIVE THERMOGRAMS FOR NA-WL, AHCL, APWL AND A-APWL.....	179
FIGURE 4.2 TIC FOR A-APWL.....	180
FIGURE 4.3 TD-MS SPECTRA OF A-APWL.....	181
FIGURE 4.4 SPECTRA OF WL, WL(500), APWL, APWL(600).....	184
FIGURE 4.5 PQH PLOT OF % AREA VS. QS FOR APWL.....	185
FIGURE 4.6 A-APWL SPECTRA.....	188
FIGURE 4.7 LNAT PLOT FOR A-APWL Fe^{2+}	189
FIGURE 4.8 DIAGRAM SHOWING PQH FITTED SPECTRA.....	190
FIGURE 4.9 PQH PLOTS OF % AREA VS. QS FOR A IN A-APWL.....	191
FIGURE 4.10 DIAGRAM SHOWING 80 K SPECTRA OF SAMPLES HEATED IN AIR.....	195
FIGURE 4.11 RELATIVE AREAS OF PHASES FOR SAMPLE TREATED IN AIR.....	196

FIGURE 4.12 QS VS. HT FOR SAMPLE HEATED IN AIR.	197
FIGURE 4.13 RELATIVE AREAS OF PHASES FOR SAMPLE HEATED IN NITROGEN.	198
FIGURE 4.14 DIAGRAM SHOWING 80 K SPECTRA OF THE SAMPLE HEATED IN NITROGEN.	200
FIGURE 4.15 QS VS. T FOR SAMPLE HEATED IN NITROGEN.	201
FIGURE 4.16 DIAGRAM SHOWING SPECTRA OF THE SAMPLE HEATED IN HYDROGEN. ...	203
FIGURE 4.17 RELATIVE AREAS OF SAMPLE HEATED IN HYDROGEN.	204
FIGURE 4.18 QS VS. T FOR SAMPLE HEATED IN HYDROGEN.	205

8. Index of tables.

TABLE 2.1 UPPER LIMITS OF EXCHANGE ACHIEVED BY CONTACTING IN METHANOL...	109
TABLE 2.2 SUMMARY OF XRF RESULTS FOR EACH EXCHANGE METHOD.....	110
TABLE 2.3 LEAST SQUARES FITTING PARAMETERS FOR AHCL.....	123
TABLE 2.4 LEAST SQUARES FITTING PARAMETERS FOR AH-WL.....	125
TABLE 2.5 SHOWING LEAST SQUARES FITTING PARAMETERS FOR A-HWL.....	128
TABLE 2.6 LEAST SQUARES FITTING PARAMETERS FOR A-H-WL.....	129
TABLE 2.7 LEAST SQUARES FITTING PARAMETERS FOR A-WL.....	131
TABLE 2.8 SHOWING SUMMARY OF θ_D AND F_{291} VALUES FOR THE VARIABLE TEMPERATURE EXPERIMENTS PERFORMED.....	134
TABLE 3.1 PEAK INDEX OF VT-XRD OF AA-HWL.....	150
TABLE 3.2 FITTING PARAMETERS FOR AA.....	153
TABLE 3.3 AA ⁺ -HWL FITTING PARAMETERS FOR 3 PHASE MODEL.....	155
TABLE 3.4 AA-HWL FITTING PARAMETERS FOR "FUSION" DE-TRAPPING.....	160
TABLE 3.5 AA-HWL(48) FITTING PARAMETERS FOR "FUSION" DE-TRAPPING.....	161
TABLE 3.6 AA ⁺ -HWL FITTING PARAMETERS FOR "FUSION" DE-TRAPPING.....	161
TABLE 3.7 AA-HWL FITTING PARAMETERS FOR "DOMAIN" DE-TRAPPING.....	162
TABLE 3.8 AA-HWL(48) FITTING PARAMETERS FOR "DOMAIN" DE-TRAPPING.....	163
TABLE 3.9 AA ⁺ -HWL FITTING PARAMETERS FOR "DOMAIN" DE-TRAPPING.....	163
TABLE 4.1 SHOWING LEAST SQUARES FITTING PARAMETERS FOR A-APWL.....	187
TABLE 4.2 SUMMARY OF MÖSSBAUER PARAMETERS FOR IRON IN DIFFERENT CO- ORDINATION GEOMETRY'S.....	192
TABLE 4.3 LEAST SQUARES FITTING PARAMETERS FOR AIR HEAT TREATED SAMPLE..	194
TABLE 4.4 LEAST SQUARES FITTING PARAMETERS FOR SAMPLE HEATED IN NITROGEN.	199
TABLE 4.5 LEAST SQUARES FITTING PARAMETERS FOR SAMPLE HEATED IN HYDROGEN.	204

9. References.

1. F. Kanamaru, M. Shimada, M. Koizumi, and T. Takada, *J. Solid State Chem.*, **1973**, *7*, 1.
2. S. Kikkawa, F. Fanamaru, and M. Koizumi, *Bull. Chem. Soc. Jpn.*, **1979**, *52*, 963.
3. S. M. Whittingham, *Prog. Solid State Chem.*, **1978**, *12*, 41.
4. R. Schollhorn, A. Lerf, F. Sernetz, *Z. Naturforsch.*, **1974**, *29B*, 810.
5. *Mater. Res. Bull.*, **1974**, *9*, 1597.
6. S. F. Meyer, R. E. Howard, G. R. Stewart, J. U. Acrivos, T. H. Geballe, *J. Chem. Phys.*, **1975**, *62*, 441.
7. S. A. Solin, *Physica B+C*, **1980**, *99*, 443.
8. R. J. Nemanich, S. A. Solin, and D. Guérard, *Phys. Rev. B*, **1977**, *16*, 2965.
9. C. Underhill, S. Y. Leung, G. Dresselhaus, and M. S. Dresselhaus, *Solid State Commun.*, **1979**, *29*, 769.
10. T. R. Halbert, D. C. Johnston, L. E. McCandlish, A. H. Thompson, J. C. Scanlon, and J. A. Dumesic, *Physica B+C*, **1980**, *99*, 128.
11. M. Eibschutz and F. DiSalvo, *Phys. Rev. Lett.*, **1976**, *36*, 104.
12. R. R. Chianelli, J. C. Scanlon, M. S. Whittingham, and F. R. Gamble, *Inorg. Chem.*, **1975**, *14*, 1691.
13. R. R. Gamble, J. H. Osiecki, and F. J. DiSalvo, *J. Chem. Phys.*, **1971**, *55*, 3525.
14. G. A. Wiegers, *Physica B+C*, **1971**, *99*, 151.
15. R. L. Grim, "Clay Mineralogy", **1953**, McGraw and Hill, London, UK.
16. P. Hagemuller, J. Rouxel, J. David, A. Colin, and B. Le Neindre, *Z. Anorg. Allg. Chem.*, **1963**, *323*, 1-12.
17. P. Hagemuller, J. Portier, B. Barbe, and P. Bouclier, *Id.*, **1967**, *355*, 209.
18. J. Reichenbach, F. Rachdi, I. Lukyanchuk, M. Ribet, G. Zimmer, and M. Mehring, *J. Chem. Phys.*, **1994**, *101(6)*, 4585-4592.
19. K. Kanazawa, H. Nakanishi, Y. Ishizuka, T. Nakamura, and M. Marsumoto, *Fullerene Science and Technology*, **1994**, *2(2)*, 189-194.
20. W. Schlenk, *Justus Liebigs Ann. Chem.*, **1949**, *565*, 204.
21. W. Schlenk, *Justus Liebigs Ann. Chem.*, **1951**, *573*, 142.
22. R. Clement, R. Claude, C. Mazieres, *J. Chem. Soc., Chem. Commun.*, **1974**, 654-655.
23. A. Harada and S. Takahashi, *J. Chem. Soc., Chem. Commun.*, **1984**, 645.
24. T. C. Gibb, *J. Phys. C: Solid State Phys.*, **1976**, *9*, 2627-2642.
25. M. D. Lowery, R. J. Wittebort, M. Sorai, and D. N. Hendrickson, *J. Am. Chem. Soc.*, **1990**, *112*, 4214-4225.
26. E. Hough and D. G. Nicholson, *J. Chem. Soc., Dalton. Trans.*, **1978**, 15-18.
27. R. Clément, M. Gourdjji and L. Guibé, *Chem. Phys. Letters*, **1980**, *72*, 466.
28. T. Nalai, T. Terao, F. Imashiro and A. Saika, *Chem. Phys. Letters*, **1986**, *132*, 554-557.
29. S. J. Heyes, N. J. Clayden, and C. M. Dobson, *J. Phys. Chem.*, **1991**, *95*, 1547-1554.
30. R. M. Barrer, "Hydrothermal Chemistry of Zeolites", **1972**, Academic Press, New York, USA.
31. G. A. Ozin and J. P. Godber, "In Intrazeolite Organometallics: Spectroscopic Probes of Internal versus External Confinement of Metal Guests. *Excited States and Reactive Intermediates: Photochemistry, Photophysics and Electrochemistry*", **1986**, ACS Symposium Series 307, American Chemical Society, Washington DC, USA.
32. G. A. Ozin, J. Godber, *J. Phys. Chem.*, **1989**, *93*, 878.
33. A. Borvornwattanont, K. Moller, T. Bein, *J. Phys. Chem.*, **1989**, *93*, 4562.
34. S. T. Wilson, B. M. Lok, C. A. Messina, T. R. Cannan, and E. M. Flanigen, *J. Am. Chem. Soc.*, **1982**, *104*, 1146.
35. M. E. Davis, C. Saldarriaga, C. Montes, J. Garces, and C. Crowder, *Nature(London)*, **1988**, 698.
36. E. T. C. Vogt and J. W. Richardson, *J. Solid State Chem.*, **1990**, *87*, 469.
37. T. Lindblad and B. Rebenstorf, *J. Chem. Soc. Faraday Trans.*, **1991**, *87(15)*, 2473-2478.
38. G. A. Ozin, D. M. Haddleton, and C. J. Gil, *J. Phys. Chem.*, **1989**, *93*, 6710.
39. T. Huang and . Schwartz, *J. Am. Chem. Soc.*, **1982**, *104*, 5244.
40. N. Herron, G. D. Stucky, and C. A. Tolman, *Inorg. Chem. Acta.*, **1985**, *100*, 135.
41. T. Bein, S. J. McLain, D. R. Corbin, R. D. Farlee, K. Moller, G. D. Stucky, G. Woolery, and D. Sayers, *J. Am. Chem. Soc.*, **1988**, *110*, 1801.

42. G. A. Ozin and J. P. Godber, "In Intrazeolite Organometallics: Spectroscopic Probes of Internal versus External Confinement of Metal Guests. *Excited States and Reactive Intermediates: Photochemistry, Photophysics and Electrochemistry*", 1986, ACS Symposium Series 307, American Chemical Society, Washington DC, USA.
43. M. Koichi, S. Imamura, and J. H. Lunsford, *Inorg. Chem.*, 1984, 23, 3510.
44. E. H. Yonemoto, Y. I. Kim, R. H. Schmehl, J. O. Wallin, B. A. Shoulders, B. R. Richardson, J. F. Haw, and T. E. Mallouk, *J. Am. Chem. Soc.*, 1994, 116(23), 10557-10563.
45. Y. S. Yong and R. F. Howe, *J. Chem. Soc., Faraday Trans.*, 1986, 82, 2887.
46. G. Meyer, D. Wohrle, M. Mohl, and G. Schultz-Ekloff, *Zeolites*, 1984, 4, 30.
47. W. V. Cruz, P. C. W. Leung, and K. Seff, *J. Am. Chem. Soc.*, 1978, 100, 6997.
48. A. Lund, D. G. Nicholson, G. Lambie, and B. Beagley, *J. Mater. Chem.*, 1994, 4(11), 1723-1730.
49. A. Lund, D. G. Nicholson, R. V. Parish, and J. P. Wright, *Acta Chemica Scandinavica*, 1994, 48, 738-741.
50. M. B. Dines, *Science*, 1975, 188, 1210.
51. R. P. Clement, W. B. Davies, K. A. Ford, M. L. H. Green, and A. J. Jacobson, *Inorg. Chem.*, 1978, 17, 2754.
52. J. Rouxel, "Layered Materials and Intercalates", 1980, pp 3-11, North Holland, Amsterdam, Netherlands.
53. L. E. Campbell, G. L. Montet, and G. J. Perlow, *Phys. Rev. B*, 1977, B15, 3318.
54. N. Saito, T. Tominaga, M. Takeda, Y. Ohe, F. Ambe, and H. Sano, *Nippon Arsatapu Kaigi Hobunshu*, 1967, 231.
55. P. C. Klipstein and R. H. Friend, *J. Phys. Chem.*, 1984, 17, 2713-2721.
56. L. Lomas, P. Lacroix, J. P. Audière, and R. Clément, *J. Mater. Chem.*, 1991, 1(3), 475-476.
57. F. R. Gamble, F. J. DiSalvo, R. A. Klemm, and T. H. Gaballe, *Science*, 1970, 568-575.
58. D. O'Hare, *Chem. Soc. Rev.*, 1992, 121-126.
59. E. Rodríguez-Castellón, A. Rodríguez-Garcia, and S. Bruque, *Inorg. Chem.*, 1985, 24(8), 1187-1190.
60. P. Palvadeau, L. Coïc, J. Rouxel, F. Mènil, and L. Fournès, *Mat. Res. Bull.*, 1981, 16, 1055-1065.
61. G. Matsubayashi, S. Ohta, and S. Okanu, *Inorg. Chim. Acta*, 1991, 184, 47-52.
62. S. Okanu and G. Matsubayashi, *J. Chem. Soc., Dalton Trans.*, 1992, 2441-2445.
63. S. J. Mason, L. M. Bull, C. P. Grey, S. J. Heyes, and D. O'Hare, *J. Mater. Chem.*, 1992, 2(11), 1189-1194.
64. S. Okuno and G-E. Matsubayashi, *Chemistry Letters*, 1993, 799-802.
65. J. W. Johnson, *J. Chem. Soc. Chem. Commun.*, 1980, 263.
66. P. Aldebert and V. Paul-Boncour, *Mater. Res. Bull.*, 1983, 18, 1263.
67. P. G. Nahin, *Clays Clay Minerals*, 1963, 10, 257-271.
68. U. Hofmann, K. Endell, and D. Wilm, *Z. Krist.*, 1933, 86, 340-348.
69. C. E. Marshall, *Z. Krist.*, 1935, 91, 433-449.
70. E. Maegdefrau and U. Hofmann, *Z. Krist.*, 1937, 98, 299-323.
71. S. B. Hendricks, *J. Geol.*, 1942, 50, 276-290.
72. J. W. Jordan, *Clays Clay Minerals*, 1963, 10, 299-308.
73. R. W. Mooney, A. G. Keenan and L. A. Wood, *J. Am. Chem. Soc.*, 1952, 74, 1367-1374.
74. K. Norrish, *Disc. Faraday. Soc.*, 1954, 18, 120-134.
75. B. K. G. Theng, "The Chemistry of Clay-Organic Reactions", 1974, p10, Adam Hilger, London, UK.
76. G. F. Walker, "The X-Ray Identification and Crystal Structures of Clay Minerals.", 1961, p297-324, Mineral Soc., London, UK.
77. R. A. Leonard, *Soil Sci. Soc. Am. Proc.*, 1970, 34, 339-343.
78. B. K. G. Theng, "The Chemistry of Clay-Organic Reactions", 1974, p261, Adam Hilger, London, UK.
79. M. M. Mortland and K. V. Raman, *Clays Clay Minerals*, 1968, 16, 393-398.
80. D. H. Solomon, B. C. Loft, and J. D. Swift, *Clays Clay Minerals*, 1968, 7, 399-408.
81. H. Weil-Malherbe and J. Weis, *J. Chem. Soc.*, 1948, 2164-2169.
82. S. B. Hendricks and L. T. Alexander, *J. Am. Chem. Soc. Argron.*, 1940, 32, 455-458.
83. J. B. Page, *Soil Sci.*, 1941, 51, 133-140.
84. J. M. Bloch, J. Charbonelle, and F. Kayser, *C. R. Acad. Sci. (Paris)*, 1953, 237, 57-59.
85. V. C. Farmer, and M. M. Mortland, *J. Chem. Soc.*, 1966, 344-351.

86. M. F. Traynor, M. M. Mortland, and T. J. Pinnavaia, *Clays and Clay Minerals*, **1978**, *26*(5), 318-326.
87. G. W. Brindley and R. E. Sempels, *Clay Miner.*, **1977**, *12*, 107.
88. G. Ozin and C. Gil, *Chem. Rev.*, **1989**, *89*, 1749-1764.
89. K. C. Molloy, C. Breen, and K. Quill, *Applied Organometallic Chemistry*, **1987**, *1*, 21-27.
90. E. Kikuchi, T. Matsuda, H. Fujiki, and Y. Morita, *Appl. Catal.*, **1984**, *11*, 331.
91. R. E. Grim, "Applied Clay Mineralogy", **1962**, McGraw-Hill, New York, USA.
92. M. K. H. Siddiqui, "Bleaching Earths", **1968**, Pergamon Press, Oxford, UK.
93. J. P. Chen, M. C. Hausladen, and R. T. Yang, *Journal of Catalysis*, **1995**, *151*, 135-146.
94. B. K. Green, "Pressure-sensitive record material", **1950**, *US. Pat.*, 2,505,470.
95. F. Figueras, *Catal. Rev. Sci. Eng.*, **1988**, *30*, 457.
96. J. Stert and J.-E. Otterstedt, *Appl. Catal.*, **1988**, *38*, 131.
97. D. Tichit, F. Fajula, F. Figueras, B. Doucourant, G. Mascherpa, C. Gueguen, and J. Bousquet, *Clays Clay Miner.*, **1988**, *36*, 369.
98. J.-R. Butruille and T. J. Pinnavaia, *Catalysis Today*, **1992**, *14*, 141-154.
99. R. Burch and C. I. Warburton, *J. Catal.*, **1986**, *97*, 511.
100. M. L. Occelli, R. A. Innes, F. S. S. Hwu, and J. W. Hightower, *Appl. Catal.*, **1985**, *14*, 69.
101. J. P. Chen, M. C. Hausladen, and R. T. Yang, *J. of Catal.*, **1995**, *151*, 135-146.
102. J. A. Bittles, A. K. Chaudhuri, and S. W. Benson, *J. Polymer Sci.*, **1964**, *A2*, 1221-1231.
103. D. H. Solomon and M. J. Rosser, *J. Appl. Polymer Sci.*, **1965**, *9*, 1261-1271.
104. H. Z. Friedlander, *J. Polymer Sci.*, **1964**, *C4*, 1291-1301.
105. H. Z. Friedlander and C. R. Frink, *Polymer Letters*, **1964**, *2*, 475-479.
106. H. Z. Friedlander, *Am. Chem. Soc. Polymer Reprints*, **1963**, *4*, 300-306.
107. D. H. Solomon and B. C. Loft, *Appl. Polymer Sci.*, **1968**, *12*, 1253-1262.
108. G. Broughton, *J. Phys. Chem.*, **1940**, *44*, 180-184.
109. E. Eisma and J. W. Jurg, "Organic Geochemistry", **1969**, p676-698, Springer Verlag, Berlin, Deutschland.
110. R. C. Hansford, *Advanced Catalysis*, **1952**, *4*, 1-29.
111. B. V. Romanovski, "Proc. 5th Int. Symp. on Relations between Homog. Heterog. Catal.", **1986**, p343, VNU Science press.
112. R. Parton, D. De Vos, and P. A. Jacobs, "Zeolite Microporous Solids: Synthesis, Structure and Reactivity", **1992**, p552, Kluwer Academic Publishers.
113. B. V. Romanovski, *Acta Phys. Chem.*, **1985**, *31*, 215.
114. D. R. C. Huybrechts, R. F. Parton, and P. A. Jacobs, *Stud. Surf. Sci. Catal.*, **1991**, *60*, 225.
115. R. F. Parton, D. R. C. Huybrechts, Ph. Buskens, and P. A. Jacobs, *Stud. Surf. Sci. Catal.*, **1991**, *65*, 47-54.
116. J. W. Geus, *Applied Catalysis*, **1986**, *25*, 313-333.
117. R. L. Garten, *Mössbauer Effect Methodology*, **1976**, *10*, 69.
118. B. C. Gates, J. R. Katzer and G. C. A. Schuit, "Chemistry of Catalytic Processes", **1979**, McGraw and Hill, London, UK.
119. A. J. H. M. Kock and J. W. Geus, *Progr. Surface Sci.*, **1985**, *20*, 165.
120. R. Dutartre, P. Bussiere, J. A. Dalmon, and G. A. Martin, *J. Catal.*, **1979**, *59*, 382.
121. A. Kool and F. Riesenfeld, "Gas Purification", **1979**, 381, Gulf Publishing Company Book Division, Houston, USA.
122. H. M. Fortuin, A. J. H. M. Kock, and J. W. Geus, *J. Catal.*, **1985**, *96*, 261.
123. A. J. van Dillen, J. W. Geus, and K. P. de Jong, "Transport in Non-Stoichiometric Compounds", **1982**, 467, Elsevier Science Publishing Co., Amsterdam, Netherlands.
124. H. Bohlbro, "An Investigation on the Kinetics of the Conversion of Carbon Monoxide by Water Vapour over Iron Oxide Based Catalysts", **1966**, Gjellerup, Copenhagen, Denmark.
125. T. J. Vink, O. L. J. Gijzeman, and J. W. Geus, *Surface Sci.*, **1985**, *150*, 14.
126. J. Galuszka, T. Sano, and J. A. Sawicki, *Journal of Catalysis*, **1992**, *136*, 96-109.
127. A. Hagen, F. Roessner, I. Weingart, and B. Spliethoff, *Zeolites*, **1995**, *15*, 270-275.
128. F. J. Berry, K. K. Rao and G. Oats, *Hyperfine Interactions*, **1994**, *83*, 343-345.
129. K. Lázár, I. Manninger, and B. M. Choudary, *Hyperfine Interactions*, **1991**, *69*, 747-750.
130. D. Ballivet-Tkatchenko, G. Coudurier, and H. Mozzanegg, *Stud. Surf. Sci. Catal.*, **1980**, *5*, 309.
131. D. Ballivet-Tkatchenko and I. Tkatchenko, *J. Mol. Catal.*, **1981**, *13*, 1.
132. J. Thiele, *Ber. Dtsch. Chem. Ges.*, **1900**, *33*, 660.

133. M. Rosenblum, "Chemistry of the Iron Group Metallocene", 1965, Wiley, New York, New York, USA.
134. S. I. Goldberg and D. W. Mayo, *Chemistry and Industry*, 1959, 671.
135. M. Rausch, M. Vogel, and H. Rosenberg, *J. Organic Chem.*, 1957, 22, 900-908.
136. M. D. Rausch, *Inorganic Chemistry*, 1962, 1(2), 414-417.
137. M. D. Rausch, *J. Organic Chem.*, 1961, 20, 1802-1805.
138. R. F. Kovar, M. D. Rausch, and H. Rosenberg, *Organometallic Chemical Synthesis*, 1970, 1, 173-181.
139. D. J. Booth, G. Marr, and B. W. Rockett, *J. Organometallic Chemistry*, 1973, 227-230.
140. R. A. Marcus and N. Sutin, *Biochim. Biophys. Acta*, 1985, 811, 265.
141. D. DeVault, "Quantum Mechanical Tunnelling in Biological Systems", 1984, 2nd Edition, Cambridge University Press, Cambridge, UK.
142. R. D. Cannon, "Electron Transfer Reactions", Butterworths, 1980, Boston, MA, USA.
143. G. Williams, G. R. Moore, and R. J. P. Williams, *Comments Inorg. Chem.*, 1985, 4, 55-98.
144. J. Jortner and M. Bixon, *J. Chem. Phys.*, 1988, 88, 167-170.
145. J. W. Perry, A. E. Stiegman, S. R. Marder, and D. R. Coulter, *Organic Materials for Non-linear Optics*, 1988, 69, 189.
146. M. B. Robin and P. Day, *Adv. Inorg. Chem. Radiochem*, 1967, 10, 247.
147. G. C. Allen and N. S. Hush, *Prog. Inorg. Chem.*, 1967, 8, 357.
148. N. S. Hush, *Prog. Inorg. Chem.*, 1967, 8, 391.
149. R. J. Webb, T.-Y. Dong, G. C. Pierpont, S. R. Boone, R. K. Chadha, and D. N. Hendrickson, *J. Am. Chem. Soc.*, 1991, 113, 4806-4812.
150. R. J. Webb, S. J. Geib, D. L. Staley, A. L. Rheingold, and D. N. Hendrickson, *J. Am. Chem. Soc.*, 1990, 112, 5031-5042.
151. T.-Y. Dong, D. N. Hendrickson, C. G. Pierpont, and M. F. Moore, *J. Am. Chem. Soc.*, 1986, 108, 963-971.
152. U. Sinha, M. D. Lowery, W. W. Ley, H. G. Drickamer, and D. N. Hendrickson, *J. Am. Chem. Soc.*, 1988, 110, 2471-2477.
153. W. E. Lamb, Jr, *Phys. Rev.*, 1939, 55, 190.
154. R. L. Mössbauer, *Z. Physik*, 1958, 151, 124.
155. P. B. Moon, *Proc. Phys. Soc.*, 1950, 63, 1189.
156. H. J. Lipkin, *Ann. Phys.*, 1960, 9, 194.
157. N. N. Greenwood and T. C. Gibb, "Mössbauer Spectroscopy", 1971, Chapman and Hall, London, United Kingdom.
158. G. Breit and E. Wigner, *Phys. Rev.*, 1936, 49, 519.
159. S. Margulies and J. R. Ehrman, *Nuclear Instr. Methods*, 1961, 12, 131.

$$160. J_0(ix) = 1 + \left(\frac{x}{2}\right)^2 + \left(\frac{\left(\frac{x}{2}\right)^4}{1^2 \cdot 2^2}\right) + \left(\frac{\left(\frac{x}{2}\right)^6}{1^2 \cdot 2^2 \cdot 3^2}\right) + \dots \quad \text{Equation 1.20b}$$

161. reference 53 in C, W, G, on page 44
162. L. Levy, L. Mitrani, and S. Ormandjiev, *Nuclear Instr. Methods*, 1964, 31, 233.
163. The signal from the counter initially passes through an Ortec 109PC pre-amplifier and then an Ortec 579A amplifier.
164. Ortec 427A.
165. Ortec 406A.
166. Elscint MDR-N-5
167. Elscint MVT4
168. R. V. Pound and G. A. Rebka, Jr, *Phys. Rev. Letters*, 1960, 4, 274.
169. B. D. Josephson, *Phys. Rev. Letters*, 1960, 4, 341.
170. W. G. V. Rosser, 'An Introduction to the Theory of Relativity', Butterworths, 1964, 114.
171. Y. Hazony, *J. Chem. Phys.*, 1966, 45, 2664.
172. A. Abragam, 'The principles of Nuclear Magnetism', 1961, Clarendon Press, Oxford, UK.
173. Mössbauer Effect Reference Data Journal, 1980, 3, 99.

174. G. J. Longworth, "Mössbauer Spectroscopy Applied to Inorganic Chemistry", 1984, chapter 4, Plenum Press, New York, USA.
175. S. V. Karyagin, *Proc. Acad. Sci. USSR, Phys. Chem. Soc.*, 1964, 148, 110-125.
176. According to source code.
177. See source code.
178. Cotton, Wilkinson, and Gaus, "Basic Inorganic Chemistry", 1987, Second Edition, Wiley, UK.
179. C. Breen, K. C. Molloy, and K. Quill, *Clay Min.*, 1992, 27, 445-455.
180. T-Y. Dong, D. N. Hendrickson, K. Iwai, M. J. Cohn, S. J. Geib, A. L. Rheingold, H. Sano, I. Motoyama, and S. Nakashima, *J. Am. Chem. Soc.*, 1985, 107, 7996-8008.
181. G. Brown, B. Edwards, E. G. Ormerod and A. H. Weir, *Clay Minerals*, 1972, 9, 407.
182. C. Breen, J. S. Brooks, S. Forder, A. Maggs, G. Marshall, and G. R. Stephenson, *J. Materials Chemistry*, 1995, 5(1), 97-104.
183. Stokes' Law for a particle of radius a falling with a terminal velocity v , through a liquid medium of viscosity ϖ can be written as $F = 6a\varpi v$, where F is the force on the particle. For a spherical particle of density η , this can be re-written as $t = (9/2)\varpi(d/\eta g^2)$, where t is the time in seconds, g is the acceleration due to gravity (9.8 m s^{-2}), and d is the distance in metres. So, if $t > 16$ hours, $\varpi = 10^{-3} \text{ Kg m}^{-1} \text{ s}^{-2}$ (20°C), $d = 0.1 \text{ m}$, then the particles obtained will have a radius $a < 1.4 \text{ }\mu\text{m}$.
184. C. Breen, J. J. Flynn, and G. M. B. Parkes, *Clay Min.*, 1993, 28, 123-137.
185. G. Matsubayashi, S. Ohta, and S. Okanu, *Inorganica Chimica Acta*, 1991, 184, 47-52.
186. K. Chatakondy, C. Formstone, M. Green, D. O'Hare, J. Twyman, and P. Wireman, *J. Mater. Chem.*, 1991, 1(2), 205-212.
187. S. Okanu and G. Matsubayashi, *J. Chem. Soc. Dalton Trans.*, 1992, 2441-2445.
188. E. Rodriguez-Castellon, A. Jiminez-Lopez, M. Martinez-Lara and L. Moreno-Real, *J. Inclusion Phenom.*, 1987, 6, 335-342.
189. J. S. Brooks, C. M. Care, and S. Plimley, *Hyperfine Interactions*, 1984, 20, 151-167.
190. A. Simopoulos, D. Petridis, A. Kostikas, and N. Gangas, *Hyperfine Interactions*, 1988, 41, 843-848.
191. A. Lund, D. G. Nicholson, R. V. Parish and J. P. Wright, *Acta Chem. Scand.*, 1994, 4, 1723-1729.
192. C. LeVanda, K. Bechaard, D. O. Cowan, U. T. Muella-Westerhoff, P. Eilbracht, G. A. Candela, and R. L. Collins, *J. Am. Chem. Soc.*, 1976, 98(11), 3183-3187.
193. M. T. Carter and A. J. Bard, *J. Electroanal. Chem.*, 1987, 229, 191-214.
194. M. N. Golovin, D. P. Wilkinson, J. T. Dudley, D. Holonko, and S. Woo, *J. Electrochem. Soc.*, 1992, 139(1), 5-10.
195. D. J. Booth, G. Marr, and B. Rockett, *J. Organometallic Chem.*, 1971, 227.
196. F. Farzenah and T. J. Pinnavaia, *Inorganic Chemistry*, 1983, 22, 2210-2216.
197. S. Okuno and G-E. Matsubayashi, *Chem. Lett.*, 1993, 799-802.
198. R. J. Webb, P. M. Hagen, R. J. Wittebort, M. Sorai, and D. N. Hendrickson, *Inorg. Chem.*, 1992, 32, 1791-1801.
199. S. Plimley, G. C. Corfield, J. S. Brooks, and C. M. Care, *Hyperfine Interactions*, 1984, 20, 151-167.
200. L. Cun, P. Xin, and Y. Zeng, *Synth. React. Inorg. Met.-Org. Chem.*, 1990, 20(9), 1231-1239.
201. J. W. Geus, *Applied Catal.*, 1986, 25, 313-333.
202. R. Schoonheydt, J. Van Den Eynde, and W. Stone, *Clay and Clay Minerals*, 1993, 41(5), 598-607.
203. D. Plee, F. Borg, L. Gatineau, and J. J. Fripiat, *J. Am. Chem. Soc.*, 1985, 107, 2362-2369.
204. M. F. de Jesus-Filho, M. A. Conçalves, J. C. Bosch-Neto, and V. K. Garg, *Hyperfine Interactions*, 1992, 70, 961-964.
205. G. Roch, M. E. Smith, and S. Drachman, *Abstract from Mineralogical Society spring 1996 Meeting*, 1996, "Investigation of thermal transformations of clay minerals by ^{27}Al and ^{29}Si solid-state nuclear magnetic resonance".
206. A. Mulaba-Bafubandi, J. Helsen, A. Maes, and G. Langouche, *Hyperfine Interactions*, 1992, 70, 1049-1052.
207. K. Lázár, A. M. Szelezcky, G. Vorbeck, R. Fricke, A. Vondrova, and J. Cejka, *J. Radioanalytical and Nuclear Chemistry*, 1995, 190(2), 407-411.
208. M. Petrera, A. Gennaro, P. Gherardi, G. Gubitosa, and N. Pernicone, *J. Chem. Soc., Faraday Trans. 1*, 1984, 80, 709-720.
209. W. N. Deglass, R. L. Garten, and M. Boudart, *J. Chem. Phys.*, 1969, 50, 4603-4610.
210. W. N. Deglass, R. L. Garten, and M. Boudart, *J. Phys. Chem.*, 1969, 73, 2970-2977.

211. Z. Gao and L. V. C. Rees, *Zeolites*, **1982**, *2*, 205-214.
212. B. L. Dickson and L. V. C. Rees, *J. Chem. Soc., Faraday Trans. 1*, **1974**, *70*, 2051.
213. R. Schmidt, M. D. Amiridis, J. A. Dumesic, L. M. Zelewski, and W. S. Millman, *J. Phys. Chem.*, **1992**, *96*, 8142-8149.
214. V. Luca and C. M. Cardile, *Clay Miner.*, **1989**, *24*, 555-560.
215. B. A. Goodman, *Clay Miner.*, **1987**, *22*, 36-41.
216. C. M. Cardile and I. W. M. Brown, *Clay Miner.*, **1988**, *23*, 13-18.
217. I. Rozenson and A. Heller-Kallai, *Inorg. Chem.*, **1978**, *26*, 173-178.
218. Y. Y. Huang and J. R. Anderson, *J. Catal.*, **1975**, *40*, 143-150.
219. W. Lee and B. J. Tartarchuk, *Hyperfine Interactions*, **1988**, *41*, 661-664.

10. Postgraduate study.

10.1 Courses and conferences.

Courses and conferences attended during the period of this research are listed below.

Date	Course / conference	Location	Duration
1992-1995	School of science seminars.	Sheffield Hallam University	1 hour weekly.
1992	Mössbauer Spectroscopy course.	Sheffield Hallam University.	12 x 1 hour.
1992	Mineralogical Society, Mineralogical Applications of Surface Science.	Manchester University.	2 days.
1993	X-ray methods of analysis	Sheffield Hallam University	16 x 1 hour.
1993-1996	Mössbauer discussion group annual conference ^{◆,▼}	Nottingham University.	2 days.
1994	Rutherford Appleton Laboratory Synchrotron Workshop.	Rutherford Appleton Laboratory.	1 day.
1994	M. R. I. open day. [▼]	Sheffield Hallam University.	1 day.
1995	X-ray fluorescence workshop.	Sheffield Hallam University.	5 days.
1995	M. R. I. open day. [▼]	Sheffield Hallam University.	1 day.
1996	Mineralogical Society, Clay Minerals group, spring meeting. [▼]	Sheffield Hallam University.	2 days.

◆ A paper titled “*Organometallic cation-exchanged phyllosilicates: variable-temperature ⁵⁷Fe Mössbauer spectroscopic and related studies of the adsorption of N,N-dimethylaminomethylferrocene on clays and pillared clays*” was presented at this meeting.

▼ A poster was presented at this event.

10.2 Publications.

The following article has been published by the author.

“Organometallic cation-exchanged phyllosilicates: variable-temperature ^{57}Fe Mössbauer spectroscopic and related studies of the adsorption of N, N-dimethylaminomethylferrocene on clays and pillared clays”. Christopher Breen, John S. Brooks, Susan D. Forder and Julian C. E. Hamer, *J. Mater. Chem.*, **1996**, 6(5), 849-859.

The following manuscripts are awaiting submission for publication.

“Organometallic cation-exchanged phyllosilicates: variable-temperature ^{57}Fe Mössbauer spectroscopic and related studies of 2, 2”-bis(dimethylamino)methyl]ferrocene on clay.”

“Organometallic cation-exchanged phyllosilicates: variable-temperature ^{57}Fe Mössbauer spectroscopic and related studies of a N, N-dimethylaminomethylferrocene - aluminium pillared Texas montmorillonite composite and its thermal decomposition products”.

Organometallic cation-exchanged phyllosilicates: variable-temperature ^{57}Fe Mössbauer spectroscopic and related studies of the adsorption of dimethylaminomethylferrocene on clays and pillared clays

Christopher Breen,* John S. Brooks, Susan Forder and Julian C. E. Hamer

Materials Research Institute, Sheffield Hallam University, Sheffield, UK S1 1WB

Variable-temperature ^{57}Fe Mössbauer spectroscopy, thermogravimetry (TG), powder X-ray diffraction (PXRD) and temperature-programmed solid insertion probe mass spectrometry (TP-SIP-MS) have been used to study the interaction of dimethylaminomethylferrocene (DMAMF) with Westone-L (WL), a low iron montmorillonite. The hydrochloride salt of DMAMF, (ferrocenylmethyl)dimethylammonium chloride (FMDMA⁺Cl⁻), was prepared and studied both prior and subsequent to exchange on the interlamellar sites of WL. X-Ray diffraction confirmed that the FMDMA⁺ cations were incorporated between the clay lamellae and the observed spacing of 15.1 Å was thermally stable up to 200 °C in air. TP-SIP-MS indicated that a small proportion of the incorporated metallocene was volatilised at temperatures below 400 °C, but that the majority decomposed *via* loss of cyclopentadienyl ligands leaving the metal centre between the sheets. A similar thermal degradation path was observed for DMAMF on aluminium pillared clay (Al-PILC). ^{57}Fe Mössbauer spectroscopy revealed that the FMDMA⁺ cation occupied a similar environment in the chloride salt, FMDMA⁺-WL and DMAMF-Al-PILC insofar as the isomer shift, δ , and quadrupole splitting, Δ , of the incorporated metallocene were essentially the same in all complexes and virtually identical to that observed for FMDMA⁺Cl⁻ ($\delta = 0.34 \text{ mm s}^{-1}$, $\Delta = 2.32 \text{ mm s}^{-1}$ at 300 K). The values for the Debye temperature θ_D and recoil-free fraction f determined from variable-temperature ^{57}Fe Mössbauer spectroscopy, were typically 140 K and 0.12, respectively, for FMDMA⁺Cl⁻ and FMDMA⁺-WL, thus confirming the similar environment occupied by the cation in the chloride salt and in WL. In contrast, the corresponding values for DMAMF-Al-PILC were 118 K and 0.06, respectively, indicating that the metallocene enjoyed much greater freedom in the galleries of the Al-PILC which exceed the dimensions of the metallocene compared to FMDMA⁺-WL where the organoiron cation itself determines the layer separation.

The incorporation of metallocenes into zeolites and zeotypes continues to attract interest. One particularly attractive goal is the production of catalytically active molecular fragments or small metallic clusters within a host matrix which, in addition to its thermal stability, can impart size and shape selectivity on the product distribution. In pursuit of this goal, considerable emphasis is placed on proving that the molecule is in the channel network and not bound to the surface, the characterisation of the incorporated species, and an explanation of how it interacts with its new environment before undertaking a detailed investigation of how it degrades upon thermal treatment.

Moller *et al.*¹ have presented a detailed investigation of the pyrolysis of ferrocene in zeolites presenting EXAFS and supporting mass spectral data which indicate the presence of half-sandwich fragments bound to the oxygens of the zeolite lattice. Indeed, attempts to incorporate neutral metallocenes within the confines of the zeolite framework can prove problematic since protons arising from residual water molecules readily oxidise ferrocene to ferrocenium.^{1,2} Recent studies^{3,4} have resulted in the successful inclusion of ferrocene into the channel network of $\text{AlPO}_4\text{-5}$ and $\text{AlPO}_4\text{-8}$ from which it cannot be sublimed. ^{57}Fe Mössbauer spectroscopy³ indicates that the metallocene is (i) rapidly reorientating within the channel network and (ii) largely unchanged following incorporation. EXAFS analysis,⁴ which provided independent evidence for the presence of unaltered ferrocene at temperatures up to 200 °C, indicated that the thermally degraded composite did not show any evidence of the clustering of iron atoms through either Fe-Fe or Fe-O-Fe interactions. Cobaltocene, however, was oxidised to cobalticenium upon incorporation within the channels of VPI-5.⁵ Once produced the cobalticenium remained thermally stable up to 130 °C, even though VPI-5 converted to $\text{AlPO}_4\text{-8}$ over this temperature interval.

An increase in layer separation, which exhibits enhanced

thermal stability, usually confirms incorporation of metallocenes into layered compounds but the nature of the included species, its interaction with the host and its thermal degradation path are still important. Ferrocenylalkylammonium cations have been adsorbed into a number of layered hosts including $\alpha\text{-Sn}(\text{HPO}_4)_2\cdot\text{H}_2\text{O}$ ($\alpha\text{-SnP}$), $\alpha\text{-Zr}(\text{HPO}_4)_2\cdot\text{H}_2\text{O}$ ($\alpha\text{-ZrP}$), MoO_3 and VOPO_4 . Dimethylaminomethylferrocene (DMAMF) was readily intercalated into $\alpha\text{-SnP}$ from aqueous solution forming a bilayer of protonated amines.⁶ In MoO_3 , ^{15}N CP MAS NMR provides evidence for two distinct environments for ^{15}N between the layers.⁷ A minor resonance was tentatively assigned to a small amount of oxidised guest species whilst the major resonance was intermediate between that for $(\text{FcCH}_2\text{CH}_2^{15}\text{NH}_3)^+\text{Cl}^-$ and $\text{FcCH}_2\text{CH}_2^{15}\text{NH}_2$, where $\text{Fc} = \text{Fe}(\eta\text{-C}_5\text{H}_5)(\eta\text{-C}_5\text{H}_4)$. NMR evidence was also utilised to show that the amino group was interacting with the host layer *via* $\text{P}-\text{O}\cdots\text{H}-\text{N}$ hydrogen bonds in $\text{Zr}(\text{HPO}_4)_2(\text{FcCH}_2\text{CH}_2^{15}\text{NH}_2)_{0.5}(\text{H}_2\text{O})_x$ ($x = 0.1-0.5$).⁷ The increase in layer expansion upon incorporation of $\text{FcCH}_2\text{CH}_2^{15}\text{NH}_2$ in both $\alpha\text{-ZrP}$ and MoO_3 suggests that the guests formed bilayers between the layers of each host. Large increases in d spacing, *i.e.* layer expansion, were also observed when ferrocenylalkylammonium iodides were incorporated between the layers of VOPO_4 . The length of the alkyl bridging unit apparently influences both the layer spacing and the extent to which the ferrocene moiety is oxidised upon intercalation.⁸

DMAMF was the molecule of choice in this investigation for several reasons. Firstly, it is easily transformed into the hydrochloride salt thus allowing straightforward replacement of the Na^+ cations resident on the exchange sites of a low-iron Texas bentonite. Secondly, incorporation into H^+ -exchanged WL ($\text{H}^+\text{-WL}$) should be possible *via* the *in situ* formation of the conjugate base, ferrocenylmethyl dimethylammonium (FMDMA⁺), in the interlamellar region. This second

approach also has the added attraction of neutralising the protons which may contribute to the oxidation of the ferrocene unit.^{1,2} Thirdly, it was our intention to incorporate DMAMF into the interlamellar gallery of an aluminium pillared interlayer clay (Al-PILC) by using the protons, formed during calcination of the pillar, to produce FMDMA⁺ ions. All these approaches have proven successful and the products have been characterised using a range of instrumental techniques including X-ray fluorescence spectrometry (XRF), powder X-ray diffraction (PXRD), thermogravimetry (TG), temperature-programmed solid insertion probe mass spectrometry (TP-SIP-MS), and Fourier transform IR (FTIR) spectroscopy. Moreover, variable-temperature Mössbauer spectroscopy has been extensively employed to determine how strongly DMAMF is held within the Al-PILC, where the gallery height exceeds the dimensions of the metallocene, compared to the situation in FMDMA⁺-WL where the dimensions of the metallocene itself determines the interlayer separation.

Experimental

Materials

The clay used in all the experiments was Westone-L (WL) a Texas bentonite, supplied by ECC International, which has a cation exchange capacity (cec) of 81 mequiv (100 g)⁻¹ and a low iron content of 0.5% m/m Fe₂O₃. This clay and the procedures used to convert it into the (nominal) < 2 μm particle size, Na-exchanged form, subsequently referred to as Na⁺-WL, have been described in detail elsewhere.⁹

The H⁺-exchanged form of Westone-L, H⁺-WL, was obtained by treating Na⁺-WL with aqueous 1 mol dm⁻³ sulfuric acid for 2 h at 25 °C, and washing until the residual conductivity of the supernatant was < 30 μS. The product was dried at room temperature. Elemental analysis using XRF spectrometry indicated that this treatment, as anticipated based on related results,¹⁰ had little effect on the layer composition. This was confirmed when ²⁷Al and ²⁹Si MAS NMR spectra of WL were unchanged following the acid treatment.

The aluminium pillared clay was prepared using the method described by Schoonheydt *et al.*¹¹ Na⁺-WL was suspended in 100 cm³ of water and stirred for 6 h. An aqueous solution of NaOH (17 cm³, 0.4 mol dm⁻³) was added dropwise at 1 cm³ min⁻¹ to an aqueous solution of AlCl₃·6H₂O (17 cm³, 0.2 mol dm⁻³, 10 cec) with vigorous stirring. The resulting solution was heated at reflux for 3 h and then added dropwise at 8 cm³ min⁻¹ to the Na⁺-WL suspension. This was stirred for 12 h, and then washed with deionised water until the conductivity of the supernatant fell below 30 μS. The clay was air-dried and then calcined at 500 °C for 1 h. This yielded aluminium pillared WL (Al-PILC) with an interlayer spacing of 18.8 Å.

(Ferrocenylmethyl)dimethylammonium chloride (FMDMACl) was prepared using *N,N*-dimethylaminomethylferrocene (DMAMF) supplied by Aldrich Chemicals. DMAMF (1 g, 4.12 mmol) was added dropwise with stirring to 50 cm³ of 1 mol dm⁻³ HCl. This was evaporated (*in vacuo*) to give a green solid. Recrystallisation from CHCl₃-Et₂O gave long golden brown crystals in 87% yield. (Analysis: Found C, 55.59; H, 6.40; N, 5.02. Calc. C, 55.85; H, 6.49; N, 5.01%). The cationic portion of this salt will subsequently be referred to as FMDMA⁺.

FMDMA⁺-WL was prepared using three different methods. In the first method FMDMACl (0.23 g, 1 cec, 0.81 mmol) was dissolved in 50 cm³ of deionised water, and 1 g of powdered Na⁺-WL, dried at 120 °C, was added. The suspension was stirred for 8 h at 25 °C before the clay was isolated and the process repeated twice more. The product was then washed (5 × 120 cm³ deionised water) as above. The product is subsequently referred to as FMDMA⁺-WL(1). (Analysis: Calc. 100% exchange; C, 14.2. Found C, 11.0%, equivalent to 80%

exchange). In the second method DMAMF (0.46 g, 2 cec, 1.62 mmol) was suspended in 50 cm³ deionised water, and 5 cm³ of 1 mol dm⁻³ HCl (an excess) added dropwise with stirring to give a solution of FMDMACl. Ground Na⁺-WL powder (1 g), dried at 120 °C, was added and the resulting suspension was stirred for 18 h at 25 °C. The clay was isolated by centrifugation and the process repeated twice more. Finally, the product [referred to as FMDMA⁺-WL(2)] was washed with deionised water (5 × 120 cm³), and air dried at room temperature. In the third method, 1 g of H⁺-WL, dried at 120 °C, was added to DMAMF (0.46 g, 2 cec, 1.62 mmol) dissolved in 50 cm³ of methanol. The resulting suspension was stirred for 18 h at 25 °C, centrifuged and finally washed with methanol (5 × 120 cm³). The product [referred to as FMDMA⁺-WL(3)] was then air dried at room temperature.

DMAMF (1.29 g, 3 cec, 2.43 mmol) was suspended in 100 cm³ of deionised water, and 1 g of powdered Na⁺-WL (dried at 120 °C) was added. The suspension was left to stir for 6 h at 25 °C. The clay was then isolated by centrifugation and the process repeated twice more. The final product, DMAMF-WL, was then washed (3 × 120 cm³ H₂O, 3 × 120 cm³ MeOH, 1 × 120 cm³ H₂O).

DMAMF (0.43 g, 2 cec, 1.62 mmol) was dissolved in 50 cm³ of methanol and 1 g of the calcined pillared clay, pretreated at 120 °C, added. The suspension was stirred for 18 h, washed (5 × 120 cm³ methanol), and collected in the normal manner. The product is subsequently referred to as DMAMF-Al-PILC. (Analysis: Calc. 100% exchange; C, 14.2. Found C, 4.2% equivalent to 29% exchange).

Adsorption isotherms

Methanolic solutions (20 cm³) of DMAMF-FMDMACl in the range 0–3 cec were prepared, and the absorption at 435 nm, characteristic of both DMAMF and FMDMACl, measured. Clay (0.1 g) dried at 120 °C was then added and the suspensions shaken overnight. These were then centrifuged, and the absorbance of the supernatant measured using a Hitachi U-2000 double-beam UV-VIS spectrophotometer, with cells of path-length 1 cm.

Thermogravimetry

Thermogravimetry was performed using a Mettler TG50 thermobalance connected to a Mettler TC10A processor. Samples (5–10 mg) were heated from 25 to 800 °C, at a rate of 20 °C min⁻¹, in a dynamic atmosphere of dry N₂ gas flowing at 20 cm³ min⁻¹.

X-Ray diffraction

X-Ray diffraction traces of pressed powder samples were recorded using a Philips PW1830 diffractometer using Cu-Kα radiation (λ = 1.5418 Å) whereas a Philips PW1050, using Co-Kα radiation (λ = 1.789 Å) was used to study partially oriented samples on glass slides. A heating stage manufactured according to Brown *et al.*¹² was used to heat the partially oriented samples in the temperature range 20–400 °C.

X-Ray fluorescence

XRF analyses of samples presented as lithium tetraborate beads were obtained using a Philips PW2400 X-ray spectrometer calibrated using certified reference materials. C,H,N analyses were obtained from Medac Ltd.

Mössbauer

The Mössbauer spectrometer, cryostat, sample presentation and fitting routines have been described in detail elsewhere.⁹ Absorbers of Mössbauer *t* values < 1, with a maximum iron concentration of 7 mg cm⁻² for FMDMACl, were studied. The

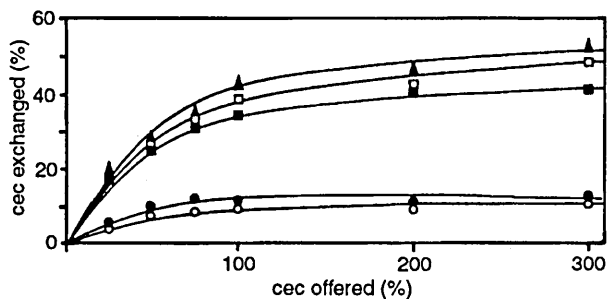


Fig. 1 Isotherms for the adsorption, from methanol, of DMAMF on Na⁺-WL (●) and Al-PILC (○) and FMDMA⁺ on Na⁺-WL (▲), H⁺-WL (■) and on Na⁺-WL in the presence of [H⁺] (□)

values of the isomer shift, δ , the quadrupole splitting, Δ , and the linewidths, Γ , quoted are relative to the source, ⁵⁷Co in a rhodium matrix at room temperature.

Results

Adsorption isotherms

The adsorption of DMAMF onto Na⁺-WL and Al-PILC from methanol resulted in an uptake equivalent to only 10% of the cec (Fig. 1). The loading on the Al-PILC was disappointing given that when the pillared clay is calcined at 500 °C, protons are released as the aluminium oxide pillars are formed, which then migrate into the layers. These protons can be enticed into the interlayer using strong bases such as ammonia.¹³ Thus it was anticipated that interaction with these protons might provide the driving force to draw DMAMF into the galleries in the pillared clay. Formation of the hydrochloride salt, FMDMA⁺Cl, followed by contact with the clay in methanol proved successful yielding 53% exchange. Production of the chloride salt *in situ*, by the addition of acid to the methanolic solutions followed by contact with the clay, was undertaken and this resulted in 48% exchange. In the final experiment of the series, DMAMF was contacted with H⁺-WL. Exchange was successful although the loading achieved was only 45% of the theoretical value, perhaps implying that the upper limit for exchange using methanol as solvent was near 50% cec.

Elemental analyses

The loadings achieved following one contact in methanol were disappointing so attempts were made to increase the level of exchange by contacting Na⁺- or H⁺-WL three times with the metallocene using water as solvent. In the main this proved more successful as the following results show. The theoretical value for the Na₂O content of fully Na⁺-exchanged WL, given a cec of 81 mequiv (100 g clay)⁻¹, is 2.09 mass% whereas the Fe₂O₃ content should increase from 0.5 to 5.6% m/m if FMDMA⁺ ions occupy all the exchange sites. Note, however, that the calculations for iron content assume that no oxidation or volatilisation of the metallocene occurred, in line with previous observations.^{3,4,9} Table 1 lists the results of the XRF and C,H,N analyses and expresses these values as the percentage of exchange sites occupied by the metallocene or vacated by the Na⁺ ions. When the metallocene is adsorbed in the cationic form the number of resident Na⁺ ions replaced should correlate with the amount of iron adsorbed given that both species carry a single positive charge. Thus the discrepancy between the number of Na⁺ ions displaced, the amount of iron adsorbed and the C,H,N analysis was a cause of initial concern (Table 1). For example, C,H,N analysis indicated that FMDMA⁺ ions occupied 80% of the exchange sites in FMDMA⁺-WL(1), a figure which agreed with the number of Na⁺ ions displaced (76% cec) but not with the amount of iron

determined by XRF (59%). The figures for DMAMF-Al-PILC behave in a similar manner. C,H,N analysis indicated that DMAMF occupied 29% of the exchange sites, whereas XRF data suggested a value of 33%. The value of 67% Na⁺ displacement when DMAMF was contacted directly with Na⁺-WL (DMAMF-WL) was unexpected. It is proposed that there were sufficient protons present during this process to protonate enough DMAMF to cause this level of exchange.

Thermogravimetry

The derivative thermograms presented in Fig. 2 were obtained after each sample had been pre-conditioned in the nitrogen purge gas for 15 min. This procedure removes much of the physisorbed water, which contributes little information, and serves to emphasise the maxima associated with desorption of strongly bonded species. The derivative thermogram for Na⁺-WL [Fig. 2(a)] shows that the desorption of the remaining physisorbed water was essentially complete by 100 °C, with dehydroxylation of the structure reaching a maximum at 680 °C.¹⁴ Liquid DMAMF boils at 200 °C and so little information regarding its decomposition was gained. The corresponding chloride salt, FMDMA⁺Cl, began to decompose at ca. 150 °C with an associated mass loss of 27%. Further mass losses of 15, 9.4 and 14.5% occurred with associated maxima at 350, 460 and 520 °C, respectively [Fig. 2(b)]. The derivative thermogram for FMDMA⁺Cl provides a useful fingerprint for the protonated moiety insofar as a number of the mass losses were also observed in FMDMA⁺-WL(1) [Fig. 2(c)]. For example, a maximum in the derivative thermogram for FMDMA⁺-WL(1) at 200 °C was clearly visible and there was evidence for the presence of a maximum at 350 °C. The maximum at 625 °C may reflect some combination of the FMDMA⁺Cl maximum at 620 °C and the structural dehydroxylation of WL which maximised at 680 °C [Fig. 2(a)]. In addition, a new maximum at 740 °C which corresponded to twice the mass loss associated with the maximum at 200 °C was observed, perhaps indicating that the FMDMA⁺ cation follows a different decomposition pathway when exchanged onto WL. The derivative thermogram for the desorption of DMAMF from Al-PILC exhibited a small maximum at 200 °C but was dominated by a peak at 550 °C, which accounted for 8% of the initial mass or 43% of the total mass loss.

TP-SIP-MS

TP-SIP-MS was used to explore the way in which the various complexes were thermally degraded. The maxima in the total ion current (TIC) for the desorption of metallocene from WL and Al-PILC correlate quite well with those observed in the derivative thermograms, which is reassuring given the different conditions under which they are obtained.¹⁵ The TIC for the thermal decomposition of the incorporated metallocene, which reached maxima for FMDMA⁺-WL and DMAMF-Al-PILC at 225 and 250 °C respectively, represented the combination of a large number of mass fractions. In particular, peaks at *m/z* 214 (NCH₂Fc), 200 (CH₂Fc), 186 (Cp₂Fe), 134 [CH₂(η^5 -C₅H₄)Fe] and 121 (CpFe) [Fc=Fe(η -C₅H₅)(η -C₅H₄); Cp= η^5 -C₅H₅] proved that iron was volatilised from the sample, although this process was essentially complete by 400 °C. Above 400 °C the decomposition products contained only ligand, with characteristic peaks at *m/z* 79 (CH₂Cp) and 66 (Cp). No iron was desorbed. This behaviour is summarised in Fig. 3 where the intensity of peaks, selected to distinguish between metallocene and ligand desorption, are plotted as a function of sample temperature. It is important not to equate TIC with the amount of metallocene desorbed. Reference to the derivative thermograms in Fig. 2, where the area under the peaks is directly related to the mass loss, indicates that the amount of material desorbed below 400 °C was not as significant as the TIC suggests, yet the mass spectra quite clearly

Table 1 Summary of elemental analysis data for the samples described in the text

	Fe content ^a (±0.1)% (m/m)	Na content ^a (±0.1)% (m/m)	Fe adsorbed ^a (% cec)	Na desorbed ^a (% cec)	metallocene adsorbed ^b
Na ⁺ -WL	0.4	1.9	—	—	—
H ⁺ -WL	0.4	0.1	—	94	—
Al-PILC	0.4	0.0	—	100	—
FMDMA ⁺ -WL(1)	3.4	0.5	59	76	80
FMDMA ⁺ -WL(2)	4.1	0.1	72	95	—
FMDMA ⁺ -WL(3)	3.4	0.1	59	95	—
DMAMF-WL	3.3	0.7	57	67	—
DMAMF-Al-PILC	2.0	0.1	33	—	29

^a Based on XRF analysis figures. ^b Based on C,H,N analysis figures.

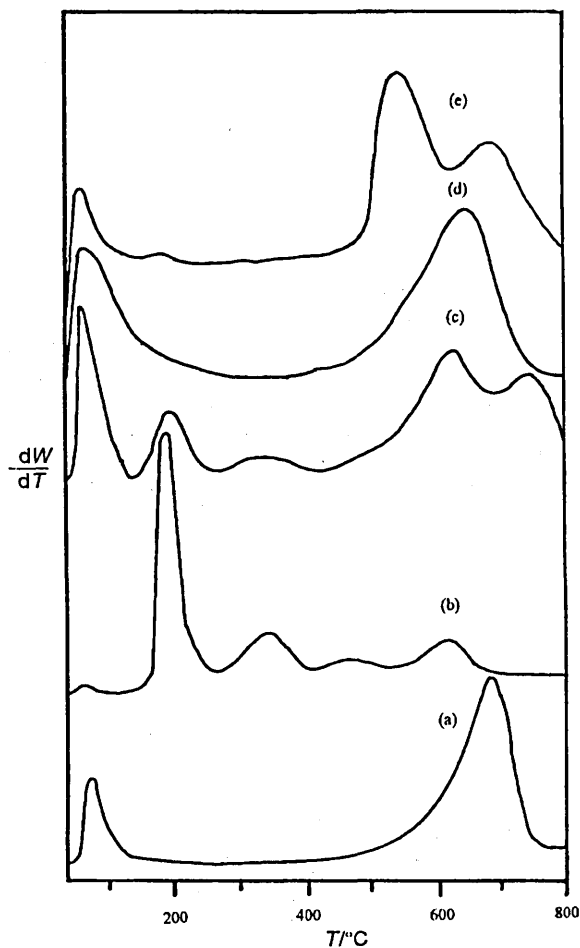


Fig. 2 Derivative thermograms for (a) Na⁺-WL, (b) FMDMA⁺-WL(1), (c) FMDMA⁺-WL(2), (d) Al-PILC and (e) DMAMF-Al-PILC

corroborate the loss of some iron which explains the discrepancies noted in the elemental analyses above. Mass spectral analysis of the peaks contributing to the large maximum at 680 °C in the TIC for the desorption of DMAMF from Al-PILC proved that this maximum was due to dehydroxylation of the structure and the pillar.

Powder X-ray diffraction

The quality of the X-ray diffraction traces collected using pressed powder samples is shown in Fig. 4 and the index for each pattern is given in Table 2. The basal spacing for Na⁺-WL was 12.5 Å, which is commensurate with one water layer between adjacent clay layers, whilst the spacing for FMDMA⁺-WL(1) [Fig 4(b)] was 15.1 Å. The diffraction trace for the Al-PILC, after firing for 1 h at 500 °C, exhibited a

spacing of 18.8 Å, thus confirming that the pillaring process had been successful.

Variable-temperature X-ray diffraction

VTXRD provides the first real indication that the metallocene cation was present within the interlayer of WL. At room temperature and humidity Na⁺-WL exhibits a *d* spacing of 12.5 Å which upon heating to 50 °C decreases to 9.6 Å. This latter value is diagnostic of an Na⁺-exchanged clay from which all the interlamellar water has been expelled. Incorporation of a large species such as the FMDMA⁺ cation between the aluminosilicate layers increases the *d* spacing and makes it more thermally stable than the corresponding water-expanded material. The 15.1 Å spacing, as evidenced by the 001 and 003 reflections, remained essentially constant until the composite was heated to 200 °C, whereupon it collapsed to 13.0 Å (Fig. 5). This reduction in the *d* spacing coincides with the onset of the first major mass loss in the derivative thermogram for FMDMA⁺-WL(1) [Fig 2(c)] and there was no evidence of a 9.6 Å spacing, characteristic of a completely collapsed clay, which indicates that the decomposition products of the FMDMA⁺ cations remained in the interlayer region. The PXRD trace for the pillared clay provided little information regarding the location of the metallocene because the spacing remained constant at 18.8 Å and no extra peaks were observed, suggesting that the metallocene was not mixed with Al-PILC in a powder form. The variable-temperature Mössbauer spectroscopic data (*vide infra*) support this observation.

Mössbauer spectroscopy

⁵⁷Fe Mössbauer data were obtained for FMDMA⁺, as the chloride salt, and after incorporation into Westone-L, FMDMA⁺-WL(1)-(3) and Al-PILC, respectively, over the temperature range 15–300 K. Selected spectra are shown in Fig. 6 and 7 and the parameters derived from the fitting process are listed in Tables 3–5. FMDMA⁺ was fitted as a resolved quadrupole doublet whereas the fitting strategies for the clay-supported complexes had to allow for the small amount of iron in the clay structure, the absorption of which became increasingly more significant as the temperature increased. It is common for the recoil-free fraction of inorganic species to decrease more slowly with temperature than that for an organometallic species. This was particularly evident in DMAMF-Al-PILC (Fig. 7) where the combination of a low loading, equivalent to 29% cec, and the much lower recoil-free fraction meant that the contribution from the structural iron in WL dominated the spectrum above 200 K. The similarity of the Mössbauer parameters, δ and Δ , for FMDMA⁺ as the chloride salt and when incorporated in the host aluminosilicate indicates that there was no substantial change in the organometallic cations upon exchange. In particular, the absence of a component with a reduced quadrupole splitting suggested that the ferrocene unit had not been oxidised

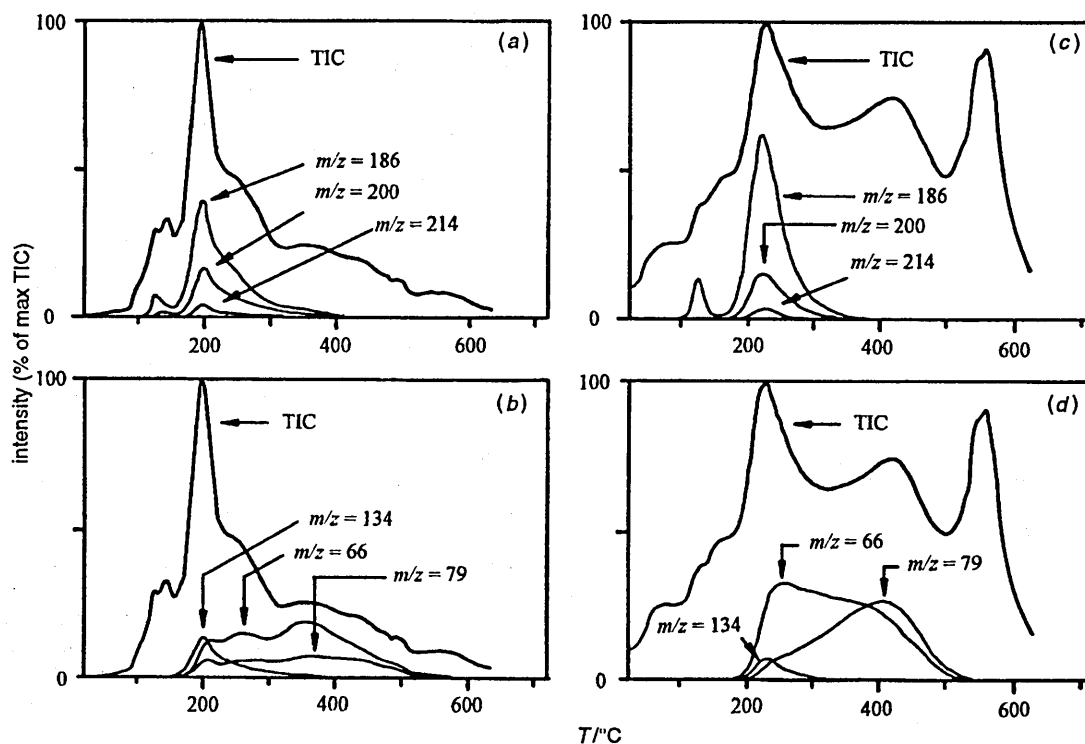


Fig. 3 TP-SIP-MS data for (a) (b) FMDMA⁺-WL(1) and (c) (d) DMAMF-Al-PILC

Table 2 PXRD data for Na⁺-WL and FMDMA⁺-WL(1)

2θ/degrees	I	h	k	l	d _{obs} /Å	d _{calc} /Å
Na ⁺ -WL ^a						
7.06	100	0	0	1	12.51	12.50
14.17	8	0	0	2	6.24	6.25
19.87	3	1	1	0	4.46	4.45
		0	2	0		
28.43	27	0	0	4	3.14	3.13
35.96	2	0	0	5	2.49	2.50
43.48	3	0	0	6	2.08	2.08
FMDMA ⁺ -WL(1) ^b						
5.86	100	0	0	1	15.10	15.10
11.65	3	0	0	2	7.59	7.55
17.65	17	0	0	3	5.02	5.03
19.84	8	1	1	0	4.47	4.45
		0	2	0		
23.62	4	0	0	4	3.76	3.78
29.63	5	0	0	5	3.01	3.02
34.71	2	1	3	0	2.58	2.60
41.91	1	0	0	7	2.15	2.16
61.94	2	0	6	0	1.49	1.50

^a a = 5.2, b = 9.3, c = 12.5 Å. ^b a = 5.2, b = 9.3, c = 15.1 Å.

upon intercalation. The variation of the absorption area data with temperature, for the organometallic cation, was analysed and the resulting plots of log (area) vs. temperature for the samples under investigation are presented in Fig. 8. The values of θ_D and f , obtained using software which uses the full Debye integral, are presented in Table 6. The illustrative data presented concentrates on FMDMA⁺-WL and DMAMF-Al-PILC, but these are representative of all the samples studied as the data in Table 6 and the plots in Fig. 8 confirm.

Discussion

The adsorption isotherm data (Fig. 1) and the results of the elemental analyses confirm that DMAMF, and the corresponding FMDMA⁺ cation, was adsorbed onto WL from both methanol and water with varying degrees of success to produce a composite with a basal spacing of 15.1 Å. The method of

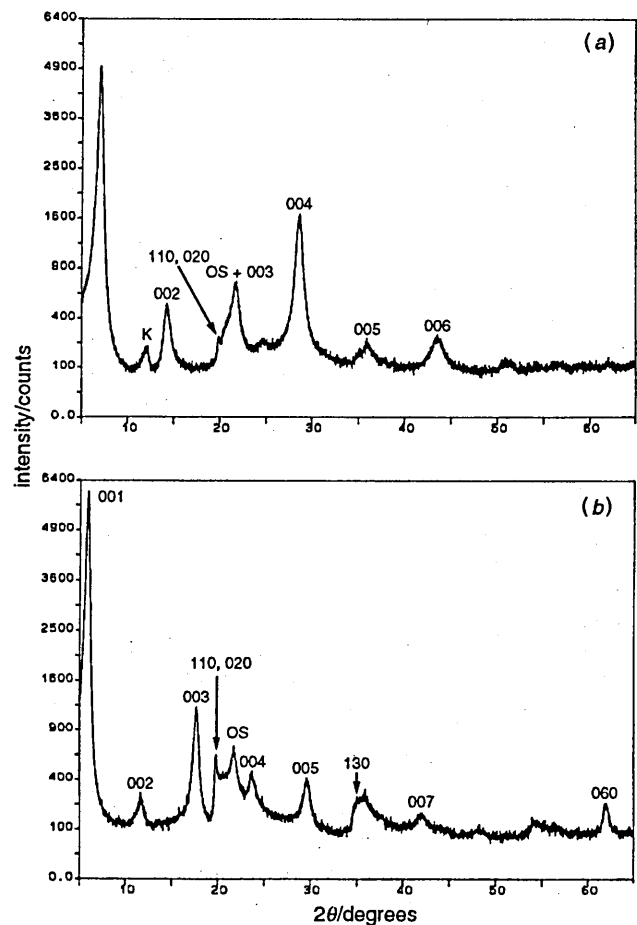


Fig. 4 PXRD profiles, obtained using Cu-K α radiation, for (a) Na⁺-WL and (b) FMDMA⁺-WL(1) (OS small quantity of fine grained opaline silica impurity, K = kaolin)

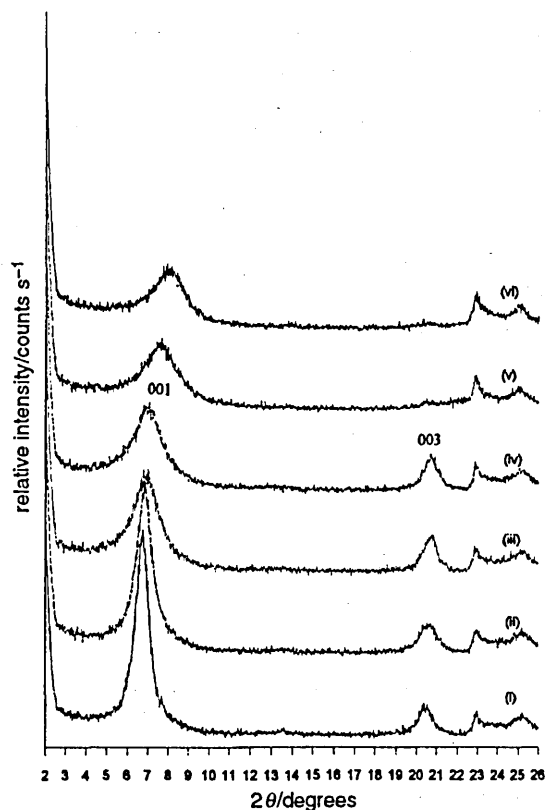


Fig. 5 XRD profiles, obtained using Co-K α radiation, for FMDMA⁺-WL(1) at (i) 20, (ii) 50, (iii) 100, (iv) 150, (v) 200 and (vi) 250 °C

introduction of the FMDMA⁺ cation into the interlayer region influences the amount of cation adsorbed but, in general, acceptable levels of incorporation are achieved from multiple contacts in water. The poor uptake of DMAMF from methanol was attributed to a combination of two distinct factors. Firstly, incomplete separation of the layers due to the solvent (methanol), and secondly, there was little to favour incorporation of a neutral species between the layers of Na⁺-WL. Indeed, similar loadings of cationic half-sandwich compounds of iron were achieved using methanol as solvent.⁹ The low loading of the DMAMF on Al-PILC, from both methanol and water, was a combination of two factors. Firstly, the protons generated during the firing process may not have been available for complexation with the dimethylamino group on the metallocene. Secondly, it is probable that sites at the periphery of the interlayer region were filled first thus preventing the diffusion of further molecules into the structure.

The observed basal spacing of 15.1 Å indicates that, in contrast to the bilayer formation in α -SnP,⁶ MoO₃ and α -ZrP,⁷ and VOPO₄,⁸ only a single layer of metallocene resides in the interlamellar region of WL. The reduction in the basal spacing from 15.1 to 13.0 Å when FMDMA⁺-WL(1) was heated to 200 °C must be attributed to the decomposition of the FMDMA⁺ cation within the interlayer region. Moreover, the final value of 13.0 Å indicates quite clearly that the decomposition was not complete. These observations are in accord with both the derivative thermograms (Fig. 2) and the TP-SIP-MS results (Fig. 3) and suggest that some residue containing iron was left between the aluminosilicate lamellae. The volatilisation of some of the metallocene, which contrasts with recent studies of organoiron species on WL⁹ and AlPO₄-5,^{3,4} at temperatures around 200 °C may contribute, at least in part, to the reduction in basal spacing. The data presented in Table 1 indicate that the FMDMA⁺ cation displaced Na⁺ ions from the exchange sites on WL; thus it is unlikely that the volatilised metallocene arose solely from surface sites,

although the possibility is not rejected. The similarity of the desorption profiles, derived from mass spectrometry (Fig. 3), for FMDMA⁺-WL(1) and DMAMF-Al-PILC suggest that the metallocene molecules are desorbed from similar sites with the proportion of strongly bonded molecules, which only lose ligand upon thermal treatment, outnumbering those which desorb near 200 °C. The mass spectral data give no indication that the aminometalmetallocene is changed upon incorporation into the host structures and this is supported by the parameters for the incorporated metallocenes derived from the ⁵⁷Fe Mössbauer data.

Fig. 5 shows that the 15.1 Å basal spacing was stable at 200 °C. The thickness of the metallocene is 6.65 Å¹⁶ which, when added to the layer thickness of 9.6 Å, should result in a *d* spacing of 16.3 Å. However, the incorporation of FMDMA⁺ cations in VOPO₄⁸ only resulted in an expansion of 5.8 Å, a value close to that of 5.5 Å observed here. It is common for metallocene expanded layered materials to display *d* spacings up to 1 Å less than the value anticipated from the molecular dimensions of the guest, particularly in swelling layer lattices such as α -Zr(HPO₄)₂,¹⁷ VOPO₄,¹⁸ and V₂O₅.^{7,19} Given the uncertainty regarding the increase in *d* spacing of metallocene expanded layered hosts, conclusions regarding the orientation of the FMDMA⁺ cation are difficult to reach. However, the observed 15.1 Å *d* spacing of FMDMA⁺-WL(1) is consistent with the cation adopting an orientation where the plane of the cyclopentadienyl ring is perpendicular to the basal surface with the side chain accommodated in the interlamellar space, thus making no contribution to the layer expansion [Fig. 9(a)]. It is more difficult to ascertain the orientation of the metallocene in DMAMF-Al-PILC because the height of the pillars, which exceed the dimensions of DMAMF, determine the interlayer spacing [Fig. 9(b)] and this spacing does not alter after the PILC has been fired.

The ⁵⁷Fe Mössbauer spectrum for FMDMACl consisted of a single symmetric doublet, with a quadrupole splitting, Δ , of 2.34 mm s⁻¹, which remained constant between 15 and 300 K, whereas the isomer shift, δ , exhibited a typical second-order Doppler shift effect, falling steadily from an initial value of 0.41 mm s⁻¹ at 15 K to a final value of 0.34 mm s⁻¹ at 300 K (Table 3). Analysis of the normalised area vs temperature data (Fig. 7) yielded a Debye temperature, θ_D , of 144 K and a recoil free fraction, $f_{291\text{ K}}$, of 0.14 when an effective recoiling mass of 57 u was assumed. The low θ_D , which is typical of organometallic compounds, may be further reduced in this instance owing to the difference in size between the large FMDMA⁺ cation and the smaller chloride anion. The halfwidth at half height, $\Gamma/2$, of the absorption peaks varied from 0.13 mm s⁻¹ at 15 K to 0.16 mm s⁻¹ at 300 K. This broadening arises owing to increased vibration within the lattice as the temperature of the solid was increased.

Fig. 6 illustrates how the ⁵⁷Fe Mössbauer spectrum for FMDMA⁺-WL varied with temperature. The sharp, outer doublet, which dominates the spectra at low temperatures, was assigned to the FMDMA⁺ cation (*vide infra*). The broad, ill defined absorption seen between the wings of this sharp, outer doublet has been attributed to two components. The first is a weak, broad doublet arising from the small amount of Fe^{III}, present owing to isomorphous substitution in the octahedral sheet of WL [Q(1) in Table 4], whilst the second is a broad singlet, characteristic of Fe⁰ [S(1) in Table 4]. This singlet arises from the small quantity of iron which was added to the graphite rod to aid machining when making the sample holders. This contribution is not normally observed, but owing to the low iron content of the materials under study, the absorption becomes significant. The broadness of the Fe^{III} doublet indicates that the iron present in the clay occupies a range of closely related sites.

When exchanged into WL the FMDMA⁺ cations exhibited isomer shifts and quadrupole splittings which were very similar to those determined for FMDMACl (Table 3) and varied little

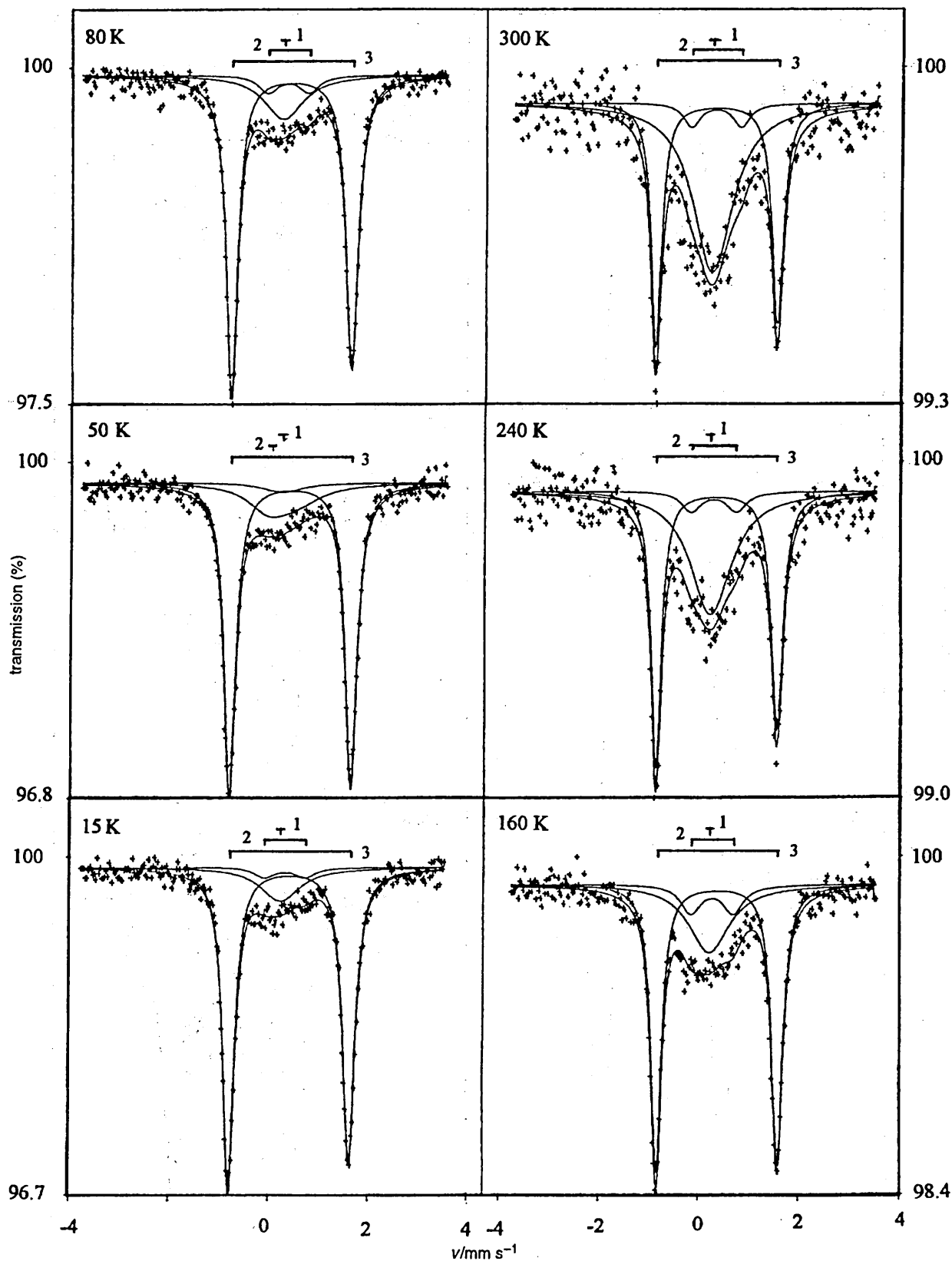


Fig. 6 Variable-temperature ^{57}Fe Mössbauer spectra collected for $\text{FMDMA}^+\text{-WL}(1)$ at the temperatures indicated

despite the different routes by which the clay/metalloocene were prepared. The similarity of these values indicates that the FMDMA^+ cations occupied similar environments in both the chloride salt and in WL. This is firm evidence that WL simply expanded to accommodate the FMDMA^+ cation, with no oxidation of the iron centre nor distortion in the orientation of the cyclopentadienyl rings. Given that the increase in the d spacing upon incorporation of the FMDMA^+ cation into WL

was 1.0 \AA less than anticipated, and that previous studies²⁰ have shown that a 9° tilt in the cyclopentadienyl rings reduces the isomer shift by 0.02 mm s^{-1} and the quadrupole splitting by 0.11 mm s^{-1} , the similarity of the observed parameters was surprising. Nonetheless, it is consistent with an earlier study where a similar low d spacing did not alter appreciably the Mössbauer parameters of half sandwich organoiron compounds when they were incorporated into WL.⁹

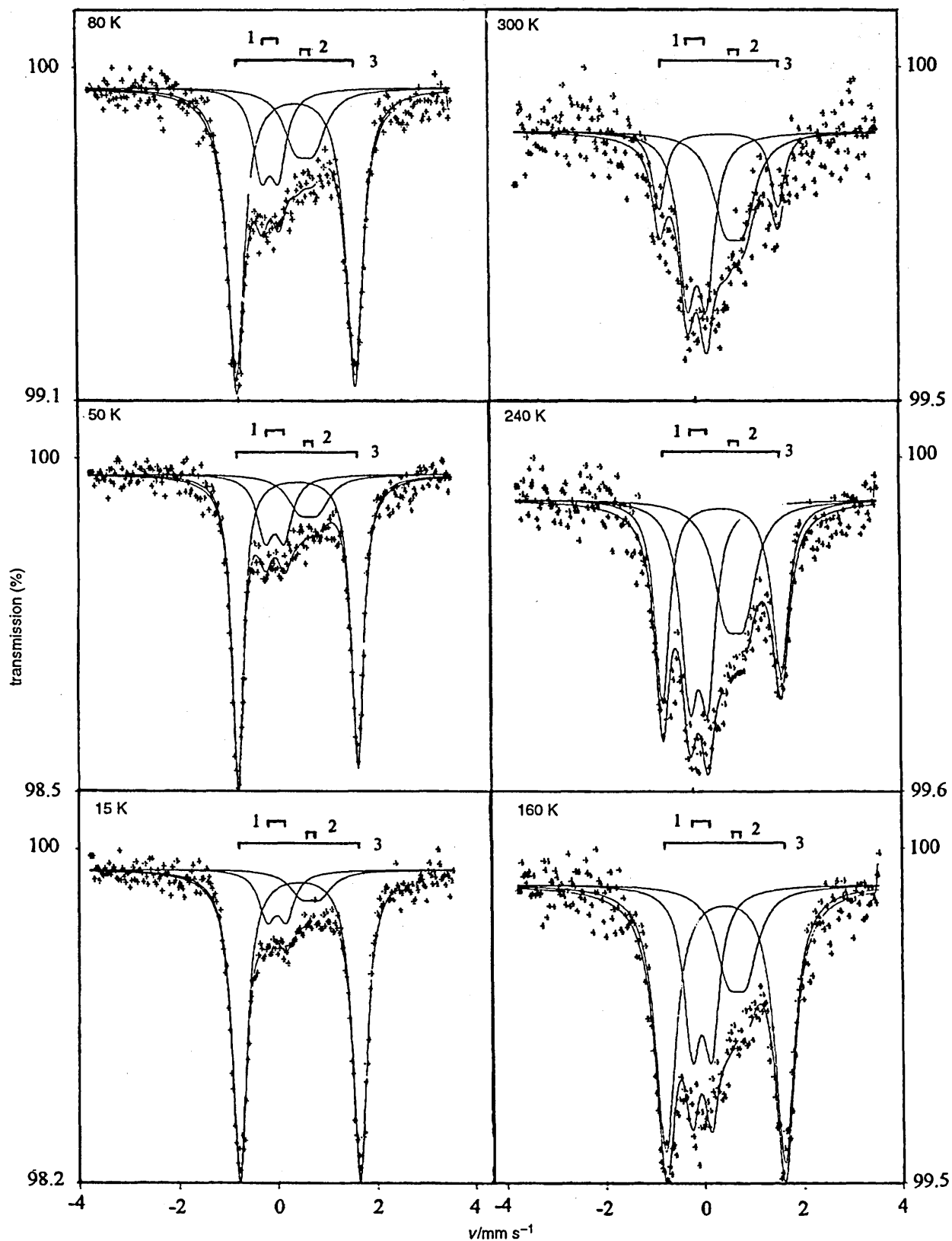


Fig. 7 Variable-temperature ^{57}Fe Mössbauer spectra collected for DMAMF-Al-PILC at the temperatures indicated

The Mössbauer spectra for the complex formed when Al-PILC was treated with DMAMF (Fig. 7) were of lower quality than those recorded for the FMDMA⁺-WL(1)-(3) samples because the amount of iron present was only equivalent to 29% cec, and the recoil-free fraction fell off much more rapidly. Nonetheless, the values of δ and Δ determined from these spectra (Table 5), together with the resistance of the incorporated metallocene to the washing procedures, suggests that the

incorporated species was the FMDMA⁺ cation. The narrow doublet [Q(1) in Table 5] became evident in the Mössbauer spectrum of the fired Al-PILC prior to contact with DMAMF. The origin of this doublet has not been studied extensively.

The consistency of the values of Δ and δ determined for the FMDMA⁺ cations in WL together with their similarity to the values for the chloride salt suggested that the organoiron species was the same in all the samples. Yet the TP-SIP-MS

Table 3 Isomer shifts, quadrupole splittings and linewidths derived from a variable-temperature ^{57}Fe Mössbauer study of FMDMACI

T/K	δ (± 0.02)/mm s $^{-1}$	$\Delta/2$ (± 0.02)/mm s $^{-1}$	$\Gamma/2(1)$ (± 0.02)/mm s $^{-1}$	$\Gamma/2(r)$ (± 0.02)/mm s $^{-1}$	normalised area	χ^2
15	0.41	1.18	0.13	0.13	2.04	0.504
33	0.41	1.18	0.13	0.13	1.89	0.772
50	0.41	1.18	0.14	0.14	1.82	1.074
80	0.40	1.17	0.16	0.15	1.56	0.663
100	0.40	1.17	0.14	0.14	1.35	1.065
120	0.39	1.17	0.16	0.15	1.21	0.872
140	0.39	1.17	0.15	0.14	1.05	0.810
160	0.39	1.17	0.17	0.16	0.93	0.897
200	0.36	1.17	0.17	0.16	0.70	0.799
250	0.34	1.16	0.18	0.16	0.46	0.975
300	0.34	1.16	0.20	0.16	0.31	1.726

Table 4 Isomer shifts, quadrupole splittings, linewidths and areas derived from a variable-temperature ^{57}Fe Mössbauer study of FMDMA $^+$ -WL

T/K	phase ^a	δ (± 0.02)/mm s $^{-1}$	$\Delta/2$ (± 0.02)/mm s $^{-1}$	$\Gamma/2(1)$ (± 0.02)/mm s $^{-1}$	$\Gamma/2(r)$ (± 0.02)/mm s $^{-1}$	normalised area	relative area ($\pm 2.5\%$)	χ^2
15	S(1)	0.24		0.48		0.18	15	0.604
15	Q(1)	0.33	0.41	0.24	0.24	0.05	5	0.604
15	Q(2)	0.43	1.21	0.14	0.15	0.93	80	0.604
50	S(1)	0.24		0.48		0.17	16	0.559
50	Q(1)	0.33	0.43	0.24	0.24	0.54	5	0.559
50	Q(2)	0.42	1.22	0.15	0.15	0.82	79	0.559
80	S(1)	0.24		0.48		0.17	18	0.582
80	Q(1)	0.33	0.41	0.24	0.24	0.07	7	0.582
80	Q(2)	0.42	1.21	0.14	0.15	0.69	75	0.582
160	S(1)	0.24		0.49		0.17	28	0.572
160	Q(1)	0.29	0.42	0.24	0.24	0.07	11	0.572
160	Q(2)	0.39	1.21	0.13	0.13	0.39	61	0.572
240	S(1)	0.24		0.50		0.20	44	0.540
240	Q(1)	0.29	0.45	0.23	0.23	0.03	7	0.540
240	Q(2)	0.35	1.20	0.12	0.14	0.23	49	0.540
300	S(1)	0.23		0.48		0.18	54	0.607
300	Q(1)	0.30	0.49	0.20	0.20	0.02	6	0.607
300	Q(2)	0.32	1.20	0.13	0.14	0.13	40	0.607

^a S(1)=Fe^{III} present in sample holder; Q(1)=Fe^{III} present due to isomorphous substitution in WL; Q(2)=Fe^{II} present in ferrocene unit of incorporated metallocene.

results suggested quite strongly that there were two adsorption sites, one where the entire metallocene was desorbed at temperatures below 400 °C, and a second environment where the metal centre was retained and only ligand was desorbed. In an effort to determine whether the fitting of the ^{57}Fe Mössbauer absorption data would support a two site model the spectra obtained at 15, 25, 50, 80, 100, 140, 180, 220 and 300 K for both FMDMA $^+$ -WL(3) and DMAMF-Al-PILC were subjected to a P(Q) analysis. The P(Q) fitting program assumes a distribution of sites and an effective distribution of electric field gradients and corresponding quadrupole splittings. Some line broadening away from the theoretical natural linewidth is expected owing to saturation effects and sample inhomogeneity. This fitting procedure indicated that there was no evidence for more than one unique site which would result in changes in the quadrupole splitting larger than the normal line broadening effects. This indicated that the Mössbauer data would only support one type of site. Consequently, it must be considered that at temperatures below 300 K the adsorption sites for FMDMA $^+$ cations were indistinguishable.

The Debye temperature, θ_D , and corresponding recoil-free fraction, f , provide information regarding how tightly the iron-containing species is bound within a structure. Previous variable-temperature Mössbauer studies of organometallic species adsorbed in clays have shown that incorporation may result in a lower Debye temperature and recoil-free fraction. The ln

(area) vs. temperature data reported by Simopoulos *et al.*²¹ for dimethyltin species adsorbed on montmorillonite exhibited a discontinuity near 210 K at which the gradient of the line increased considerably, although linearity was retained. This feature was attributed to the melting of the interlayer water which resulted in a lower recoil-free fraction for the Sn atoms. Dehydration of the samples removed the discontinuity, hence corroborating the interpretation. In contrast, the Debye temperature and recoil-free fraction of the *N*-methyl-3-(triphenylstannyl)pyridinium cation changed little upon adsorption onto the cation-exchange sites in montmorillonite,²² whereas the half-sandwich iron cations, tricarbonyl(η^5 -2,4-dimethylcyclohexadienyl)iron(1+), and tricarbonyl(η^5 -2-methoxycyclohexadienyl)iron(1+), typically gave Debye temperatures 30 K lower when occupying the exchange sites in WL than when incorporated in a PF₆⁻ lattice.⁹ This was attributed to the cations being less tightly bound when incorporated between the layers of the clay than when locked within the anionic (PF₆⁻) lattice. Clearly, the more hydrophobic the incorporated organometallic species, the less influence the melting of incorporated solvent has on the recoil free fraction, hence no discontinuities are observed.

The values for θ_D and $f_{291\text{ K}}$ for the samples studied here are collected in Table 6. The similar Debye temperatures obtained for the FMDMA $^+$ cation in WL, irrespective of preparation method, suggests that the recoiling mass in WL is

Table 5 Isomer shifts, quadrupole splittings, linewidths and areas derived from a variable-temperature ^{57}Fe Mössbauer study of DMAMF-Al-PILC

T/K	phase ^a	δ (± 0.02)/mm s ⁻¹	$\Delta/2$ (± 0.02)/mm s ⁻¹	$\Gamma/2(1)$ (± 0.02)/mm s ⁻¹	$\Gamma/2(r)$ (± 0.02)/mm s ⁻¹	normalised area	relative area ($\pm 2.5\%$)	χ^2
14	Q(1)	-0.03	0.19	0.20	0.20	0.10	13	0.674
14	Q(2)	0.66	0.19	0.30	0.30	0.07	9	0.674
14	Q(3)	0.43	1.22	0.18	0.18	0.61	78	0.674
25	Q(1)	-0.03	0.19	0.20	0.20	0.11	14	0.586
25	Q(2)	0.66	0.19	0.30	0.30	0.07	10	0.586
25	Q(3)	0.43	1.22	0.18	0.18	0.57	76	0.586
50	Q(1)	-0.03	0.19	0.20	0.20	0.12	18	0.591
50	Q(2)	0.66	0.19	0.30	0.30	0.09	14	0.591
50	Q(3)	0.43	1.22	0.14	0.15	0.42	68	0.591
80	Q(1)	-0.08	0.17	0.20	0.20	0.09	17	0.720
80	Q(2)	0.63	0.19	0.30	0.30	0.09	17	0.720
80	Q(3)	0.42	1.20	0.21	0.21	0.34	66	0.720
100	Q(1)	-0.03	0.19	0.20	0.20	0.11	22	0.599
100	Q(2)	0.66	0.19	0.30	0.30	0.08	16	0.599
100	Q(3)	0.41	1.21	0.20	0.20	0.31	62	0.599
140	Q(1)	-0.05	0.19	0.20	0.20	0.10	25	0.573
140	Q(2)	0.66	0.19	0.30	0.30	0.08	19	0.573
140	Q(3)	0.41	1.20	0.25	0.25	0.23	56	0.573
180	Q(1)	-0.05	0.19	0.20	0.20	0.10	32	0.575
180	Q(2)	0.68	0.19	0.30	0.30	0.08	24	0.575
180	Q(3)	0.40	1.20	0.17	0.17	0.14	44	0.575
220	Q(1)	-0.08	0.18	0.20	0.20	0.09	35	0.571
220	Q(2)	0.66	0.19	0.30	0.30	0.07	28	0.571
220	Q(3)	0.39	1.20	0.18	0.18	0.09	36	0.571
300	Q(1)	-0.08	0.19	0.20	0.20	0.09	45	0.594
300	Q(2)	0.68	0.19	0.30	0.30	0.07	35	0.594
300	Q(3)	0.37	1.20	0.16	0.17	0.04	20	0.594

^a Q(1)=Fe^{III} present in fired Al-PILC; Q(2)=Fe^{III} present due to isomorphous substitution in WL; Q(3)=Fe^{II} present in ferrocene unit of incorporated metallocene.

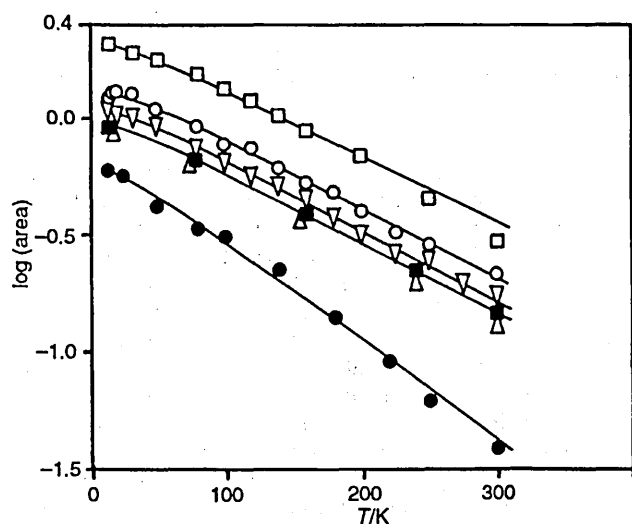


Fig. 8 Variation of Mössbauer absorption line area with temperature for \square , FMDMACl; Δ , FMDMA⁺-WL(1); \circ , FMDMA⁺-WL(2); ∇ , FMDMA⁺-WL(3); \blacksquare , DMAMF-WL and \bullet , DMAMF-Al-PILC

the same as that in chloride salt. In contrast, the Debye temperature, θ_D , and corresponding recoil-free fraction, $f_{291\text{K}}$, for the DMAMF-Al-PILC complex were much lower at 118 K and 0.06, respectively, revealing that the metallocene was much less tightly bound. This is commensurate with a model in which the metallocene, which is probably the FMDMA⁺ cation, resides in a much freer environment in the PILC where the gallery height is larger than the FMDMA⁺ cation. This

Table 6 Values for the Debye temperature and recoil free fraction for samples described in the text

sample	$\theta_D(\pm 4)/\text{K}$	$f_{291\text{K}}(\pm 0.01)$
FMDMACl	144	0.14
FMDMA ⁺ -WL(1)	139	0.13
FMDMA ⁺ -WL(2)	144	0.15
FMDMA ⁺ -WL(3)	139	0.12
DMAMF-WL	138	0.12
DMAMF-Al-PILC	118	0.06

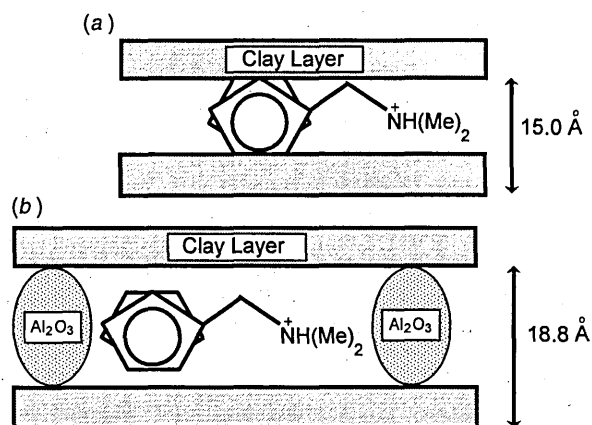


Fig. 9 Schematic illustrations of the probable orientation of the FMDMA⁺ cation in (a) WL and (b) Al-PILC

contrasts with the situation in FMDMA⁺-WL where the organoiron cation itself determines the layer expansion. Consequently, it is envisaged that in FMDMA⁺-WL the rings of the metallocene unit are keyed into the aluminosilicate layer and are tightly held [Fig. 9(a)]. This would account for the lower than expected layer expansion and would mean that the Fe would be the only recoiling mass. In the DMAMF-Al-PILC it is reasonable to assume that the metallocene is anchored *via* the dimethylamino group and that the cyclopentadienyl rings are not tightly held [Fig. 9(b)]. Hence the metallocene unit would enjoy considerably more freedom in the gallery space of the PILC than in the cramped, interlayer environs of FMDMA⁺-WL(1)-(3).

Other workers³ have found that unsubstituted ferrocene, which is essentially spherical with an effective diameter of 7 Å, appears to have almost complete three-dimensional freedom at room temperature in AlPO₄-5 and AlPO₄-8, both of which have channels of diameter greater than 7.8 Å. This rapid rotation of the ferrocene molecule changes the average electric-field gradient for ⁵⁷Fe to zero and consequently a singlet is observed in the Mössbauer spectrum. In FMDMA⁺-WL and DMAMF-Al-PILC, a doublet is observed at all temperatures indicating that the aminomethylmetallocene does not rotate rapidly within these layered hosts. Fig. 9, which depicts the schematic orientation of FMDMA⁺ ion in both WL and Al-PILC, shows that there is little room for the FMDMA⁺ cation to rotate in WL and the bulky side chain must prevent this cation rotating within the larger gallery space in Al-PILC. The influence of bulky side chains on the freedom of organoiron species in clays has been noted previously.⁹

Conclusions

FMDMACl has been prepared and characterised using a number of techniques. FMDMA⁺ cations have been successfully used to displace the resident Na⁺ cations from the interlamellar exchange sites in WL and loadings up to 80% cec have been achieved. PXRD indicates that a single layer of metallocene is incorporated between the sheets and the resulting layer spacing of 15.1 Å is lower than anticipated, suggesting some keying of the molecule into the aluminosilicate layer. The single-layer complex is stable to 200 °C whereupon it collapses to 13.0 Å. TP-SIP-MS data clearly show that a small proportion of the incorporated metallocene is volatilised at temperatures below 400 °C, but that the majority of the metallocene degrades *via* loss of the cyclopentadienyl ligands. A similar thermal degradation path was observed for

DMAMF-Al-PILC. ⁵⁷Fe Mössbauer spectroscopy revealed that the FMDMA⁺ cation occupied a similar environment in the chloride salt, FMDMA⁺-WL and DMAMF-Al-PILC, insofar as the isomer shift and quadrupole splitting of the incorporated metallocene were essentially the same in all complexes. However, variable-temperature ⁵⁷Fe Mössbauer spectroscopy confirmed that the metallocene enjoyed much greater freedom in the galleries of the Al-PILC.

We are indebted to Dr. Rob Brown and Gareth Parkes of the Catalysis Research Unit at Leeds Metropolitan University for the TP-SIP-MS results.

References

- 1 K. Moller, A. Borvornwattananont and T. Bein, *J. Phys. Chem.*, 1989, **93**, 4562.
- 2 G. A. Ozin and J. Godber, *J. Phys. Chem.*, 1989, **93**, 878.
- 3 A. Lund, D. G. Nicholson, R. V. Parish and J. P. Wright, *Acta Chem. Scand.*, 1994, **48**, 738.
- 4 A. Lund, D. G. Nicholson, G. Lamble and B. Beagley, *J. Mater. Chem.*, 1994, **4**, 1723.
- 5 M. Endregard, D. G. Nicholson, M. Stocker and B. Beagley, *J. Mater. Chem.*, 1995, **5**, 485.
- 6 E. Rodriguez-Castellon, A. Jimenez-Lopez, M. Martinez-Lara and L. Moreno-Real, *J. Inclusion Phenom.*, 1987, **6**, 335.
- 7 S. J. Mason, L. M. Bull, C. P. Grey, S. J. Heyes and D. O'Hare, *J. Mater. Chem.*, 1992, **2**, 1189.
- 8 S. Okuno and G. Matsubayashi, *J. Chem. Soc., Dalton Trans.*, 1992, 2441.
- 9 C. Breen, J. S. Brooks, S. Forder, A. A. Maggs, G. Marshall and G. R. Stephenson, *J. Mater. Chem.*, 1995, **5**, 97.
- 10 C. Breen, J. Madejová and P. Komadel, *J. Mater. Chem.*, 1995, **5**, 469.
- 11 R. Schoonheydt, J. van den Eynde and W. Stone, *Clays Clay Miner.*, 1994, **41**, 598.
- 12 G. Brown, B. Edwards, E. G. Ormerod and A. H. Weir, *Clay Miner.*, 1972, **9**, 407.
- 13 A. Molinard, PhD thesis, The University of Antwerp, 1994.
- 14 C. Breen, A. T. Deane and J. J. Flynn, *Clay Miner.*, 1987, **22**, 169.
- 15 P. A. Barnes and G. M. G. Parkes, *J. Thermal Anal.*, 1993, **39**, 607.
- 16 N. N. Greenwood and A. Earnshaw, *Chemistry of the Elements*, Pergamon Press, Oxford, 1984, p. 1236.
- 17 J. W. Johnson, *J. Chem. Soc., Chem. Commun.*, 1980, 263.
- 18 P. Aldebert and V. Paul-Boncour, *Mater. Res. Bull.*, 1983, **18**, 1263.
- 19 C. F. Lee, L. K. Myers, K. G. Valentine and M. E. Thompson, *J. Chem. Soc., Chem. Commun.*, 1992, 201.
- 20 M. Hillman and A. G. Nagy, *J. Organomet. Chem.*, 1980, **184**, 433.
- 21 A. Simopoulos, D. Petridis, A. Kostikas and N. Gangas, *Hyperfine Interact.*, 1988, **41**, 843.
- 22 K. C. Molloy, C. Breen and K. Quill, *Appl. Organomet. Chem.*, 1987, **1**, 21.

Paper S/05572E; Received 22nd August, 1995